Contents

List of Figures

List of Tables

Glossary of Symbols

Chapter 1

(X, Y)	Melanoma site coordinates
$(randX, randY)$	Random melanoma site coordinates

Chapter 2

ξ	Local or material coordinate
ϕ_n	Lagrange basis function
ψ_n^m	Hermite basis function
$\mathbf{u}_n$	FE geometry (x,y,z) or field value at node n
$\mathbf{u}(\xi)$	FE continuum field evaluated at ξ
$\left.\frac{\partial \mathbf{u}}{\partial \xi}\right\|_n$	FE geometry (x,y,z) or field derivative at node n
s	Arc-length
L	Arc-length scale-factor
$\mathbf{z}_d$	Global coordinates of data point d
D	Least-squares distance function
F	Fitting objective function
w_d	Weight of data point d
F_s	Sobolev smoothing term
N	Total number of data points
α_i, $i = 1..5$	Sobolev weighting terms
η_i, $i = 1..3$	Slave mesh material coordinates
ξ_i, $i = 1..3$	Host mesh material coordinates

Chapter 4

N_X	Approximate number of elements in the X-direction per grid unit
N_Y	Approximate number of elements in the Y-direction per grid unit
G	Side dimension of a body map grid unit
$(rand\xi_1, rand\xi_2)$	Local coordinates of a random melanoma site $(randX, randY)$

Chapter 6

θ	Angle of Sappey's midline plane
$\mathbf{u}, \mathbf{v}, \mathbf{w}$	Geometric coordinates (x,y,z) on Sappey's midline plane
$\mathbf{n}$	Normal vector to Sappey's midline plane
$\mathbf{u}_m$	Melanoma site coordinate
e	Equation of Sappey's midline plane
e_m	Equation of a plane passing through melanoma site $\mathbf{u}_m$
w_v	Vertical width of ambiguous drainage on the trunk
w_h	Horizontal width of ambiguous drainage on the trunk
n_t	Number of trials
p_i, $i = 1..k$	Probability trial classified in category i, out of k categories
Y_i, $i = 1..k$	Number of times outcome i observed out of k categories
f_i, $i = 1..q$	Likelihood of drainage to node field i
β_i, $i = 0..k$	Multinomial model parameters
γ_i, $i = 1..k$	Linear predictor
$\hat{\sigma}^2$	Estimate of the error variance
K	Number of multinomial model parameters
(ξ_{1r}, ξ_{2r})	Local coordinates of a reflected melanoma site
n_c	Number of samples for cluster classification
m	Number of characteristics to define samples
X_{ij}, $i = 1..n_c$, $j = 1..m$	Number of objects in sample i, classified by characteristic j
d_{ik}, $i = 1..n_c$, $k = 1..n_c$	Euclidean distance between samples i and k
d_{check}	Check distance
n	Number of observations
$\mathbf{x}$ or x_i, $i = 1..n$	Set of n observations
$s(\mathbf{x})$	Statistic of interest of observation $\mathbf{x}$
$\mathbf{x}^{*i}$, $i = 1..B$	Set of B bootstrap samples
$s(\mathbf{x}^*)$	Sample statistic

Glossary of Acronyms

1D	One-Dimensional
2D	Two-Dimensional
3D	Three-Dimensional
AAO-HNS	American Academy of Otolaryngology-Head and Neck Surgery
ABI	The University of Auckland's Bioengineering Institute
AIC	Akaike Information Criterion
AJCC	American Joint Committee on Cancer
CLND	Complete Lymph Node Dissection
CMGUI	CMISS Graphical User Interface
CMISS	Continuum Mechanics, Image analysis, Signal processing and System Identification
CT	Computed Tomography
DOF	Degree of Freedom
FE	Finite Element
GEE	Generalised Estimator Equation
GLM	Generalised Linear Model
L2	Second Lumbar Vertebra
L3	Third Lumbar Vertebra
L4	Fourth Lumbar Vertebra
LL	Lower Left
LR	Lower Right
LS	Lymphoscintigraphy
MRI	Magnetic Resonance Imaging
RMS	Root Mean Square
SNB	Sentinel Node Biopsy
SMU	Sydney Melanoma Unit
SN	Sentinel Node
SPECT	Single Photon Emission Computed Tomography

TIS	Triangular Intermuscular Space
UL	Upper Left
UR	Upper Right
VH	Visible Human

Chapter 1

Introduction

1.1 Motivation

Cutaneous melanoma is an aggressive form of skin cancer which has increased in incidence over recent decades in most Western countries (Thompson, Scolyer & Kefford 2005). In particular, both New Zealand and Australia have very high incidence rates of the disease. The most recent statistics available show that in 2004 melanoma was the most common cancer affecting 25 - 44 year old males in New Zealand, and the most common cancer affecting 15 - 24 year old females (NZHIS 2007). Meanwhile for the same year in Australia, melanoma was the fourth most common cancer in men and the third most common cancer in women (AIHW 2008).

Melanoma that is left untreated can spread quickly throughout the body, significantly decreasing a patient's chance for survival. Usually a primary melanoma on the skin will first metastasise via the lymphatic system to regional lymph nodes, before spreading to more distant sites. Currently there is no highly effective treatment for disseminated disease, and early diagnosis and treatment remain vital to reduce disease mortality. Studies have shown that the single most important prognostic factor for melanoma is whether there is metastatic disease in regional lymph nodes draining the primary tumour (Balch, Soong, Gershenwald et al. 2001). The ability to locate lymph nodes that drain the primary melanoma for biopsy is therefore crucial for optimum patient management.

The way melanoma spreads from the skin to lymph nodes is not clinically predictable however, and significant variability exists between patients. It has been reported that predictions of skin lymphatic drainage based on historical assumptions are probably incorrect in 30% of individuals (Thompson & Uren 2005). Individualised treatment is therefore necessary in each patient, to track which lymph nodes will receive the first cancerous cells if melanoma has spread beyond the skin.

This can be conducted using lymphoscintigraphy (LS) imaging which locates the lymph nodes draining the primary melanoma. Accumulated LS data shows patterns of lymphatic drainage, indicating likely routes of melanoma spread from the skin.

Opportunity now exists to improve visualisation and analysis of lymphatic drainage of the skin using melanoma LS data, thereby providing clinicians with a better understanding of melanoma metastasis. Researchers at the Auckland Bioengineering Institute (ABI)[1], at the University of Auckland, New Zealand, have developed computationally efficient methods for accurately modelling anatomical structures (Crampin et al. 2004). These models provide the ability to incorporate physiological function into the anatomical geometry, creating fully integrated anatomical models.

This project has been conducted at the ABI in collaboration with the Sydney Melanoma Unit (SMU)[2], at Royal Prince Alfred Hospital in Sydney, Australia. The SMU has been treating patients with melanoma since it was established in the 1960s (SMU 2005). Over the last four decades it has become the world's largest melanoma unit, treating approximately one third of all melanoma patients in New South Wales. It is also a major referral centre for melanoma patients around the world where approximately 1200 new patients and 8000 follow-up patients are treated each year. Nuclear medicine physicians at the SMU have been performing LS imaging for over 20 years, accumulating a comprehensive dataset of over 5000 patients which has been used in this study.

The remainder of this chapter provides background on cutaneous melanoma, how it can spread through the lymphatic system, and current forms of treatment. Previous studies of lymphatic anatomy and historical views about skin lymphatic drainage are discussed. A full description of the SMU's method of lymphatic mapping using LS is provided, followed by information regarding how the SMU have recorded and previously visualised their LS data in two-dimensions (2D). The ability to develop highly detailed anatomical models at the ABI is then discussed and the underlying techniques are proposed as a method to improve visualisation of lymphatic drainage patterns in three-dimensions (3D) using the SMU's LS data. Lastly, an overview of this thesis is given.

1.2 Cutaneous melanoma

Cutaneous melanoma is a highly malignant tumour of the melanocytes, the skin's pigment cells. It arises in the epidermis of the skin, usually appearing as a darkly pigmented lesion termed the 'primary' melanoma (Figure 1.1). The disease is associated with excessive sun exposure, particularly in people of European origin with fair skin.

[1] http://www.bioeng.auckland.ac.nz/
[2] http://www.smu.org.au/

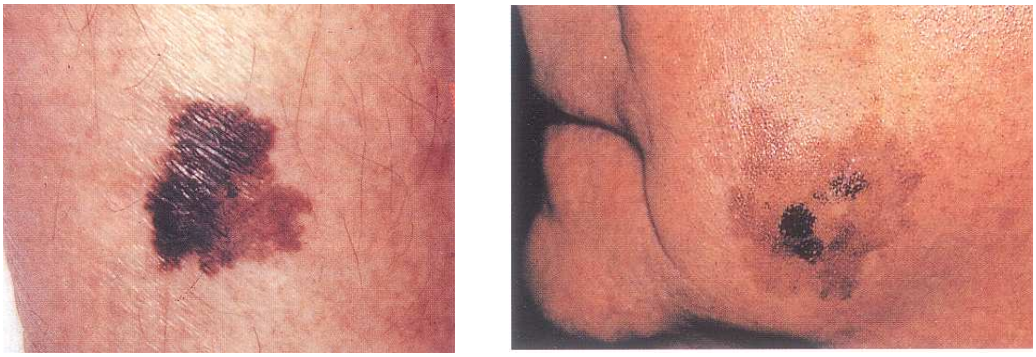

(a) (b)

Figure 1.1: Cutaneous melanoma. Reproduced from Balch et al. (1998).

Primary melanomas can develop anywhere on the skin, even in sites that have not been previously exposed to the sun. Although it is rare, melanoma can also occur in the eye, nervous system and mucous membranes. The likelihood of developing the disease is increased according to various factors. Major risk factors include: having fair-skin, a history of severe sunburn, excessive sun exposure, a family history of melanoma, and having a large number of unusual moles or freckles (Thompson et al. 2004).

Without treatment, a primary melanoma can grow deeper into the skin, enabling cancerous cells to enter lymphatic vessels or blood vessels. Cells that have entered lymphatic vessels can then travel to lymph nodes to create secondary tumours. From the lymph nodes, melanoma can metastasise to distant sites to create additional tumours, for example, within the lungs or the brain. Although it is less common, melanoma cells can also metastasise directly from the primary melanoma to distant sites through the bloodstream. Figure 1.2 schematically shows the typical sequence of melanoma spread throughout the body.

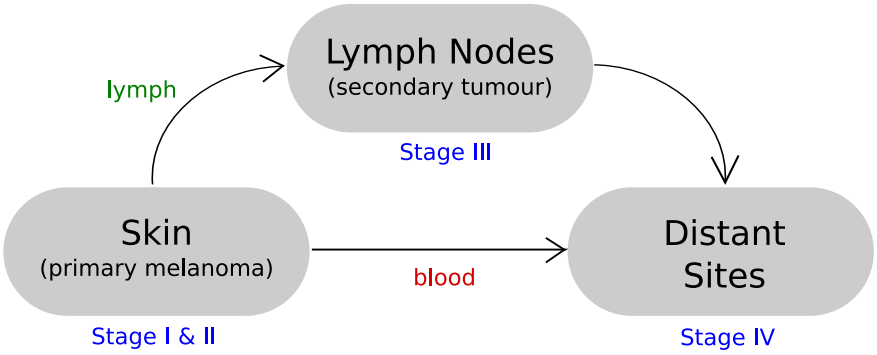

Figure 1.2: The sequence of melanoma spread through the body.

1.2.1 Staging

Patient prognosis and treatment plans are largely determined by how far the cancer has spread. Clinical categorisation (also called staging) is carried out via various diagnostic and imaging techniques to determine the extent of the disease and where it is located in the body. The American Joint Committee on Cancer (AJCC) have defined clinical stages for melanoma according to various prognostic factors (Balch, Buzaid, Soong et al 2001), which has been validated by a major study conducted across 13 cancer centres and organisations of 17,600 melanoma patients (Balch, Soong, Gershenwald et al. 2001). Table 1.1 outlines each of these stages.

Stage	Extent of the disease
IA	Tumour $\leq$1.0mm without ulceration and Clark level II/III tumour; no lymph node involvement; no distant metastases
IB	Tumour $\leq$1.0mm with ulceration or Clark level IV/V tumour, or tumour 1.01 - 2.0mm without ulceration; no lymph node involvement; no distant metastases
IIA	Tumour 1.01 - 2.0mm with ulceration, or tumour 2.01 - 4.0mm without ulceration; no lymph node involvement; no distant metastases
IIB	Tumour 2.01 - 4.0mm with ulceration, or tumour $\geq$4.0mm without ulceration; no lymph node involvement; no distant metastases
IIC	Tumour $>$4.0mm with ulceration; no nodal involvement; no distant metastases
IIIA	Tumour of any thickness without ulceration, with 1-3 lymph nodes containing micrometastases
IIIB	Tumour of any thickness without ulceration, with 1-3 positive lymph nodes, at least 1 containing macrometastasis, or tumour of any thickness with ulceration with 1-3 positive nodes and micrometastases, or in-transit metastasis/satellite(s) without metastatic nodes
IIIC	Tumour of any thickness with ulceration with 1-3 lymph nodes, at least 1 containing macrometastasis, or tumour of any thickness with 4 or more metastatic nodes, or matted nodes, or in-transit metastases/satellites with metastatic nodes
IV	Tumour of any thickness with distant metastases

Table 1.1: Clinical stages of melanoma (Balch, Soong, Gershenwald et al. 2001).

The first step involved in staging melanoma is to measure how deep the primary tumour extends into the skin in millimetres, as shown on the vertical axis in Figure 1.3. This vertical thickness measurement is termed the Breslow thickness (Breslow 1970), and provides a reliable indicator of how likely it is that the primary melanoma has spread to other parts of the body. A thin melanoma is considered to have Breslow thickness $<$1.0 mm; an intermediate thickness melanoma has Breslow thickness between 1.01 mm and 4.0 mm; while a thick melanoma has Breslow thickness $>$4.0 mm. There are also a number of additional factors that influence the prognosis, including the presence or absence of ulceration. Ulceration is defined as the absence of an intact epidermis overlying a major

portion of the primary melanoma (Balch et al. 1980), where the prognosis is worse if a primary melanoma has ulceration. Clark level is also assessed, which is defined as the level of invasion into the skin of the primary melanoma according to its anatomic layers. This is shown in Figure 1.3 on the horizontal axis, where Clark levels range from levels I to V (Clark Jr et al. 1969).

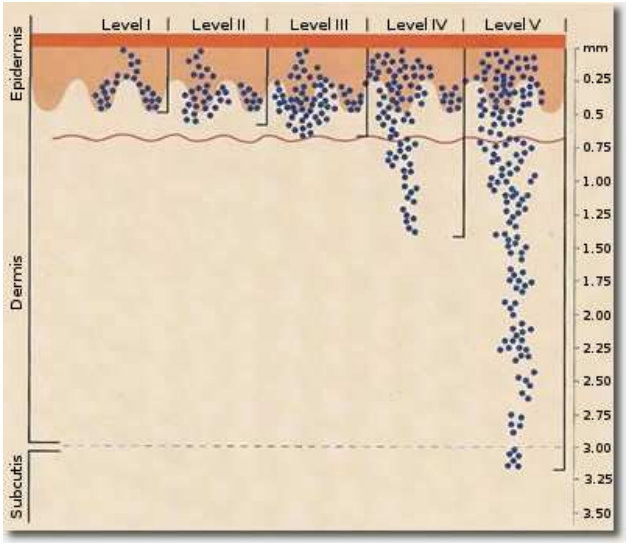

Figure 1.3: Schematic demonstrating the melanoma staging systems of both Clark and Breslow. Modified from SMU (2005).

The AJCC stages in Table 1.1 also include additional clinical features, which are defined as follows. Micrometastases, also called clinically occult metastases, are a small number of cancer cells that have spread from the primary tumor to other parts of the body which cannot be detected in a screening or diagnostic test. Macrometastases are metastases that are clinically detectable. In-transit metastases are any skin or subcutaneous metastases that are more than 2 cm from the primary melanoma, but not beyond the regional nodal basin; where the regional nodal basin is defined as lymph nodes located within a particular region of the body, such as the groin. Satellite lesions are considered intralymphatic extensions of the primary melanoma. A group of nodes that appear connected and move as a unit is said to be ‘matted’.

1.2.2 Treatment

Different treatment options are indicated according to the stage of the disease, where surgery is the primary form of treatment. At all stages the primary melanoma and skin either side of the lesion are surgically removed. The amount of skin that is removed increases in proportion to the Breslow thickness.

At the SMU, all patients with intermediate and thick melanomas, or patients with thin melanomas that are ulcerated or have other adverse features present, undergo a sentinel node biopsy (SNB). A SNB is used to detect whether melanoma cells have metastasised to the draining lymph nodes. These lymph nodes are termed 'sentinel nodes' (SNs), and are defined as 'any node receiving direct lymphatic drainage from a primary tumour site' (Thompson & Uren 2000). SNs are detected using LS, which is a nuclear medicine scan used to map the pattern of lymphatic drainage from the primary melanoma site to draining SNs. Studies have shown that if a SN is tumour free then the remaining lymph nodes in the regional lymph node basin will also be tumour free (Reintgen et al. 1994). However, if a SN contains metastases, other nodes in the regional basin may also contain metastatic melanoma and a complete lymph node dissection (CLND) is performed to remove all lymph nodes within that basin.

Recently, a study conducted to test the SNB procedure, showed that it improved disease-free survival (Morton et al. 2006), which means survival without evidence of recurrence or metastasis. This trial also showed an improvement in overall survival for patients with metastatic nodal disease who had an immediate CLND. Hence, SNB has now been clearly established as a staging procedure for melanoma and as a guide to determine patient prognosis (Thompson & Shaw 2007), and has recently been declared by the World Health Organisation as the standard of care for patients with melanoma (Cascinelli 1999).

Multiple clinical trials are presently underway to assess current approaches for melanoma treatment, and to investigate new forms of treatment. These include further assessment via magnetic resonance imaging (MRI) and computed tomography (CT) to determine whether the cancer has spread to more distant sites in the body. Radiotherapy, chemotherapy or immunotherapy are all possible adjunct therapies that can be given at later stages of the disease.

1.3 Lymphatic anatomy

Tumour metastasis is a complex process, and the ability to understand melanoma spread requires a thorough knowledge of lymphatic anatomy. The lymphatic system is regarded as a component of the circulation system, comprised of lymphatic vessels, lymph nodes, lymphoid tissue and lymphatic organs. It has three main functions, which are: to absorb excess interstitial fluid called 'lymph' and return it to the bloodstream, to absorb lipids in the gut to return to the bloodstream, and to defend the body against disease.

In contrast to the blood circulation system, relatively little research has been conducted to characterise the anatomy of the lymphatic system. This limited knowledge of lymphatic anatomy has

contributed to a lack of understanding of the patterns of lymphatic metastasis (Swartz 2001). However, in recent years it has become the focus of much research owing to its recognised importance in cancer spread. The following section details the anatomy of lymphatic vessels and lymph nodes, with particular focus on the lymphatics that drain the skin, which are of primary interest in this thesis.

1.3.1 Lymphatic vessels

Lymphatic vessels are found in all regions of the body apart from the bone marrow, central nervous system, and tissues that lack blood vessels such as the epidermis. Figure 1.4 shows selected lymphatic vessels and nodes.

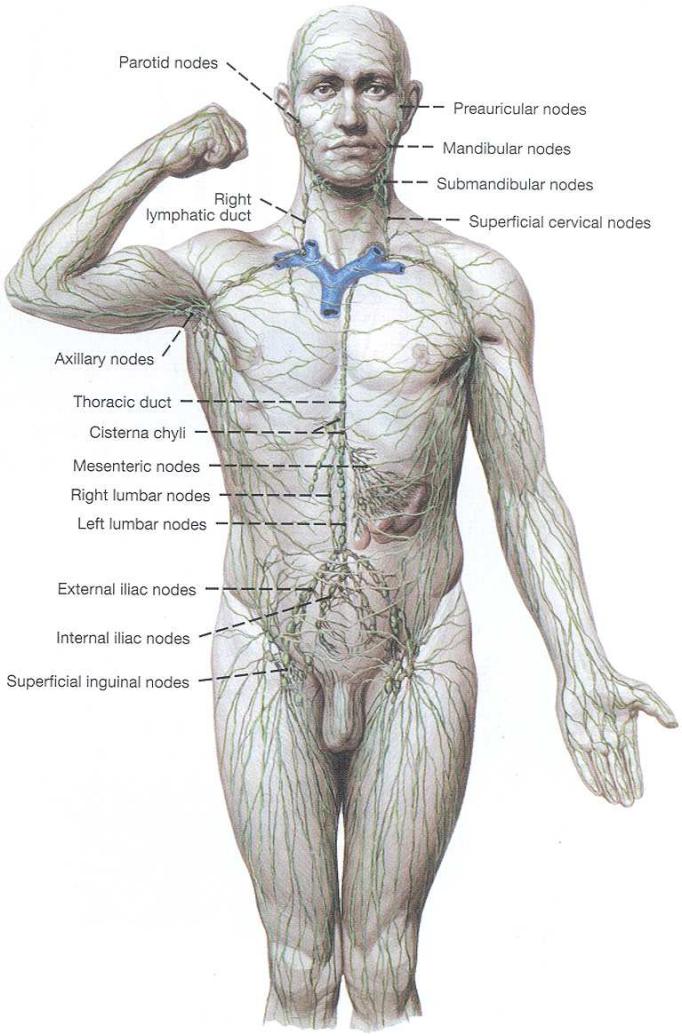

Figure 1.4: Schematic of certain lymphatics of the head, abdomen, pelvis and limbs. Reproduced from Clemente (1997).

The smallest lymphatic vessels are called lymphatic capillaries, and are comprised of a single layer of endothelial cells. In the skin they begin in the dermal papillae just below the epidermis. Lymphatic capillaries are optimally suited for fluid and particle uptake, since excess fluid easily flows into them through large gaps between adjacent endothelial cells (Swartz & Skobe 2001). This characteristic is exploited during melanoma metastasis, since this allows melanoma cells to easily enter lymphatic vessels as demonstrated in Figure 1.10 in Section 1.5.

Lymphatic capillaries eventually join to form larger lymphatic collecting vessels, which have valves spaced at regular intervals which function to move the lymph fluid unidirectionally. The flow of lymph through lymphatic vessels can be increased by heat, massage, inflammation, movement or an increase in hydrostatic pressure within the vessel lumen. An increase in the interstitial pressure can also increase the rate of lymph flow (Fischer et al. 1996). Meanwhile flow can be decreased by cold, lack of movement or external pressure.

Along the course of the lymphatic vessels lie lymph nodes. Lymph travels through these nodes, before passing to one of two lymphatic ducts where it will be emptied back into the bloodstream. The right lymphatic duct drains lymph from the right side of the head, neck, thorax, and right upper limb into the right subclavian vein. Lymph from the rest of the body flows into the thoracic duct which empties into the left subclavian vein.

1.3.2 Lymph nodes

Lymph nodes are often called glands, and are found in various locations around the body along the course of lymphatic vessels. Lymph nodes are ovoid or bean-shaped structures usually between 5 to 15 mm long. They are commonly located alongside blood vessels, and large clusters of nodes can be found in the armpits, groin, neck and abdomen. Lymph nodes act as filters to fight and destroy bacteria and viruses contained within lymph, and to initiate the immune response for fighting pathogens in draining tissue.

Figure 1.5 shows a schematic of a typical lymph node. Lymph fluid enters lymph nodes via afferent lymphatic vessels and drains into the subcapsular sinus. The subcapsular sinus drains into the cortical and medullary sinuses. A fine mesh of reticulin fibres are contained in the sinuses, which are lined with lymphocytes and phagocytes to trap and fight foreign particles. The medullary sinuses converge at the hilum, a slight indentation on one side of the node. Lymph fluid leaves the node at the hilum, via an efferent lymphatic vessel.

Regions where clusters of lymph nodes are located are called ‘node fields’. The SMU recognises 25 separate node fields that directly drain the skin, which are therefore possible sites for melanoma

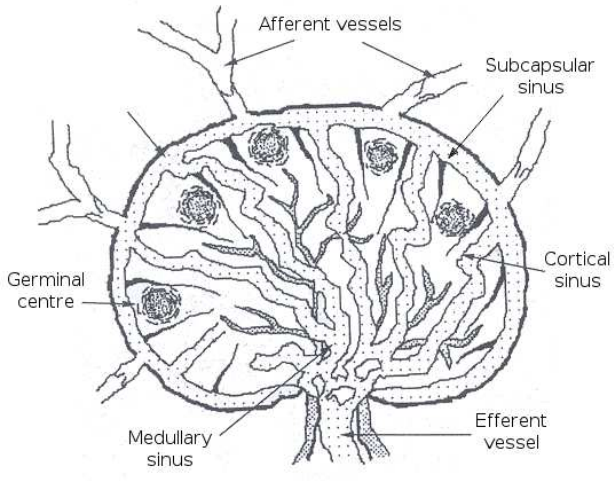

Figure 1.5: Schematic of a lymph node. Reproduced from Uren et al. (1999).

spread. Sometimes lymph nodes are located in a region of the body with no predefined node field. These nodes are called 'interval nodes' and are defined as lymph nodes draining regions of skin which lie on the course of a lymphatic vessel between the skin and a recognised node field (Uren et al. 2000). Figure 1.6 shows the location of each node field that drains the skin, as defined by the SMU, on the anatomical model constructed in Section 2.6. Table 1.2 through to Table 1.5 detail the names of each node field along with a description of its anatomical location.

Node Field	**Location**
Occipital	At the back of the head
Preauricular	In front of the ear
Postauricular	Behind the ear
Cervical:	In the neck, these nodes are categorised into five levels:
- level I	- anterior to the sternocleidomastoid muscle (includes submental nodes, but the SMU label these separately)
- level II	- around the upper third of the sternocleidomastoid muscle
- level III	- around the middle third of the sternocleidomastoid muscle
- level IV	- around the lower third of the sternocleidomastoid muscle
- level V	- posterior to the sternocleidomastoid muscle (includes supraclavicular fossa nodes, but the SMU label these separately)
Supraclavicular fossa	Above the clavicle in the 'hollow' dip
Submental	Under the chin

Table 1.2: Head and neck node field locations.

The anatomical location of the first five cervical node fields levels in the neck have been defined according to current classifications given by both the American Academy of Otolaryngology-

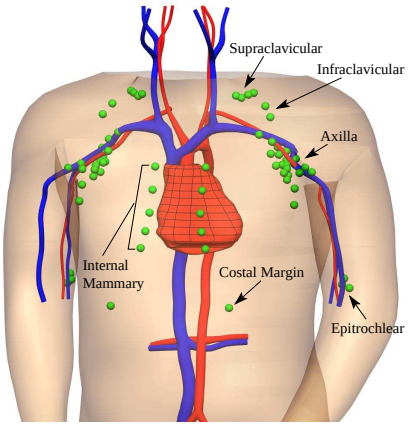

(a) Anterior

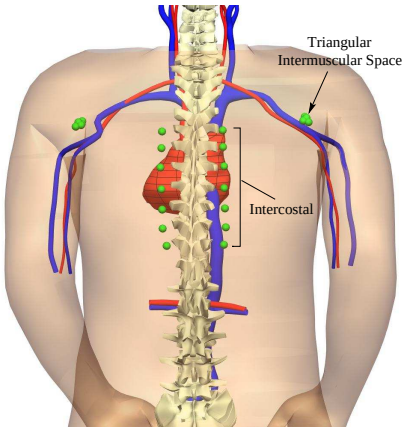

(b) Posterior

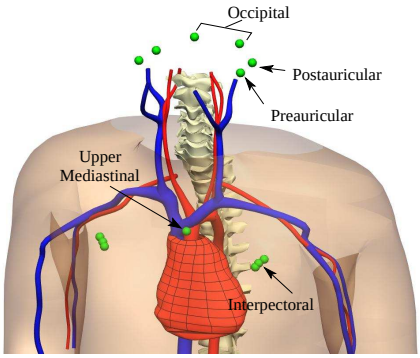

(c) Anterior

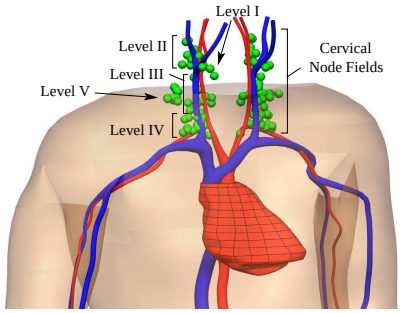

(d) Anterior

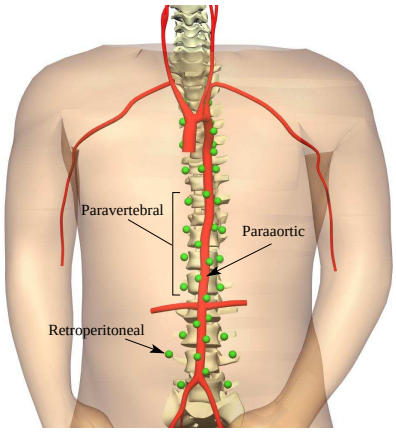

(e) Anterior

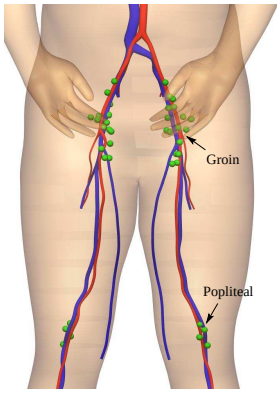

(f) Anterior

Figure 1.6: Lymph node model visualising different node field locations, shown relative to various blood vessels and the vertebral bones. The skin of the head and neck is not shown here since it was based on a different dataset than that used to create the lymph node model, so they were not in the correct geometric space relative to each other.

Head and Neck Surgery (AAO-HNS) (Robbins et al. 2002), and the AJCC (*AJCC Cancer Staging Manual* 2002). Note however, that although cervical level I technically includes submental nodes, the SMU have classified these nodes separately because they could not be classified as being in the left or right cervical level I node field. Also, cervical level V technically includes supraclavicular fossa nodes, however the SMU has classified this as a separate field. Cervical level VII nodes have been coded as upper mediastinal nodes (as detailed in Table 1.3), while cervical level VI nodes did not appear to drain the skin and therefore have not been included.

Node Field	**Location**
Axillary	Under the armpits
Epitrochlear	In the upper limb, just above the elbow crease on the medial side
Infraclavicular	Below the clavicle and beside the cephalic vein
Triangular Intermuscular Space (TIS)	Between three muscles on the back: teres major, teres minor and the long head of the triceps
Interpectoral	Between the chest muscles
Internal mammary	On either side of the sternum
Costal margin	Superficial nodes near the lower edge of the chest
Intercostal	Between the ribs
Paravertebral	Alongside the vertebrae
Paraaortic	Alongside the aorta
Retroperitoneal	Just behind the peritoneum
Upper mediastinal	Just behind the upper part of the sternum

Table 1.3: Upper limb node field locations.

Node Field	**Location**
Groin	In the groin, the superficial group of nodes are known as femoral or inguinal nodes, while the deep group of nodes are called iliac or obturator nodes
Popliteal	Behind the knee next to the popliteal artery and vein

Table 1.4: Lower limb node field locations.

Node Field	**Location**
Interval	These nodes do not lie within a generic lymph node region but between them, they can be located anywhere and are commonly located draining the skin of the back

Table 1.5: Other node field locations.

1.4 Previous lymphatic anatomy studies

As mentioned in Section 1.3, there are relatively few detailed studies of the human lymphatic system. In particular, few studies have been conducted to investigate lymphatic vessels that drain the skin. Lymphatic vessels are usually invisible to the naked eye and are very difficult to visualise effectively. Techniques have therefore been developed to enable visualisation of these vessels, including distension of the vessels, and using a substance to dye them.

In 1874, the Frenchman Sappey conducted a study on the lymphatics (Sappey 1874), by injecting mercury into the interstitial tissue and into lymphatic vessels of cadavers. He published his results in an extensive atlas which contained a number of highly detailed anatomical drawings. Figure 1.7 shows two of these drawings, delineating the superficial lymphatic vessels of the anterior and posterior trunk. Sappey's atlas and conclusions about lymphatic drainage were accepted as correct for over 100 years by the scientific and medical community. He claimed that lymphatic drainage from skin of the trunk never crossed the midline of the body, nor a theoretical horizontal line drawn around the waist. These lines were termed 'Sappey's lines' and defined four zones of skin on the trunk, from which Sappey claimed lymphatic drainage would occur to the corresponding axillary or groin node field. These lines were adopted by clinicians treating melanoma patients as a guideline for predicting metastatic spread.

Sappey's concepts of skin lymphatic drainage were challenged in the 1970's, 80's and 90's, largely due to LS studies in melanoma patients. Sugarbaker & McBride (1976) showed that lymphatic drainage was unpredictable from a strip of skin 2.5 cm either side of Sappey's lines (as shown in Figure 1.8). They suggested new clinical guidelines to include this area of ambiguous drainage, however they still maintained that skin outside these zones would follow Sappey's original predictions.

Additional studies over the years, including those by Fee et al. (1978), Meyer et al. (1979), Sullivan et al. (1981), Bergqvist et al. (1984) and Eberbach & Wahl (1989), demonstrated further variability of skin lymphatic drainage. Through these studies it was shown that Sugarbaker and McBride's guidelines were not always correct. Later, Norman et al. (1991) expanded the area of ambiguous drainage to include the head and neck and a much larger area of skin on the trunk, up to 11 cm either side of Sappey's lines (as shown in Figure 1.9).

LS studies conducted at the SMU have also visualised variable patterns of skin lymphatic drainage, some which had not been previously reported. They observed that in all areas of skin ipsilateral drainage tended to occur, however contralateral drainage was not uncommon. Some of the unusual patterns that were seen included: drainage to internal mammary nodes from peri-umbilical skin

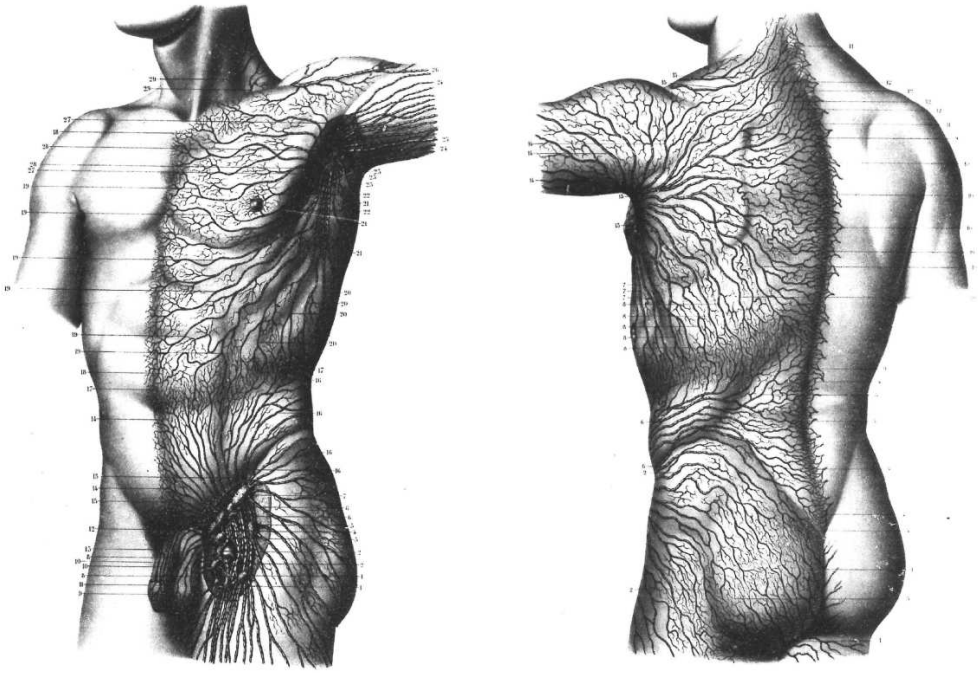

(a) (b)

Figure 1.7: Sappey's detailed drawings showing superficial lymphatic vessels of the (a) anterior trunk and (b) posterior trunk. Reproduced from Sappey (1874).

(Uren et al. 1995), drainage to the TIS node field from skin of the back (Uren et al. 1996), and drainage to paravertebral and retroperitoneal nodes from the back (Uren, Howman-Giles, Thompson & McCarthy 1998). These SMU studies confirmed that lymphatic drainage from skin of the head and neck is highly complex, often involving multiple node fields (de Wilt et al. 2004). Furthermore, results proved again that Sappey's assertions about the predictability of lymphatic drainage could not be relied upon, and it was estimated that his guidelines would predict drainage to the incorrect node field in 30% of patients (Thompson & Uren 2005).

LS studies at multiple cancer centres around the world also confirmed that deterministic clinical prediction of lymphatic drainage from almost any skin site is not possible. Studies conducted in the United States (Leong et al. 1999), in the United Kingdom (O'Toole et al. 2000), and in Europe (Statius Muller et al. 2002) have all demonstrated clinical unpredictability. In addition, LS studies have shown that previous surgery or radiotherapy can disturb normal lymphatic drainage patterns. An example of this was seen at the SMU from a patient who had unexpected drainage to internal mammary nodes from skin on the anterior chest (Thompson, Uren, Saw & Stevens 2005), after having an axillary dissection as well as radiotherapy to axillary, supraclavicular and paraaortic nodes many years earlier.

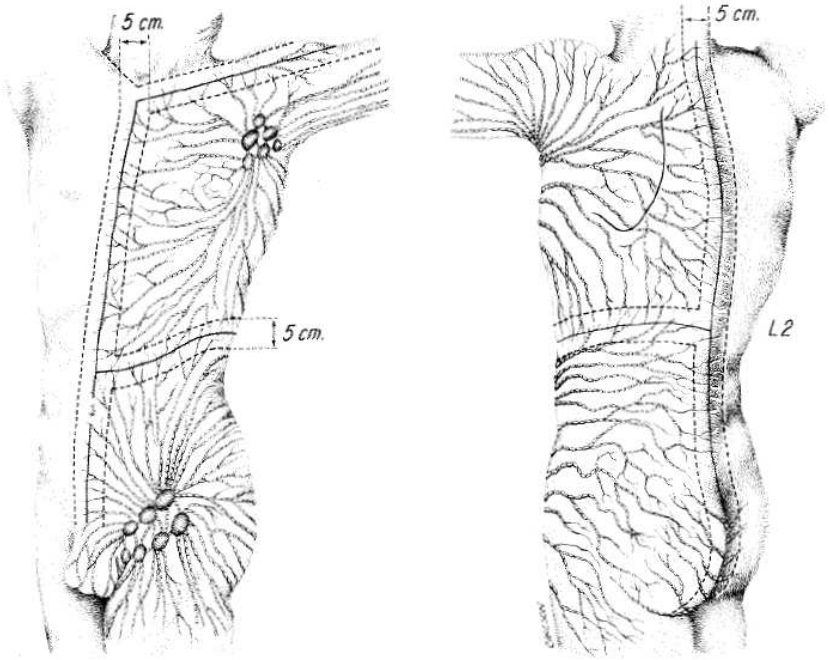

(a) (b)

Figure 1.8: A zone of ambiguous lymphatic drainage defined 2.5 cm either side of Sappey's lines shown on the (a) anterior trunk and (b) posterior trunk. Reproduced from Sugarbaker & McBride (1976).

Other lymphatic studies carried out in the last decade include those by Suami et al. (2005), who developed a new technique to identify the lymphatics in adult human cadavers. This technique has been conducted using radiographic injections followed by meticulous dissection of the vessels, and has been applied to delineate lymphatics of the upper limb. A large number of lymph node atlases have also been developed as an essential clinical tool to assist defining target volumes for cancer radiation treatment. These atlases have been largely based on MRI and CT images. Martinez-Monge et al. (1999) developed a cross-sectional nodal atlas using CT images, defining clinical target volumes of the head and neck, thorax, abdomen, male and female pelvis, while Poon et al. (2004) developed a population-based lymph node map of the head and neck using MRI images.

Another recent study has taken the idea of a lymph node atlas one step further, creating a volumetric 3D atlas of lymph node topography rather than limiting the atlas to 2D. This 3D atlas was created by Qatarneh et al. (2006) using images from the Visible Human male dataset (Spitzer et al. 1996). Approximately 1200 lymph nodes were localised on image slices which were then compared and verified with current lymphatic atlases. These located lymph nodes were then added to a whole 3D body database with the purpose of assisting radiotherapy treatment planning.

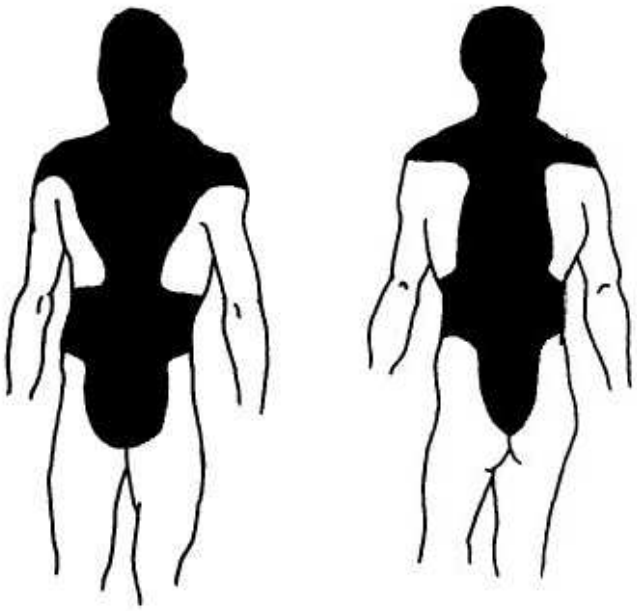

(a) (b)

Figure 1.9: Areas of skin with ambiguous lymphatic drainage shaded in black, (a) anterior and (b) posterior views. Reproduced from Norman et al. (1991).

1.5 Lymphatic mapping and sentinel node biopsy

Lymphatic mapping via LS imaging is a technique utilised during the SNB procedure (introduced in Section 1.2.2). This procedure was first described by Morton et al. (1992) for melanoma, and involves three steps: (1) lymphatic mapping to locate the SNs, (2) surgery to remove SNs and (3) examination of the SNs. The following describes how these steps are implemented at the SMU (Uren et al. 2004):

1. **Lymphatic mapping to locate sentinel nodes.**
   Lymphatic mapping via LS imaging is conducted on each melanoma patient to accurately locate SNs before they are surgically removed for assessment.

   A radioactive isotope is injected intradermally around the primary melanoma or excision biopsy site. Radiocolloids with diameter 5 - 50 nm are ideal for lymphatic mapping of the skin based on the microanatomy of the lymphatic capillaries (as shown in Figure 1.10). The SMU and other melanoma centres across Australia uses 99m-Technetium antimony sulfide colloid that has a fairly uniform particle size of around 10 nm, with some particles measuring up to 50 nm. The type of radiopharmaceuticals used differ around the world, according

to availability and approved practice. For example, only large particle radiocolloids are approved for human use in some countries, including the US, which require filtration through a 100 to 200 nm filter to produce an adequate product for LS of the skin (Alazraki et al. 1997).

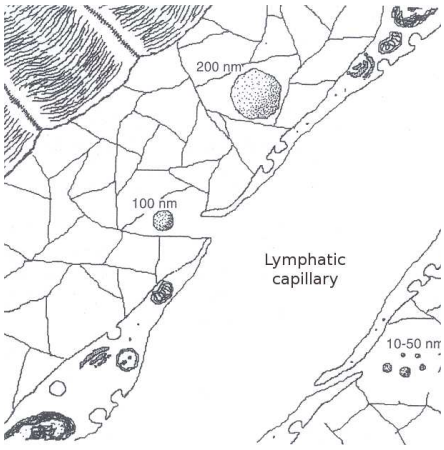

Figure 1.10: A lymphatic capillary with gaps between adjacent endothelial cells allowing particles to enter. Reproduced from Uren et al. (1999).

Typically four injections are required, although this will depend on the size of the primary melanoma. Almost immediately this tracer enters the lymphatic vessels draining that area of skin. Particle entry can be enhanced by massage, which significantly increases the gap between endothelial cells. The tracer then travels through the vessels to lymph nodes where it is recognised as foreign, and becomes trapped through opsonisation of the colloid. The opsonised radiocolloid is then phagocytosed by the macrophages and tissue histiocytes which line the subcapsular sinus and other sinuses of the lymph node (Uren et al. 2006). The majority of the injected radiocolloid will remain at the injection site, so the relative radioactivity in SNs is small.

LS imaging is started immediately after injections are given, using a gamma camera (a high resolution collimator) to detect radiation from the tracer. Different imaging protocols are implemented depending on the primary melanoma site, designed to detect all SNs. Figure 1.11(a) shows a patient lying in a supine position with the camera positioned above them, giving anterior LS images. Appropriate posterior, lateral, oblique or vertex views are also taken if required to accurately locate the SNs (Uren, Howman-Giles & Thompson 2003).

There are two types of imaging conducted: static and dynamic. Dynamic imaging, also known as early or flow imaging, is conducted for the first 10 to 20 minutes post-injection (Figure 1.12(a)). Movement of the radiocolloid through the lymphatic system can be seen, as it travels from the injection site into lymphatic vessels and then to lymph nodes. If required,

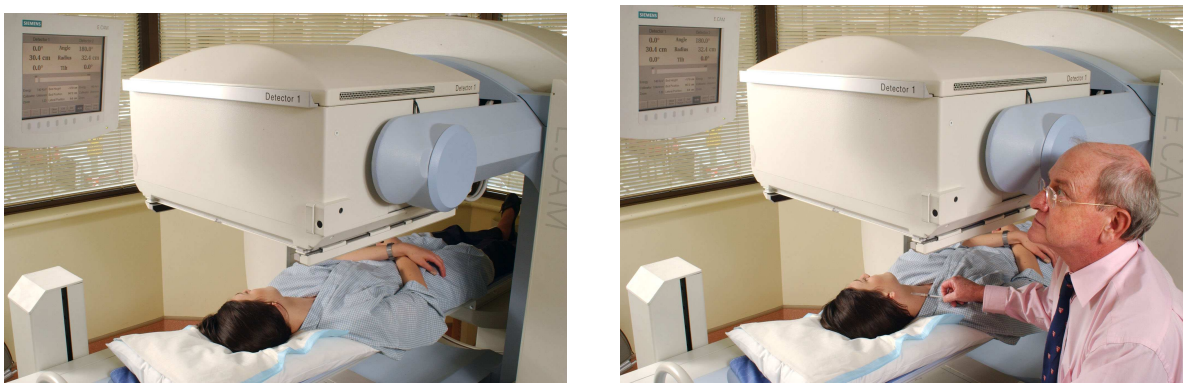

(a) (b)

Figure 1.11: LS imaging: (a) patient positioned under the gamma camera, (b) clinician searching for a SN using a radioactive point source.

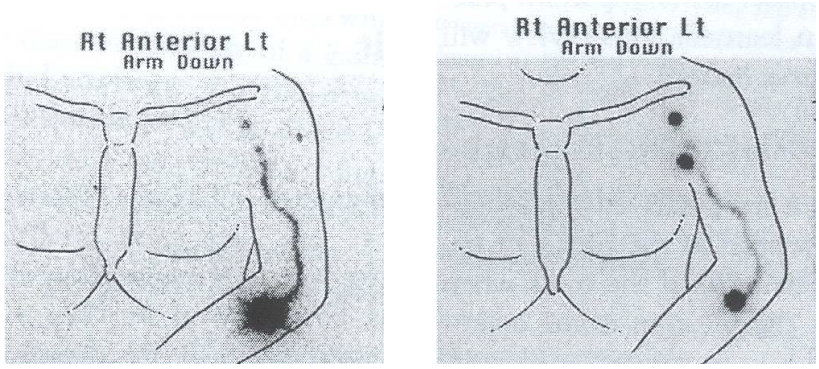

(a) Early dynamic image (10 mins post-injection) tracks the lymph vessel draining the skin

(b) Late static image (2&1/2 hrs post-injection) shows two SNs located in the axilla

Figure 1.12: LS images of a patient with a primary melanoma on the left forearm and two SNs in the left axilla. Reproduced from Thompson & Uren (2004).

dynamic scans can be stacked via a computer assisted summation algorithm to visualise the full activity of the tracer over the 20 minute period.

Dynamic images allow the confident identification of SNs as the lymphatic channels can be clearly seen draining directly to them. It is important during imaging to distinguish between true SNs and second tier nodes, which is any lymph node that has received lymph which has previously passed through a SN. Visualising the movement of the tracer through the lymphatics enables this differentiation.

LS studies have shown that lymph flow rates vary between different parts of the skin. By

assessing dynamic LS images, Uren, Howman-Giles, Thompson, Roberts & Bernard (1998) showed that the fastest average flow rates can be seen in the skin of the extremities, while the slowest flow rates are observed from the skin of the head and neck. The average flow rate for the leg and foot was 10.2 cm/min; the arm and shoulder 2.0 cm/min; while the forearm and hand measured 5.5 cm/min. The head and neck lymphatics flowed at an average 1.5 cm/min, the anterior and posterior trunk at 2.8 cm/min and 3.9 cm/min respectively. Differences in flow rates affect the speed with which SNs are located during dynamic imaging.

Static imaging, also known as late imaging, is performed 2 to $2\frac{1}{2}$ hours post-injection (Figure 1.12(b)). Images are acquired for 5 to 10 minutes of all regions that could possibly drain the primary melanoma site. Sometimes faint lymph nodes can be seen on static images that did not have a visible lymph channel draining to it on the dynamic images. If this is in a new node field it is by definition a true SN, since it is possible a distinct lymphatic vessel drained directly to it from the injection site.

A radioactive transmission source is routinely used on static images, placed behind the patient. The patient's body attenuates the signal to create body outlines on the LS images. This creates a frame of reference, thereby allowing the images to be interpreted clearly. Often these images are repeated without the transmission source however, to ensure that faint SNs in new node fields are not obscured by scattered activity from the source.

Once all SNs are located, their position is marked before surgery. Figure 1.11(b) shows a clinician using a radioactive point source to ensure correct location of each SN, before the overlying skin is marked with an 'X' using indelible ink (Figures 1.13(a) and 1.13(b)). A permanent point tattoo of carbon black is sometimes also applied to aid patient follow up over subsequent years. The depth of each SN from the skin is measured in centimetres and recorded. The depth is measured from the images directly or with electronic calipers, using orthogonal views with a radioactive marker held over each skin mark.

2. **Surgery to remove sentinel nodes.**
   Surgery to remove all SNs is usually conducted the day after lymphatic mapping. The 'X' marks on the skin overlying each SN and the recorded depth beneath the skin are used by the surgeon to locate the SNs. Blue dye is injected intradermally just prior to surgery to stain the lymphatic vessels and nodes blue, to further aid location. A hand-held gamma probe is also utilised during this procedure, to detect radiation from the SNs. Even 24 hours post lymphatic mapping, SNs are usually the most radioactive lymph nodes. Using the combined techniques of intraoperative blue dye mapping and the gamma probe improves the accuracy and speed of locating all SNs for surgical removal.

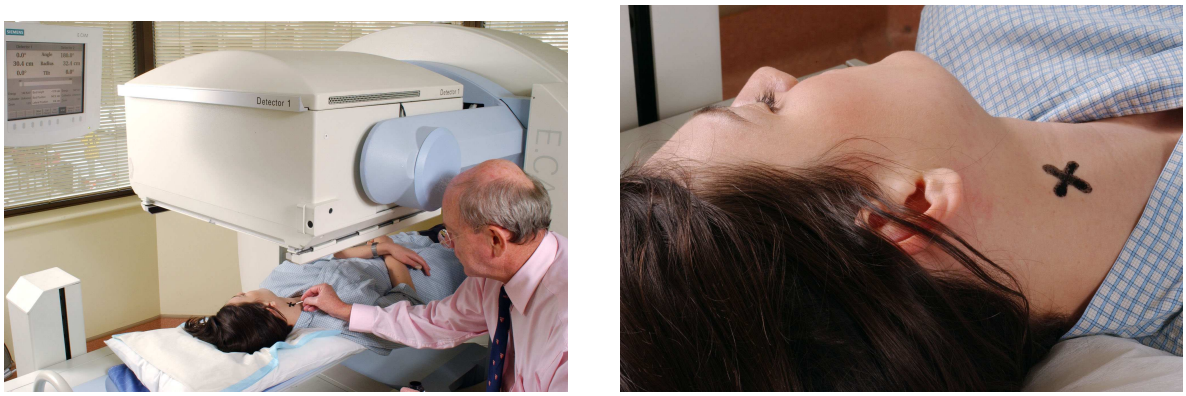

(a) (b)

Figure 1.13: LS imaging: (a) marking the SN skin location, (b) SN location marked with an X.

3. **Examination of sentinel nodes by a pathologist.**
   Each SN removed at surgery is assessed by a pathologist to determine whether it contains metastatic melanoma. The SNs are cut into a series of small blocks which are processed with fixatives and embedded in parafin wax. These blocks are then cut into approximately 10μm slices using a microtome. Tissue sections are then stained with chemicals such as haematoxylin and eosin, and examined under a microscope. Very small clusters of tumour cells can also be identified using immunohistochemistry techniques.

   Sometimes during examination, tumour cells may be missed due to a lack of sensitivity in the techniques used to sample and analyse the SN. SNs receive afferent drainage in a compartmentalised fashion, with a particular area of the skin draining not only to a specific lymph node but also to a specific area within the node (Morton et al. 2003). The distribution of tumour cells in the lymph node is localised rather than random, which means tumour cells can easily be missed by staining sections that represent only 1 - 2% of the total nodal volume. This problem can be minimised by sectioning the entire SN, however this is impractical in both time and cost. Carbon dye mapping is described as a partial solution to this difficulty. This technique labels a node as sentinel and identifies the intranodal site of lymphatic drainage for the pathologist, thus highlighting the most likely target of tumour cells.

Although LS is not a perfect method for locating SNs, studies have shown that the method is reliable (Morton et al. 1999), highly reproducible (Uren et al. 2007), and is only estimated to fail in detecting a SN in under 1% of patients overall (Uren 2007). The clinical reliability of the technique therefore validates the accuracy of the data analysed in this thesis.

1.6 Sydney Melanoma Unit's lymphoscintigraphy database

LS data from 5239 melanoma patients treated at the SMU between 27 July 1987 and 16 December 2005 have been used in this study. All LS studies were performed at the Nuclear Medicine and Diagnostic Ultrasound, Missenden Medical Centre, Camperdown in Sydney, on patients that had been referred by the SMU. The following details how the location of the primary melanoma site, the SN fields and additional details have been recorded for each patient.

1.6.1 Recording the primary melanoma site

Each patient's primary cutaneous melanoma location on the skin were recorded as an X and Y coordinate on one of six body outline maps, shown in Figure 1.14. The maps were separated into different regions of the body and have each been drawn manually by SMU clinicians. Figure 1.15(a) shows the direction of axes for Map 1. On this map there are 38 grid units in the X-direction, and 56 grid units in the Y-direction.

The method used to determine X and Y coordinates for each patient was by eye. SMU clinicians reference previously recorded clinical drawings of the primary melanoma site, and also visually inspect the melanoma site location to match it to a grid position on one of the generic body maps. As a result, there will be a small element of human error present in these coordinates. A preferred method to record the skin site coordinates might be to overlay LS images on the body maps, however this is not currently possible due to different body morphology between patients and the range of imaging orientations required for different primary melanoma site locations.

The width of each grid square on the body maps equates to between 1.5 - 2 cm on the skin. Due to this coarse grid resolution a number of patients will have their melanoma site recorded in the same grid square. To allow these individual cases to be visualised as discrete dots without being superimposed the SMU has added a random number to each coordinate, allowing the density of points in the same grid unit to be displayed. The random numbers generated were between -0.499 and +0.499 and added to each of the X and Y values to give $randX$ and $randY$. For example, if a melanoma has an X coordinate of 10 then $randX$ will be a number between 9.501 and 10.499. For each Y coordinate however, $randY$ has been recorded as the number calculated by subtracting Y and the random number from 100. So a Y value of 22 will have a $randY$ coordinate value between 77.501 and 78.499. It is important to remember these values are for display purposes only and do not add any extra spatial information. Figure 1.15 shows the display produced by using $randX$ and $randY$ as opposed to simply X and Y.

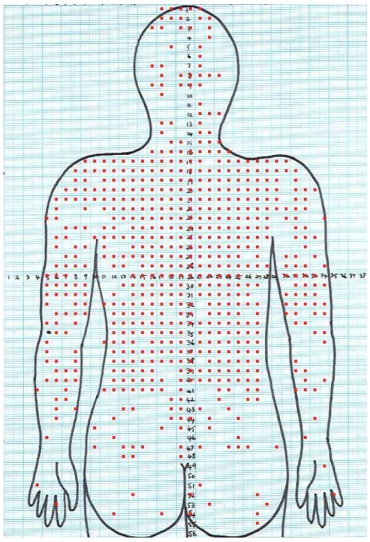

(a) Map 1: Posterior Torso

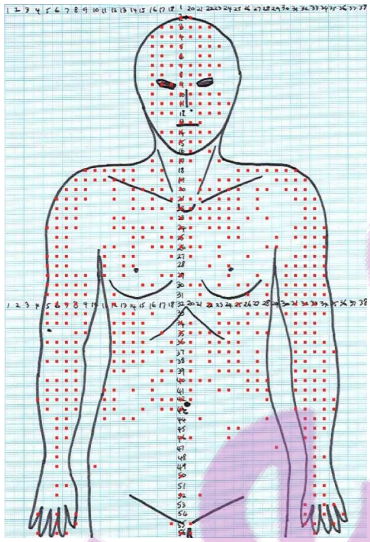

(b) Map 2: Anterior Torso

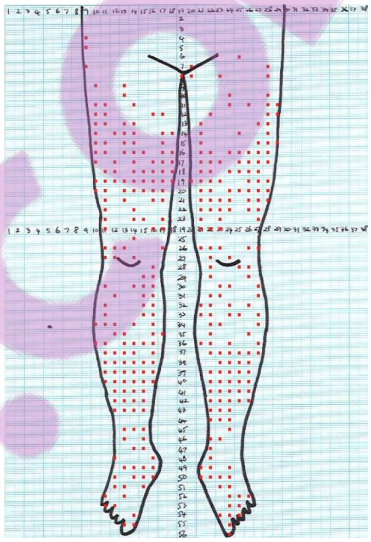

(c) Map 3: Anterior Legs

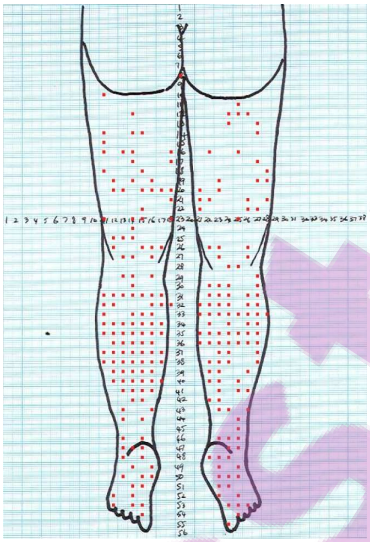

(d) Map 4: Posterior Legs

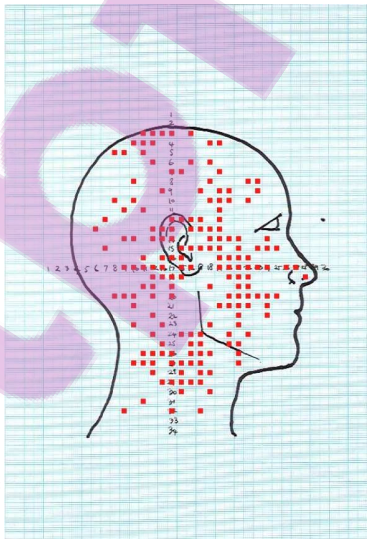

(e) Map 5: Right Head

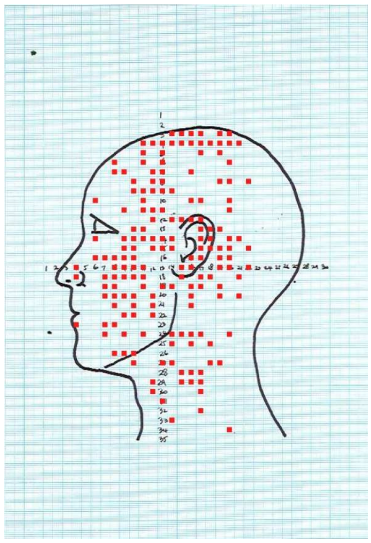

(f) Map 6: Left Head

Figure 1.14: Body maps used to record primary melanoma site, with (X,Y) coordinates plotted for the full patient database.

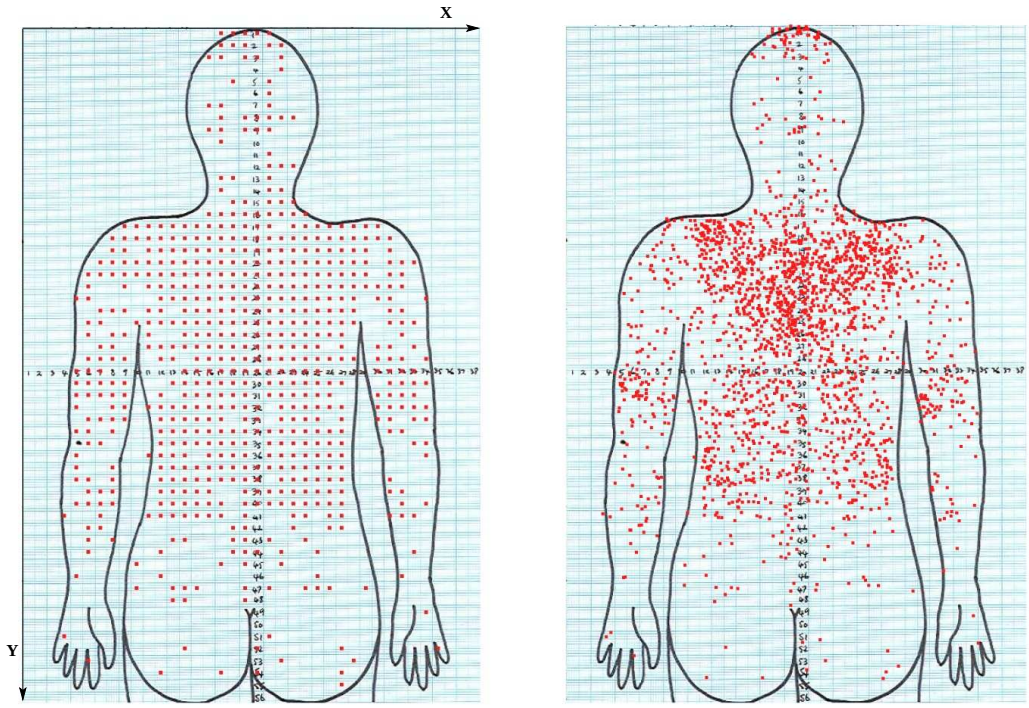

(a) X and Y plot (b) $randX$ and $randY$ plot

Figure 1.15: Melanoma sites plotted on the posterior torso body map for the full patient database.

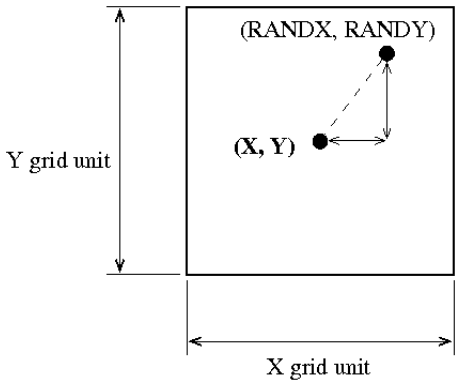

Figure 1.16: An example body map grid unit.

1.6.2 Recording the sentinel nodes

A number of lymph node fields directly drain the skin (as defined in Section 1.3.2) and are regarded as generic regions for SNs to be located. The SMU has specified 25 node fields, where 18 of these fields are located on both left and right sides of the body to give a total of 43 separate node fields.

A list of these SN fields and the codes SMU clinicians have used to record them in their database is given in Appendix A. It is important to note that the number of SNs for each patient may not equate with the number of node fields, since multiple SNs may be located in the same field.

1.6.3 Additional data recorded

As well as input fields regarding each patient's primary melanoma site and SN fields, other details have been recorded. Each patient has been assigned a record number, and their full name, age, sex, and the date of the LS study have been included in the database. These details were added to the fields regarding the primary melanoma site and SN fields which involved: a body map number, X, Y, $randX$, $randY$, SN fields, number of node fields and the number of interval nodes (these terms have been defined in Section 1.3.2).

Over the period of data collection, as the SMU's understanding of the epidemiological significance of input fields has developed, input variables have been refined. Initially the depth of each SN from the skin was measured, however these values were discarded since each patient had a different body morphology, hampering direct comparison. The radiocolloid flow rate has previously been recorded after a difference was noted between various parts of the body. For most patients this measurement did not impact management, and it therefore was ceased to be added to the database. Currently, the flow rate is only reported when it is very slow, to provide additional information for the surgeon to reference for blue dye injection during SNB.

1.6.4 Data visualisation

The SMU has published numerous articles presenting its LS findings, in both tabular format and in 2D displays, relating primary melanoma sites to draining node fields. Work that has been carried out to display this data graphically has involved using a software package called ArcView®[3]. This software has been designed for geographical applications, and has required 2D images of the body to be created as 'countries' and melanoma sites to be plotted as 'towns'. Queries were made to the SMU's database about particular patterns of lymphatic drainage, so that files were outputted that could be read into ArcView® and displayed.

Figure 1.17 shows an example of one of these displays, visualising all melanoma sites in the database that have shown lymphatic drainage to the left axilla. Both anterior and posterior views are given, and melanoma sites are shown using dots. For each of these displays the random

[3] ArcView® GIS by Environmental Systems Research Institute, Inc., Redlands, California 92373, USA.

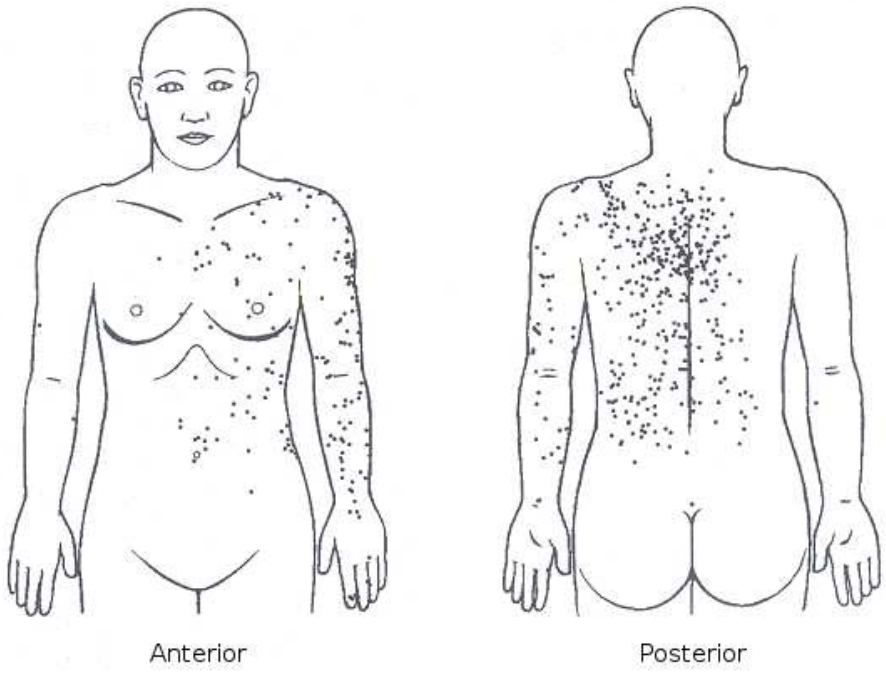

Figure 1.17: SMU display showing melanoma sites that drain to the left axillary node field. Reproduced from Uren et al. (1999).

$(randX, randY)$ coordinates (as explained in Section 1.6.1) have been plotted, to enable melanoma sites that had the same original (X, Y) coordinates to be effectively visualised.

More complex displays have also been generated, investigating additional aspects of lymphatic drainage. For example, Figure 1.18 shows the location of all melanoma sites on the skin of the trunk that have shown drainage to the left or right groin node field, or both groin node fields. Melanoma sites that have shown drainage to both groin node fields have been plotted as boxed crosses, while melanoma sites that have drained to the left or right groin are plotted with crosses or circles respectively. This demonstrates the ability to plot multiple sets of data on the 2D displays.

Displays have also been generated to investigate the accuracy of historical assumptions about lymphatic drainage, rather than simply plotting melanoma sites that have drained to specified node fields. Figure 1.19 shows a display generated to visualise melanoma sites that have shown lymphatic drainage across Sappey's horizontal line around the waist. Again, sites have been plotted using different shapes. Crosses have been used to plot sites that have shown lymphatic drainage across Sappey's horizontal line up towards the axilla, while circles indicate melanoma sites that have drained downwards across Sappey's horizontal line to the groin.

To the author's knowledge, LS data for melanoma has not previously been presented in a more insightful manner than the SMU's technique described above. However, although the SMU's dis-

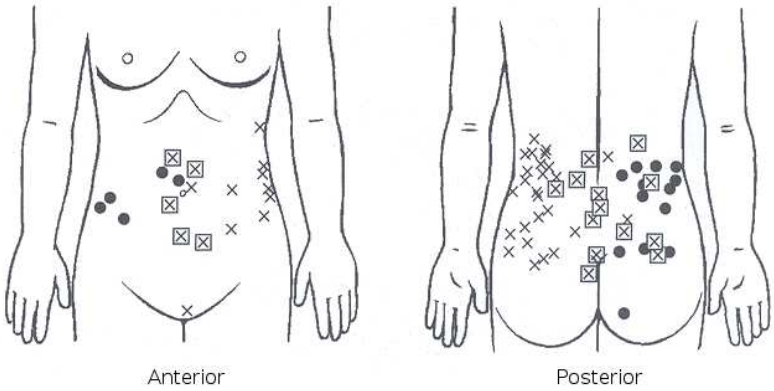

Figure 1.18: SMU display showing melanoma sites on the trunk that drain to the groin. Circles show sites that drain to the right groin, crosses show sites that drain to the left groin while boxed crosses drain to both groin node fields. Reproduced from Uren et al. (1999).

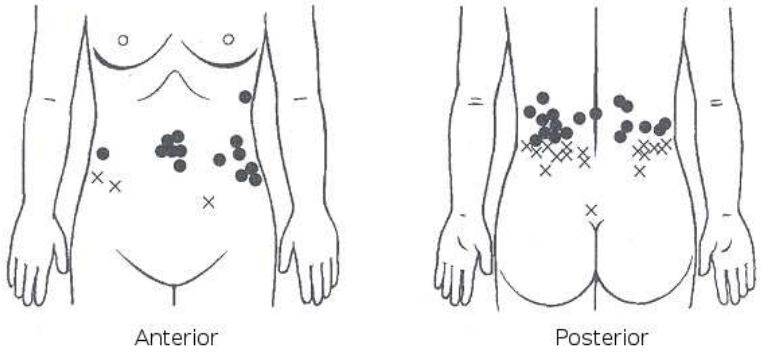

Figure 1.19: SMU display showing melanoma sites that drain across Sappey's horizontal line around the waist. Circles correspond with sites that drain to the groin, while crosses show sites draining up to the axilla. Reproduced from Uren et al. (1999).

plays have been informative, there are inherent limitations. The data has been restricted to 2D, and comprehensive statistical analysis of the data has been limited. This study sought to improve the methods of visualisation to display the SMU's LS data, using anatomical modelling techniques available at the ABI as described in the following section.

1.7 Anatomical modelling

Advanced mathematical modelling techniques have been implemented and developed at the ABI, enabling the creation of complex anatomical models of human anatomy. These models have been used to analyse and investigate various aspects of anatomy and physiology, providing additional insight into the structure and function of the human body.

1.7.1 Finite element models

At the ABI, finite elements (FEs) have been used extensively to model human anatomy, owing to their ability to accurately describe detailed geometries. In brief, FEs are used as a technique to discretise a continuous domain into a set of sub-domains, providing a more computationally efficient way to describe an object. They are often used in engineering analysis to simulate various conditions, allowing for complex numerical analysis to be applied.

Complex 3D models of various organs have been developed that combine both the geometric structure of the organ with its physiological function. For example, researchers have developed a FE model of the coronary blood vessels (Smith et al. 2000), as shown in Figure 1.20(a). Simulation of blood flow through these vessels has then been conducted and coupled to cardiac contraction. A model of the lungs has also been created (Tawhai & Burrowes 2003), as shown in Figure 1.20(b). Detailed anatomy of the airways and a section of the lung lobe surface can be seen.

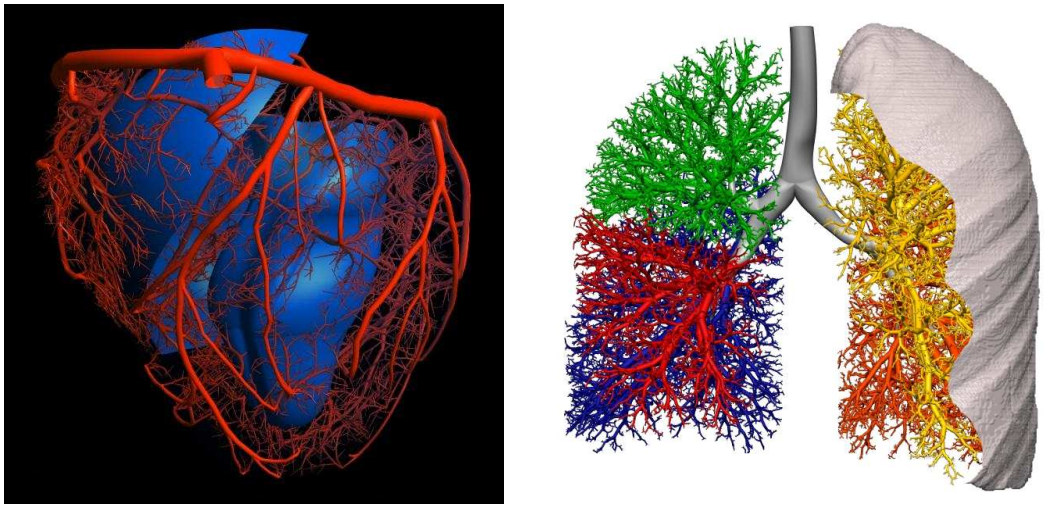

(a) (b)

Figure 1.20: Models of (a) the heart and (b) the lungs developed at the ABI.

Advanced models of other organ systems have also been developed, including the gastrointestinal system (Pullan et al. 2004) and the musculo-skeletal system (Fernandez et al. 2004). Figure 1.21 shows a model of the muscles in the forearm and the hand, along with the associated bones (Reynolds et al. 2004). These FE models and the techniques developed to create them provide a set of tools which underpins a more advanced visualisation and analysis of the SMU's LS data.

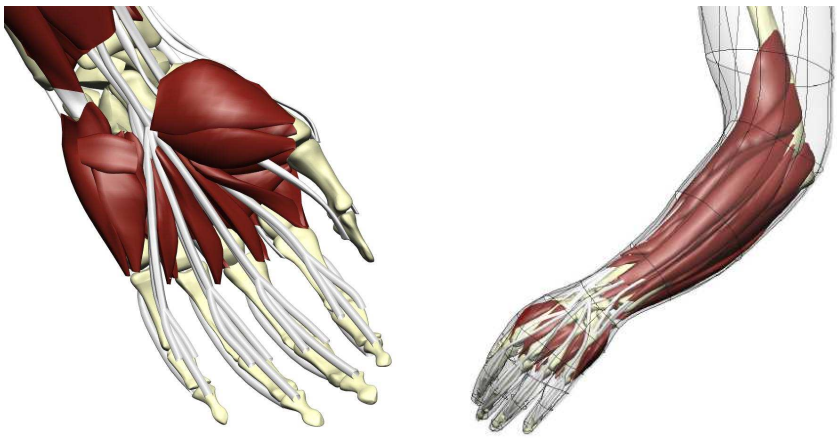

(a) (b)

Figure 1.21: Musculo-skeletal model of the the forearm and hand, (a) palmar view of the hand and (b) anterior view of the model (Reynolds et al. 2004).

1.7.2 Software

The models developed for this study have been created using the software package CMISS[4], which is a mathematical modelling environment that allows the application of finite element analysis, boundary element and collocation techniques to a variety of complex bioengineering problems. This software has been developed over the past 30 years by researchers and graduate students in the Engineering Science department at the University of Auckland, and more recently at the ABI[5].

The software contains both a computational back-end and a graphical front-end called CMGUI. The computational back-end has been specifically used in this study for geometric fitting, model customisation via host-mesh fitting and field fitting; while CMGUI has been used extensively to provide advanced 3D model visualisation.

1.8 Thesis overview

This thesis details the development of an anatomical modelling framework to enable visualisation and analysis of skin lymphatic drainage in 3D using melanoma LS data from the SMU. The modelling process involved creation of a FE skin model and a discrete lymph node model. Data projection techniques have then been carried out to map the SMU's LS data onto this modelling

[4]CMISS stands for Continuum Mechanics, Image analysis, Signal processing and System identification
[5]http://www.cmiss.org/

framework. Following mapping, novel data visualisation methods and quantitative statistical analysis were implemented to extend and quantify the understanding of skin lymphatic drainage. Software tools have been developed to provide improved dissemination of this data to clinicians and medical educators. All modelling procedures were carried out at the ABI, in collaboration with the SMU. The following outlines the contents in each of the subsequent chapters:

Chapter two details the development of the anatomical models. The steps required to create a FE skin model are outlined, which are: data digitisation, initial linear mesh construction and fitting. Model customisation using the free-form deformation method 'host-mesh' fitting is also described. The resultant skin model and discrete lymph node model are then presented.

Chapter three outlines the methods utilised to map the SMU's LS data from 2D images onto the 3D skin and lymph node models. Various procedures used to map the primary melanoma sites on the skin are detailed, as well as the methods used to map SNs.

Chapter four describes visualisation methods implemented to display the mapped LS data on the anatomical geometry. The process of field fitting is detailed, and the effects of Sobolev smoothing on the resultant fields discussed. Development of an interactive skin selection tool is also outlined, which enables predictions of melanoma spread from any area of skin.

Chapter five presents the visualisation results showing patterns of skin lymphatic drainage. Heat maps displaying the likelihood that drainage will occur to specified node fields and numbers of node fields are shown and discussed and results shown via the skin selection tool are also presented. Limitations of the model and its potential clinical utility are outlined.

Chapter six describes statistical methods developed to further analyse lymphatic drainage of the skin, including methods to: analyse Sappey's lines, determine whether lymphatic drainage is likely to be symmetric, and also functionally group similar regions of skin. Additionally, methods for determining appropriate confidence intervals are detailed.

Chapter seven presents the statistical analysis results, quantifying the inaccuracy of Sappey's lines. Symmetry test results are outlined, as well as clustering results that indicate regions of skin that drain in a similar manner. Confidence intervals are also given to indicate the statistical significance of drainage predictions.

Chapter eight summarises the contributions and conclusions of this thesis. Possible extensions of this study are discussed in a future work section.

Chapter 2

Anatomical Geometry

Highly detailed anatomically based models of the skin and lymph nodes were required as a framework to enable 3D visualisation of the SMU's LS database. This chapter describes the finite element (FE) approach which has been used to model anatomical geometry in this thesis. The three steps involved in model construction have been outlined below: data digitisation, construction of an initial linear mesh, and fitting of this linear mesh to the digitised data points. The ability to customise FE models via a free-form deformation method, also called 'host-mesh' fitting, is described and has been utilised during the mapping procedures in Chapter 3. Detailed models of the skin and lymph nodes created using the Visible Human (VH) dataset and a separate head and neck model are then presented. The work presented here has been published, and can be seen in Appendix C.

2.1 Finite element basis functions

Finite elements (FEs) have been used to model the anatomical geometry created for this study. Geometry to be modelled has been discretised into smaller domains called 'elements', which were then joined together by nodes. Values at any location within an element have been calculated via interpolations of the nodal values using appropriate basis functions.

Two families of basis functions that are often used for FE modelling are known as Lagrange and Hermite. For the purposes of this thesis cubic Hermite interpolation has been used. Cubic Hermite interpolation ensures continuity of both nodal values (C_0 continuity) and nodal first derivatives (C_1 continuity) across elements. In contrast linear Lagrange interpolation only maintains C_0 continuity. Hence, nodal derivative values are stored for cubic Hermite FE meshes, while they are not required for linear Lagrange FE meshes. Cubic Hermite interpolation is particularly useful for anatomical

modelling, since most anatomical structures are smooth in shape and continuous derivatives ensure that the geometries are physically realistic, even for relatively computationally efficient low resolution meshes.

The difference between these two classes of interpolation can be demonstrated via their basis functions. The two linear Lagrange basis functions (as shown in Figure 2.1(a)) are defined by:

$$\begin{aligned} \phi_1(\xi) &= 1 - \xi \\ \phi_2(\xi) &= \xi \end{aligned} \tag{2.1}$$

while the four cubic Hermite basis functions (as shown in Figure 2.1(b)) are given by:

$$\begin{aligned} \psi_1^0(\xi) &= 1 - 3\xi^2 + 2\xi^3 \\ \psi_2^0(\xi) &= \xi^2(3 - 2\xi) \\ \psi_1^1(\xi) &= \xi(\xi - 1)^2 \\ \psi_2^1(\xi) &= \xi^2(\xi - 1) \end{aligned} \tag{2.2}$$

where ξ is the local or material coordinate with $\xi \in [0, 1]$. The subscript labels 1 and 2 indicate the node number, while superscripts 0 and 1 indicate the nodal value and first derivative.

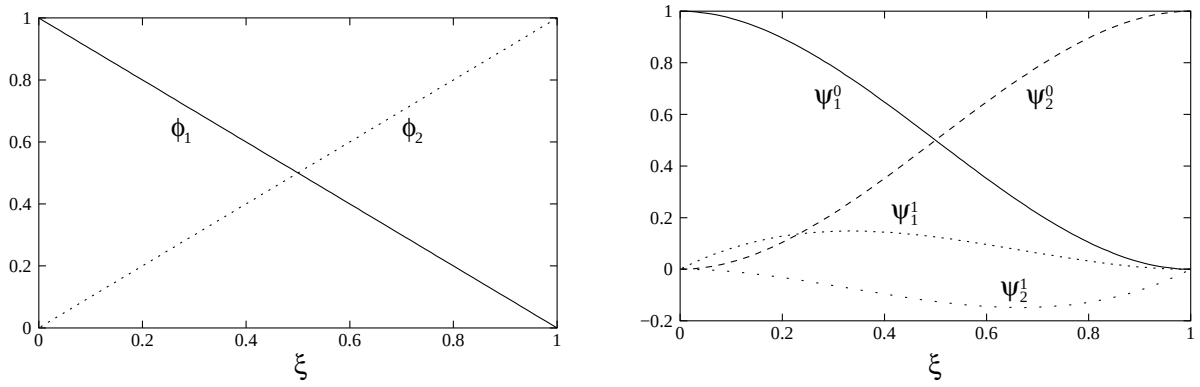

(a) Linear lagrange

(b) Cubic Hermite

Figure 2.1: Finite element basis functions.

Figure 2.2(a) shows a one-dimensional (1D) element interpolated using linear Lagrange basis functions, and Figure 2.2(b) also shows a 1D element which has been interpolated using cubic Hermite basis functions.

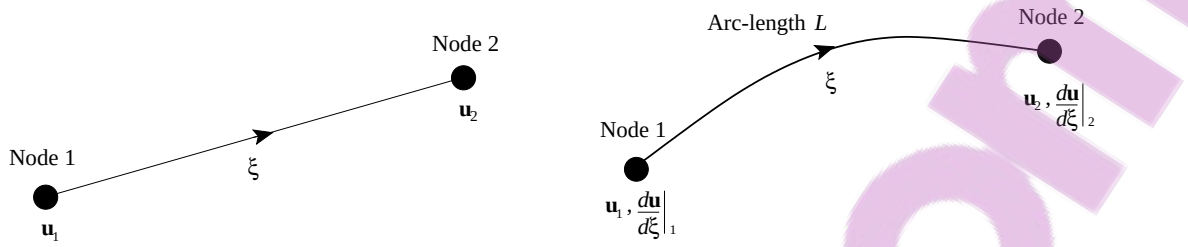

(a) Linear lagrange line element

(b) Cubic Hermite line element

Figure 2.2: One-dimensional finite elements.

To interpolate values along a 1D linear Lagrange element the following equation is used:

$$\mathbf{u}(\xi) = \phi_1 \mathbf{u}_1 + \phi_2 \mathbf{u}_2 \tag{2.3}$$

meanwhile interpolation along a 1D cubic Hermite element is calculated by:

$$\mathbf{u}(\xi) = \psi_1^0(\xi)\mathbf{u}_1 + \psi_2^0(\xi)\mathbf{u}_2 + \psi_1^1(\xi)\frac{d\mathbf{u}}{d\xi}\bigg|_1 + \psi_2^1(\xi)\frac{d\mathbf{u}}{d\xi}\bigg|_2 \tag{2.4}$$

where $\mathbf{u}$ is a value at a node, either its global coordinate or a field value such as pressure or temperature. $\frac{d\mathbf{u}}{d\xi}$ is the derivative of this value with respect to the local element coordinate ξ. This equation ensures continuity of the derivatives in local ξ space, however it does not ensure global space continuity. Therefore derivative values are expressed in terms of the line arc-length parameter s instead, and the partial derivatives are scaled by the element arc-length scale factor L. As a result, partial derivatives with respect to arc-length are nearly continuous across elements.

By using the chain rule, local element derivatives are converted into physical derivatives:

$$\left(\frac{d\mathbf{u}}{d\xi}\right) = \left(\frac{d\mathbf{u}}{ds}\right)\left(\frac{ds}{d\xi}\right) \tag{2.5}$$

where the parameter s is defined as the arc-length along the line. The scale factor L is given by:

$$\frac{ds}{d\xi} = \frac{\Delta s}{\Delta \xi} = \frac{L}{1.0} = L \tag{2.6}$$

Substituting the arc-length based derivatives and the element scale factor L into Equation 2.4 will

give the following:

$$\mathbf{u}(\xi) = \psi_1^0 \mathbf{u}_1 + \psi_2^0(\xi)\mathbf{u}_2 + \psi_1^1(\xi)\frac{d\mathbf{u}}{ds}\bigg|_1 L + \psi_2^1(\xi)\frac{d\mathbf{u}}{ds}\bigg|_2 L \tag{2.7}$$

where L is the arc length scale-factor given by:

$$L = \int_0^1 \sqrt{\left(\frac{dx}{d\xi}\right)^2 + \left(\frac{dy}{d\xi}\right)^2 + \left(\frac{dz}{d\xi}\right)^2}\, d\xi \tag{2.8}$$

2.2 Visible human data

The anatomical geometry created in this study has been largely based on data from the Visible Human (VH) male dataset (Spitzer et al. 1996). This dataset is comprised of digital MRI, CT, and anatomic images of a male cadaver, created by the National Library of Medicine for the purposes of medical education and virtual simulation (Spitzer & Whitlock 1998).

The VH dataset has been adopted by the medical community as a standard anatomical database, and has provided the framework for many research investigations. At the ABI for example, a detailed musculo-skeletal model was entirely developed using VH images (Fernandez et al. 2004). Also, as mentioned in Section 1.4, VH images have been used by Qatarneh et al. (2006) to create a 3D atlas of lymph node topography.

Since the creation of the male VH, a full VH female has also been created. Owing to the immense amount of detailed anatomical information available in these datasets and their potential research value, a VH Korean male (Park et al. 2006) and VH Chinese male and female (Zhang et al. 2003) have also been created. The growing number of datasets will allow for a more detailed analysis of individual, gender and ethnic differences in human anatomy.

2.3 Creating a finite element model

Creation of an FE model involves three steps: data digitisation, initial linear mesh creation and fitting. The following sections explain each of these steps in detail.

2.3.1 Data digitisation

Initially, a set of data points is required to discretely approximate the structure being modelled. Data digitisation can be carried out either manually, automatically or using a laser scanner. Manual digitisation involves visual location of the appropriate anatomical structure on VH images in CMGUI, and has been used in this thesis to digitise the skin below the neck (as described in Section 2.5). A series of data points can be created by clicking around the boundary of the appropriate structure. This method relies upon an individual's knowledge of anatomy and their ability to visually locate the desired structure. Difficulties can arise however, especially when digitising small structures, if the image resolution is too low to accurately identify the boundaries. Figure 2.3(a) shows an example of manual digitisation of the torso skin surface on a VH image slice, and Figure 2.3(b) shows a 3D data cloud created by stacking and digitising the skin on a series of 2D VH image slices.

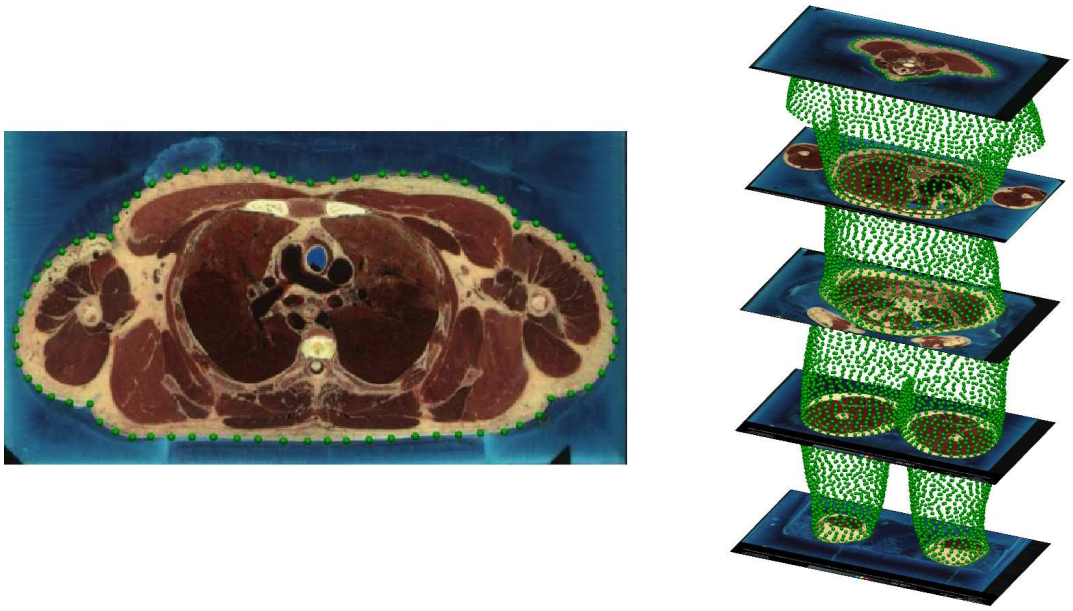

(a) Digitised VH slice (b) Digitised data cloud

Figure 2.3: Manually digitising the VH skin.

Automatic digitisation can be carried out in CMGUI if the anatomical boundary location is readily identifiable and not masked by noise. This process involves creating a volume texture from the stacked image slices and extracting an isosurface where the voxel intensity changes. For example, the VH skin boundary could have been detected automatically where the image colour changes from a specified shade of blue to 'skin-colour' (however an explanation detailing why this auto-

matic method was not utilised for this study is given in Section 2.5). Once the boundary isosurface has been extracted a density of data points can be calculated over the isosurface to create a 3D data cloud.

Alternatively, creation of a 3D data cloud can be carried out by using a laser scanner such as the hand-held Polhemus^{TM}Fastscan laser scanner (Applied Research Associates, NZ Ltd) shown in Figure 2.13. This laser scanner has been used in this thesis to digitise the skin of the head and neck (as detailed in Section 2.5.2). Data points can be collected by sweeping the handheld laser scanning wand over an object. The resultant data cloud is highly accurate, where errors range between 1 - 2 mm.

Figure 2.4: The Polhemus laser scanner.

2.3.2 Initial linear mesh

After digitisation, a linear mesh is constructed to initially approximate the anatomical geometry. Construction of this initial linear mesh is required to ensure the mesh topology adequately captures the geometry of the anatomical structure, while also utilising a minimal number of elements to reduce the number of degrees of freedom (DOFs). Initial linear mesh construction involves manually selecting data points from the digitised data cloud at regular intervals. These selected points are then used as nodes to create linear elements (interpolated using linear basis functions), like those shown in Figure 2.5(a) for the skin of the torso.

The skin model has been created with 2D surface elements, which typically contain 4 nodes per element as shown in Figure 2.6(a). The direction of local coordinates for surface elements are defined by the order in which nodes are joined together. The ξ_1-direction is defined by the first two

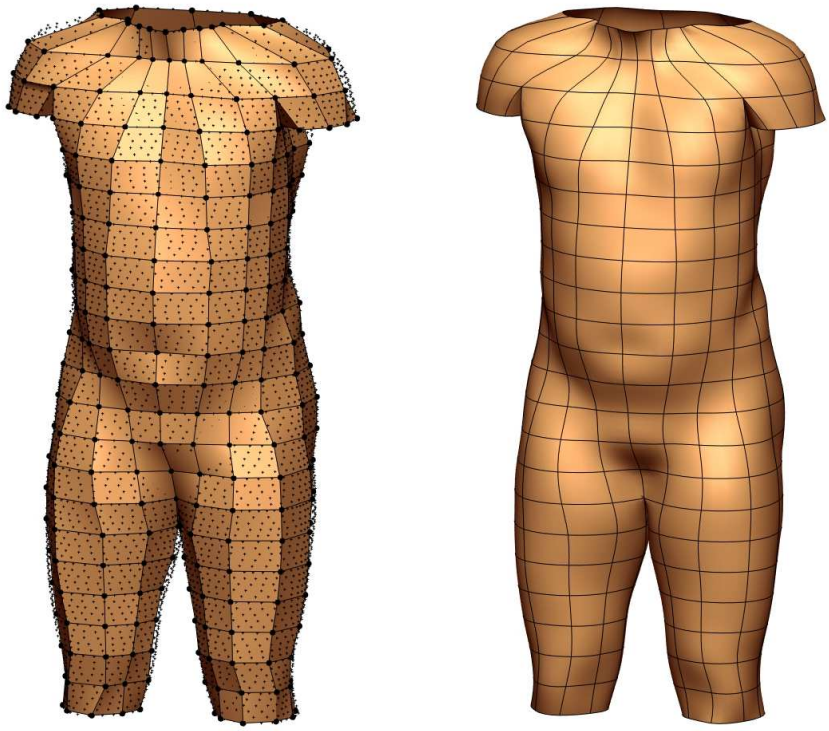

(a) Initial linear mesh (b) Fitted mesh

Figure 2.5: Fitting the torso and thigh skin surface.

nodes that are selected to define the element, while the ξ_2-direction is defined by the first and third nodes. Figure 2.6(a) demonstrates a surface element that is created by joining nodes in the order 1-2-3-4, with the corresponding ξ-directions labelled. In certain cases collapsed surface elements are required to describe the model geometry accurately. Collapsed elements contain three nodes as shown in Figure 2.6(b), which are defined by repeating the third node in the order 1-2-3-3. Often collapsed elements are used at structural bifurcations or at the top and bottom of cylindrical and spherical shaped meshes to ensure they can be closed.

It is important for FE meshes to maintain consistent ξ-directions to ensure that the resultant geometry is smooth at element boundaries. In order to do this, nodal versions of derivative values are sometimes required, which are defined with respect to associated elements. For standard meshes only one derivative value is stored at nodes for each ξ-direction, however in the case of a collapsed element usually two or more derivative values at specified nodes are needed to ensure the mesh is continuous. For example, Figure 2.7(a) shows five collapsed surface elements each sharing node 3. As a result, there are five different values required for the ξ_2 derivatives and hence five different versions of this derivative value are stored at this node. Figure 2.7(b) shows another collapsed

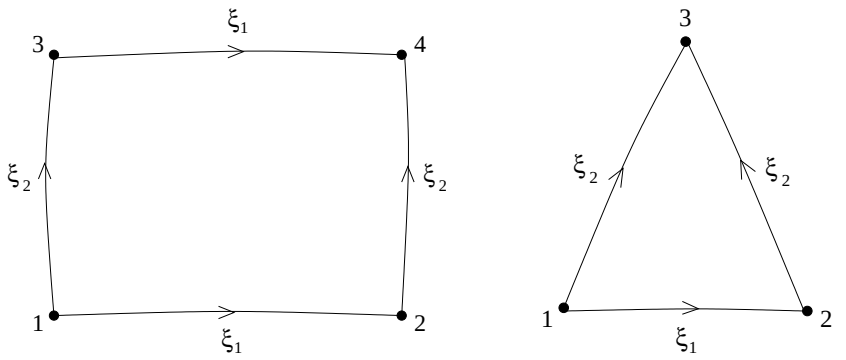

Figure 2.6: (a) Standard surface elements and (b) collapsed surface elements.

element with standard elements around it. Node 3 is shared between each of the five elements, which requires three versions of the ξ_2 derivative. For both of these examples nodal versions are needed to store multiple ξ_2 derivative values, however other mesh topologies may require multiple versions for the ξ_1 derivatives as well.

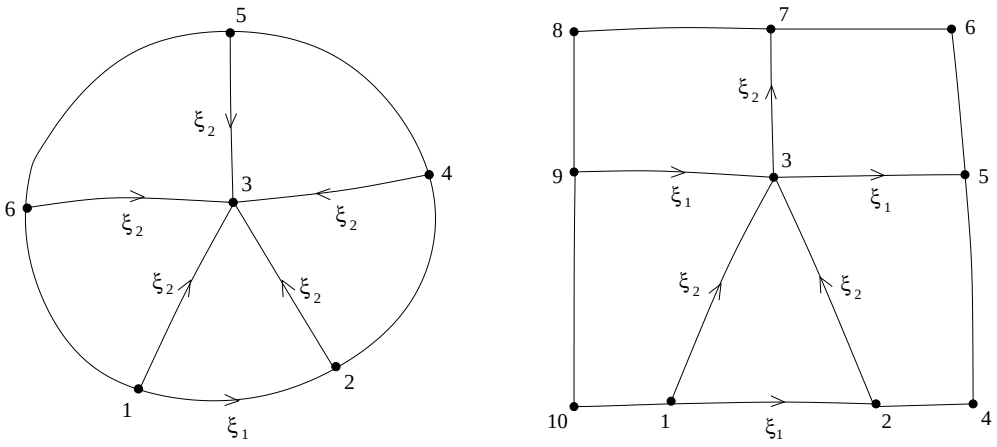

Figure 2.7: Mesh designs with collapsed elements requiring nodal versions.

2.3.3 Fitting

Once an initial linear mesh is constructed, it is fitted to the set of digitised data points. This step is carried out iteratively using a non-linear fitting algorithm which has been described previously

by Bradley et al. (1997) and Fernandez et al. (2004). A summarised description of this process is provided below.

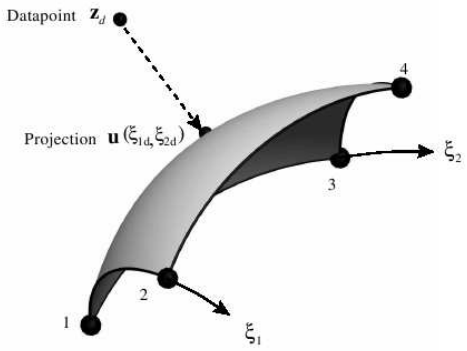

Figure 2.8: Datapoint $\mathbf{z}_d$ orthogonally projected onto the face of a surface element to give the closest point $\mathbf{u}(\xi_{1d}, \xi_{2d})$.

The fitting process seeks to minimise the distance between each data point and its orthogonal projection onto the FE mesh surface. Figure 2.8 schematically demonstrates a datapoint $\mathbf{z}_d$ projected onto a surface element, where the distance value is found by the least-squares distance function:

$$D(\xi_{1d}, \xi_{2d}) = \| \mathbf{u}(\xi_{1d}, \xi_{2d}) - \mathbf{z}_d \|^2 \tag{2.9}$$

where $\mathbf{z}_d$ is the global coordinate of the data point and (ξ_{1d}, ξ_{2d}) are the local material coordinates of the projected data point on the surface element, which is used along with the nodal parameters $\mathbf{u}_n$ to interpolate global coordinates of the projection onto the mesh.

The data error values are then summed over all points in the digitised data cloud and utilised in the first component of the fitting objective function, which is given by:

$$F(\mathbf{u}_n) = \sum_{d=1}^{N} w_d \| \mathbf{u}(\xi_{1d}, \xi_{2d}) - \mathbf{z}_d \|^2 + F_s(\mathbf{u}_n) \tag{2.10}$$

where N is the total number of data points and w_d is a weight associated with each data point, usually kept at 1.0 for geometric fitting. The second component in this equation, $F_s(\mathbf{u}_n)$, is a smoothing constraint. This constraint is a Sobolev smoothing penalty function (Bradley et al. 1997) introduced to maintain smoothness of the mesh where data is noisy or insufficient, and is

defined by:

$$F_s(\mathbf{u}_n) = \int_0^1 \int_0^1 \left\{ \alpha_1 \left\| \frac{\partial \mathbf{u}}{\partial \xi_1} \right\|^2 + \alpha_2 \left\| \frac{\partial \mathbf{u}}{\partial \xi_2} \right\|^2 + \alpha_3 \left\| \frac{\partial^2 \mathbf{u}}{\partial \xi_1^2} \right\|^2 + \alpha_4 \left\| \frac{\partial^2 \mathbf{u}}{\partial \xi_2^2} \right\|^2 + \alpha_5 \left\| \frac{\partial^2 \mathbf{u}}{\partial \xi_1 \partial \xi_2} \right\|^2 \right\} d\xi_1 d\xi_2 \tag{2.11}$$

The objective function defined in Equation 2.10 has been minimised by changing the vector of nodal mesh parameters $\mathbf{u}_n$. For a surface mesh each node has 4 DOFs: a coordinate value, two first-order derivatives in the ξ_1- and ξ_2-directions, and a cross-derivative. Hence for each standard 4-noded element there are 16 DOFs.

The amount of smoothing desired during the fitting process can be modified by altering the Sobolev weights $\alpha_i (i = 1..5)$ in Equation 2.11. Each of the weights influence a different feature of the fitted mesh. Changing α_1 or α_2 will influence the element arc-lengths in the ξ_1- and ξ_2-directions respectively, altering the weights α_3 or α_4 will change the arc-curvature also in the ξ_1- and ξ_2-directions respectively, while α_5 influences the face area.

Fitting is carried out iteratively until a desired result is acquired. Iteration is necessary since local coordinates of each projected data point changes as the mesh is fitted. The accuracy of the fitted mesh is given by calculating the root mean square (RMS) error between the data points and mesh surface. This is found using the following equation:

$$RMS = \sqrt{\frac{\sum_{d=1}^{N} \parallel \mathbf{u}(\xi_{1d}, \xi_{2d}) - \mathbf{z}_d \parallel^2}{N}} \tag{2.12}$$

where each subsequent fit reduces the RMS value. Once the RMS value converges, and the fitted mesh is assessed subjectively to determine whether the geometry is appropriately defined, the fitting is complete. The resultant fitted torso and leg skin mesh is shown in Figure 2.5(b), which had an RMS error of 2.03 mm.

2.4 Customising finite element models

Once a generic FE model has been created, often it is desired that this model is customised to a specific geometry or position. A technique called 'host-mesh' fitting can be used for this purpose, which is a free-form deformation technique. In previous studies at the ABI, for example by (Fernandez 2004) and (Cox 2007), this method has been used to morph initial generic FE models to create patient-specific models. In this study, host-mesh fitting has been used in Chapter 3 to

enable the mapping of LS data from 2D images onto the 3D skin model, as well as to morph the arm of the skin model from an initial anterior position to a lateral position.

The FE mesh that is being customised during this procedure is termed the 'slave-mesh', and is completely embedded within an FE 'host-mesh'. As a result, all slave-mesh material coordinates (η_1, η_2, η_3) can be expressed in terms of the host-mesh material coordinates (ξ_1, ξ_2, ξ_3):

$$\begin{aligned} \eta_1 &= f_1(\xi_1, \xi_2, \xi_3) \\ \eta_2 &= f_2(\xi_1, \xi_2, \xi_3) \\ \eta_3 &= f_3(\xi_1, \xi_2, \xi_3) \end{aligned} \tag{2.13}$$

This method exploits the fact that any deformation of the host-mesh will cause deformation of the embedded slave-mesh, since the slave's material coordinates are fixed at material points within the host-mesh. Note that for a slave-mesh that is in plane, with only two global coordinates (x, y) then a 2D (area) host-mesh can be used. However, for a slave-mesh in 3D space with global coordinates (x, y, z) a 3D (volume) host-mesh is needed to completely embed it.

The host-mesh is usually a volume mesh with a simpler geometry and less DOFs than the slave-mesh, and ensures important anatomical features of the slave-mesh to be articulated are adequately captured. An example volume host-mesh surrounding a volume slave-mesh is shown in Figure 2.9(a). Landmark (initial) data points shown in red are chosen from the original slave-mesh and target (final) data points shown in green are selected from the desired patient-specific location. Each landmark point has a corresponding target point and as a rule, all landmark points are required to be inside the host-mesh.

The distance between the target and landmark points is minimised via deformation of the host-mesh, as shown in Figure 2.9(b). Equation 2.10 is the objective function minimised where $\mathbf{z}_d$ are the global target point coordinates and $\mathbf{u}(\xi_{1d}, \xi_{2d}, \xi_{3d})$ are the interpolated landmark point coordinates, extended to 3D for a volume host-mesh. The Sobolev smoothing constraint in this equation (also extended to 3D for a volume host-mesh) ensures that deformation of the host-mesh does not overly distort the new slave-mesh.

Once the optimal host-mesh nodal DOFs are obtained using Equation 2.10, the deformed slave mesh coordinates can be determined. The global coordinates of the slave nodes as well as the nodal first derivatives and higher order derivatives are updated relative to the deformed host-mesh. Since the local coordinates of the slave-mesh within the host-mesh remain unchanged after deformation, the updated slave nodal positions are obtained by substituting the slave local coordinates relative to the host into the host interpolation functions, using the deformed host nodal parameters.

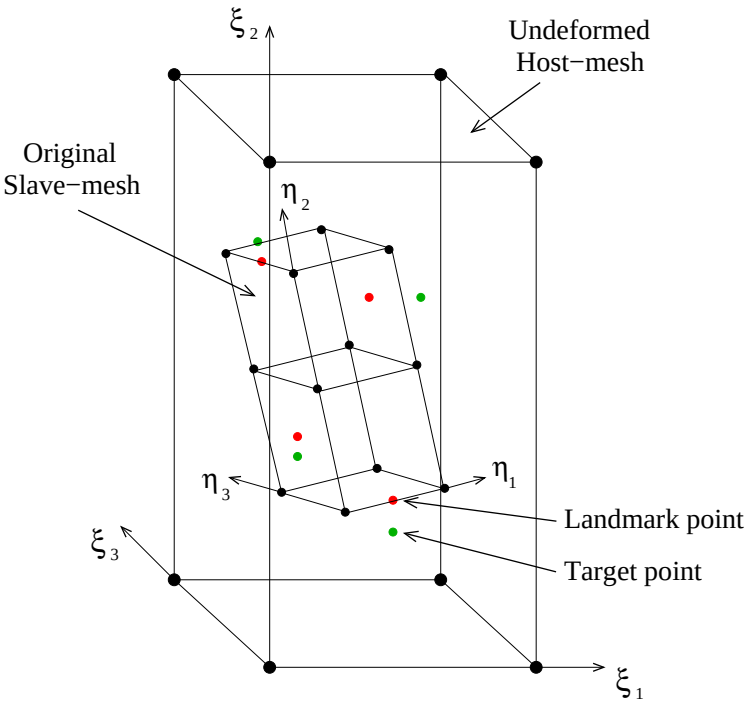

(a)

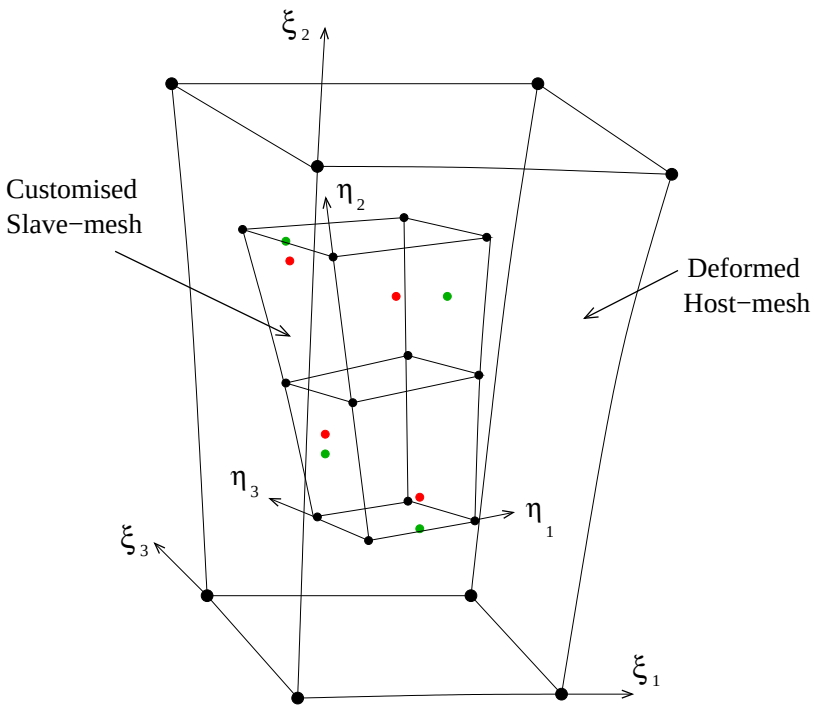

(b)

Figure 2.9: The host-mesh fitting process (a) before deformation and (b) after deformation.

The new slave nodal first derivative values are calculated by expanding Equation 2.13 using the chain rule:

$$\frac{\partial \mathbf{u}}{\partial \eta_1} = \frac{\partial \mathbf{u}}{\partial \xi_1}\frac{\partial \xi_1}{\partial \eta_1} + \frac{\partial \mathbf{u}}{\partial \xi_2}\frac{\partial \xi_2}{\partial \eta_1} + \frac{\partial \mathbf{u}}{\partial \xi_3}\frac{\partial \xi_3}{\partial \eta_1} \tag{2.14}$$

$$\frac{\partial \mathbf{u}}{\partial \eta_2} = \frac{\partial \mathbf{u}}{\partial \xi_1}\frac{\partial \xi_1}{\partial \eta_2} + \frac{\partial \mathbf{u}}{\partial \xi_2}\frac{\partial \xi_2}{\partial \eta_2} + \frac{\partial \mathbf{u}}{\partial \xi_3}\frac{\partial \xi_3}{\partial \eta_2} \tag{2.15}$$

$$\frac{\partial \mathbf{u}}{\partial \eta_3} = \frac{\partial \mathbf{u}}{\partial \xi_1}\frac{\partial \xi_1}{\partial \eta_3} + \frac{\partial \mathbf{u}}{\partial \xi_2}\frac{\partial \xi_2}{\partial \eta_3} + \frac{\partial \mathbf{u}}{\partial \xi_3}\frac{\partial \xi_3}{\partial \eta_3} \tag{2.16}$$

expanding Equation 2.14 and writing in matrix form gives:

$$\begin{bmatrix} \frac{\partial x}{\partial \xi_1} & \frac{\partial x}{\partial \xi_2} & \frac{\partial x}{\partial \xi_3} \\ \frac{\partial y}{\partial \xi_1} & \frac{\partial y}{\partial \xi_2} & \frac{\partial y}{\partial \xi_3} \\ \frac{\partial z}{\partial \xi_1} & \frac{\partial z}{\partial \xi_2} & \frac{\partial z}{\partial \xi_3} \end{bmatrix} \begin{bmatrix} \frac{\partial \xi_1}{\partial \eta_1} \\ \frac{\partial \xi_2}{\partial \eta_1} \\ \frac{\partial \xi_3}{\partial \eta_1} \end{bmatrix} = \begin{bmatrix} \frac{\partial x}{\partial \eta_1} \\ \frac{\partial y}{\partial \eta_1} \\ \frac{\partial z}{\partial \eta_1} \end{bmatrix} \tag{2.17}$$

The coefficient matrix in Equation 2.17 is called the Jacobian matrix of transformation of the host-mesh, at the slave node which is under consideration. The derivatives in the Jacobian matrix are defined using the host-mesh nodal parameters at the local coordinates (ξ_1, ξ_2, ξ_3) of the slave node embedded within the host-mesh. While the derivatives in the right hand side vector are the nodal derivatives of the slave defined by its local coordinate η_1. The unknowns in the equation remain the same before and after deformation, and are calculated using the undeformed host and slave-mesh parameters. After solving Equation 2.17 for the unknown local coordinate derivative values, these are substituted back into the same equation to find the first derivatives of the transformed slave using:

$$\begin{bmatrix} \frac{\partial x}{\partial \eta_1} \\ \frac{\partial y}{\partial \eta_1} \\ \frac{\partial z}{\partial \eta_1} \end{bmatrix}_T = \left[\frac{\partial(x,y,z)}{\partial(\xi_1,\xi_2,\xi_3)}\right]_U^{-1} \left[\frac{\partial(x,y,z)}{\partial(\xi_1,\xi_2,\xi_3)}\right]_D \begin{bmatrix} \frac{\partial x}{\partial \eta_1} \\ \frac{\partial y}{\partial \eta_1} \\ \frac{\partial z}{\partial \eta_1} \end{bmatrix}_O \tag{2.18}$$

where the subscripts T, U, D and O define the transformed slave, undeformed host, deformed host and the original slave mesh respectively. The term $\left[\frac{\partial(x,y,z)}{\partial(\xi_1,\xi_2,\xi_3)}\right]$ is the Jacobian matrix of the host. Calculation of the second derivatives is also carried out via the same process, and has been outlined in detail by Fernandez (2004).

2.5 Skin model construction

Using the FE interpolation, digitisation and fitting techniques outlined above, a detailed FE model of the human skin has been constructed using two separate datasets. VH images were utilised to create the skin model of the torso and limbs, while a separate 3D head model was used for the skin of the head and neck. The following section details the construction of the model, which forms the anatomical framework for this project.

2.5.1 Torso and limbs

Skin models of the torso and limbs were based on high resolution axial VH images as shown in Figure 2.3. These images slices are 1 mm in thickness, have a pixel size of 0.32 mm^2 and measure 1760 x 1024 pixels (Spitzer & Whitlock 1998).

The skin model of the torso (including the thighs), upper and lower limbs have been created separately before being combined in a common reference frame. This is because detailed musculoskeletal models of the upper and lower limbs were created for previous projects, including Reynolds et al. (2004) as shown in Figure 1.21, which included models of the overlaying skin. Hence the limb skin models were constructed before the torso skin model.

Manual digitisation (as described in Section 2.3.1) was carried out for each component of the skin model rather than automatic digitisation. This was due to inability of the automatic digitisation procedure to adequately capture the complex geometry of the fingers and toes for the limb skin models. Although the skin boundary could be readily located, an error of approximately 1-5 mm between the actual surface location and generated data cloud caused the adjacent fingers and toes to intersect with each other. To maintain accuracy and consistency with the limb skin models, the skin of the torso has also been manually digitised. Although this process was more labour intensive than automatic digitisation, the resultant data cloud was more accurate.

For the torso section, the skin was digitised at points approximately 20 mm apart along the skin boundary on every 10th VH slice, to give data points 10 mm apart in the vertical direction (as shown in Figure 2.3). The skin surface of the upper limbs and legs have been digitised approximately 10 mm apart on each image slice, and at 5 mm intervals in the vertical direction.

A higher resolution of data points was required to accurately describe the anatomy of the hands and toes, therefore the hands were digitised using slices separated at 2 mm and the toes using slices separated at 3 mm. In total, 23,549 data points were digitised to define the VH skin surface (excluding the head and neck), as detailed in Table 2.1.

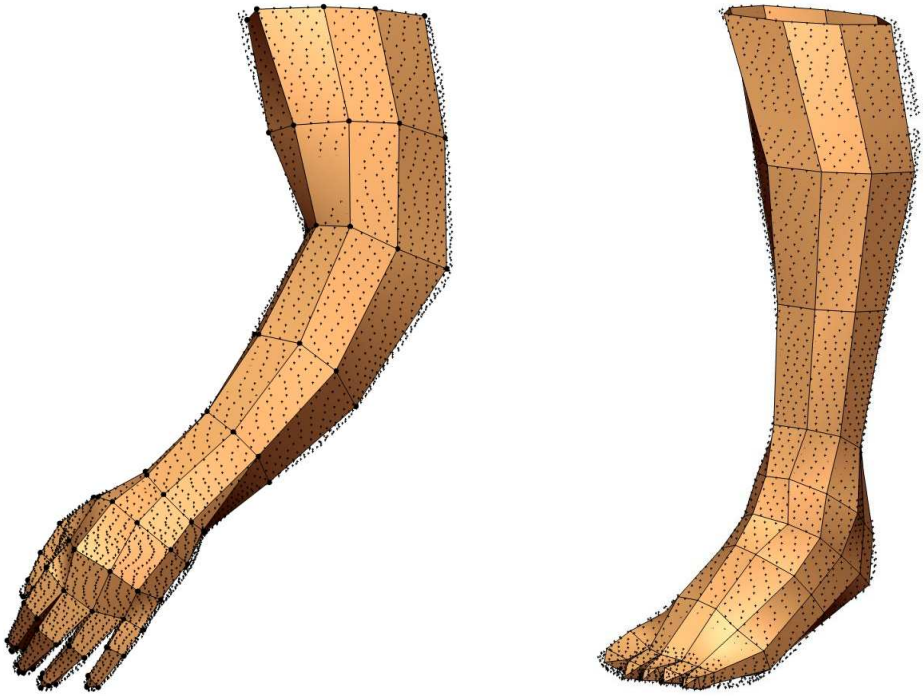

(a) (b)

Figure 2.10: The initial linear mesh of the (a) left upper limb and (b) left leg and foot skin models.

To create each initial linear mesh nodal points have been selected from the digitised data cloud. Figure 2.5(a) and Figure 2.10 show the initial linear meshes constructed for the torso and both limbs respectively. Most elements that have been used are standard 4-noded elements, however at geometrically complex regions such as the armpits, groin, finger and toe bifurcations, collapsed elements with nodal versions (see Section 2.3.2) were required.

Examples of collapsed elements are shown in Figure 2.11 for the hand and foot. The fingertips and tips of the toes utilised collapsed elements to close the meshes, similar to the schematic given in Figure 2.7(a). Collapsed elements were utilised at the wrists and ankles to reduce the number of elements in the arm while maintaining continuity with the increased number of elements required to accurately model the fingers and toes. Bifurcations present in the mesh at the fingers and toes also required collapsed elements with nodal versions. Adjacent fingers and toes share some of the same nodes, which resulted in the mesh containing elements with opposing ξ-directions. To accommodate this, nodal derivatives between the fingers and toes were kept fixed during the fitting process to ensure adjacent elements remained joined.

The upper limb and leg from one side of the body were fitted individually and then reflected to produce the opposing limbs. The fitted torso and thigh mesh (shown in Figure 2.5(b)) was then

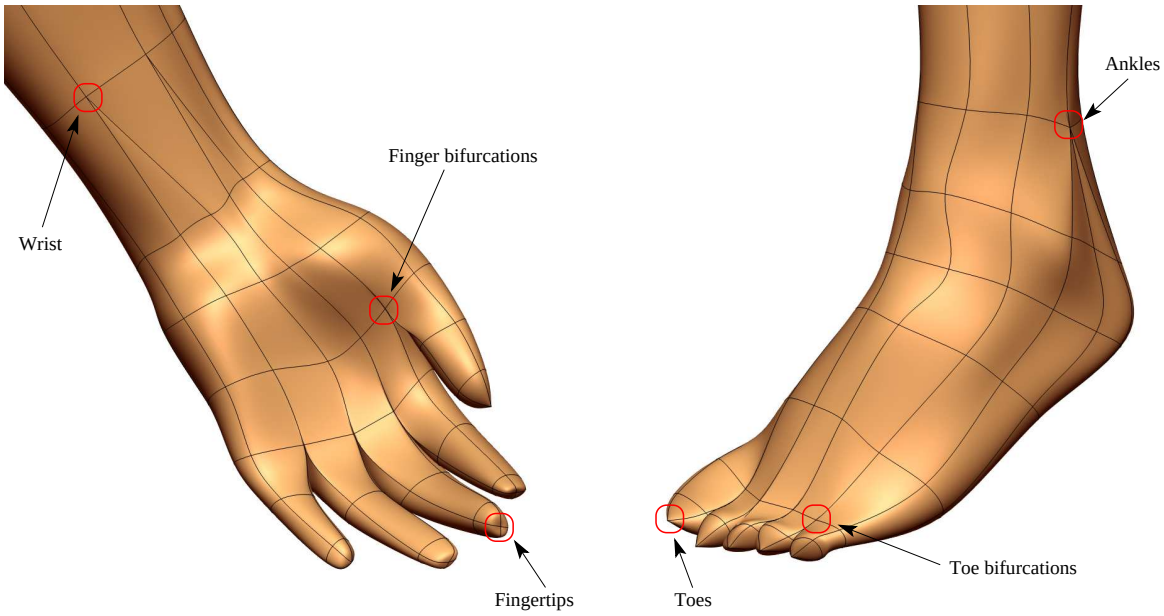

(a) (b)

Figure 2.11: Collapsed elements with nodal versions on the skin of the (a) hand and (b) foot.

connected to the upper limb and leg meshes, to create a joined skin mesh as shown in Figure 2.12. The coordinate system is also visualised in Figure 2.12, where the z-direction is aligned vertically, in a direction normal to a transverse plane through the skin model. Meanwhile the y-direction is normal to a coronal plane, and the x-direction is normal to a sagittal plane through the skin model.

Table 2.1 gives information regarding each of the separate fits that have been carried out, indicating that the RMS error between the data points and the fitted skin surface ranges from 1.66 to 2.50 mm (disregarding the head and neck model). Before the head and neck model were joined to the skin mesh (in Section 2.5.2) a total of 842 nodes and 886 elements were used.

Body Part	**# Data pts**	**# Nodes**	**# Elements**	**RMS error (mm)**
Torso and thigh	6649	378	362	2.03
Left upper limb	4717	131	138	2.50
Right upper limb	4717	131	138	2.50
Left leg & foot	3733	117	124	1.66
Right leg & foot	3733	117	124	1.66
Head & neck	25271	201	212	1.59
Combined Model	48820	1027	1098	1.94

Table 2.1: Skin mesh fitting parameters.

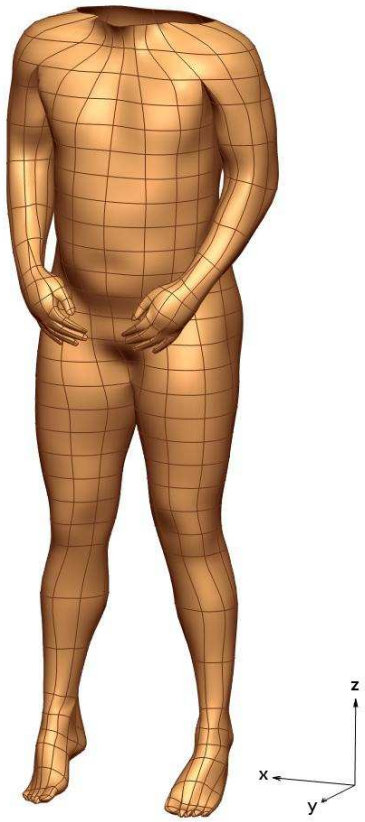

Figure 2.12: The fitted VH skin mesh with the torso and limbs connected together.

2.5.2 Head and neck

Skin lymphatic drainage of the head and neck is very complex (de Wilt et al. 2004), and therefore a high level of detail was required for this region of the skin model to ensure LS data could be accurately mapped onto it. The VH dataset was deemed unsuitable for this purpose since it has an abnormally short neck. Therefore investigation was conducted to locate an alternative data source.

The data source for the head and neck model was required to fit a number of criteria. Firstly, it needed to have a well defined neck region so the melanoma sites on the neck as well as node fields located in the neck could be adequately visualised. Secondly, the model was required to have a generic looking male face so that it would suit the male VH skin model constructed in Section 2.5 onto which it would be attached. Thirdly the model needed to have no hair, so that the skin on the scalp could be seen. Lastly the model needed to be anatomically accurate.

The most readily available data source which fit the criterion was determined to be a 3D adult head model from Sawbones® (Pacific Research Laboratories, Inc., USA), as shown previously in Figure 2.4. This model includes a skull, facial muscles and overlaying skin. The skull was constructed

Figure 2.13: The Sawbones head and neck model.

from a casting of a cadaver, the muscles were hand sculpted, and the skin came from a casting of a volunteer. Since the skin was taken from a real person it was anatomically accurate, and had the additional benefit that during data collection there would be no error introduced by model movement. Also, the model was considered a potential data source for future projects conducted at the ABI which require integrated head models including facial muscles and the skull.

The surface of the Sawbones model was scanned using the hand-held Polhemus^{TM}Fastscan laser scanner (as defined in Section 2.3.1 and shown in Figure 2.13). The raw data from this scan (Figure 2.14) was very dense, therefore a smaller dataset has been created to use during fitting by taking every 10th data point. Also the Sawbones model was not completely symmetric on both sides, so data from the left side of the head model has been reflected to give data on the right side of the head, creating a data cloud of 27999 points.

An initial linear mesh was constructed by selecting data points from this symmetrical data cloud. Since the data cloud was symmetric, data points have been chosen from one side of the head and neck to form nodes and then reflected to form nodes on the other side. Care was taken to ensure that the mesh could eventually be joined to the existing skin mesh in Figure 2.12, so the same number of nodes and elements were chosen circumferentially around the base of the neck as was used for the top of the torso model.

Mesh topology was designed to give a minimal number of nodes and elements while still allowing all important anatomical features to be accurately represented. The eyes, nose, mouth and ears needed to be well defined so that the LS data could be accurately mapped relative to these features (outlined in Chapter 3). Due to the complex nature of these anatomical features, a number of

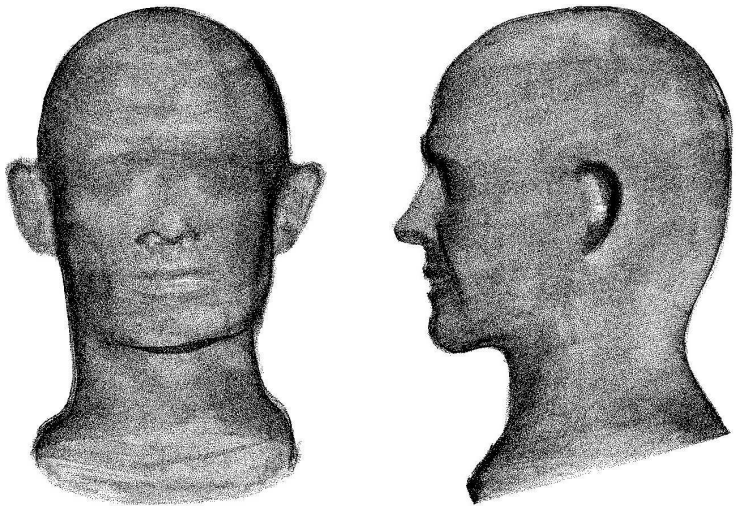

(a) Anterior (b) Left

Figure 2.14: Raw scanned data of the Sawbones head model.

collapsed elements (refer to Section 2.3.2) were required. Collapsed elements with nodal versions were incorporated at the edges of the eyes, mouth, around the nostrils and at the top of the nose, on the ears and at the top of the head. In total, 20 separate nodes required versions to define them.

During mesh construction consideration was given to the development of the skin selection tool outlined in Section 5.2, which visualises cumulative lymphatic drainage from individual skin elements. For this clinical tool it was beneficial to create skin elements with boundaries at important anatomical locations. For example, an element boundary was created to separate the left and right sides of the head as well as posterior and anterior portions of the head. Figure 2.15 shows the initial linear mesh and fitted mesh of the Sawbones head and neck model. This mesh utilises 201 nodes and 212 elements, and was fitted to give an RMS error of 1.41 mm.

After the head and neck mesh was created using the Sawbones data, it was attached to the remainder of the skin mesh. Before the models could be joined together however, a series of modifications to the head mesh were required. Firstly, as shown in Figure 2.16, the Sawbones head model dimensions were compared with the original VH's head to determine whether they were in correct proportion to each other. The VH has a very short, thick neck and his head dimensions were approximately 110% larger than the Sawbones model.

Additionally, the nodal coordinates around the base of the neck of the Sawbones mesh did not match up with the existing skin model. For these two meshes to be joined, the head mesh needed to be refitted and modified accordingly. To scale the head to the correct size, both the initial linear

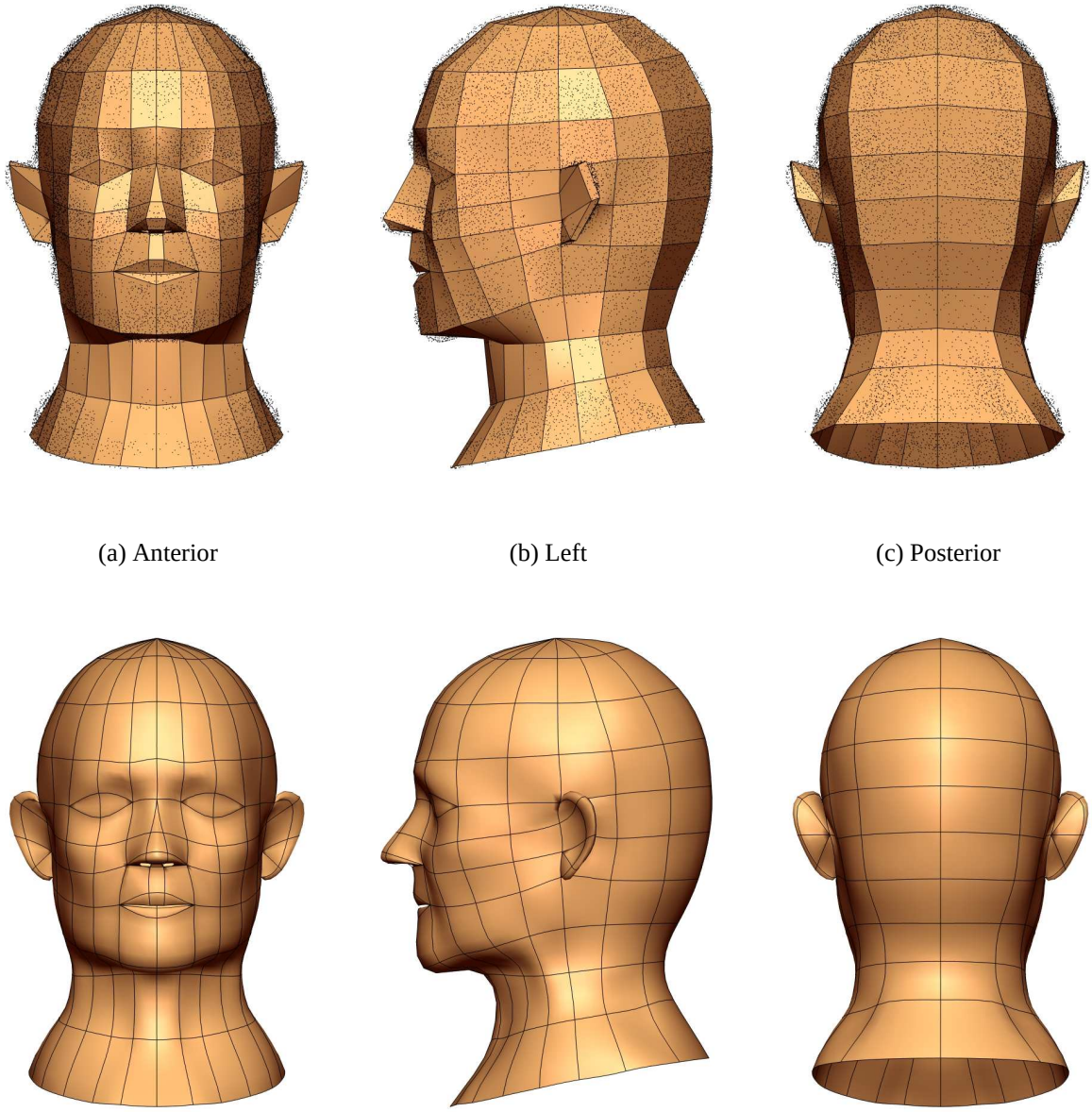

(a) Anterior (b) Left (c) Posterior

(d) Anterior (e) Left (f) Posterior

Figure 2.15: Sawbones head and neck skin mesh (a-c) linear mesh and (d-f) fitted bicubic mesh.

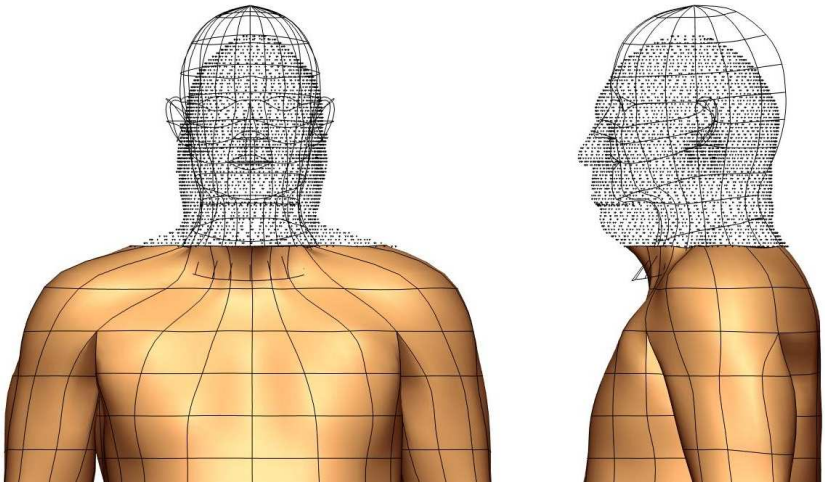

(a) Anterior (b) Left

Figure 2.16: Comparing VH head data to the initial Sawbones fitted model.

mesh and the Sawbones data have been scaled by 110%. Also, selected nodal coordinates at the base of the Sawbones mesh were altered to match those in the torso mesh. As shown in Figure 2.17, posterior and lateral neck nodes have been taken from the torso model (shown in black) to enable a smooth representation of the top of the shoulders. Meanwhile anterior neck nodes were chosen from the Sawbones data cloud (shown in red), since the anterior nodes on the torso were positioned too far forward relative to the Sawbones model.

This modified head and neck mesh has then been refitted to create a model which was subsequently joined to the torso. The data points that were used during this second fitting process have been taken from both the Sawbones head and neck data cloud and the digitised VH neck. Since the nodal coordinates for the neck had been altered to match those on the torso, a combination of data points from the Sawbones model and the VH were required to model this region. Hence, data for the lateral sides of the neck extending to the top of the shoulders has been taken from the digitised VH images, while data for the anterior and posterior neck was taken from the Sawbones data cloud (as shown in Figure 2.17). After refitting, this final head and neck model had an RMS error of 1.59 mm, and was constructed using 201 nodes and 212 elements (detailed in Table 2.1).

The head and neck model was then joined to the remainder of the skin mesh to give the final skin model shown in Figure 2.18. This model contained 1027 nodes and 1098 elements. Note that the model shown here presents the arms oriented lateral to the body instead of the initial VH's anterior arm orientation. Methods for this articulation and justification are outlined in Section 3.1.2.

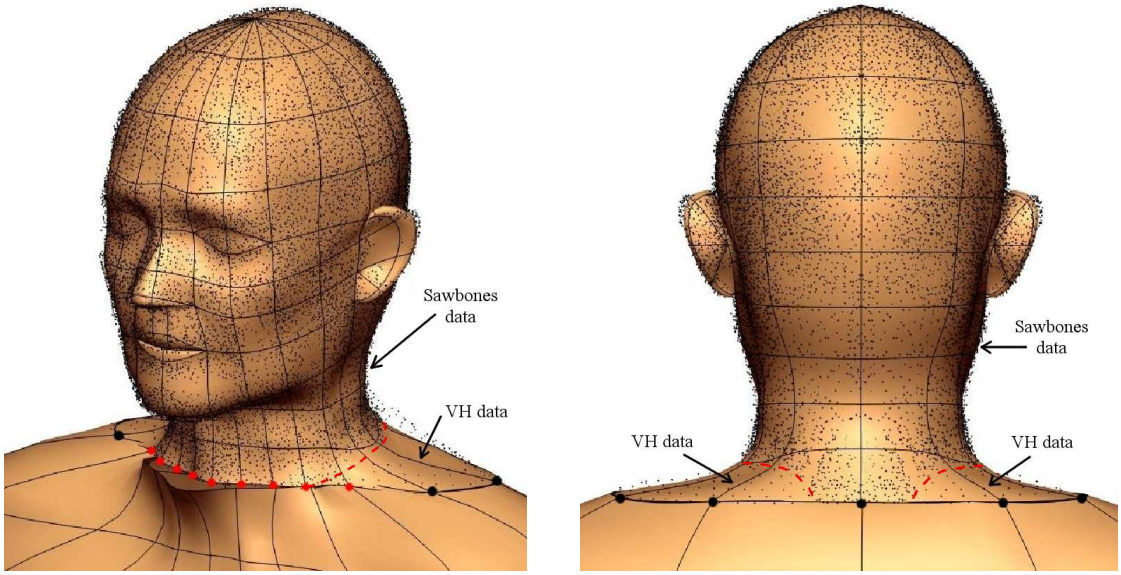

(a) (b)

Figure 2.17: Refitting the head and neck model before joining to the skin mesh.

2.6 Lymph node model construction

In addition to the FE skin model, a detailed lymph node model has been created. This model provides the anatomical basis for mapping SN node field locations from the LS database. Models of each node field that directly drains the skin as defined by the SMU (and listed in Appendix A) have been created. Nodes have been represented as discrete structures in 3D space, in contrast to the skin model which has been modelled with surface FEs.

Image slices from the VH were used to define the geometric locations of each node field in the model. For example, Figure 2.19 shows a VH slice of the head with some visible cervical and parotid lymph nodes. This ensured that the position of each field would be in the correct space relative to the skin model. It is important to note however, that since the head and neck of the skin model has been based on a different dataset, the anatomical position of node fields in this region could not be positioned relative to the skin of the head and neck.

Due to their small size, lymph nodes were often difficult to visually detect on VH slices. Therefore the geometric position of each node has been determined via a dual method of digitising all visible nodes on VH images, and then positioning the remaining nodes relative to adjacent anatomical structures using the literature as detailed in Table 2.2. Commonly the referenced node field locations were determined from a combination of sources. Descriptions of the anatomical location of

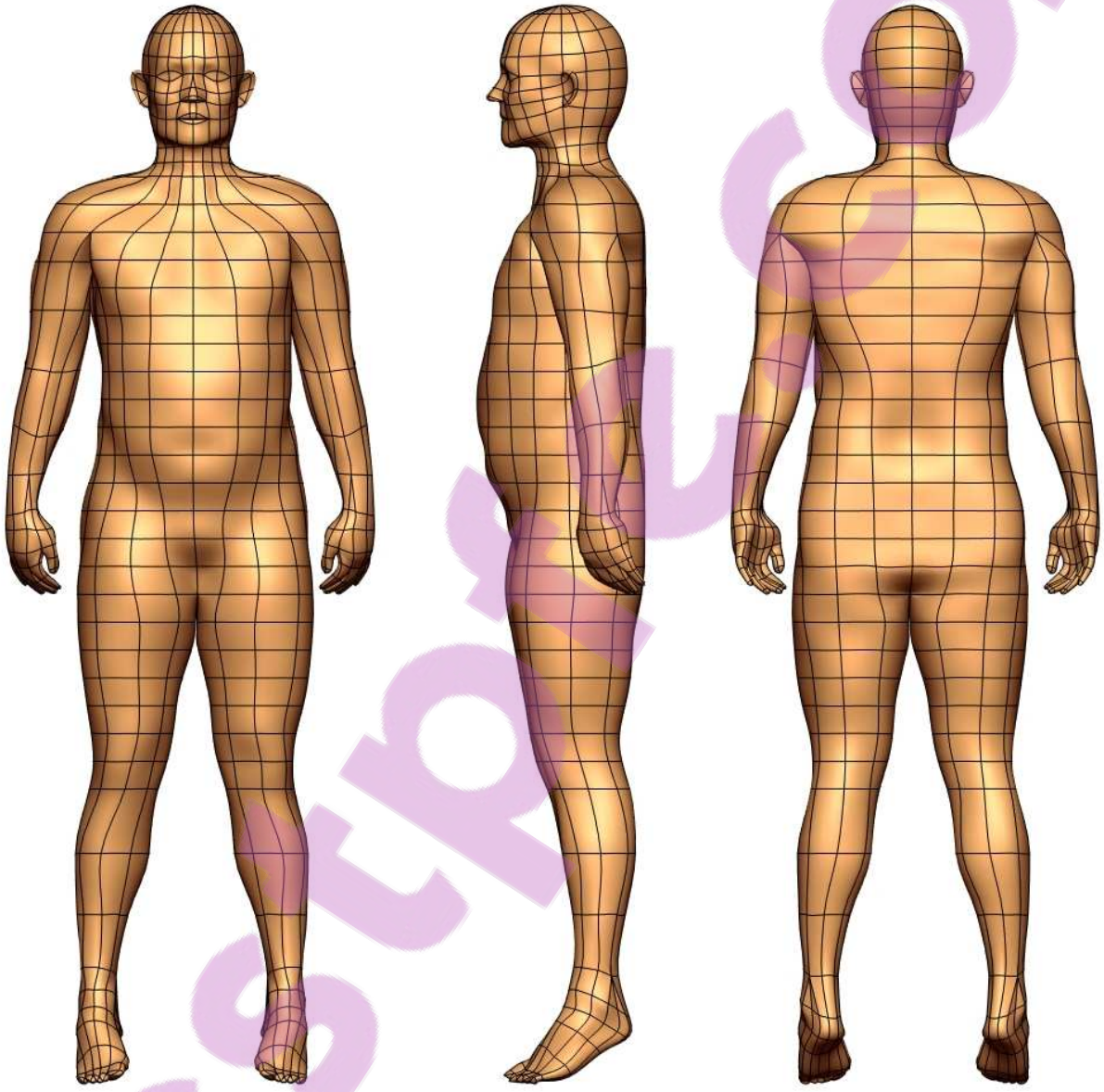

(a) Anterior (b) Left (c) Posterior

Figure 2.18: Final combined skin model.

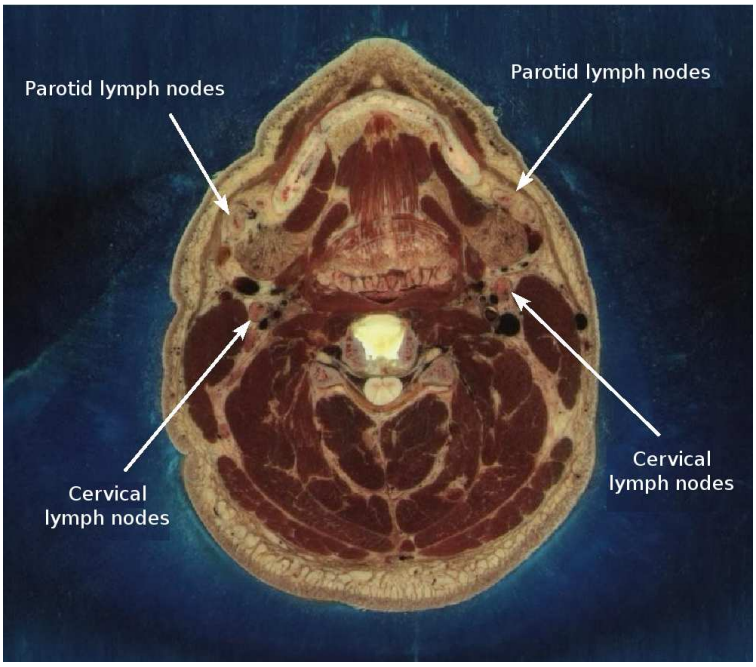

Figure 2.19: Axial VH image of the head with identifiable lymph nodes.

each node field has been given in Section 1.3.2. Table 2.2 also gives the number of nodes in each field of the lymph node model.

The full lymph node model is shown in Figure 2.20, while node field locations can be seen individually labelled in Figure 1.6. Note that the head and neck of the skin model has not been included in these images, since it was not based on VH data and therefore is not in the correct position relative to the lymph node fields. All node fields located on both sides of the body (excluding occipital, preauricular, postauricular and cervical level I) have been positioned on one side of the body and then reflected to give the opposing node field.

A number of lymph nodes were visible in the head and neck of the VH. Occipital, preauricular and postauricular nodes have been modelled with only one node in each field. There was only one node visible in the right occipital and right postauricular node fields, while the other nodes have been positioned relative to the anatomy. Similarly, only one submental node was visible, while a few nodes could be seen in the supraclavicular fossa. Additional nodes in each of these two fields have then been added relative to the chin and clavicle respectively.

All cervical nodes have been manually digitised, and then division of these nodes into each of the five levels has been carried out by referring to adjacent anatomical structures. In particular, the sternocleidomastoid muscle which marks the boundaries of levels I and V, and divides in thirds to give levels II to IV, has provided an important anatomical reference for these fields.

Node field	Reference	#Nodes	
		Left	Right
Occipital	Netter p.68, Gray p.844	1	1
Preauricular	Clemente p.455, Gray p.844, Netter p.68	1	1
Postauricular	Clemente p.455, Gray p.844, Netter p.68	1	1
Cervical:			
- level I	Clemente p.455, Gray p.843-845, Netter p.68 & 69, Textbook of Melanoma p.296	3	3
- level II	(same as level I)	12	12
- level III	(same as level I)	10	10
- level IV	(same as level I)	14	14
- level V	(same as level I)	10	10
Supraclavicular fossa	Clemente p.6, Netter p.68	4	4
Submental	Clemente p.455, Netter p.68 & 69	4	
Axilla	Clemente p.12 & 15, Gray pp.845-848, Netter p.177, 466	20	20
Epitrochlear	Gray p.846, Netter p.466	3	3
Infraclavicular	Gray p.846	2	2
TIS	(Uren et al. 1996), Netter p.409	5	5
Interpectoral	Gray p.847, Netter p.177	3	3
Internal mammary	Clemente p.6, Netter p.177	5	5
Costal margin	Clemente p.93	1	1
Intercostal	Gray p.841 & 856, Netter p.235 & 258	7	7
Paravertebral	Clemente p.247, Gray p.850	20	
Paraaortic	Clemente p.247, Gray p.850	14	
Retroperitoneal	Gray pp.1336-1342, Netter p.258	2	
Upper mediastinal	Clemente p.119 & 144, Netter p.530	1	
Groin	Clemente p.243 & 315, Gray p.849 & 854, Netter p.258, 306, 329, 386-388 & 528	16	18
Popliteal	Gray p.849, Netter p.528	4	4
Interval	(Uren et al. 2003)	-	

Table 2.2: Node field location references used to construct the lymph node model and the number of nodes in each field of the model.

The axillary node field is highly complex, where nodes are organised into five different groups. Although a number of nodes were visible on VH image slices, it was difficult to locate nodes in every group. In total, 20 axillary nodes have been modelled, both digitised directly on image slices and placed relative to blood vessels and adjacent muscles. The groin node field is also very detailed, including both superficial inguinal nodes and deep obturator nodes. Nodes could be readily seen in this region, so the entire field has been digitised on both sides of the body with VH images.

There were a number of node fields that could not be seen at all on VH images. In these cases all nodes contained within a given field have been positioned relative to adjacent anatomical struc-

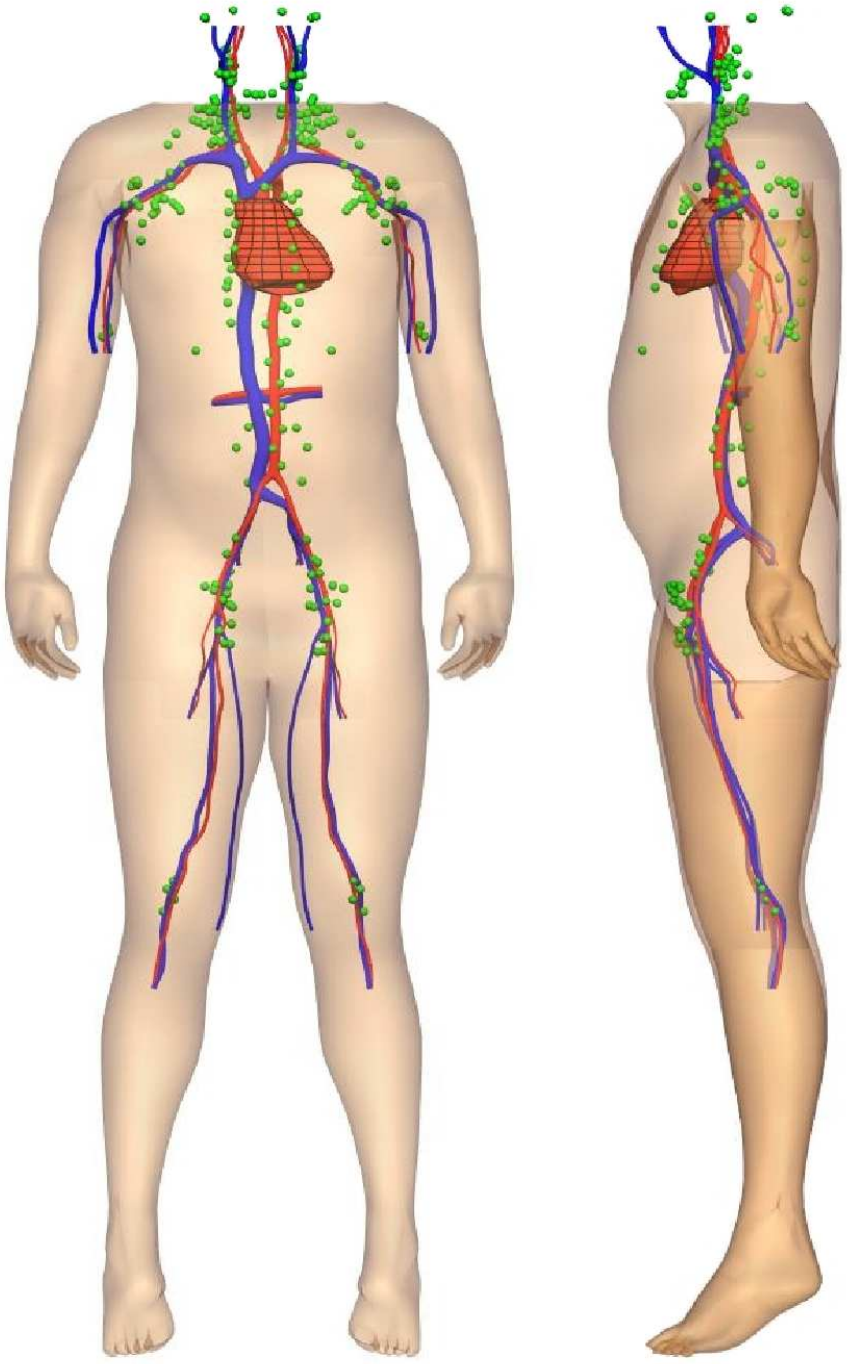

(a) Anterior (b) Left

Figure 2.20: Lymph node model visualising all node fields. The skin of the head and neck is not shown here since it was based on a different dataset than that used to create the lymph node model, so they were not in the correct geometric space relative to each other.

tures. These include the TIS, upper mediastinal, interpectoral, costal margin and popliteal node fields. Only one node was visible in the infraclavicular and internal mammary node fields, while intercostal nodes have been positioned relative to the ribs.

Paraaortic, paravertebral and retroperitoneal nodes were particularly difficult to see. Often lymph nodes located in the trunk are very small and although some could be seen in these fields the majority of nodes have been positioned relative to the aorta and vertebral bones. The retroperitoneal node field has simply been represented as one node on each side of the body, behind the peritoneum.

Interval nodes have not been represented in this full lymph node model, since they do not lie in a generic node field location but between them. During visualisation of LS data in Chapters 4 and 5, interval nodes have been represented as a single node outside the body.

2.7 Summary

This chapter detailed the underlying modelling techniques behind, as well as the creation of, anatomically based models used in this study. FEs with cubic Hermite interpolation have been introduced, and the processes used to create an FE model via digitisation, initial linear mesh construction and fitting has been described. Host-mesh fitting as a method to morph FE models to a set of patient-specific conditions was outlined and demonstrated. Construction of a complete skin and lymph node model was then described, which has been created using the VH dataset and a separate Sawbones head and neck model. The following chapter describes how the SMU's LS data has been mapped onto this skin and lymph node model.

Chapter 3

Mapping Lymphoscintigraphy Data onto Anatomical Geometry

The skin and lymph node model created in the previous chapter provided the anatomical framework onto which the SMU's LS data could be mapped. This chapter outlines the methods utilised to map the LS data from 2D images onto the 3D skin and lymph node model. Mapping the primary melanoma site locations has been carried out differently for separate skin regions, through the application of tailored free-form deformation and projection techniques. Meanwhile the SN locations have been mapped onto a reduced lymph node model modified from Section 2.6. Subsequently, these mapped data have provided the basis for novel 3D visualisation and detailed statistical analysis of skin lymphatic drainage, which has been carried out in the following chapters. The work presented here has been published, and can be seen in Appendix C.

3.1 Mapping the primary melanoma site

The methods utilised by the SMU to record primary melanoma sites on 2D body maps have been previously outlined in Section 1.6.1. Mapping these coordinates from 2D onto the 3D skin model posed challenges, specifically since the SMU body map outlines were oriented differently to the skin model. The primary melanoma site coordinates have therefore been mapped onto the skin model (constructed in Section 2.5) using different techniques for separate regions of skin. The following sections detail the projection methods used for the different skin regions: the torso and legs, the arms, the hands and feet, and the head and neck.

3.1.1 Torso and lower limbs

The torso and leg melanoma sites have been mapped using a direct linear projection. Figure 3.1(a) demonstrates how the anterior torso body map (introduced previously in Section 1.6.1) did not initially match up with outline of the skin model. Therefore, the host-mesh fitting technique (as described in Section 2.4) has been applied to morph the 2D body map outlines to correspond with the boundaries of the 3D skin model.

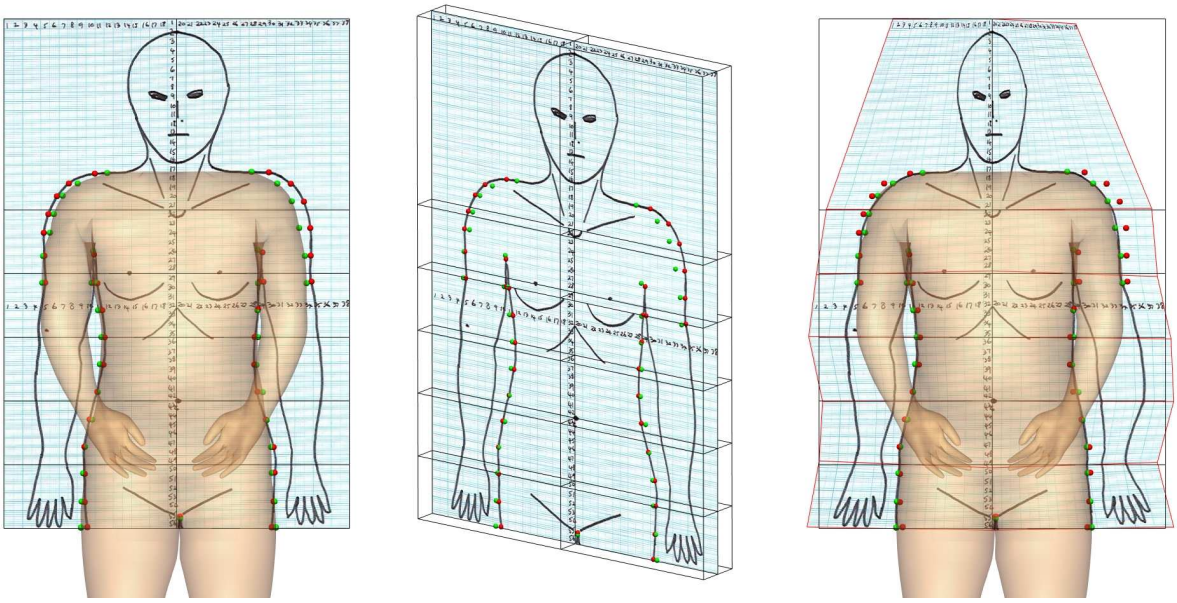

(a) (b) (c)

Figure 3.1: Host-mesh fitting to align the anterior torso body map with the skin model. (a) Before fitting, (b) the body map slave-mesh embedded within a trilinear host-mesh, and (c) after fitting. Landmark points are shown in red and target points in green.

Melanoma sites are often described relative to the midline of the body, the umbilicus and groin, therefore before fitting was carried out the body maps have been aligned with these corresponding features on the skin model. Some nodal coordinates were subsequently fixed during fitting so the deformed body maps maintain these important locations.

Figure 3.1(a) shows the landmark (initial) points in red digitised on the undeformed body map outlines, and the target (final) points in green taken from the boundary of the skin model when viewed anteriorly. Target points have then been projected orthogonally in the y-direction onto the same 2D plane as the landmark points on the body maps. Thus host-mesh fitting has been reduced to a 2D problem, only requiring fitting in the x- and z-directions.

Note that the arms, hands, head and neck have not been included in this process. The arms of the skin model were not in the correct orientation relative to the body maps, and required articulation via host-mesh fitting before mapping (described in Sections 3.1.2). The hands of the skin mesh could not be oriented with the body maps for a direct orthogonal projection, and so they have been manually positioned as described in Section 3.1.3. Meanwhile melanoma sites on the head and neck were mapped separately, since the head and neck model was created after the rest of the body and was not available for mapping when the torso sites were projected. The methods for mapping the head and neck sites have been detailed in Section 3.1.4.

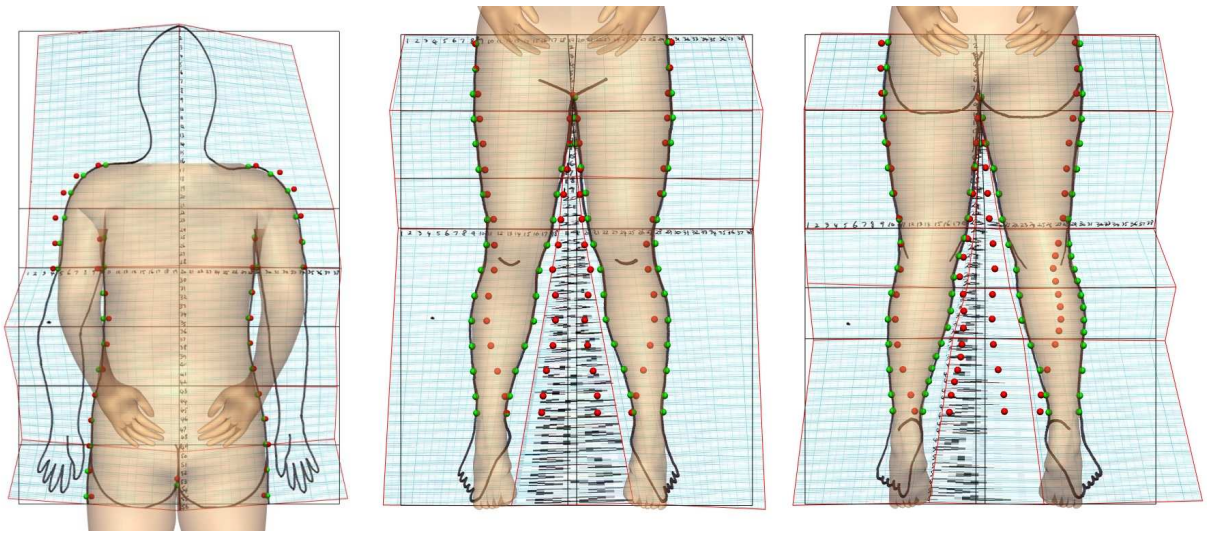

(a) Map 1: Posterior torso (b) Map 3: Anterior legs (c) Map 4: Posterior legs

Figure 3.2: Host-mesh fitted body maps aligned with the skin model. Landmark points are shown in red and target points in green.

Trilinear elements have been used for the host-mesh, and bilinear elements for the embedded slave-mesh (Figure 3.1(b)). Although the slave is comprised of 2D elements, each node has three global coordinates and therefore a volume (3D) host-mesh was required to completely embed it. The number of elements in the slave and host-mesh was progressively refined from one to a higher number of elements to increase the number of mesh degrees of freedom (DOFs) and thereby increase the accuracy of the fit. Figure 3.1(c) shows the final host-mesh fitted body map for the anterior torso. The remaining deformed body maps are shown in Figure 3.2 with the undeformed body map boundaries shown in black.

The initial body map outlines have drawn the anterior and posterior legs very close together (see Figure 1.14) as opposed to the skin model which has the legs further apart. Therefore to ensure the body map legs could be deformed appropriately, thin elements have been placed in between the

legs in both the host-mesh and slave-mesh (see Figure 3.2). Table 3.1 details parameters from each body map host-mesh fit, where the RMS error values have been kept below 3.50 mm.

Map #	Body Map	# Nodes	# DOFs	# Elements	RMS error (mm)
1	Posterior torso	42	66	12	3.17
2	Anterior torso	42	64	12	3.32
3	Anterior legs	38	68	12	3.22
4	Posterior legs	46	82	15	3.40

Table 3.1: Host-mesh fitting details for the torso and leg body maps.

After host-mesh fitting, the global coordinates of each primary melanoma site have been updated relative to the deformed slave-mesh and then projected orthogonally in the y-direction onto the skin mesh (Figure 3.4(a)). To enable direct orthogonal projection the skin model was first reduced from 3D to 2D, by setting all mesh y-coordinates and their derivatives to zero. Note however, that for each of the four projections only the skin elements pertaining to the corresponding body map have been reduced to 2D. For example, as shown in Figure 3.3 only the anterior torso skin elements have been flattened for the anterior torso melanoma sites projected from body map 2. This was to ensure that coordinates did not project incorrectly to the posterior torso due to all skin elements being in the same 2D plane.

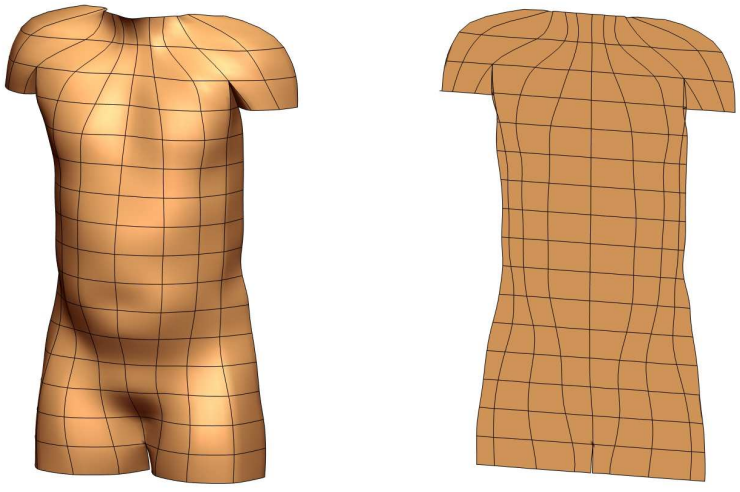

(a) (b)

Figure 3.3: Converting the anterior torso skin mesh from (a) 3D to (b) 2D.

Local material coordinates of each projected melanoma site on the 2D skin mesh have been used to interpolate global melanoma coordinates on the 3D bicubic skin mesh (Figure 3.4(b)). This pro-

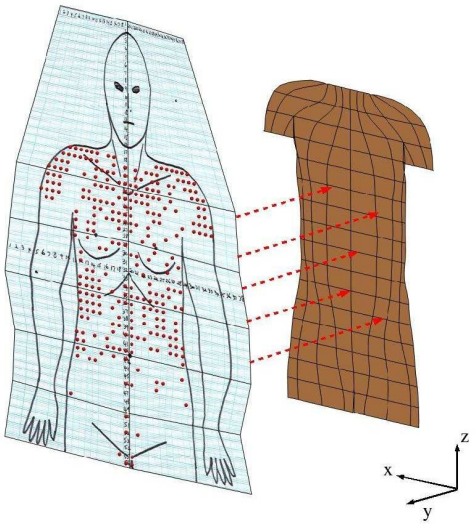

(a)

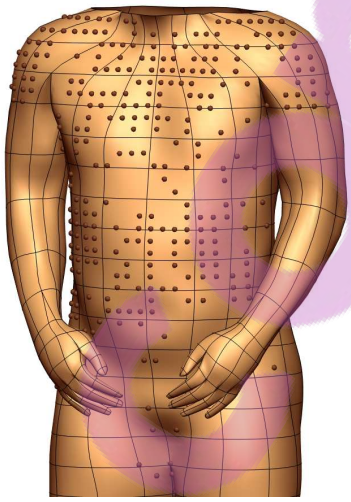

(b)

Figure 3.4: (a) Projecting melanoma (X,Y) coordinates orthogonally onto the 2D anterior torso skin mesh and (b) the final interpolated melanoma coordinates on the 3D skin mesh.

jection created a small error, particularly at elements with high curvature. Figure 3.5 schematically demonstrates a body map (X,Y) melanoma coordinate projected onto a 2D skin element and then the interpolated position within the corresponding 3D skin element. Local ξ coordinates are the same for both elements, however the high curvature at Node 2_{3D} and element arc-length causes a change in the global x-coordinates. This also occurs in the global z-coordinates. This error is particularly increased at elements with high curvature, and at skin elements that are aligned approximately normal to the x-plane at the sides of the body and interior legs. Table 3.2 details the resultant error for each projection.

Table 3.2 details the resultant error for each projection, which has been kept below 1.60 mm. Since each grid unit equates to between 1.5 and 2 cm^2, the error is below 11% of a grid unit. Therefore these projected melanoma sites on the 3D skin model are highly accurate, and are well within the body map resolution. The smallest RMS error of 0.85 mm is present for projected posterior torso melanoma sites. This is due to a high concentration of melanoma sites at the middle upper back where the elements are largely flat because their adjoining nodes have a low curvature.

3.1.2 Upper limbs

The VH dataset used to create the skin mesh has the arms oriented anterior to the body, in contrast to the arms' lateral orientation on the body maps (as shown in Figure 1.14). As a result, arm

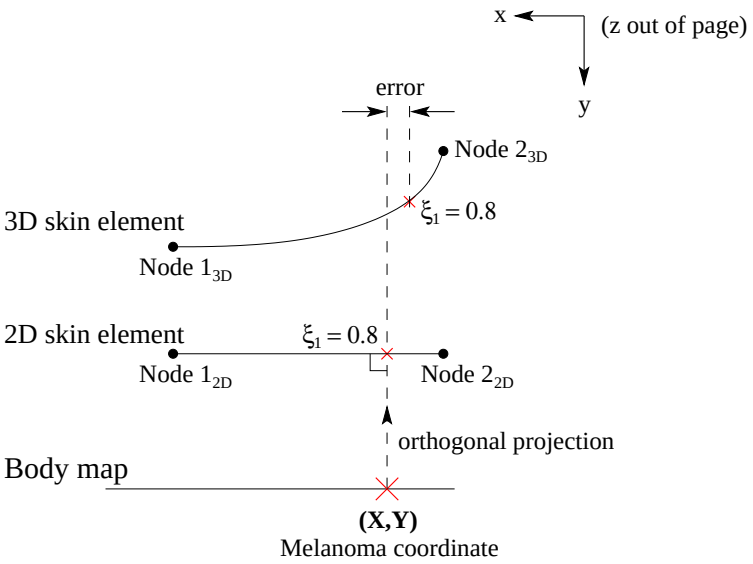

Figure 3.5: Error created during interpolation of projected torso and leg melanoma coordinates from the 2D to 3D skin mesh.

Map #	Body Map	# Melanoma pts	RMS error (mm)
1	Posterior torso	1774	0.85
2	Anterior torso	527	1.17
3	Anterior legs	631	1.59
4	Posterior legs	406	1.35

Table 3.2: Projection details for the torso and leg melanoma sites.

melanoma sites could not be linearly projected in the same manner as the torso and leg melanoma sites. Instead, to enable mapping of these sites, the arms have first been articulated using host-mesh fitting from their initial anterior position to a lateral position at the sides of the body. This fitting has been carried out via an extension of the arms at the elbow joints.

The elbow is a hinge joint which only allows movement in one direction (i.e. flexion or extension), comprised of the humerus in the upper arm and the ulna and radius in the forearm. FE models of these bones created previously (Fernandez et al. 2004) have been used for this transformation. These bones have been treated as rigid bodies that do not undergo deformation during transformation (as would be expected under normal physiological conditions), in contrast to the skin which is a soft tissue that can shear and stretch.

The radius and ulna geometries were translated and rotated manually about the humerus from an initial anterior position to a lateral orientation (Figure 3.6(a)). A total of 31 landmark points have been defined on the surface of the radius and ulna, and 31 corresponding target points were calculated by applying this resultant transformation matrix to the landmark point coordinates.

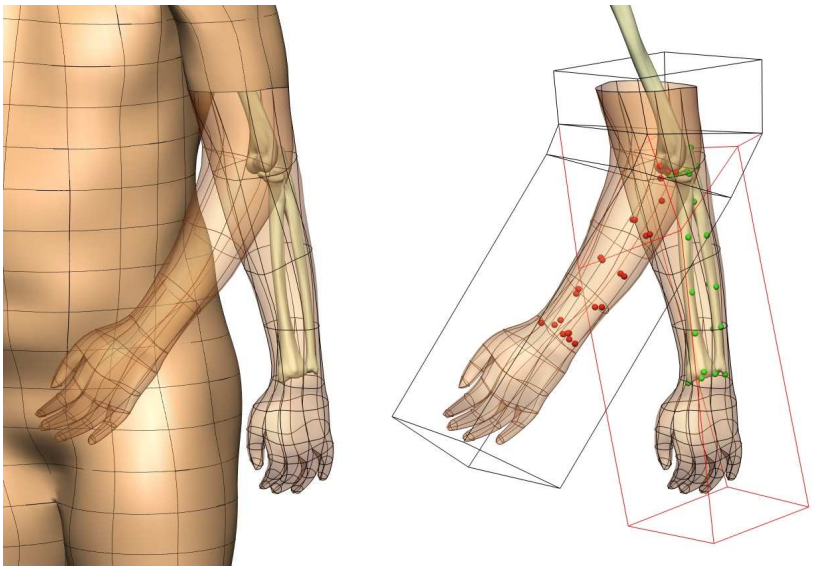

(a) (b)

Figure 3.6: The left arm host-mesh fitted about the elbow joint. (a) Initial and final arm mesh with the radius and ulna in the final transformed position, and (b) the arm slave-mesh embedded within a trilinear host-mesh before and after deformation.

Three trilinear elements have been used for the host-mesh, to embed the bicubic skin slave-mesh (Figure 3.6(b)). Nodal coordinates at the upper host-mesh element were fixed to ensure the top nodes of the slave-mesh would remain unchanged after fitting and maintain continuity with the remainder of the skin mesh. The middle element surrounds the elbow joint and has undergone the most significant deformation during fitting. The right and left arms have been fitted separately, giving an RMS error of 4.17 mm and 4.24 mm respectively between the deformed arm and target points.

After fitting, in order to project the melanoma (X,Y) coordinates the skin mesh arms have been flattened from 3D to 2D. Each arm cross-section has been separated into anterior and posterior arm segments. Figure 3.7(a) illustrates a cross-section of the arm with the anterior segment reduced to 2D. Segment edge nodes (nodes 1, 5, 9 and 13) were joined to create 2D bilinear elements. Internal nodes (nodes 2 - 4 and 10 - 12) have then been orthogonally projected onto the element edges and joined to create refined 2D elements with the same topology as the original 3D skin mesh arms (Figure 3.7(b)).

Correlation between these 2D arm elements and the body maps was established by discretising the arms on the body maps into elements with the same topology. To do this the vertical distance ($\triangle$z) between arm edge nodes (Figure 3.7(b)) has been divided by the total vertical distance of the arm

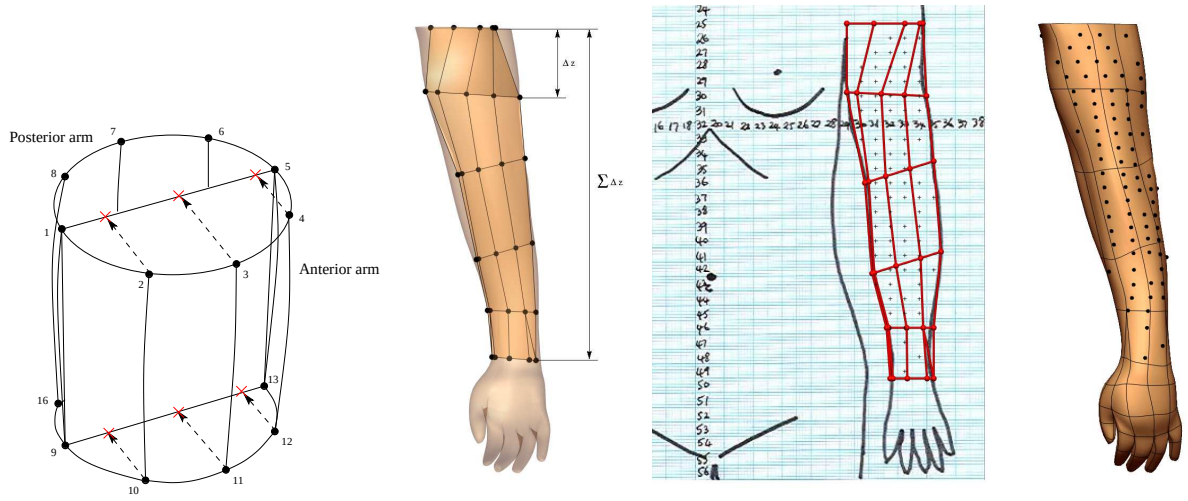

(a) (b) (c) (d)

Figure 3.7: Projection method for the arm melanoma sites.

($\sum \triangle$z). This gave a proportion which has been used to determine the relative sizes of elements on the body map arms and associated nodal positions (as shown in Figure 3.7(c)).

It was important to ensure continuity between the projected melanoma sites on the torso and arms, since they were projected using two different methods. Therefore, the nodal coordinates used for the 2D arms at the junction of the flattened torso and arms have been taken from the 2D torso (the 2D anterior torso can be seen in Figure 3.3(a)). For the anterior arm projections this junction is located at the armpits. For the posterior arm projections the junction is located one element below the armpits.

Following this, the local coordinate of each melanoma site on the body map elements has been calculated, which corresponds to the 2D arm element local coordinates. Subsequently the final melanoma coordinates on the 3D arm (Figure 3.7(d)) have then been calculated via interpolation of these local coordinates.

3.1.3 Hands and feet

The hand and foot outlines on the body maps (see Figure 1.14) could not be oriented with the skin mesh to enable a direct orthogonal projection, so these melanoma sites have been positioned manually. To do this, all possible sites on the hands and feet of the body maps have been defined, and then corresponding sites were manually placed on the skin mesh (Figure 3.8). Each melanoma site on the hands or feet that were present in the database were ascertained from these sites.

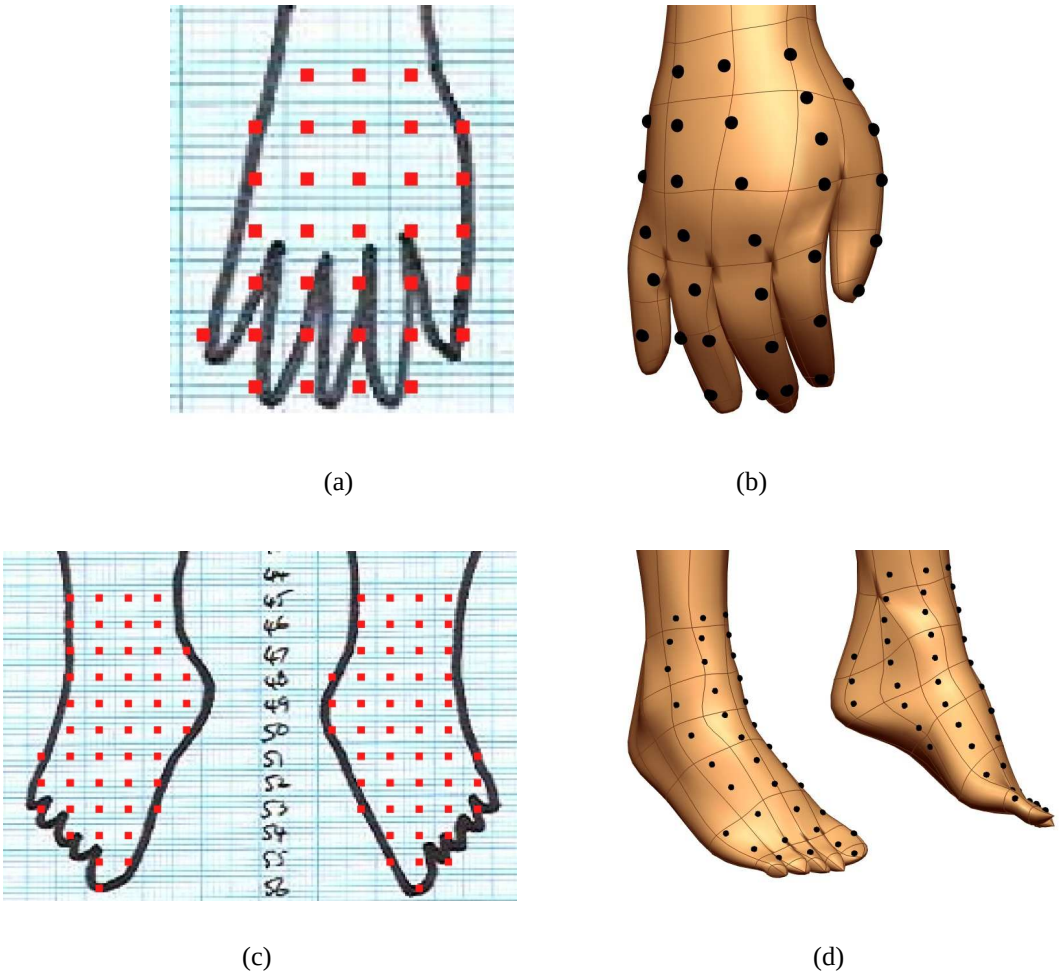

(a) (b)

(c) (d)

Figure 3.8: All possible melanoma sites on the body maps for the (a) dorsum of the right hand and (c) the anterior feet. Corresponding manually placed sites on the (b) right hand skin mesh and (d) skin mesh feet.

3.1.4 Head and neck

Melanoma sites on the head and neck have been recorded on four out of the six body maps (as shown in Figure 1.14). Anterior and posterior views are given on the torso body maps 1 and 2, while lateral views are drawn on maps 5 and 6. The method utilised to map these melanoma sites onto the skin model is similar to that used for the torso and leg sites (as described in Section 3.1.1). The head and neck of each appropriate body map has initially been host-mesh fitted to the outline of the skin model, and then a direct orthogonal projection has been carried out.

As mentioned previously, the torso melanoma sites had been projected onto the skin model before a head and neck model was available. Therefore the head and neck outlines on the anterior and posterior torso body maps have first been separated from the rest of the body before fitting. During

mapping, it was important to maintain consistency between melanoma sites on the upper torso and the lower neck. To ensure this, the initial position of each separated head and neck outline was placed level with the shoulders of the morphed anterior and posterior torso body maps (shown in Figures 3.1(c) and 3.2(a)). Nodal coordinates at the base of the neck have been completely fixed during fitting to ensure they remained in the same position. The final host-mesh fit of the anterior and posterior head and neck views are shown in Figure 3.9.

The anterior head utilises 48 landmark and target points. It was important to ensure that the facial features were morphed correctly, therefore landmark points were positioned at the lips, nose and eyes as well as the head boundary outline to maintain anatomical consistency after deformation. Note that there are no ears drawn on either anterior or posterior head views, so these features could not be matched. Posterior head fitting uses 27 pairs of target and landmark points, comparatively less than the anterior head. During fitting 20 elements have been used for the anterior head, and 8 elements for the posterior head. Less DOFs and target points were required for the posterior head since there were no specific additional features to fit apart from the head outline. Table 3.3 outlines the number of nodes, DOFs and elements used for each fit. The complex geometry of the anterior head and neck in contrast to the posterior view is reflected in the larger RMS value of 3.13 mm versus 1.98 mm.

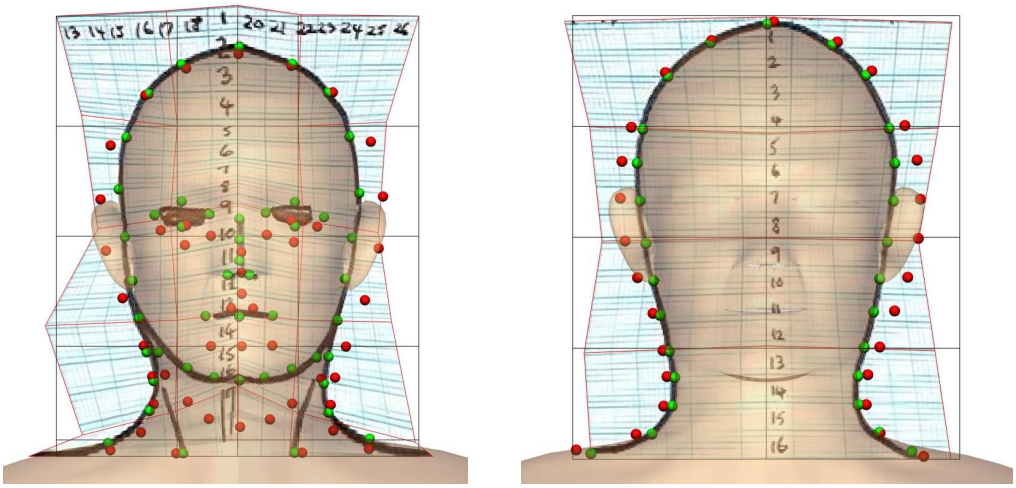

(a) (b)

Figure 3.9: Host-mesh fitting the (a) anterior and (b) posterior head body maps to the skin mesh.

Figure 3.10 demonstrates the lateral head view body maps fitted to the head mesh outline. Fitting these two body maps was highly complex, requiring a relatively large number of elements and DOFs for the host-mesh. As can be seen in Figures 3.10(a) and 3.10(c), the initial positioning of the ears relative to the other facial features was significantly higher on the body maps than the skin

model. In order to morph the maps accordingly, two elements were placed around the ears to allow the ears to be dragged downwards during fitting.

For both left and right lateral fits the same number of nodes and elements were used for the slave-mesh and host-mesh. Also, the same number and locations of the landmark and target points were used for each fit. As detailed in Table 3.3, 80 nodes and 28 elements were used for the host-mesh. Although the lateral head maps were almost entirely symmetric they were not exact reflections of each other, so fitting has been carried out separately for each side. Similar to the torso and leg host-mesh fitting, the process is reduced to a 2D problem in the x- and z-directions for the anterior and posterior head mapping. In the case of lateral head melanoma site mapping, fitting is reduced to the y- and z-directions.

A total of 75 target points were positioned on the body maps and 75 corresponding landmark points placed on the skin mesh. Additional points were placed in the centre of the neck, cheeks, between the eyes and ears, and top of the head. These points were important, as they ensure that melanoma sites mapped onto the model after deformation, maintained correct positioning relative to facial anatomical features. During fitting, similar to the anterior and posterior head and neck fits, nodal coordinates at the base of the neck have been completely fixed. All other nodes, excluding those on the edge of the body maps and two nodes in front of the ears and one just below the jaw, have been fixed in the y-direction enabling fitting in only the vertical z-direction. This ensured that the grid map square deformation was limited.

The RMS errors for both fits is calculated as 3.97 mm, which is relatively large compared to the RMS value for the posterior head at 1.98 mm. This was considered reasonable however, since fitting the lateral head was significantly more complex than the posterior head. Also, as previously mentioned, a large amount of deformation was required to match the skin model's ears (as shown in Figures 3.10(b) and 3.10(d)).

Map #	Head View	# Nodes	# DOFs	# Elements	RMS error (mm)
1	Posterior	30	44	8	1.98
2	Anterior	60	78	20	3.13
5	Right lateral	80	110	28	3.97
6	Left lateral	80	110	28	3.97

Table 3.3: Host-mesh fitting details for the head and neck body maps.

Melanoma coordinates for each of the host-mesh fitted body maps were then orthogonally projected onto the skin model. To enable this projection, the head and neck have first been reduced to 2D. Anterior and posterior views required all y-coordinates and their derivatives to be set to zero, while lateral views required all the x-coordinates and their derivatives to be set to zero.

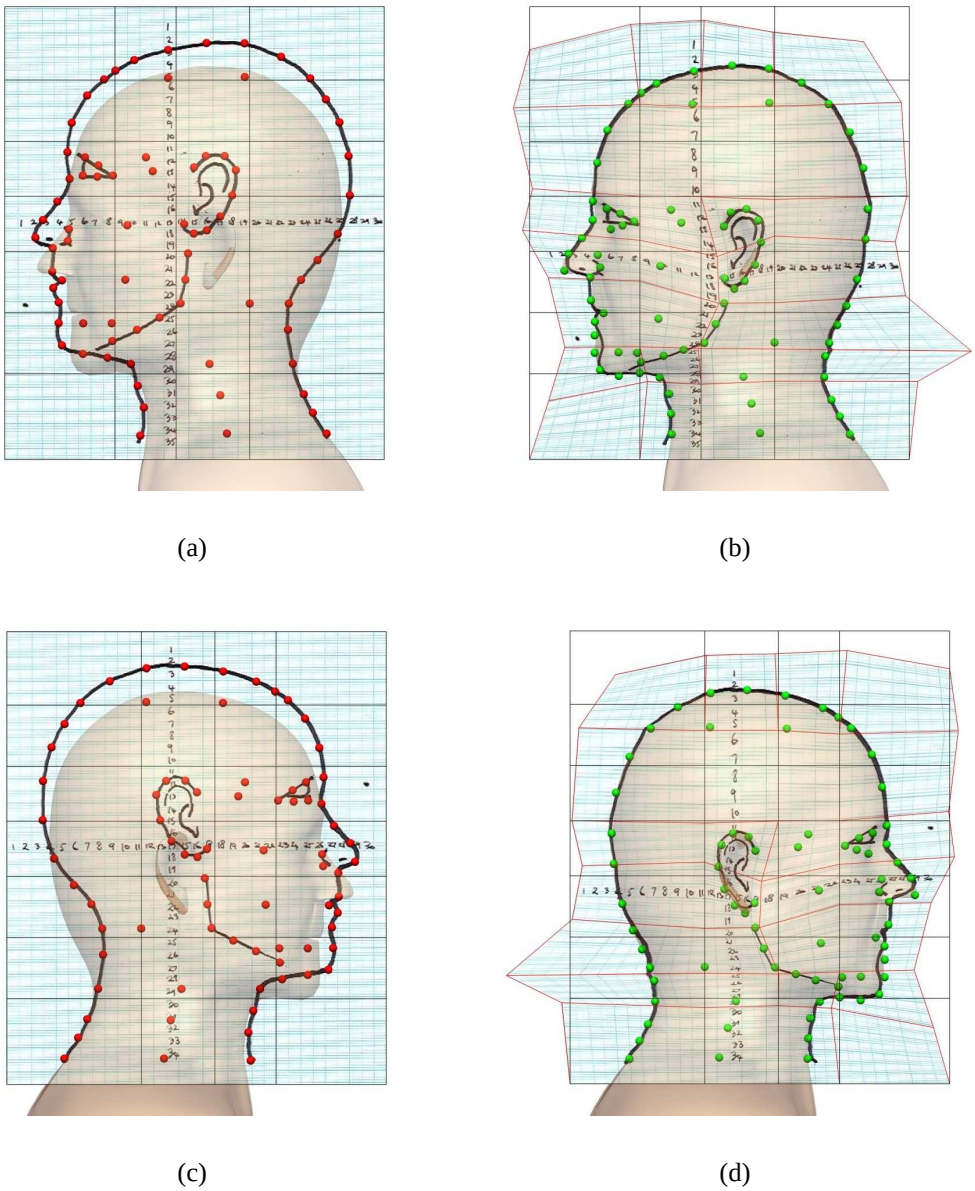

(a) (b)

(c) (d)

Figure 3.10: Host-mesh fitting the lateral head body maps to the skin mesh. Left lateral head fitting (a) before and (b) after deformation, and right lateral head fitting (c) before and (d) after deformation.

After projecting melanoma sites onto the 2D mesh, local coordinates were interpolated to give the final melanoma coordinates on the 3D skin mesh as shown in Figure 3.11. Sites projected from the anterior body map can be seen in black, sites shown in red were projected from the posterior body map, while sites in yellow correspond with the lateral body maps. Interestingly, there is overlap between lateral sites and those from the anterior and posterior maps. In particular, there is a significant amount of overlap on the cheeks, primarily due to sites recorded on the anterior body

map that have been projected onto elements closely aligned with the projection direction.

The RMS errors between the 2D melanoma sites and those projected and interpolated on the 3D model (demonstrated schematically in Figure 3.5) are given in Table 3.4. The RMS values are below 1.0 mm for each fit apart from the posterior head mapping which is 1.52 mm. This slightly larger error is partly due to a large number of sites being located on the top of the head, where elements have a large curvature.

Map #	Head View	# Melanoma pts	RMS error (mm)
1	Posterior	133	1.52
2	Anterior	207	0.72
5	Right lateral	300	0.68
6	Left lateral	296	0.68

Table 3.4: Projection details for the head and neck melanoma sites.

3.2 Mapping the sentinel nodes

In addition to mapping primary melanoma sites onto the skin model, each patient's SN fields have been mapped onto the lymph node model created in Section 2.6. The location of each patient's SNs have been recorded by SMU clinicians as detailed in Section 1.6.2.

In the absence of exact locations for each SN, the detailed lymph node model shown in Figure 2.20 has been reduced to one representative node in each field, onto which the SN field locations could be mapped. Figure 3.13 shows this reduced model, where node fields have been labelled according to their codes as listed in Appendix A.

Node fields in the head and neck can be seen in Figures 3.13(a) and 3.13(b). The original model of these node fields were based on VH data and were therefore not in the correct space relative to the head and neck of the skin model. The skin of the head and neck was based on Sawbones data (outlined in Section 2.5.2), which did not contain lymph nodes, nor models of the muscles or bones for anatomical reference. Therefore, the only way to determine an approximate location for each of these fields was by manually positioning nodes relative to the skin model.

Figures 3.13(c) and 3.13(d) display each of the remaining node fields below the neck. Note that interval nodes (detailed in Section 1.3.2) have been represented outside the skin model since they are not in a location that is common between individuals. Some node fields contained only one node in the full model and have therefore not been modified for the reduced model. These include the preauricular, postauricular, occipital, upper mediastinal and costal margin node fields.

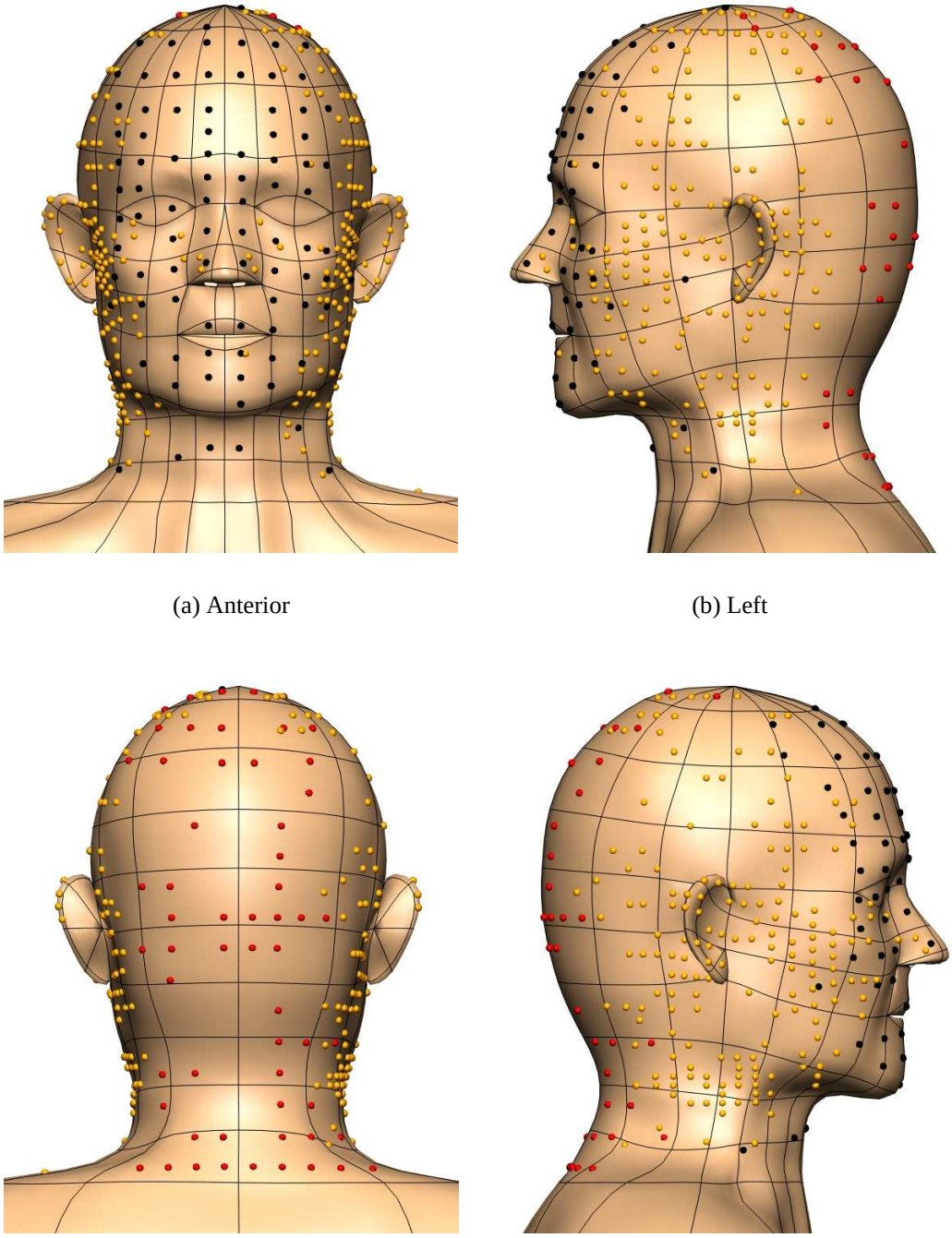

(a) Anterior

(b) Left

(c) Posterior

(d) Right

Figure 3.11: Mapped melanoma sites on the head and neck, with anterior sites shown in black, posterior sites in red and lateral sites in yellow.

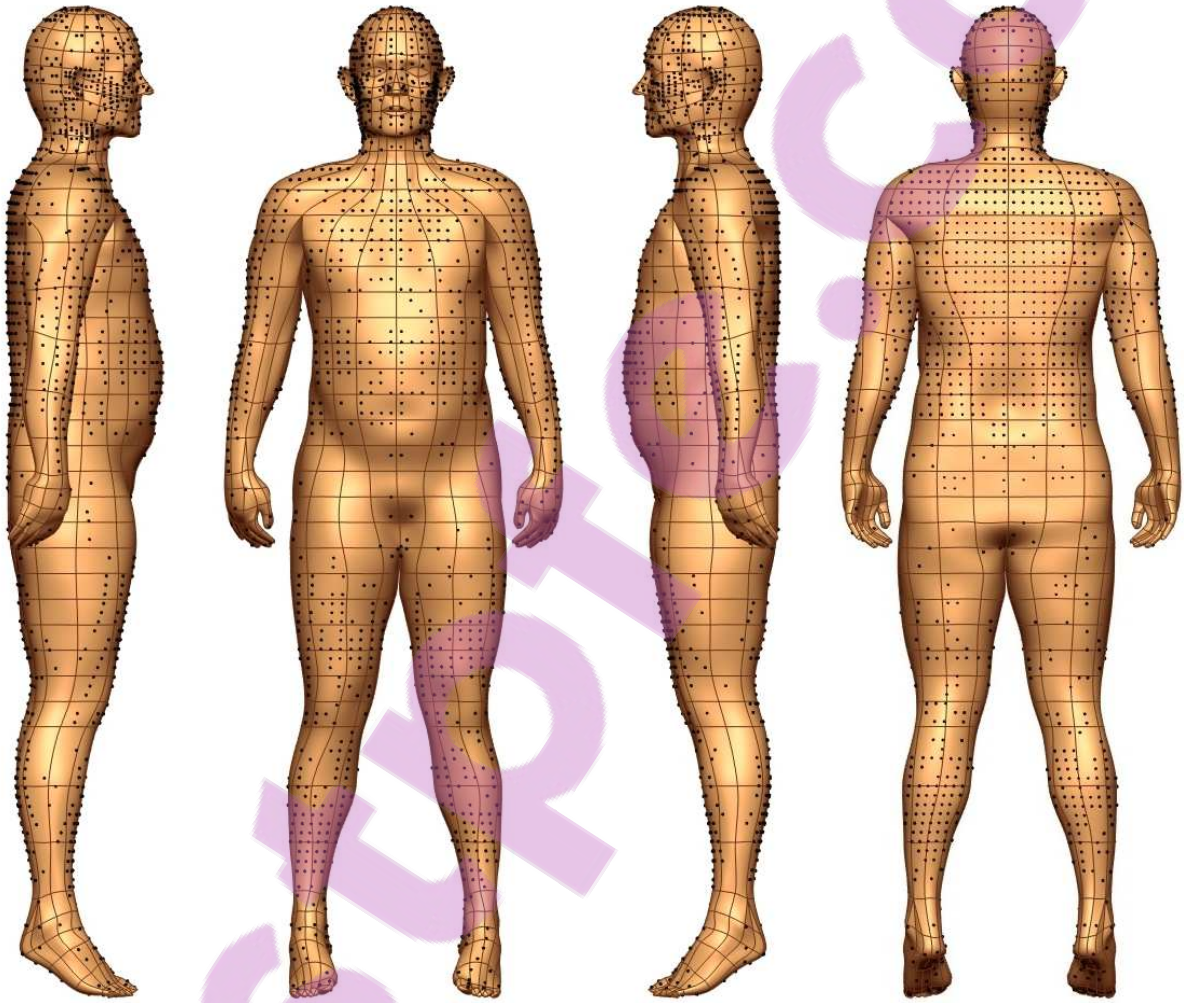

(a) Right (b) Anterior (c) Left (d) Posterior

Figure 3.12: Mapped (X, Y) melanoma coordinates on the skin mesh for the full patient database.

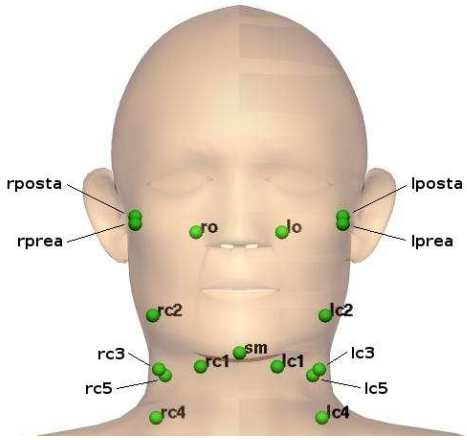

(a) Anterior

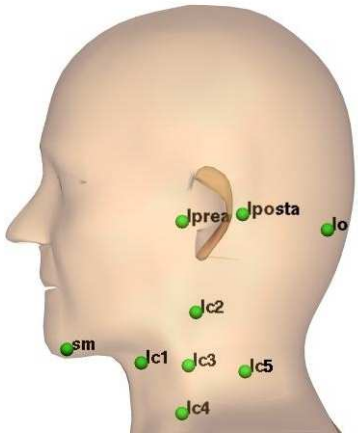

(b) Left

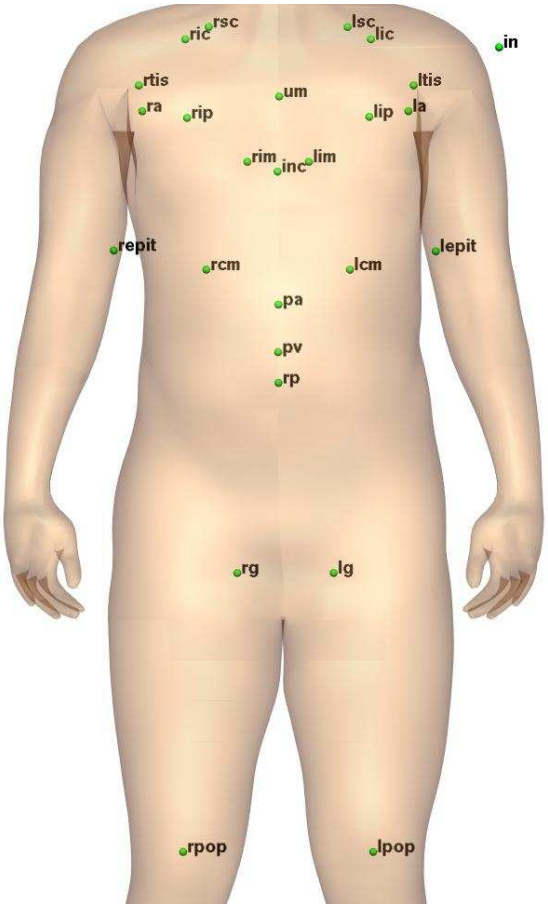

(c) Anterior

(d) Left

Figure 3.13: Lymph node model reduced to one representative node in each field, labelled according to their codes given in Appendix A. Node fields located in (a,b) the head and neck and (c,d) below the neck.

Each of the remaining nodes have been positioned at the approximate anatomical midpoint of the field. Cervical node fields have been significantly reduced from the original model which contained a number of nodes at each level. Multiple nodes were also located in the axilla and the groin, so each representative node in these fields approximate large regions where lymph nodes are found. The intercostal, paraaortic and paravertebral node fields are not located on both the left or right sides of the body, although they do contain nodes on the left and right sides of the body's midline. These node fields covered large, elongated areas and were therefore more challenging to position at the anatomical midpoint of the field. Again however, the approximate anatomical midpoint of each field has been used to represent these node fields.

3.3 Discussion

There are a number of errors that were created by the mapping process, which are important to be aware of during subsequent data analysis. Error produced by interpolating coordinates from 2D to 3D have been described above (and schematically demonstrated in Figure 3.5). In addition to this error, an aliasing error was also inherent in the grid maps, due to using grid squares to record melanoma sites rather than a continuous field. Melanoma (X, Y) coordinates were located at the centre of each grid unit, however if these sites had been positioned in one of the four grid unit corners instead, the resultant mapped coordinates could be significantly different. The centralised coordinates however, represent an average location for each melanoma site and were therefore the most accurate position to use for projecting onto the skin model.

Error has also been created by the grid square resolution on the 2D body maps. Since each melanoma site was recorded within a 2D grid unit sized between $1.5 - 2$ cm^2, this recording error has been magnified when projected onto the 3D model. This is demonstrated schematically in Figure 3.14 for two different skin sites. Note that the error created during interpolation of melanoma coordinates from the 2D to 3D skin mesh (shown in Figure 3.5) was independent of this grid resolution error. Melanoma coordinates such as (X_2, Y_2) which were nearly perpendicular to the skin mesh induced a magnified recording error on the 3D model, while sites that were close to parallel to the screen such as (X_1, Y_1) had little or no error magnification.

A heat map of this recording error magnification is shown in Figure 3.15, demonstrating the relative error induced by the linearly projected torso and leg melanoma sites. The largest errors occurred at the lateral sides of the body and the interior legs, where the skin is nearly perpendicular to the projection direction. At these locations the error magnification approached infinity.

There are some elements on the skin mesh that do not have any melanoma coordinates projected

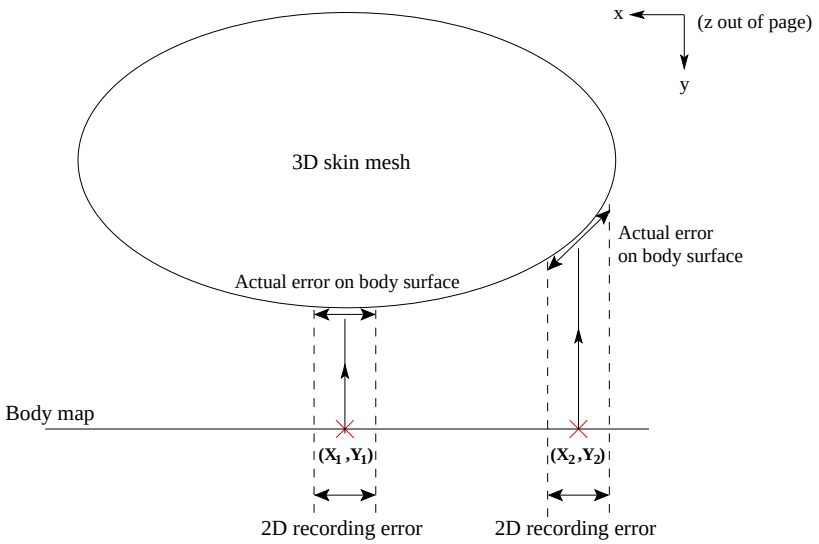

Figure 3.14: Magnification of the melanoma site recording error.

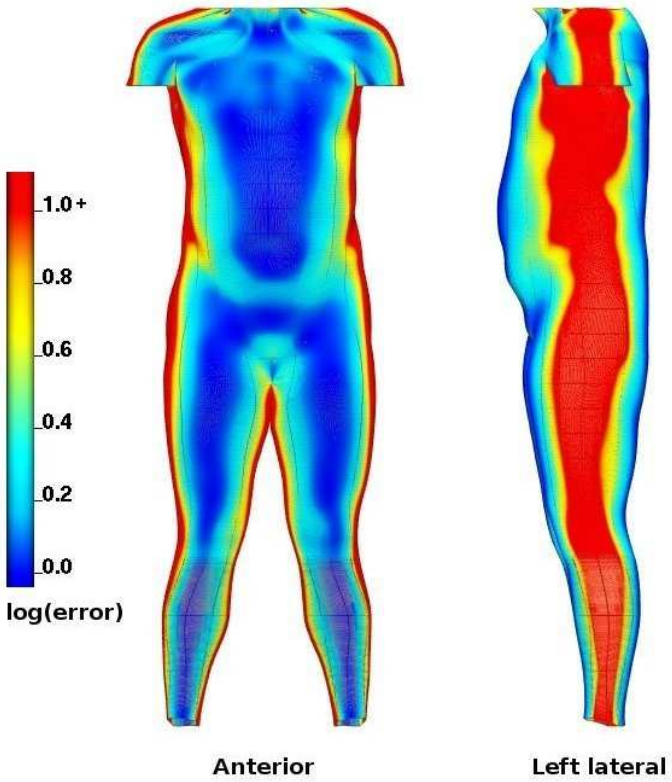

Figure 3.15: Heat map displaying the recording error magnification for the torso and leg melanoma sites projected from 2D onto the 3D skin model.

onto them, either due to a sparsity of sites in that skin region or as a result of 3D data being recorded in 2D. In particular, there were few melanoma sites located on elements oriented in the x-plane, i.e. lateral torso elements and lateral and medial leg elements. There is also some error introduced into the mapped arm coordinates. Arm segment internal nodes (as shown in Figure 3.7(a)) induced an error when they were projected onto 2D arm element boundaries since the nodes were not all in the same z-plane, however it was relatively small.

Clinicians were also likely to have introduced error in the database due to the body maps' coarse grid resolution, in particular for sites located on the hands and feet. It is highly likely that patients with melanomas on different fingers, for example, have had their melanoma site recorded in the same grid square, and hence the same finger. Additionally, some melanoma (X, Y) coordinates were difficult to place on the skin mesh. As shown in Figure 3.8(a), some coordinates were located between the fingers and hence the melanoma site could be interpreted as being on either adjacent finger. To ensure correct site placement on the skin mesh each of the coordinates on the hands and feet have been verified with SMU clinicians. It is important to be aware of the potential introduction of error via this manual transformation, although the patterns of lymphatic drainage were unlikely to be affected since adjacent fingers show similar behaviour in terms of draining node fields, as do adjacent toes.

Mapping head and neck melanoma sites was potentially more accurate than mapping melanoma sites onto the remainder of the body, since lateral views have been given in addition to anterior and posterior views. Although error was still created by projecting 2D coordinates onto the 3D skin model, the fact that melanoma sites could be recorded on lateral views rather than only on anterior or posterior views reduced the potential recording error. These lateral views were particularly useful for recording sites either close to, or on the ears, which is a very common melanoma location.

In an ideal situation, mapping the SNs would have been carried out by projecting each SN location from the original LS images (as shown in Figure 1.12) onto the model. This was not possible however, since the LS image resolution was too low and they were not often registered with respect to anatomical features. At times additional information has been recorded regarding the number of SNs in each field and the depth of each SN below the skin. However, since each patient would have had different sized anatomical features, it was inappropriate to directly compare these depth measurements so they have not been used.

3.4 Summary

This chapter detailed the methods used to map LS data onto the skin and lymph node models created in Chapter 2. Primary melanoma sites have been projected onto the skin model via different projection methods for separate regions of skin. The torso and leg sites have been projected orthogonally onto the skin mesh, while the upper limbs required host-mesh fitting before melanoma sites could be projected onto them. Melanoma sites on the hands and feet have been positioned manually, and the head and neck sites have been projected orthogonally. The full lymph node model has been reduced to one representative node in each field, onto which SN field locations have been mapped. These mapped data provided the basis for conducting detailed visualisation and analysis of LS data in 3D, as outlined in the following chapters.

Chapter 4

Visualisation Methodology

The previous chapter detailed mapping methods used to transform the SMU's full LS database from 2D images onto the 3D anatomical model created in Chapter 2. This mapped model now provides the framework for improving visualisation of skin lymphatic drainage in 3D. This chapter outlines the mapping methods implemented to display data density using the SMU's random coordinate approach described in Section 1.6.1. The limitations of this approach are outlined, and serve as a motivation for the new data display methods proposed. Field fitting is introduced as a technique to display lymphatic drainage patterns from any area of skin to specified node fields. Sobolev smoothing is discussed as a constraint which aids the fitting process. Finally, development of an interactive skin selection tool is presented, which allows predictions of SN fields from any element on the skin model.

4.1 Introduction

The SMU's entire LS database was mapped onto the skin and lymph node model in the previous chapter. Each primary melanoma site that has been mapped onto the skin model has a 3D geometric coordinate value. A number of these melanoma coordinates have multiple patients recorded at the same skin site. This is because the body maps used by SMU clinicians (as shown in Figure 1.14) had a low grid square resolution, thereby providing only a limited number of possible melanoma site locations on the body.

As detailed in Section 1.6.1, cumulative (X, Y) coordinates within the same grid square could not initially be visualised at the SMU. Therefore, in addition to recording (X, Y) coordinates for each patient's primary melanoma site, SMU clinicians have also generated a random coor-

dinate $(randX, randY)$ which was intended to allow visualisation of the density of melanoma sites within each grid square. In order to maintain consistency with the SMU's database and their previously published displays (shown in Section 1.6.4), these random coordinates have also been projected onto the skin model as outlined below.

4.2 Random melanoma coordinates

Random melanoma sites $(randX, randY)$ located on the torso, lower and upper limb, head and neck have each been mapped with the same methods used for the original melanoma sites (X, Y), as described in Sections 3.1.1, 3.1.2 and 3.1.4. During mapping some of these sites did not project correctly onto the 3D skin model however, because they were located just outside the body outlines drawn on the body maps. This occurred at coordinates which were located within grid squares containing the body outline. Although the original coordinate was located within the body outline, an offset random coordinate was not necessarily within this boundary. This can be clearly seen for a number of sites on the top of the head in Figure 1.15(b). To ensure that these random coordinates were adequately mapped onto the skin model, they have been moved manually within the body map outlines before projection, while still ensuring that they remained within the same grid unit.

Meanwhile, random melanoma sites on the hands and feet have been mapped using a different method than that carried out for the original coordinates described in Section 3.1.3. Manually positioning each point was considered too labour intensive, since multiple random coordinates have been recorded for sites within the same grid square unlike the original coordinates.

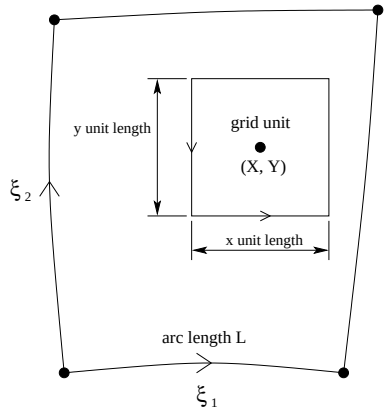

Figure 4.1: Schematic demonstrating a melanoma site (X, Y) contained within a skin element. The relative size of the body map grid unit is determined relative to this skin element.

Instead, for each melanoma site located within skin elements on the hands and feet, the approximate number of elements per grid unit in each of the X- and Y-directions, denoted N_X and N_Y,

has been calculated. The positive ξ_1-direction runs circumferentially around the skin mesh, and corresponds approximately with the positive X-direction on the body maps; while the positive ξ_2-direction runs longitudinally up the skin mesh, and is approximately aligned with the body maps' negative Y-direction (as shown in Figure 4.1). Hence, approximate values for the number of elements per grid unit have been calculated by:

$$N_X = \frac{2G}{L_{\xi_{1=0}} + L_{\xi_{1=1}}}$$
$$N_Y = \frac{2G}{L_{\xi_{2=0}} + L_{\xi_{2=1}}} \tag{4.1}$$

where G is the width of the body map grid unit, and L denotes the arc-length at specified element boundaries. Width G ranges from 1.5 - 2 cm, however in this case it has been taken at the minimum value of 1.5 cm. This is to ensure that even for the smallest sized grid unit, each projected random melanoma site would remain within the same grid square. The arc-lengths at the element boundaries for each ξ-direction have been used to determine average arc-length value to approximate the width and height of each element. For collapsed surface elements (as shown in Figure 2.6(b)), which have only one arc-length value in a particular ξ-direction, the average arc-length has been approximated by dividing the known arc-length in half. To then calculate local random coordinates $(rand\xi_1, rand\xi_2)$ for these melanoma sites, the following equations have been used:

$$\begin{aligned} rand\xi_1 &= \xi_1 + N_X(X - randX) \\ rand\xi_2 &= \xi_2 - N_Y(100 - Y - randY) \end{aligned} \tag{4.2}$$

which provide a random offset to the local coordinates (ξ_1, ξ_2). These random local coordinates have been calculated by multiplying the approximate number of elements per grid unit in each direction, N_X and N_Y, by random offset values which are between -0.499 and +0.499. Note that the method implemented by the SMU to record the coordinate $randY$, as detailed in Section 1.6.1, has required the random Y-offset to be subtracted from 100. These new random local coordinates $(rand\xi_1, rand\xi_2)$ have then been applied as local FE material coordinates which were interpolated on the skin model to give global random coordinate values for melanoma sites on the hands and feet. During this calculation, a very small number of random local coordinates have extended beyond the limits of 0 and 1. In such cases the values were fixed at the limits of 0 and 1 respectively.

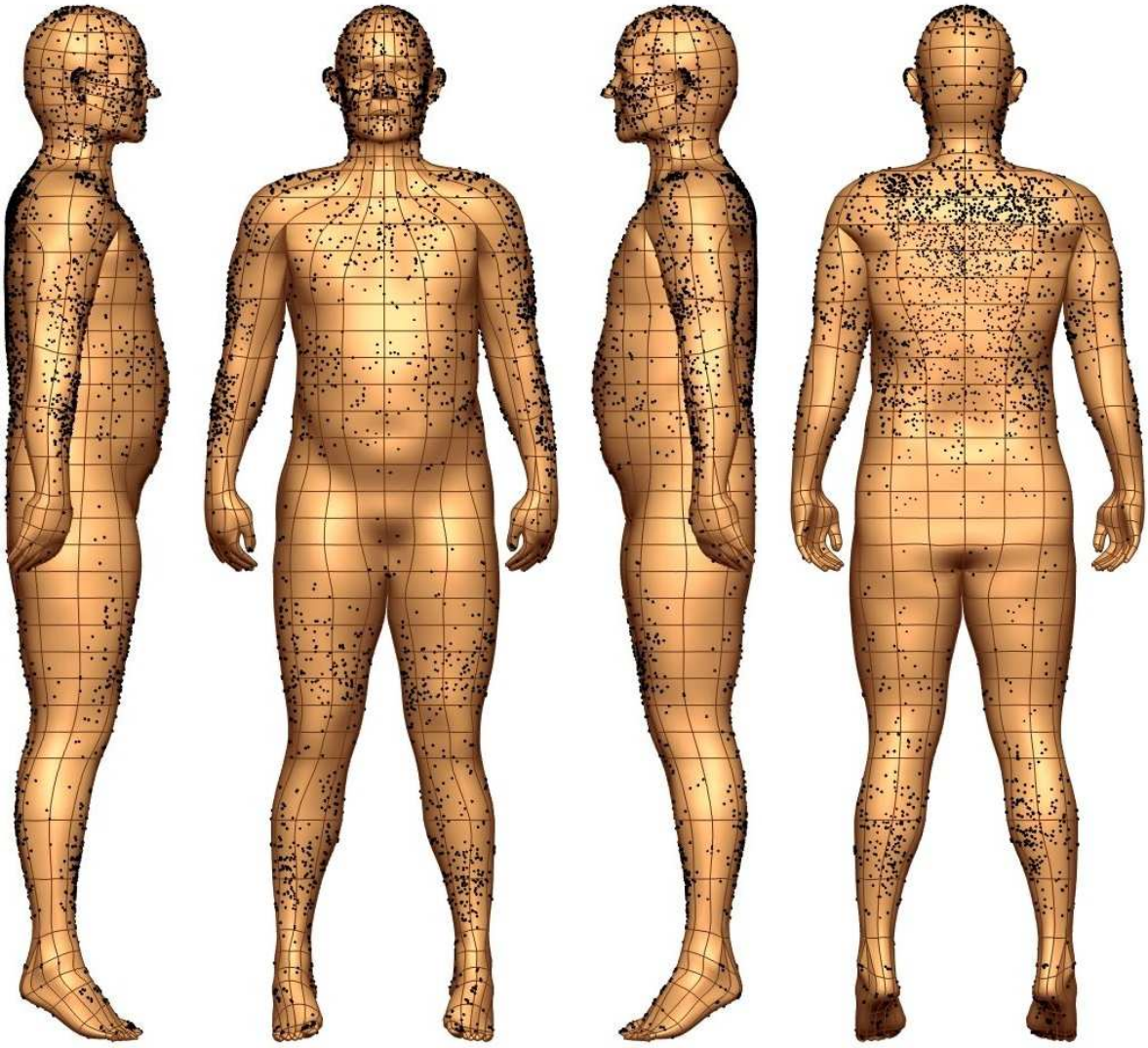

(a) Right (b) Anterior (c) Left (d) Posterior

Figure 4.2: Mapped $(randX, randY)$ melanoma coordinates on the skin model.

Figure 4.2 shows the random melanoma coordinates mapped onto the skin mesh for the entire LS database. A high density of sites can be seen particularly on the upper back, forearms, legs and the ears, while a sparsity of data is shown on other skin regions including the groin and the hands. In contrast, Figure 3.12 shows the original (X, Y) coordinates plotted for the full database which does not visualise the density of melanoma sites on the skin.

Although these random coordinates have enabled visualisation of data density, there is no additional spatial information present over the original coordinates. Now that each (X, Y) coordinate

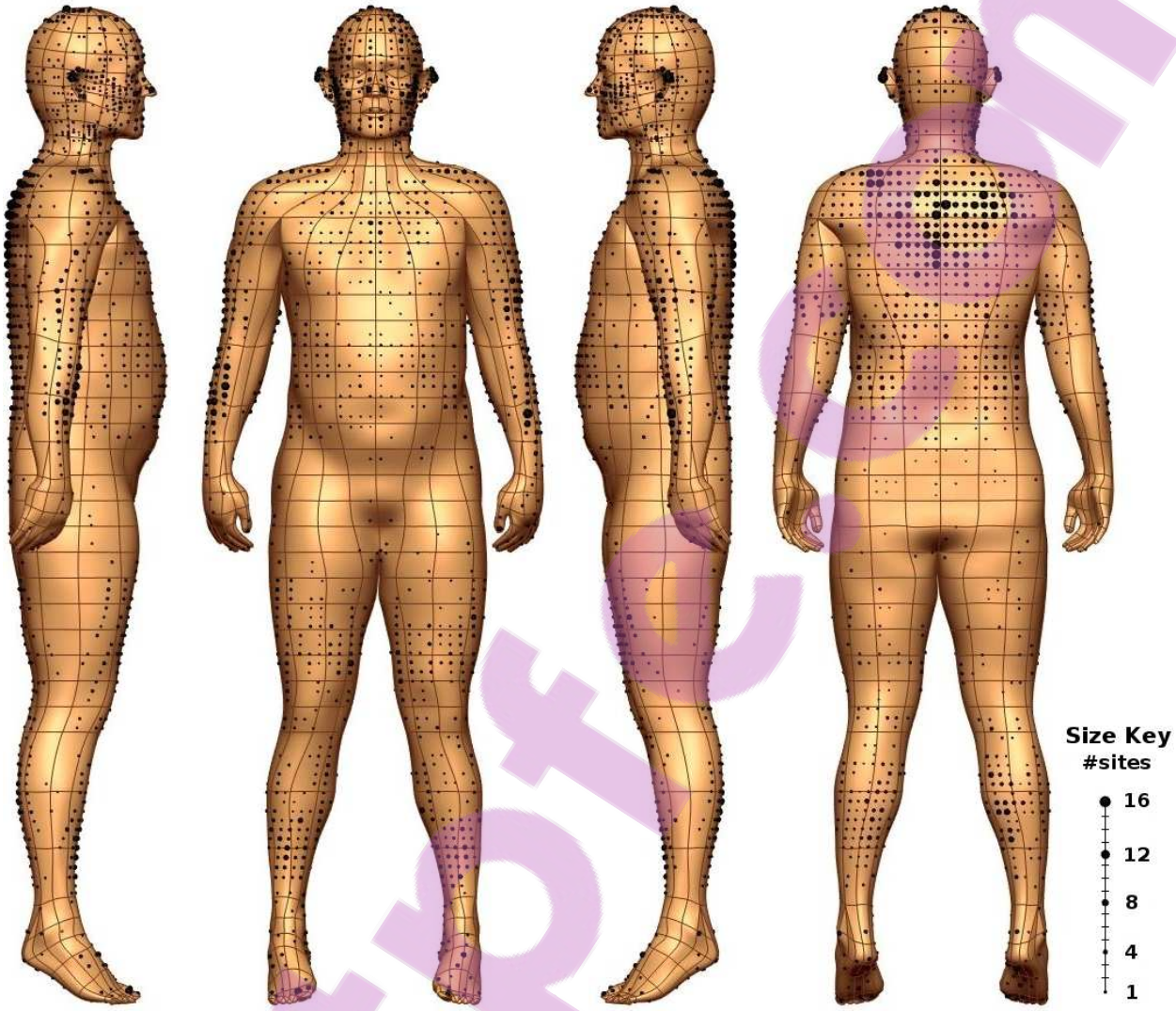

(a) Right (b) Anterior (c) Left (d) Posterior

Figure 4.3: Frequency of primary melanoma sites (X, Y) on the skin model.

has been mapped onto the 3D FE skin model, the opportunity is available to display data density without requiring the addition of a random variable. As well as storing a 3D geometric coordinate for each melanoma site, CMISS software (described in Section 1.7.2) provides the ability to record field values at each site. Examples of these field values include pressure or temperature measurements, which can then be scaled, manipulated and coloured for visualisation purposes.

Applying this technique to the mapped model produces displays such as that given in Figure 4.3. This shows the frequency of melanoma sites on the skin, where frequency field values have been

scaled in size and range from 1 to a maximum of 16 patients. This display is now presenting the same information as that given in Figure 4.2 for the random coordinates, without requiring random offset values.

Using the mapped database, the relationship between each patient's primary melanoma site and draining SNs can also be visualised in this manner. These displays will enable visualisation of the lymphatic drainage of the skin and hence the potential patterns of melanoma spread. To create such displays, the mapped database has been queried for primary melanoma sites that follow a particular drainage pattern of interest. For example, querying for all melanoma sites that drain to the left axilla will output 1644 individual patients in the database with SNs in that node field. Figure 4.4(a) shows the original (X, Y) coordinates plotted on the skin model. Meanwhile, Figure 4.4(b) displays the random $(randX, randY)$ coordinates on the skin model, showing a large density of melanoma sites on the upper back and on the lateral arms, indicating a similar density distribution when compared with the SMU's earlier published displays (Figure 1.17).

4.3 Spatial heat maps

Although these discrete plots are informative, methods to develop more advanced displays of this mapped data have been applied. Colour-coded spatial heat maps have been produced by using the mapped (X, Y) coordinates, each with an associated field value, and fitting these field values over the skin model. By creating spatial heat maps, data was easier to understand and interpret since common patterns contained within the data were delineated. The following section describes field fitting in more detail.

4.3.1 Field fitting

Field fitting is a technique which can be used to define a set of discrete data points located on a FE model in a continuous manner. A field is defined over a FE model in terms of its nodal parameters, which can then be interpolated via appropriate basis functions throughout the mesh.

The mathematical process for field fitting is the same as geometric fitting, which has been used to create the skin model (described in Section 2.3.3). Field values are initialised at the nodes on the FE mesh, and then fitted to the discrete data values using the fitting objective function defined in Equation 2.10. This fitted field serves to give an accurate representation of the data point field values, by minimising the difference between nodal field parameters and the data points. The

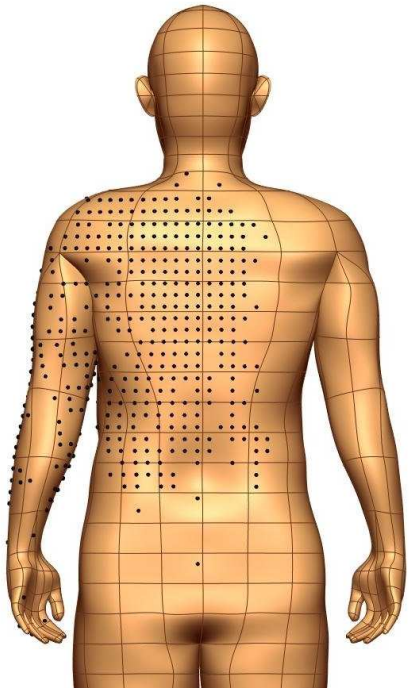

(a) (X, Y) coordinates

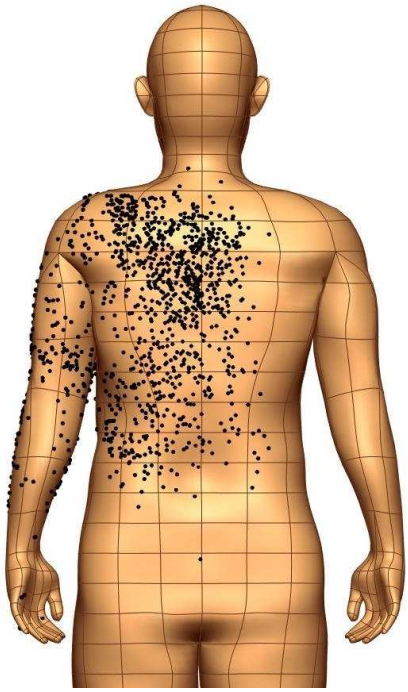

(b) $(randX, randY)$ coordinates

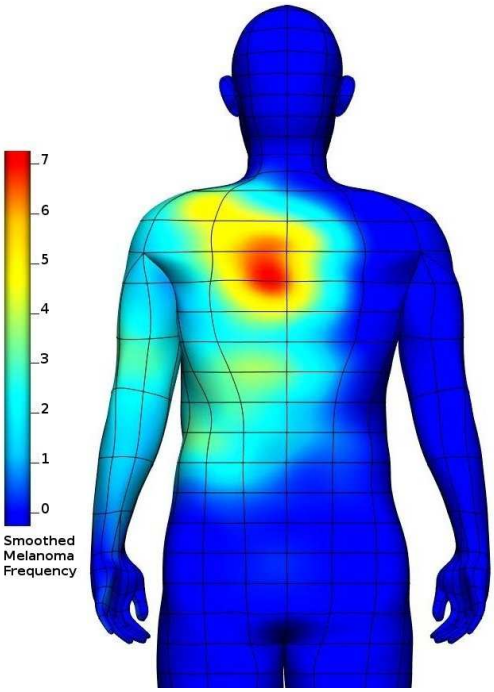

(c) Frequency heat map

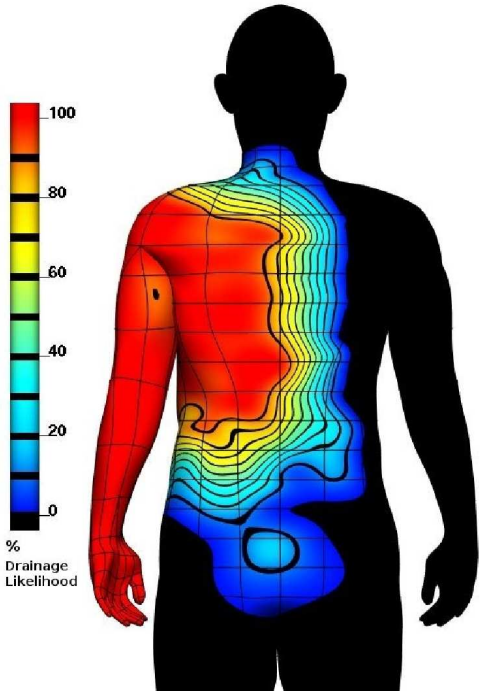

(d) Drainage likelihood heat map

Figure 4.4: Posterior views of the skin mesh, displaying regions of skin that showed drainage to the left axillary node field with different visualisation methods.

objective function is only solved once for field fitting, rather than iteratively as implemented for geometric fitting, since the ξ coordinates of the data points do not change.

Unfortunately, there will often be errors in the discrete data which can be due to noise in the sampled population, also differences between individuals, as well as any measurement noise created during data collection. When there is significant noise, ideally there should be a large quantity of data available during field fitting compared to mesh DOFs, and the data should be evenly distributed over the model. However this is often not the case, and errors may also be produced in the fitted field as a result. To address this problem, a Sobolev smoothing penalty function is defined in the objective function and can be modified during fitting, so that the effect of such sources of error can be reduced.

Sobolev smoothing (earlier defined in Equation 2.11) helps to reduce excessive curvature in a fitted surface. Weight values $\alpha_i (i = 1..5)$ influence different aspects of the fitted model: element arc-lengths, arc-curvatures and element face area. It is important to select appropriate values for these weights so that noise is filtered and there is an appropriately smoothed variation of the field across the model. This process requires consideration of the RMS error for the fitted field, as well as ensuring that the field shows a reasonable approximation to the discrete data values. A Sobolev weighting that is too low (under-smoothed) can result in a fitted field with a small RMS error but a high local curvature, whereas a Sobolev weighting that is too high (over-smoothed) can produce a field with a large RMS error and a low curvature that does not sufficiently match the data.

Field fitting has been applied to the skin model to visualise the number of cases draining to the left axillary node field, using the frequency values associated with each (X, Y) melanoma coordinate. The resultant heat map display is shown in Figure 4.4(c). In comparison with the original plots given in Figures 4.4(a) and 4.4(b), this method of display enables smooth representation of the frequency data which is more visually aesthetic, while still remaining informative. The scale bar indicates that the smoothed melanoma frequency values range from 0 through to 7, where high frequencies are coloured red. A red region can be seen on the upper back, showing that a large number of melanoma sites are located there. Areas shaded in dark blue indicate regions of skin with no drainage to the left axillary node field. Details of the methods used to generate this frequency heat map, as well as heat maps to visualise the likelihood of drainage to specified node fields, are now outlined.

4.3.2 Methodology

All heat maps that have been generated to display the SMU's mapped data have used the original (X, Y) coordinates with an associated field value. Maps visualising the frequency of melanoma sites draining to specified node fields, as shown in Figure 4.4(c), have been created by fitting these discrete data values to nodal parameters on the skin model. All melanoma sites including those with zero frequency counts have been used during the analysis. Data points have been assigned uniform weight values (w_d) equal to 1.0 (see Equation 2.10).

In addition to fitting frequency fields, the mapped model provides the capability to develop more advanced displays visualising the likelihood that particular patterns of lymphatic drainage will occur. This information has not been visualised previously, and is much more informative than frequency displays since it will enable predictions of the possible patterns of melanoma spread.

To generate these drainage likelihood heat maps, the following methods have been used. For each discrete melanoma skin site, the number of patients fulfilling a particular drainage criteria has been divided by the total number of patients at that skin site. This will derive a percentage likelihood value from each skin site, as demonstrated in Figure 4.5(a) which displays the likelihood of drainage to the left axillary node field. This heat map shows a large number of red melanoma sites on the left arm and left side of the posterior torso, indicating that 100% of patients from these sites had SNs in this node field. Meanwhile, a large number of dark blue sites with values at 0% are plotted on the head, neck, right arm and areas of the torso, indicating that lymphatic drainage does not occur to the left axilla from these sites.

To enable smooth representation of these data, field fitting has then been applied. Weights have been assigned to the fitting objective function (given in Equation 2.10) according to the frequency of patients at each melanoma site. This was to ensure that areas of skin with more data present would have an increased effect on the resultant fitted field, and that outlying values would not overly skew the results.

These discrete data values have then been fitted over the skin model. Various Sobolev weights were tested to determine appropriate values, where results from selected weight values are detailed in Table 4.1. As expected, there was too much smoothing of the data for high Sobolev weights, demonstrated in Figure 4.5(b). By comparing this heat map to the discrete data plot in Figure 4.5(a), the zone where drainage is expected to occur to the left axillary node field is shown to be over-estimated, where a relatively high RMS error value is given at 12.36%. In contrast, Sobolev weights that were too low did not provide enough data smoothing, as demonstrated in Figure 4.5(c). Although the RMS error value was reduced, this heat map showed undesirable high local curvatures

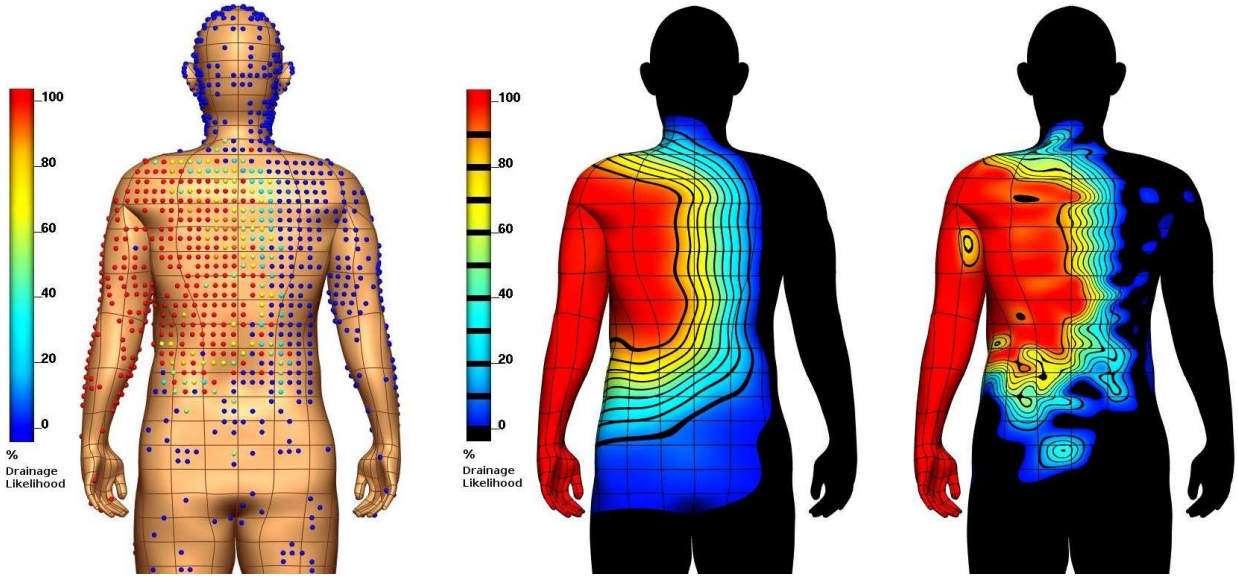

(a) (b) $\alpha_i(i = 1..5) = 1.0$ (c) $\alpha_i(i = 1..5) = 0.01$

Figure 4.5: Heat map displaying the likelihood that the skin will drain to the left axilla, using different Sobolev smoothing values. (a) The original discrete data values, (b) fitted heat map using Sobolev smoothing values that are too high, producing too much smoothing and (c) Sobolev smoothing values that are too low, not producing enough smoothing.

across the fitted field. The most appropriate weight values were chosen to be $\alpha_i(i = 1..5) = 0.1$, which gave an RMS error of 10.77%. These weights gave the heat map shown in Figure 4.4(d), which sufficiently represented the data while ensuring there was enough smoothing present. To enable direct comparison between multiple heat maps, the same Sobolev weights have been used for all frequency and drainage likelihood heat maps.

	Sobolev smoothing weights		
	$\alpha_i(i = 1..5) = 1.0$	$\alpha_i(i = 1..5) = 0.1$	$\alpha_i(i = 1..5) = 0.01$
RMS error (%)	12.36	10.77	9.35

Table 4.1: RMS error values for different Sobolev weights used to fit a field displaying the likelihood of drainage to the left axilla.

4.4 Interactive skin selection tool

In addition to these heat maps, an interactive skin selection tool has been developed to enable dynamic prediction of possible patterns of melanoma spread from any area of skin. While the heat

maps visualise the likelihood that the skin will drain to specified node fields, this skin selection tool can visualise all possible draining node fields from a selected region of skin.

4.4.1 Methodology

To develop this predictive tool, melanoma sites have been grouped together into regions. This has been carried out by using the 1098 finite elements (as described in Section 2.5), which provide discretisation of the skin model into discrete regions.

For each of these skin elements, the drainage properties have been calculated by aggregating the contained LS data. For each case, the draining node fields have been listed, and associated frequency and percentage drainage likelihood values calculated. For example, Figure 4.6 shows a skin element from the right side of the anterior torso. This element contained three melanoma sites, labelled a, b and c. The details of each of these melanoma sites are given in Table 4.2, which includes the case numbers, melanoma sites and the draining node fields. Note that there are two entries in the table for melanoma site c, since there were two cases present in this location.

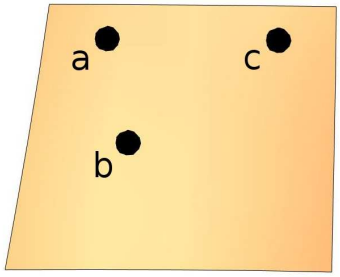

Figure 4.6: An example skin element containing three melanoma sites.

Case	Site	Node fields
1	a	Right groin, Right axilla, Interval node
2	b	Right groin
3	c	Right groin, Right axilla
4	c	Right groin

Table 4.2: Details regarding the draining node fields from each case on the example skin element.

Using these details, statistical metrics have been calculated to quantify the aggregated drainage behaviour from this element, detailed in Table 4.3. The number of cases draining to each node field is given, from which a percentage drainage likelihood value has been calculated. This value is given by the number of cases draining to each node field, divided by the total number of cases

contained within the element. For example, there are two cases that have SNs in the right axillary node field, and since there are four cases in total, there is a 50% chance of drainage to this node field from this skin element.

Code	Node field	# Cases	% Drainage Likelihood
rg	Right groin	4	100
ra	Right axilla	2	50
in	Interval node	1	25

Table 4.3: Statistics calculated for the example skin element, including the number of cases and the percentage likelihood that drainage will occur to each node field.

Note that out of the 1098 elements on the skin model, 472 of them contained no LS data and could therefore not be used to predict lymphatic drainage. Hence, there were 626 elements for which drainage statistics could be calculated. Figure 4.7 shows the skin mesh, where elements with no LS data are coloured black. This display can be directly compared with Figure 3.12, which highlights regions of skin with little LS data, commonly located on the groin, lateral sides of the body and the hands.

4.4.2 Software

Using these drainage statistics, a software tool has been developed which allows interactive display of the data. This tool has been created using CMGUI (described in Section 1.7.2), by building upon the capabilities available in this software package. A script has been developed which allows specified functions to be executed when an element is selected by the user. In this case, after a skin element has been selected, all of the possible draining node fields have been displayed which are associated with that element.

During display of draining node fields, the selected skin element was highlighted and the total number of cases available displayed on the element. Associated draining node fields also appeared, whose locations were based on the reduced lymph node model shown in Figure 3.13. Figure 4.8 shows the draining node fields for the example skin element described above. To display additional detail, alongside each representative lymph node, drainage information has been displayed. This was either the code name of the draining node field as defined in Appendix A (see Figure 4.8(a)); the number of cases draining to each field (see Figure 4.8(b)); or the percentage likelihood values (see Figure 4.8(c)). Each draining node field has been represented with a green sphere which has been scaled in size according to the percentage drainage likelihood value.

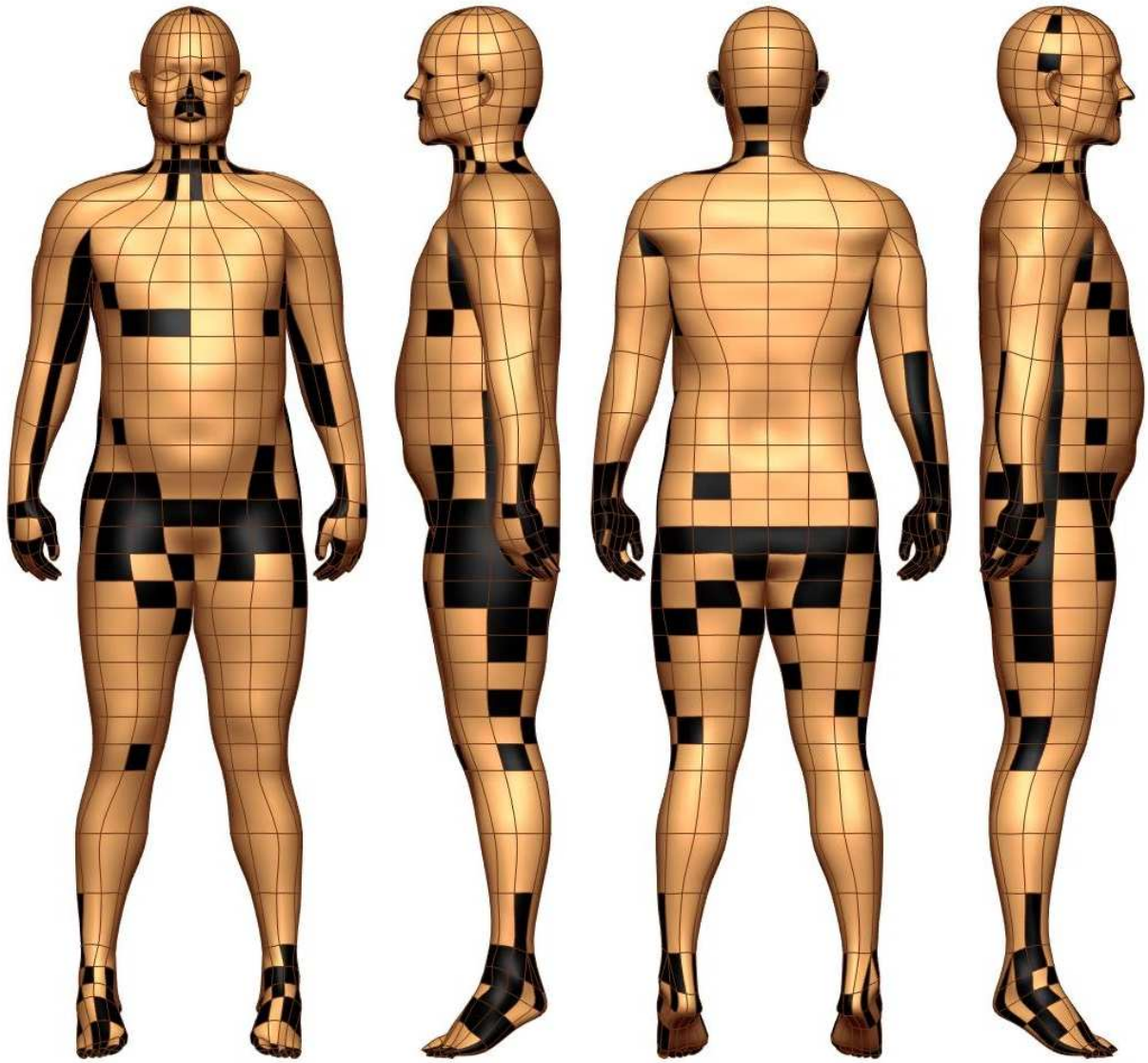

(a) Anterior (b) Left (c) Posterior (d) Right

Figure 4.7: The skin model showing elements that do not contain LS data in black.

This software tool allows full 3D rotation and magnification of the skin model, and provides all capabilities available in the CMGUI software. During this study however, it was important that this tool could be quickly and easily accessed internationally with a range of different hardware and software technologies. To achieve this goal, a reduced software tool has been developed and provided online (see Appendix E), which does not require installation of CMGUI.

The tool has been developed to ensure that it works on all operating systems, and as such it will work on any web browser. In order to create this online tool, images have been output for each

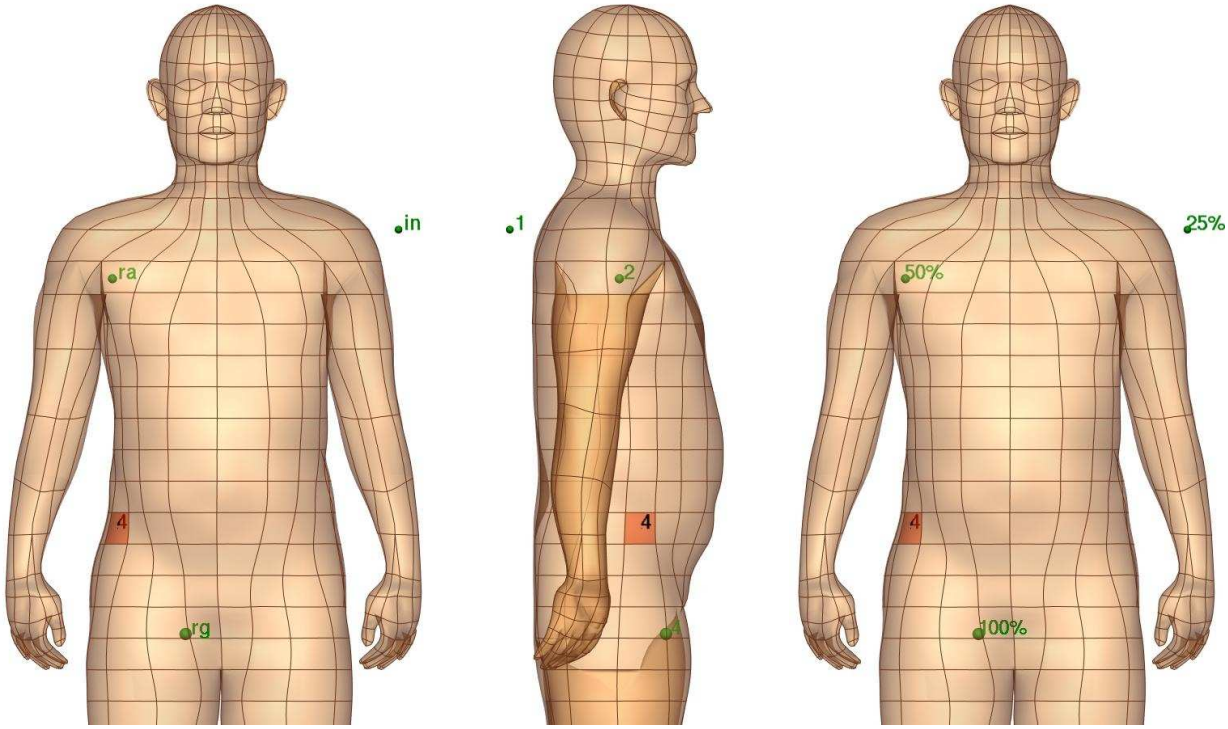

(a) SN codes (b) # Cases (c) % Drainage likelihood

Figure 4.8: The skin selection tool displaying draining node fields from the example skin element. Each display labels the representative node fields with additional information, and the number of patient cases available on the selected skin element is also given.

skin element from the CMGUI skin selection tool, visualising the draining node fields. These images have then been displayed on the website, which utilised both HTML and JavaScript code. 'Image maps' have then been implemented to allow the user to interactively select individual skin elements, to provide a way to link a set of coordinates within an image to a set of JavaScript commands.

For this tool, the corner pixel coordinates of each skin element on the images have been determined using functions available in CMGUI. When a skin element corresponding to a set of corner coordinates was selected, it activated a JavaScript function which changed the image to show the corresponding skin element. Drainage statistics were also displayed that corresponded to the selected element. This was done by reading in an XML file containing the drainage statistics into a predefined table within the browser window. The primary disadvantage of this reduced tool was that unlike the full CMGUI software tool, the skin model could not be rotated in 3D to allow the model to be viewed from any angle.

4.5 Summary

This chapter detailed methods developed to visualise the SMU's LS data on the skin and lymph node models. Previous methods of data density visualisation implemented by the SMU have been applied to the skin model to ensure consistency between datasets. The application of data visualisation using techniques available at the ABI have been outlined, including field fitting to generate heat maps which display areas of skin that are likely to follow specified drainage patterns of interest. In addition, methods developed to create a novel skin selection software tool have been presented, allowing a user to click on a region of skin on the skin model so that potential draining node fields will be displayed. The following chapter presents the results of these visualisation methods applied to the mapped LS database.

Chapter 5

Visualisation of Mapped Lymphoscintigraphy Data

This chapter presents novel displays of the SMU's LS data on the anatomical model, created using visualisation methods described in Chapter 4. Heat map results and a skin selection software tool are presented, which show the relationship between the skin and draining node fields. Patterns of lymphatic drainage highlighted by these displays are outlined, where predictable versus unpredictable drainage behaviour is described. Limitations of the model are then discussed, and the clinical applicability of the model proposed. Selected work presented here has been published (see Appendix D).

5.1 Spatial heat maps

Spatial heat maps have been created to visualise patterns of lymphatic drainage of the skin, using methods outlined in Section 4.3. Heat maps displaying both the likelihood of drainage to specified node fields, as well as the number of node fields that a given site may drain to have been created. These displays provide an improved means for understanding and analysing skin lymphatic drainage and thereby the potential patterns of melanoma spread.

The SMU's LS database (described in Section 1.6) contained 5239 cases in total. Seven of these cases, however, did not have complete information regarding either the primary melanoma site or SNs so they have been excluded. Hence, 5232 cases were mapped onto the skin and lymph node model (as carried out in Chapter 3), where a total of 929 cases were located on the head and neck and 4303 cases were located below the neck.

As mentioned in Section 1.4, unexpected lymphatic drainage patterns can occur in patients who have had previous nodal or other major surgery, since it can disrupt their initial skin lymphatic drainage. There were three such cases in the database, which have therefore been excluded during subsequent analysis, leaving a total of 5229 cases.

Two of the cases with previous surgery included patients who had undergone a right axillary dissection prior to lymphatic mapping. One of the patients showed drainage from the right anterior torso to a right internal mammary lymph node, and the other patient showed unexpected contralateral drainage from the right arm to the left axilla, as well as drainage to the right supraclavicular fossa and upper mediastinal node fields.

The third patient who has been removed from the analysis had a melanoma site located on the distal right leg. This patient had previously had an excision biopsy of lymph nodes in the right groin, and showed contralateral lymphatic drainage to the left groin as well as ipsilateral drainage to the right groin. This specific case has been reported in the literature, demonstrating that drainage to the contralateral groin can occur if the ipsilateral groin has been disturbed by previous nodal surgery (Thompson et al. 1997).

Table 5.1 details the number of cases in the mapped LS database draining to each node field. The number of cases draining to SNs located in the left and right node fields are given, from melanoma sites located on the head and neck as well as below the neck. The total number and percentage of patients draining to each node field are also detailed. Draining node fields from the three patients with previous surgery have been indicated in brackets, however these have been excluded from the total case values.

The axilla was the most common draining node field, with 62% of all cases in the database. This highlights the fact that the most common site for melanomas is the skin of the back, which is an area that usually drains to one or both axillae. The second most common node field was the groin, with 29% of all cases. Over 10% of all cases drained to SNs in the cervical level II node field, making it the most common node field location for skin on the head and neck. All other SN node field locations were drained from less than 10% of all melanoma sites in the database. Interval nodes were common, and were drained to by nearly 9% of all cases. Interestingly, although SNs can be located in the paraaortic node field, the database showed no cases of drainage to this field. This was because during LS imaging (as described in Section 1.5), SMU clinicians found it very difficult to distinguish between SNs located in the paraaortic and paravertebral regions, therefore all SNs within these node fields have been classified as paravertebral nodes.

Since there were so many possible heat maps, only a selected number are presented and discussed here, while additional heat maps are given in Appendix B. Also, due to the low number of SNs in

NODE FIELD	#Cases on head & neck		#Cases below neck		Total cases (Left + Right)	
	Left	Right	Left	Right	n	%(5229)
Head & neck node fields						
Occipital	40	51	1	1	93	1.78
Preauricular	184	160	-	-	344	6.58
Postauricular	91	79	-	1	171	3.27
Cervical level I	86	100	-	1	187	3.58
Cervical level II	268	290	6	5	569	10.88
Cervical level III	71	48	11	4	134	2.56
Cervical level IV	44	30	14	16	104	1.99
Cervical level V	110	122	99	79	410	7.84
Supraclavicular fossa	34	36	172	157 (1)	399	7.63
Submental	41		1		42	0.80
Torso & upper limb node fields						
Axilla	5	5	1638 (1)	1597	3245	62.06
Epitrochlear	-	-	43	36	79	1.51
Infraclavicular	-	-	8	8	16	0.31
TIS	-	1	95	96	192	3.67
Interpectoral	-	-	2	1	3	0.06
Internal mammary	-	-	2	4 (1)	6	0.11
Costal margin	-	-	2	5	7	0.13
Intercostal	-		5		5	0.10
Paravertebral or Paraaortic	-		36		36	0.69
Retroperitoneal	-		27		27	0.52
Upper mediastinal	-		1 (1)		1	0.02
Lower limb node fields						
Groin	-	-	780 (1)	759 (1)	1539	29.43
Popliteal	-	-	31	52	83	1.59
Other node fields						
Interval	66		404		470	8.99

Table 5.1: Number of cases draining to each node field, from the mapped LS database. Draining node fields of three patients with previous surgery are given in brackets, which have been excluded from the total case values.

certain locations, heat maps could not be accurately generated for all node fields. Instead, discrete (X, Y) frequency plots have been created for these node fields, and are also given in Appendix B.

5.1.1 Torso and limb node fields

Figure 5.1 shows heat maps generated for the left and right axillary lymph node fields, showing the percentage likelihood that skin sites will have lymphatic drainage to SNs within these fields. These heat maps were based on 1643 patients with SNs in the left axilla and 1602 patients with SNs in the right axilla.

It can be readily seen that melanoma sites located on the arm or torso above the umbilicus commonly drained to the ipsilateral axillary node field. However, these heat maps also quantitatively show that lymphatic drainage often occurred across Sappey's lines, both across the midline and across Sappey's horizontal line through the umbilicus. These two axillary heat maps were not exact reflections of each other, however they did have sufficient commonality to show skin regions in which drainage to the ipsilateral axilla is almost certain, and the range of sites where drainage to the ipsilateral or contralateral axilla should be considered possible or probable.

Contour lines indicate a small number of anomalous patients, which account for the most dramatic asymmetries. For example, two patients with primary melanomas on the left anterior torso (Figure 5.1(a)) and one patient with a primary melanoma on the right anterior torso (Figure 5.1(b)) showed direct lymphatic drainage solely to interval nodes, decreasing the percentage of drainage to the ipsilateral axillary node field below 100% in those regions. Two patients with primary melanomas near the right posterior wrist (Figure 5.1(b)) showed drainage to a right epitrochlear and an interval node respectively, and a patient with a primary melanoma on the right thumb showed unusual drainage to the right infraclavicular and right cervical level IV node fields, completely bypassing the right axilla.

Drainage from the torso can also occur from a large region of skin on the posterior torso to the triangular intermuscular space (TIS) node fields. Heat maps for these node fields are given in Figure B.1, which indicates that the posterior torso may have up to 20% probability of draining to SNs in this location. Often if a patient has lymphatic drainage to the TIS, they will also have drainage to an axillary node field.

Heat maps that visualise drainage to the left groin are given in Figure 5.2(a), while drainage to the right groin is shown in Figure 5.2(b). These were based on 780 patients who had drainage to the left groin and 759 patients which showed drainage to the right groin. Similar to the axillary heat maps, drainage across Sappey's lines was noted to occur often, however a very distinct region almost

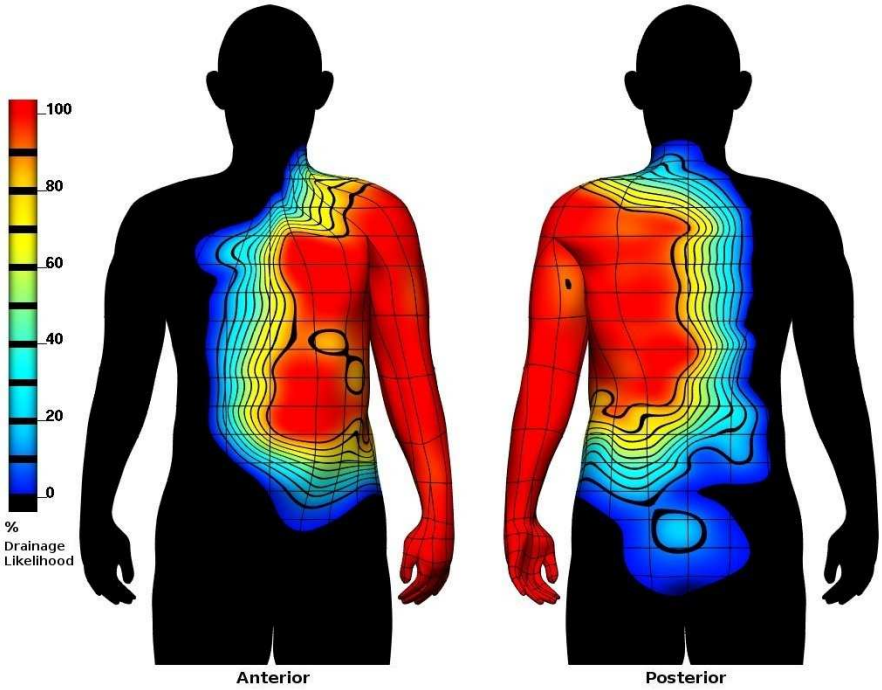

(a)

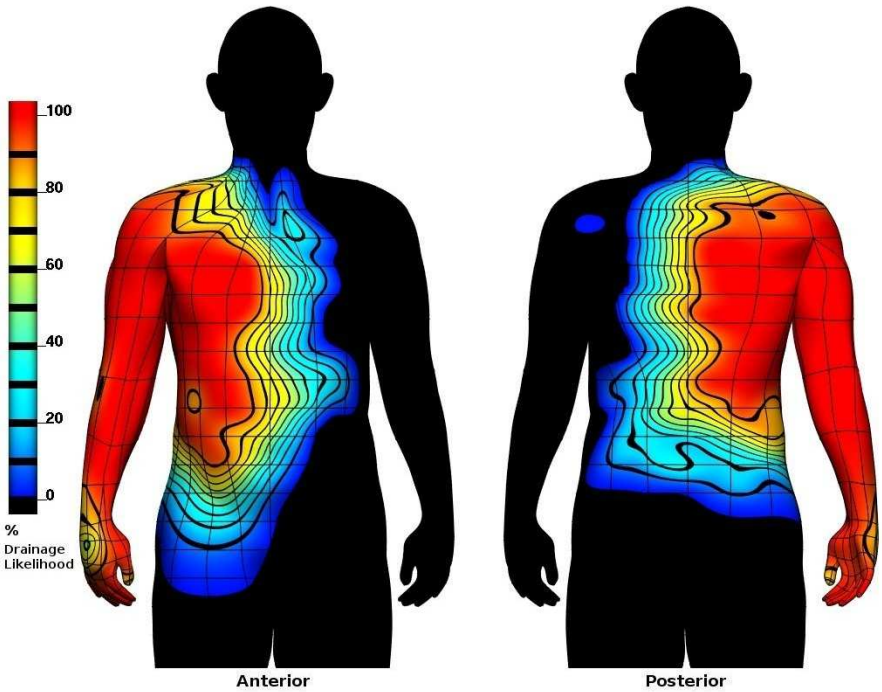

(b)

Figure 5.1: Heat map displaying the percentage likelihood that lymphatic drainage will occur to the (a) left and (b) right axillary node fields.

always drained to the ipsilateral groin. All primary melanoma sites on the left lower limb had lymphatic drainage to SNs in the left groin and all right lower limb melanoma sites had drainage to the right groin node field. Melanoma sites on the lower limbs also showed drainage to interval nodes (see Figure B.20) and to the popliteal node field (see Figure B.3), however, the data showed that for these sites, drainage also always occurred to the groin.

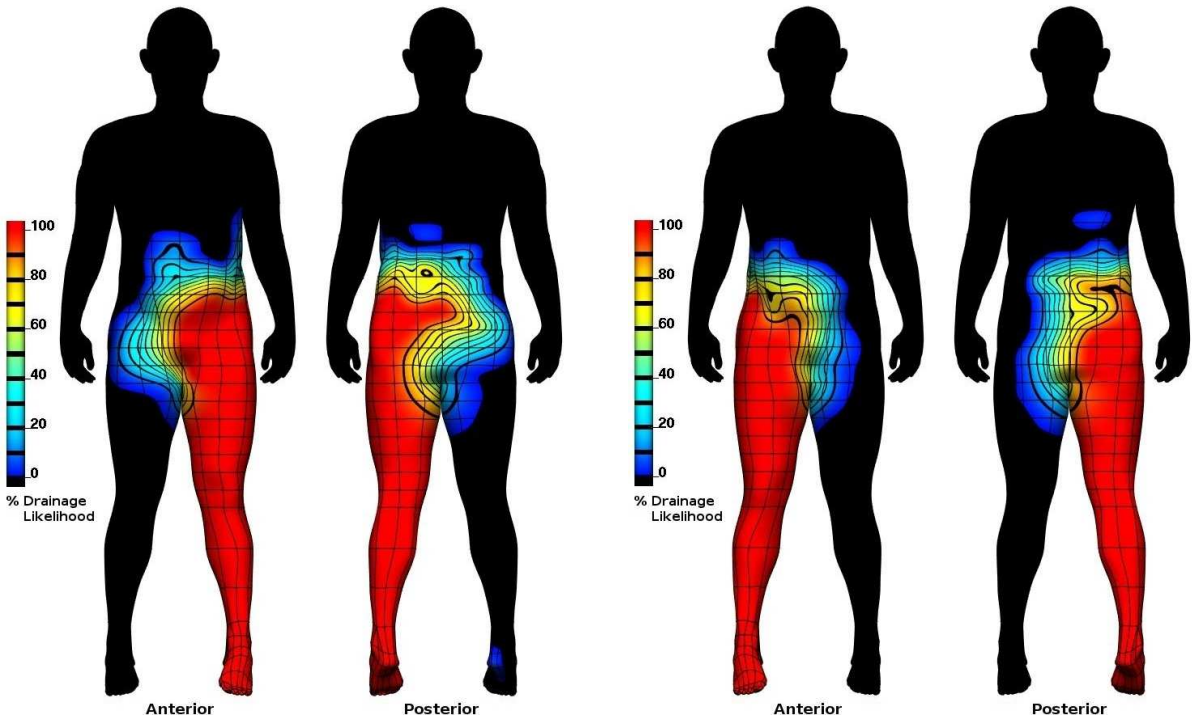

(a) (b)

Figure 5.2: Heat map displaying the percentage likelihood that lymphatic drainage will occur to the (a) left and (b) right groin node fields.

Hence, these heat maps show that lymphatic drainage of the lower limbs is highly predictable. There was one case, however, that showed unexpected contralateral drainage from a melanoma site on the right heel to the left groin (Figure 5.2(a)) and ipsilateral drainage to the right groin and right popliteal node fields. This was the only patient in the database without previous surgery who did not show exclusive drainage to the ipsilateral groin node field.

Both the axillary and groin heat maps showed some asymmetry on the lower torso region both anteriorly and posteriorly. The density of primary melanoma sites in the skin regions was particularly low (see Figure 4.3), and therefore heat maps over these regions were based on extrapolations from the nearest skin regions in which data was available. Therefore, the asymmetry shown in the heat maps probably is a result of the sparsity of data in these regions.

5.1.2 Head and neck node fields

As described in Section 1.4, lymphatic drainage of the head and neck has been shown in previous LS studies to be highly complex, with SNs commonly found in multiple node fields. In addition, SNs in the head and neck are usually small in size and frequently situated near the primary melanoma site, making them difficult to locate.

Drainage from the head and neck has been demonstrated by the SMU to one or more of 13 possible lymph node fields as indicated in Table 5.1. Heat maps of the most common node fields draining the head and neck are presented in this section, while heat maps of less common head and neck node fields can be seen in Appendix B. The results showed that there were some node fields in the head and neck that consistently drained localised areas of skin, including the preauricular node field which was the second most common node field draining the head and neck.

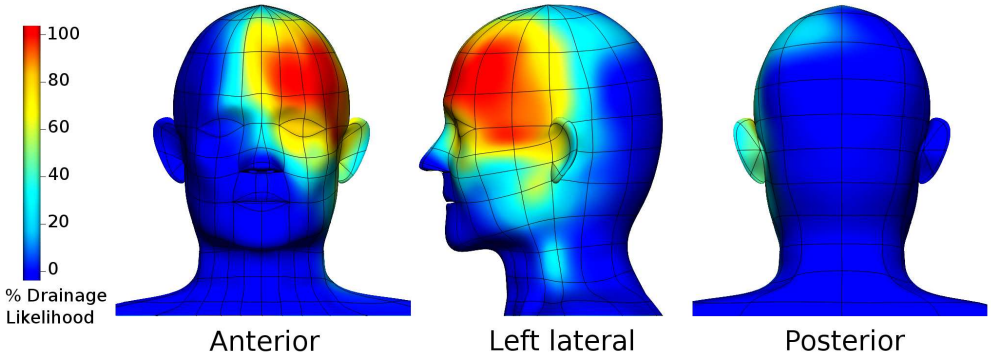

(a)

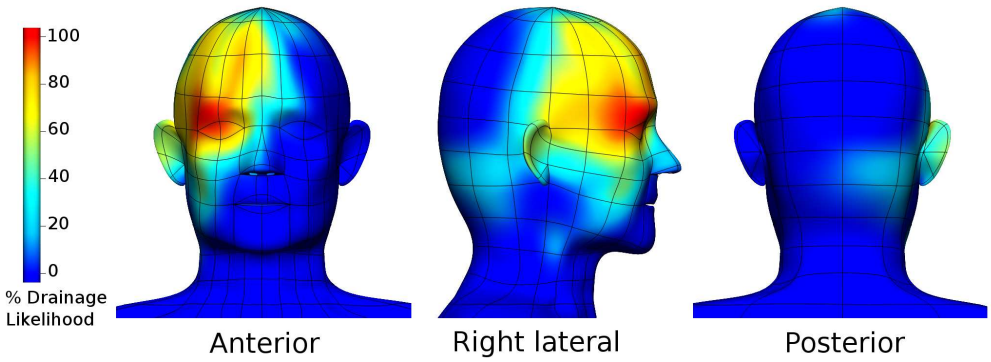

(b)

Figure 5.3: Heat map displaying the percentage likelihood that lymphatic drainage will occur to the (a) left and (b) right preauricular node fields.

Heat maps showing the likelihood of drainage to the preauricular node fields (which also include the parotid nodes) are given in Figure 5.3. There were 184 patients with drainage to the left preauricular node field (Figure 5.3(b)) and 160 to the right preauricular node field (Figure 5.3(a)). A distinct red region can be seen on the left preauricular heat maps, showing that the left anterior scalp and part of the left side of the face always drained to this node field. The right preauricular heat maps show a slightly lower likelihood of drainage from the corresponding region of skin, but the main areas shown as having at least a 60% chance of draining to the preauricular node field are similar between the two sides. Two other features are apparent. Drainage across the midline does occur but is relatively rare compared with most node fields, and drainage to the preauricular node field is rare from skin on the lower half of the face, and particularly from the neck or skin posterior to the coronal plane.

It is useful to compare these heat maps with current clinical recommendations for node field dissection, given by O'Brien et al. (1995) and Pathak et al. (2001). These guidelines have been developed based on the current understanding of melanoma spread. According to these clinical recommendations, the face, anterior and coronal midline scalp, anterior and coronal upper neck and the ear can all drain to the preauricular node field. While the LS data confirm most of these drainage patterns, the neck drainage differs in one important respect, namely that while coronal neck sites do drain to this field, drainage was not seen in any of the 49 patients with primary melanoma sites on the anterior upper neck. The heat maps also show that drainage from sites outside those clinically predicted in the literature is not only possible, but may occur in as many as one in four patients from sites posterior to the ear.

Drainage to the postauricular (Figure B.4), occipital (Figure B.5) and submental (Figure B.6) node fields also showed strong localisation, with large areas of the head and neck showing no drainage to these fields, although these conclusions are based on fewer patients than for the preauricular node fields. The skin areas drained by the postauricular and occipital node fields show striking posterior localisation.

In contrast, heat maps showing the likelihood of drainage to the cervical level II node fields show a very wide distribution of skin sites. Figure 5.4(a) shows drainage to the left cervical level II node field calculated from 274 patients, and Figure 5.4(b) shows drainage to the right cervical level II node field from 295 patients.

These heat maps show that any skin region on the head or neck can drain to the ipsilateral cervical level II node field, and large regions of the face, scalp and coronal neck drain here in at least 60% of patients. Past clinical guidelines state that all skin regions except the lower neck will drain to this node field, but the heat maps reveal that at least 20% of the patients with primary melanomas

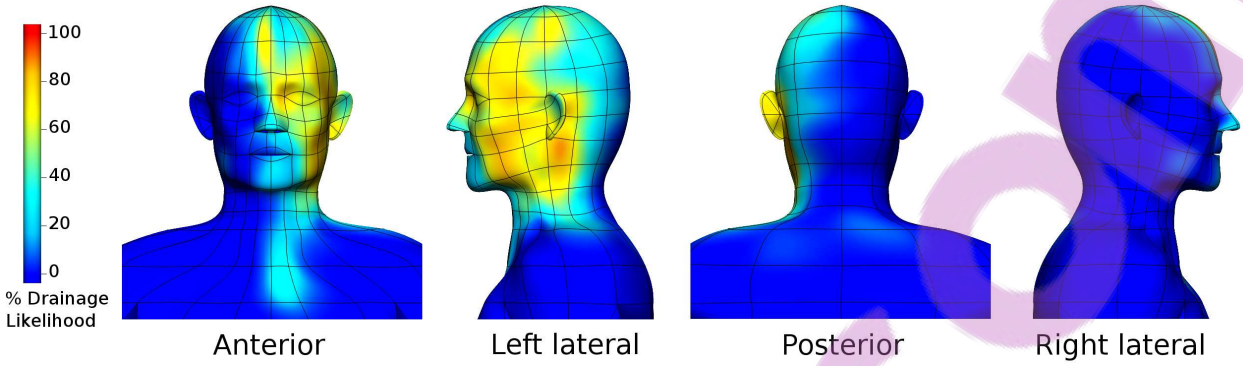

(a)

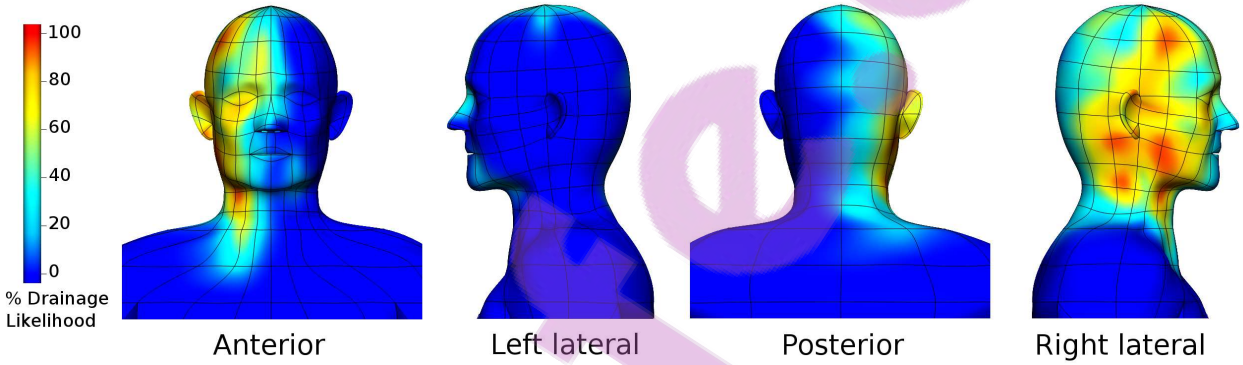

(b)

Figure 5.4: Heat map displaying the percentage likelihood that lymphatic drainage will occur to the (a) left and (b) right cervical level II node fields.

on the lower neck have a SN in this field. A small number of patients (11 in total) even showed upwards drainage from melanoma sites on the upper chest and upper back. Contralateral drainage is also possible, for example, one melanoma site on the lower face from each side of the head showed contralateral drainage to the opposing cervical level II node field.

Heat maps of areas draining to cervical level I lymph nodes (shown in Figure B.7) showed an interesting contrast with those for cervical level II nodes. The areas with the lowest probability of draining to cervical level II lymph nodes, especially the nose, lips and chin, tended to have a high probability of draining to cervical level I nodes. This suggests these fields show complementary drainage patterns. As mentioned in Section 1.3.2, the SMU node field classifications include submental nodes in cervical level I, and indeed the heat maps for submental and cervical level I fields (Figure B.6 and Figure B.7) are very similar, so that aggregating the data would not substantially change the cervical level I heat maps.

Cervical level III and IV node fields show broadly similar drainage patterns (shown in Figure B.8 and Figure B.9), suggesting they may functionally be part of the same field, and that their anatomical separation is potentially arbitrary. The drainage patterns of cervical level V (see Figure B.10) are quite distinct from the other cervical node fields, and are more reminiscent of the posterior drainage patterns of the occipital and postauricular node fields. Lymphatic drainage patterns to supraclavicular fossa nodes (see Figure B.11) appear similar to cervical level V nodes, although subtle differences are apparent between them. Supraclavicular fossa nodes drain a larger area of the anterior torso than cervical level V, and they also drain skin of the upper limbs while cervical level V does not. This suggests that although supraclavicular fossa nodes are now classified as part of cervical level V nodes, they drain more inferior areas of skin, consistent with their inferior relationship to the cervical level V nodes.

The heat maps for the postauricular, occipital, cervical level V and supraclavicular fossa node fields demonstrate that skin posterior to a coronal plane through the ears, largely drains to these lymph node fields. Conversely, drainage from skin anterior to the ear almost always occurs to node fields located in front of the ear. To visualise this phenomenon more effectively, node fields were grouped into anterior and posterior regions and combined heat maps generated as shown in Figure 5.5. Anterior node fields comprised the preauricular, submental, cervical levels I, II, III and IV node fields, while posterior node fields comprised the postauricular, occipital, cervical level V and supraclavicular fossa nodes.

Heat maps generated for the anterior and posterior head and neck node fields showed that they were strikingly complementary. While this result initially suggests an anatomical divergence between the lymphatic vessels entering these two sets of lymph node fields, it is evident that there must still be considerable overlap between the two sets of vessels. In considering the posterior view of the drainage to the posterior fields in Figure 5.5(b), the intense area of red surrounding the occiput indicates that 100% of patients in that area drained to at least one of the posterior node fields. However, in examining the same posterior view of drainage to the anterior fields in Figure 5.5(a), the areas of light blue in the occipital skin regions indicate that up to 40% of patients here also drained to anterior node fields. Hence despite the skin areas drained by these two groups of node fields being apparently complementary, even sites that always drain to one of these groups often also drain to the other. Collectively, these results confirmed that the skin of the head and neck has some of the most complex lymphatic drainage in the human body.

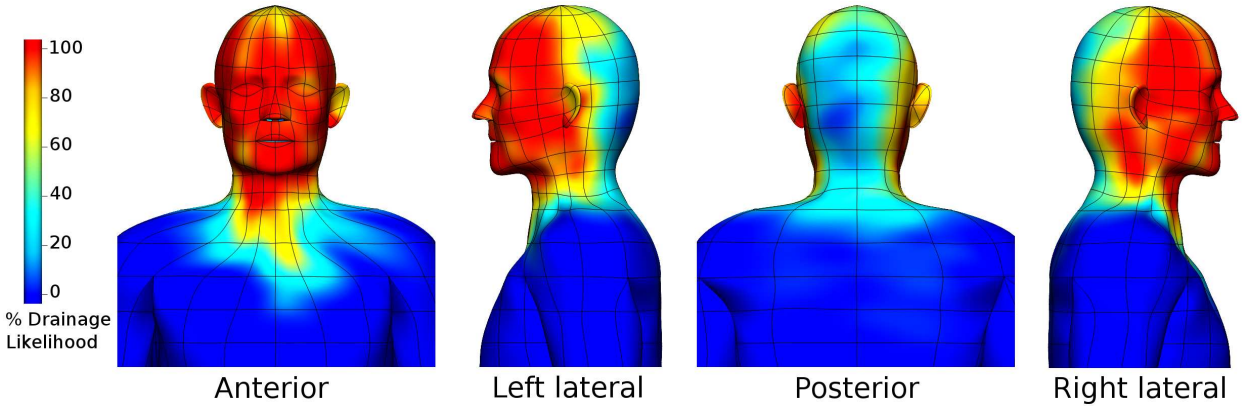

(a)

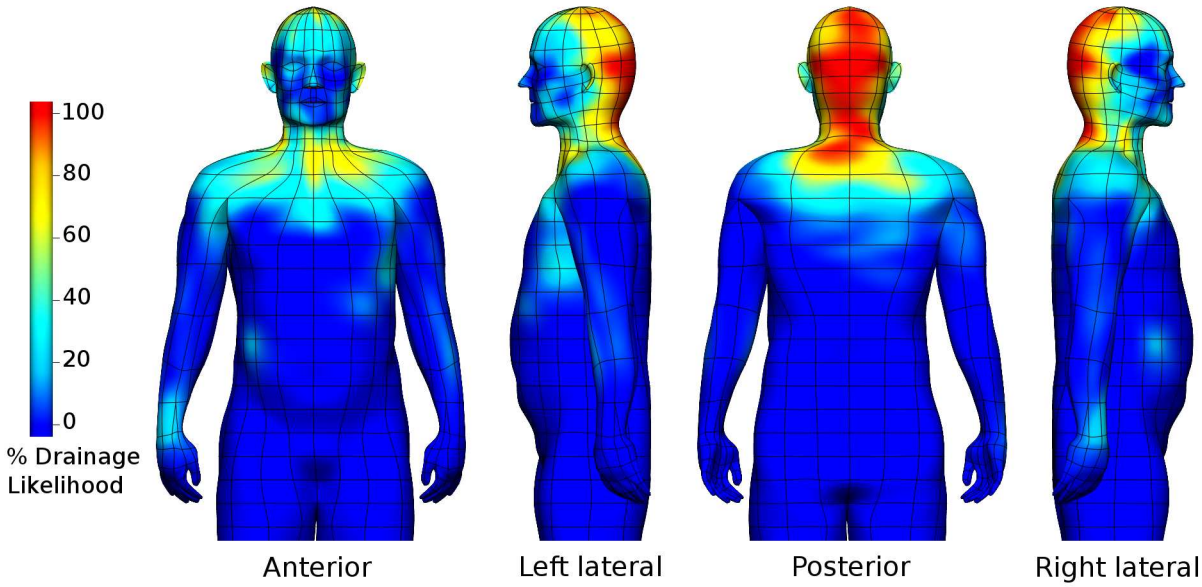

(b)

Figure 5.5: Heat map displaying the percentage likelihood that lymphatic drainage will occur to (a) anterior head and neck node fields: preauricular, submental, cervical levels I, II, III and IV, and (b) posterior head and neck node fields: postauricular, occipital, cervical level V and supraclavicular fossa.

5.1.3 Number of draining node fields

Since lymphatic drainage is often observed to multiple node fields from an individual patient, heat maps have also been generated to display this data. Table 5.2 details the number of patients draining to different numbers of node fields from both melanoma sites on the head and neck, melanoma sites below the neck, and the total number and percentage of cases. Again, patients with previous surgery have been removed from this analysis.

#Node fields	Cases on head & neck		Cases below neck		Total Cases	
	n	%(929)	n	%(4300)	n	%(5229)
1	263	28.31	2907 (1)	67.58	3170	60.62
2	396	42.63	993 (1)	23.10	1389	26.56
3	191	20.56	313 (1)	7.30	504	9.64
4	67	7.21	69	1.60	136	2.60
5	8	0.86	16	0.37	24	0.46
6	3	0.32	2	0.05	5	0.10
8	1	0.11	0	0	1	0.02

Table 5.2: Number of cases draining to one or multiple node fields. The number of draining node fields of the three patients with previous surgery are given in brackets, which have been excluded from the total case values.

The majority of patients had drainage to only one node field (61%), however over a quarter of patients drained to two node fields while the remaining patients drained to three or more node fields. Most patients with melanomas on the head and neck (72%) had lymphatic drainage to two or more node fields, in contrast to the skin below the neck where only 32% of patients had drainage to two or more node fields. In some extreme cases, drainage occurred to SNs in as many as six or even eight node fields. The single patient with eight draining node fields was a 65-year-old male with a primary melanoma on the posterior upper scalp. He had SNs located in both left and right occipital, right cervical levels II and V, left cervical levels III, IV and V, and the left postauricular node fields.

Figure 5.6 shows heat maps created to display the number of node fields to which melanoma sites drained. Regions of skin that had drainage to only one node field are shown in Figure 5.6(a), while Figure 5.6(b) illustrates the probability that drainage from the region was to more than one node field. These heat maps show the regions of skin where lymphatic drainage was most straightforward. For example, Figure 5.6(a) shows large red regions on the legs indicating that melanoma sites in these areas of skin drained to a single node field, in this instance, the ipsilateral groin. Also, red regions on the upper limbs and near the armpits indicate skin that will most likely drain

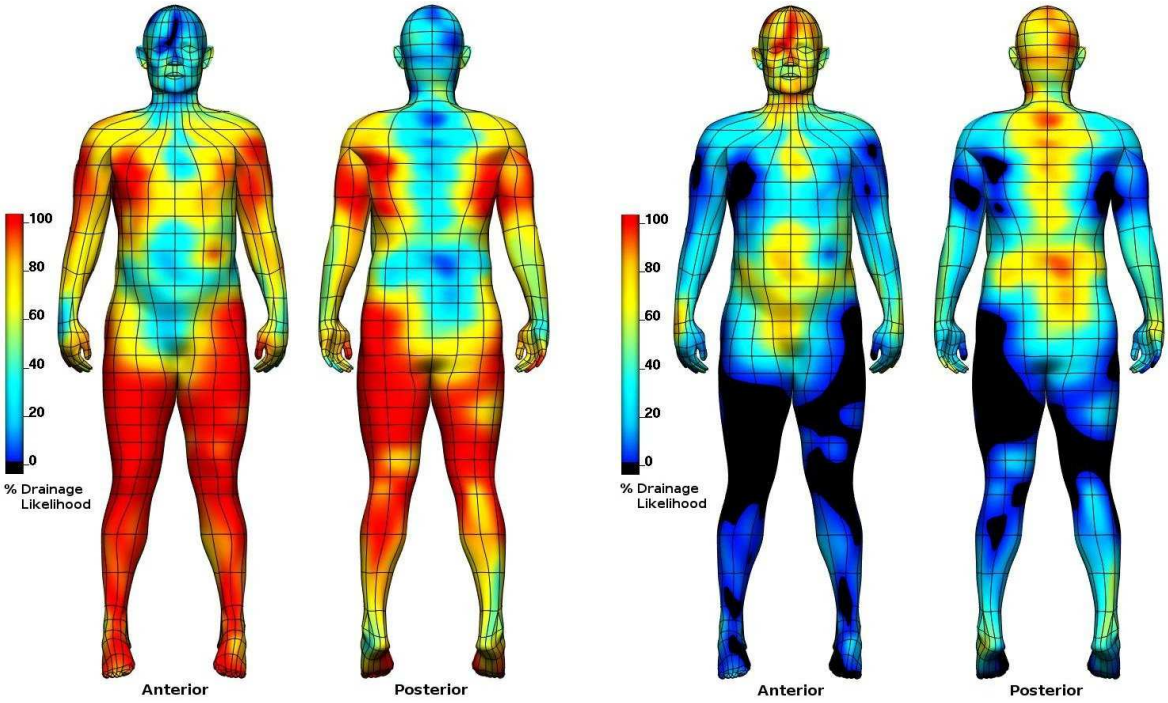

(a) One node field

(b) Two or more node fields

(c) Three or more node fields

(d) Four or more node fields

Figure 5.6: Heat map displaying the percentage likelihood that lymphatic drainage will occur to different numbers of node fields.

to the ipsilateral axilla. In contrast, Figure 5.6(b) shows that there are some areas of skin in which drainage was never to a single node field (the red areas on the upper and lower back and parts of the head) and are therefore highly complex.

It is also immediately apparent that there is no region of skin on the head or neck with consistent drainage to only one node field. Many skin regions on the head and neck showed approximately 100% likelihood of drainage to two or more node fields, including the anterior scalp, coronal scalp, the middle of the anterior neck and sections of the posterior scalp. The cheeks showed some of the lowest likelihood values (20-60%), indicating that at least 40% of patients with primary melanoma sites had drainage to a single node field; however even in these cases, the single node field draining this site differed between patients.

The potential complexity of melanoma spread is shown in Figure 5.6(c) and Figure 5.6(d)), which indicates the likelihood that drainage will occur to three or more and four or more node fields respectively. For example, more than 20% of patients in some of these areas drained to at least four different node fields. Regions with the highest likelihood of drainage to many node fields are close to Sappey's lines and on the head and neck. However, regions outside the torso, most notably on the distal leg and especially the hand and forearm, can also drain to three or more node fields. Skin sites that commonly drain to many node fields do not always drain to the same subset of fields, indicating again that these regions have highly complex lymphatic pathways.

5.2 Interactive skin selection tool

To further display the mapped LS data, an interactive skin selection tool was developed using methods outlined in Section 4.4. This tool allowed dynamic display of skin lymphatic drainage, and the variations in drainage patterns across the body. Examples of drainage behaviour observed within selected regions of skin, which highlight areas with complex lymphatic drainage versus those that are more straightforward, are given below.

5.2.1 Results

Two examples of significantly different drainage patterns on the skin model are given in Figure 5.7 and Figure 5.8, where two different elements on the posterior torso have been selected and corresponding SN node fields have been displayed. Figure 5.7(a) shows a region of skin near the midline and waist of the posterior torso, where 21 patients in the dataset had cutaneous melanoma. Eight potential draining node field locations were dynamically displayed when this skin element

was selected. As explained in Section 3.2, in the absence of a precise anatomical location, interval nodes have been depicted outside the body.

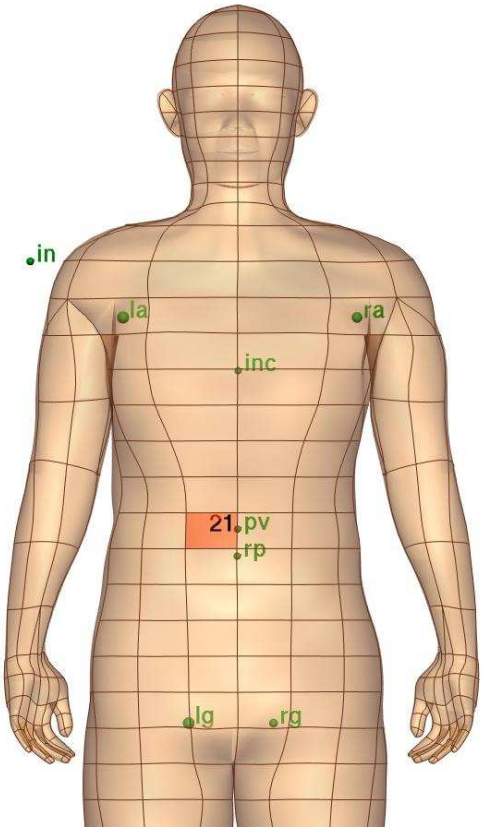

(a)

STATISTICS:

Code	Nodefield	# Cases	Drainage
la	Left Axilla	15	71.4%
ra	Right Axilla	11	52.4%
inc	Intercostal	1	4.8%
pv	Paravertebral	1	4.8%
rp	Retroperitoneal	1	4.8%
lg	Left Groin	14	66.7%
rg	Right Groin	5	23.8%
in	Interval Node	2	9.5%

(b)

Figure 5.7: The interactive skin selection tool, showing (a) complex lymphatic drainage for a selected posterior torso element and (b) associated drainage statistics.

Figure 5.7(b) details the associated drainage statistics for this element. The most common node field was the left axilla, where 71.4% of all cases had SNs in this node field. It can be seen that drainage was possible from this region of skin to any of the axillary and groin node fields, contrary to Sappey's assumptions that state lymphatic drainage should be to only one of these node fields from skin of the trunk (detailed in Section 1.4). Drainage was shown to also occur from this skin region to the less common paravertebral and retroperitoneal node fields (see Figure B.17 and Figure B.18). These drainage predictions can be directly compared with the heat maps in Figure 5.6, which confirms that areas of skin near Sappey's lines were likely to drain to drain to multiple node fields.

In contrast, Figure 5.8(a) shows a region of skin near the left axilla which had a much simpler drainage pattern. All 10 patients with melanoma located within this skin element had a single SN

in the left axilla. This can be directly compared with the heat map given in Figure 5.6(a) which also shows that this element is 100% likely to have only one draining node field. Additionally, through comparison with the heat map given in Figure 5.1(a), which displays the likelihood of drainage to the left axilla, it is apparent that the sole draining node field is indeed the left axilla.

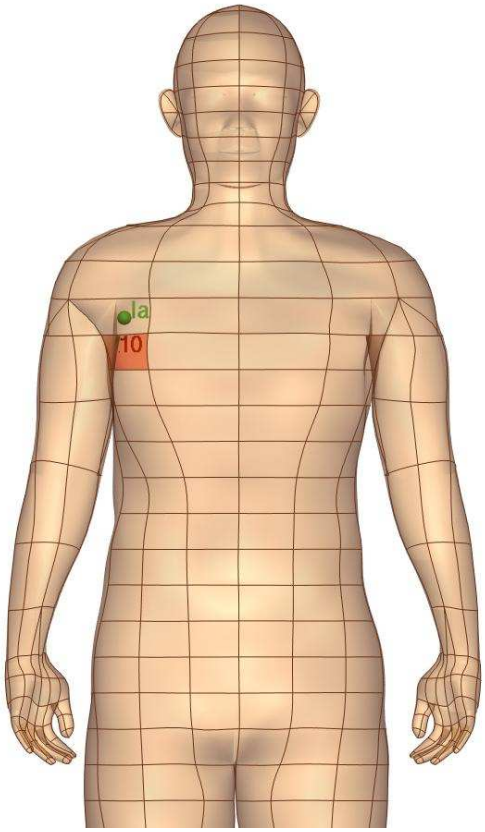

STATISTICS:

Code	Nodefield	# Cases	Drainage
la	Left Axilla	10	100.0%

(a) (b)

Figure 5.8: The interactive skin selection tool, showing (a) simple lymphatic drainage for a selected posterior torso element and (b) associated drainage statistics.

As mentioned previously, lymphatic drainage of the head and neck is highly variable. The skin selection tool also enables the complex drainage in the head and neck to be displayed. For example, Figure 5.9(a) shows a skin element selected on the left upper face and Figure 5.9(b) details the corresponding drainage statistics. Accumulated data from 18 patients with melanoma sites in this element showed lymphatic drainage to seven different node fields. These node fields included the left preauricular, left cervical levels I to V node fields, as well as interval nodes. Similarly, this drainage behaviour can be compared with the head and neck node field heat maps given in Section 5.1.2, and in Appendix B.

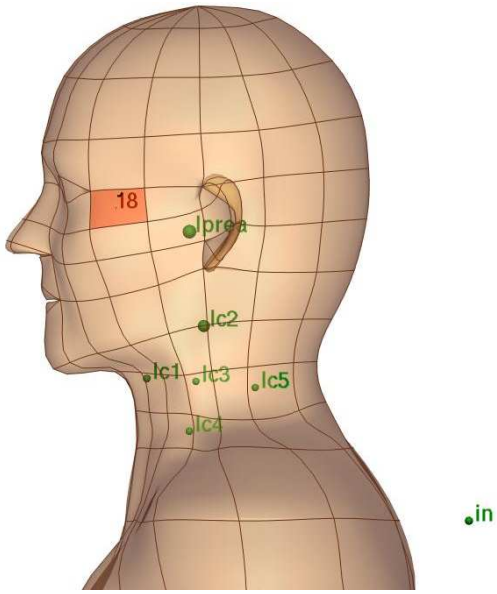

(a)

STATISTICS:

Code	Nodefield	# Cases	Drainage
lprea	Left Preauricular	17	94.4%
lc1	Left Cervical Level I	2	11.1%
lc2	Left Cervical Level II	13	72.2%
lc3	Left Cervical Level III	1	5.6%
lc4	Left Cervical Level IV	1	5.6%
lc4	Left Cervical Level IV	1	5.6%
lc5	Left Cervical Level V	1	5.6%
in	Interval Node	3	16.7%

(b)

Figure 5.9: The interactive skin selection tool, showing (a) complex lymphatic drainage for a selected element on the left side of the head and (b) associated drainage statistics.

5.3 Discussion

Both the heat maps and skin selection tool provide novel methods for improving visualisation of the SMU's LS data. The heat maps visualise the likelihood that any area of skin will drain in a specified manner, while the skin selection tool allows the opposite approach by showing all draining node fields from a selected region of skin. While these displays greatly improve upon previous methods of LS data visualisation, there are still limitations and potential sources of error that need to be considered.

It is possible that some patients who have had previous surgery have not been removed from the analysis and therefore may pose a source of error in the subsequent analysis. The SMU's LS database did not record details about whether each patient had had previous surgery, and therefore to determine whether they did has required patient records to be individually checked by SMU clinicians. In the absence of this information, and to reduce the extensive time that would be required to check each patient's records, only cases in the database that showed highly unexpected drainage patterns in the heat maps have been checked. Although this was not ideal, it was considered appropriate, since the number of patients with previous surgery was estimated to be less than 1% of all patients in this study, based on the knowledge of nuclear medicine physicians at the SMU (Uren 2007).

The process of generating heat maps is essentially a method to provide an averaged representation of the discrete data values. As a result, any outlying values may not be seen on the smoothed heat maps, even though it is particularly important for clinicians to be aware of such unexpected patterns of drainage. These heat maps can therefore only be analysed as representations of a large sample of a population, and cannot be directly applied to an individual. Although numerous reports have detailed the clinical unpredictability of lymphatic drainage, there are still patterns that emerge from the data that show the common lymphatic drainage behaviour.

A particular disadvantage of the model is the lack of data in some regions of skin. As shown in Figure 4.3, the mapped LS data is clearly not evenly distributed across the skin. Data is sparsely distributed on skin regions including the groin and lateral sides of the torso and legs, and the number of DOFs available during field fitting to represent the LS data greatly outweighs the information supplied. This means that areas with sparse data may include a large amount of data extrapolation in the fitted heat maps. For example, Figure 4.4(d) in the previous chapter shows that the entire left hand is 100% likely to drain to the left axilla, however, there is a sparsity of sites in this location (see Figure 4.5(a)). During heat map interpretation, it is important to remember the sample size in each region of skin since statistical accuracy will vary across the model (dealt with specifically in Chapter 7). Additionally, there is a degree of error present in the mapped coordinates due to both recording procedures at the SMU and the mapping process (as detailed in Section 3.3).

The data sparsity limitation extends to the skin selection tool, where skin elements with a low number of cases will not have a high degree of accuracy in their drainage predictions. The tool also has limitations imposed by the element discretisation. Although grouping melanoma sites according to existing elements provides a convenient way to aggregate data, division of the skin surface into elements during initial linear mesh construction (carried out in Section 2.5) did not give equal sized skin elements. Due to this size variation and the non-uniform distribution of primary melanoma sites, there is a large variation in the number of cases on each element. This is particularly seen on elements located on the upper back which are both large and correspond with an area of skin with a large frequency of cases. In contrast, there are a number of elements containing no cases of melanoma at all (as shown in Figure 4.7). Therefore, care must be taken when interpreting these results since the statistical accuracy of elements with little data will be very low. To help address this issue, the number of cases that the drainage statistics is based on is displayed on the selected element, to prevent over-interpretation of the data.

Even with these caveats, the developed model still provides the opportunity for clinical utility. The interactive software tool could particularly help with planning ultrasonography or clinical follow-up by identifying the appropriate node fields that need to be monitored. It may also be helpful in discussions with patients before surgery when gaining informed consent.

A further clinical application of this model would be if LS showed drainage from the melanoma site to an SN, but did not show drainage to a node field that the model predicted for 90 to 100% of patients. In this situation, this other predicted node field should also be monitored during clinical and ultrasonography follow-up because in some patients with clinically normal lymph nodes, metastatic occlusion of a lymphatic collector can prevent a true SN receiving radiocolloid on LS. Another use of this model and the interactive displays could be for teaching medical and nursing undergraduates and postgraduate surgical trainees.

Although lymphatic drainage is clinically unpredictable, there are still clear patterns of drainage shown in the heat maps. Some node fields drain relatively circumscribed areas of skin, particularly the axillary, groin and preauricular node fields. Even though there are inherent limitations in both of these methods of data visualisation, they greatly improve previous methods that have been used. The ability to show the likelihood of drainage from any area of skin fulfilling a drainage pattern of interest has not been carried out before. Additionally, the skin selection tool is the first tool that enables dynamic display of accumulated LS data in 3D.

5.4 Summary

This chapter presented the visualisation results of the LS data mapped onto the skin and lymph node model. Patterns of lymphatic drainage were shown via heat maps and an interactive skin selection tool, highlighting areas of skin with the most and least predictable drainage patterns. Skin on the head and neck, and on the torso near Sappey's lines were confirmed as having the most variable patterns of lymphatic drainage. In contrast the upper and lower limbs were more straightforward, showing that they were highly likely to drain to the ipsilateral axillary and groin node fields respectively. The limitations of the model have been discussed, and the clinical utility of these displays have been proposed. The following chapters further analyse the mapped LS database using quantitative statistical techniques.

Chapter 6

Statistical Analysis Methodology

The model developed in this study now provides a means to conduct the first detailed statistical analysis of skin lymphatic drainage in 3D. This chapter outlines the methods used to conduct this, which builds on the data visualisation work carried out in Chapters 4 and 5. Techniques to investigate the accuracy of Sappey's lines are given. Statistical significance testing by fitting a multinomial model to the data is then presented and proposed as a way to determine whether lymphatic drainage is symmetric, i.e. the same on the left and right sides of the body. Clustering analysis is then described as a method to functionally group regions of skin with similar drainage behaviour. Lastly, non-parametric bootstrapping is outlined to determine appropriate confidence intervals for the data.

6.1 Introduction

Review of relevant literature indicates that statistical analysis of lymphatic drainage of the skin has been very limited and, to the author's knowledge, has not been previously conducted in 3D (a discussion of previous studies into lymphatic anatomy with particular emphasis on skin lymphatic drainage is given in Section 1.4). This lack of knowledge highlights a need for detailed quantitative statistical analysis of the lymphatics draining the skin.

Predictions of lymphatic drainage based on Sappey's lines have been shown to be highly inaccurate and they pose problems as a clinical guideline for melanoma spread (Uren et al. 1999). In addition, visualisation of the SMU's mapped LS data in Chapter 5 has shown that regions of skin close to Sappey's lines have some of the most variable drainage patterns (seen in Figure 5.6). To further analyse skin lymphatic drainage, the following questions have been addressed in this chapter:

- How accurate are Sappey's lines at predicting lymphatic drainage?
- Is lymphatic drainage the same on the left and right sides of the body?
- Is there a better way to functionally group regions of skin that drain in a similar manner?

Each of these questions seek to improve current understanding of skin lymphatic drainage. Determining the predictive accuracy of Sappey's lines will provide a quantitative measure of their reliability. Meanwhile, statistically comparing drainage from the left and right sides of the body will test whether lymphatic drainage is symmetric. If drainage is symmetric, the mapped LS data can then be reflected from each side of the body to the other. This would increase the data density, potentially reducing uncertainty in the model's drainage predictions in the heat maps and skin selection tool presented in Chapter 5. Taking the analysis further, the model can now be used to determine regions of skin that drain in a similar manner based purely on the LS data. This will allow the data itself to define patterns of drainage, without reference to any previous knowledge of the lymphatic anatomy. The following sections outline the methods designed to address each of these questions.

6.2 Analysing Sappey's Lines

As detailed in Section 1.4, Sappey's lines demarcate four separate regions of skin on the trunk, where the upper regions of skin were expected to drain to the ipsilateral axilla, and the lower regions of skin to the ipsilateral groin (Sappey 1874). Sappey's vertical line is defined down the midline of the body, while Sappey's second line is located around the waist. The exact positioning of this second transverse line has been described variably across the literature. For example, Fortner et al. (1965) defined a transverse line on the trunk as running from the mid-epigastrium along the eighth rib to approximately the level of the eighth or ninth thoracic vertebra, although Sappey's lines were not directly referenced in their study. Sugarbaker & McBride (1976) defined Sappey's transverse line as running from 2 cm above the umbilicus and curving gently upwards to the level of the second and third lumbar vertebra, meanwhile clinicians at the SMU have defined the line as being positioned from the umbilicus anteriorly to the level of the second lumbar vertebra posteriorly (Uren et al. 1999). To maintain consistency with the LS data that has been used in this thesis, the SMU's definition of Sappey's transverse line around the waist has been used.

6.2.1 Methodology

The mapped model has been used to determine the accuracy of Sappey's lines to predict lymphatic drainage, and also to determine whether there is an optimal position for these lines which will minimise the number of cases crossing over them. A case that crosses over Sappey's lines is defined as any melanoma site located on the trunk, which does not exclusively drain to its predicted node field but instead 'crosses' over Sappey's lines to drain to other axillary or groin node fields.

To conduct this analysis, Sappey's lines were initially defined relative to the skin model. As shown in Figure 6.1, Sappey's vertical line has been defined by a plane normal to the x-direction located at the vertical centre of the model (referred to as the 'vertical plane'). Sappey's transverse line around the waist has also been defined using a plane (referred to as the 'midline plane'). These planes define four regions of skin on the trunk labelled as the upper left (UL), upper right (UR), lower left (LL) or lower right (LR) regions. Utilising planes to define Sappey's lines provided a computationally efficient means of calculating in which region each melanoma site was located.

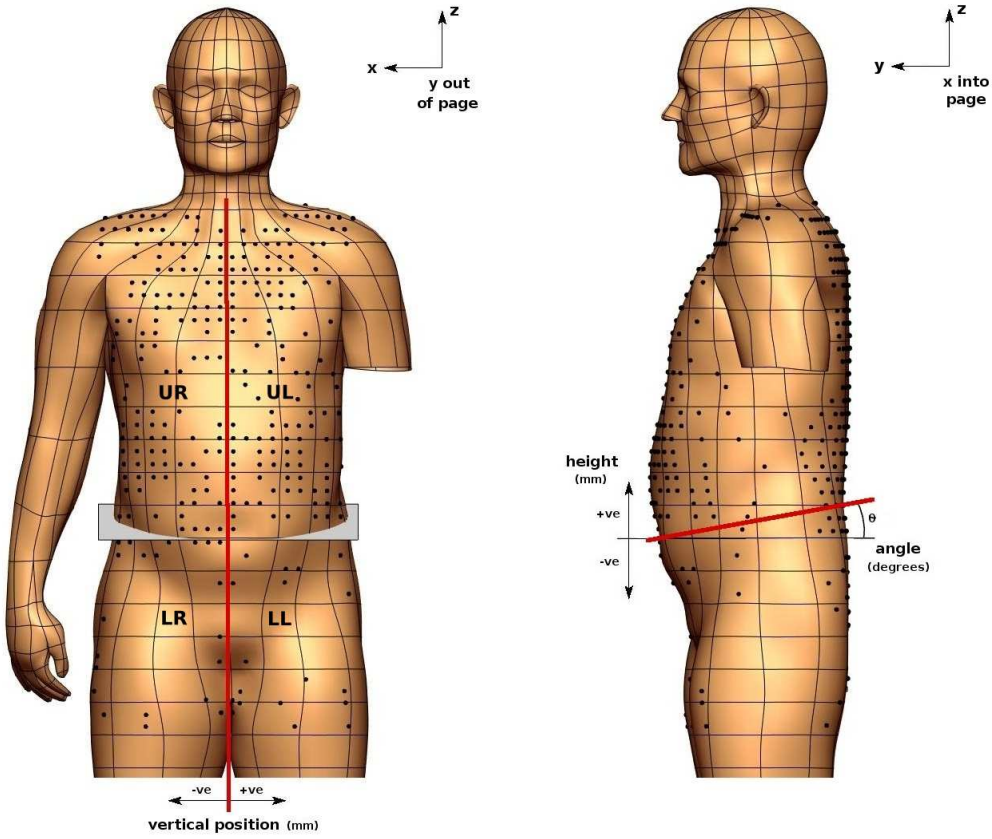

(a) (b)

Figure 6.1: Defining Sappey's lines on the skin model, (a) anterior and (b) left lateral views.

Both the vertical plane and midline plane were moved to investigate different positions for Sappey's lines. The position of the vertical plane was moved to the left and right of the true anatomical midline in the x-direction (as shown in Figure 6.1(a)), while the height of the midline plane was moved up and down relative to the umbilicus in the z-direction. In addition, the midline plane has been set at an angle θ similar to the way Sappey's transverse line curves upwards towards the back (see Figure 6.1(b)). Note that the angle θ has rotation about only the x-axis to ensure that the body would be divided symmetrically either side of Sappey's vertical line.

The location of each melanoma site has been determined relative to the position of Sappey's lines for a variety of different line positions. The x-coordinate value of each melanoma site relative to the x-coordinate of the vertical plane was used to determine whether it was on the left or right side. To calculate whether the melanoma site was above or below the midline plane a number of steps were required. Sappey's midline plane has been defined by specifying three points that lie in the plane. The first point is given by the coordinate of the umbilicus, denoted by $\mathbf{u}$ as shown in Equation 6.1. Two additional points in the plane have been determined by offsetting this umbilicus coordinate. The second coordinate $\mathbf{v}$ is calculated using the angle θ to offset the y- and z-coordinates (Equation 6.2), while the third coordinate $\mathbf{w}$ is given by offsetting the x-coordinate by an arbitrary value (Equation 6.3).

$$\mathbf{u} = \begin{pmatrix} x \\ y \\ z \end{pmatrix} \tag{6.1}$$

$$\mathbf{v} = \begin{pmatrix} x \\ y + cos(-\theta) \\ z + sin(-\theta) \end{pmatrix} \tag{6.2}$$

$$\mathbf{w} = \begin{pmatrix} x + \delta x \\ y \\ z \end{pmatrix} \tag{6.3}$$

Using these three coordinates, the normal vector to this plane (denoted by $\mathbf{n}$) can be found by:

$$\mathbf{n} = (\mathbf{v} - \mathbf{u}) \times (\mathbf{w} - \mathbf{u}) \tag{6.4}$$

to give the following equation for the midline plane:

$$\mathbf{n} \cdot \mathbf{u} = e \tag{6.5}$$

where e is a constant. To then determine the relative location of each melanoma site, the vector $\mathbf{n}$ has been normalised and then dot-producted with each melanoma coordinate $\mathbf{u}_m$, giving the equation of a parallel plane (shown schematically in Figure 6.2) which passes directly through each melanoma site:

$$\frac{\mathbf{n}}{\|\mathbf{n}\|} \cdot \mathbf{u}_m = e_m \tag{6.6}$$

The relative value of e in Equation 6.5 and e_m in Equation 6.6 defined whether the site was above or below Sappey's midline plane. Since the origin was located above the plane and $\mathbf{n}$ was always pointing towards the origin, when $e_m > e$ then the melanoma site was in one of the upper quadrants, whereas for $e_m < e$ the melanoma site was in one of the lower quadrants.

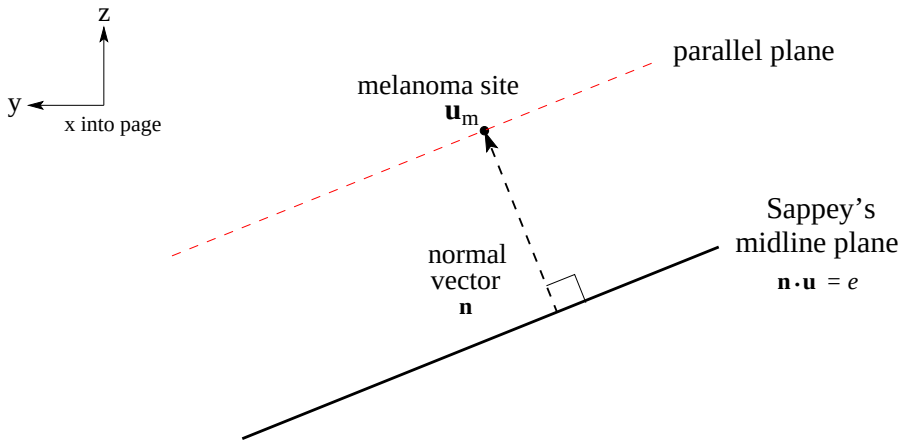

Figure 6.2: Calculating a plane parallel to Sappey's midline plane that passes through melanoma site $\mathbf{u}_m$, to determine its relative position.

Note that during this analysis, only melanoma sites with drainage to the axillary and groin node fields have been taken into consideration while patients without drainage to these node fields have been ignored. Additionally, only melanoma sites located on the torso have been considered since Sappey's lines applied to lymphatic drainage specifically of the trunk.

At each location of Sappey's vertical and midline plane, the number of cases draining from each of the four skin regions across Sappey's lines has been determined. Table 6.1 shows the tabular format required for this analysis. The rows represent the melanoma site skin region while the columns represent the draining node fields. The first row for example, is given for melanoma sites in the UR

REGION	NODE FIELDS				TOTAL
	Right Axilla	Left Axilla	Right Groin	Left Groin	
UR	o	x	x	x	
UL	x	o	x	x	
LR	x	x	o	x	
LL	x	x	x	o	

Table 6.1: Determining the number of cases from each torso region draining across Sappey's lines. x's indicate melanoma sites that cross Sappey's lines while o's indicate sites that do not.

skin region. Cases that drain to the right axilla are consistent with Sappey's assumptions, while cases that drain to the left axilla, right groin or left groin are inconsistent with Sappey's assumptions. Hence, entries in each of the cells on the diagonal obey Sappey's assumptions (indicated by an 'o') while the remainder do not (indicated by an 'x'). The last column records the total number of cases for each skin region draining across Sappey's lines. It is important to be aware that this value is not simply an addition of all values in the corresponding rows that cross Sappey's lines, since there are some cases which appear in multiple cells with drainage to more than one axillary or groin node field.

In addition to varying the position of Sappey's lines, a zone of unpredictable drainage defined either side of the lines has been investigated. As detailed in Section 1.4, Sugarbaker & McBride (1976) proposed that a strip of skin 2.5 cm either side of Sappey's lines had ambiguous drainage, while later investigators claimed that this zone was much larger. The zone of ambiguous drainage can now be quantified, by defining widths either side of Sappey's lines on the skin model (as shown in Figure 6.3). Melanoma sites located within this zone are considered to have unpredictable drainage and thereby are not considered to have crossed Sappey's lines. The vertical width of ambiguous drainage is denoted w_v while the horizontal width is denoted w_h.

6.3 Symmetry Testing

As implied but not fully confirmed by Sappey's lines, it has been previously assumed that lymphatic drainage of the skin is symmetric between the left and right sides of the body. However the literature does not contain a thorough quantitative analysis to confirm this assumption. Methods to test the hypothesis that a region of skin on one side of the body has the same drainage characteristics as the corresponding region of skin on the other side of the body are outlined in this section. This analysis has been used to justify reflecting LS data from one side of the body to the other, to provide a larger sample from which to draw conclusions about skin lymphatic drainage.

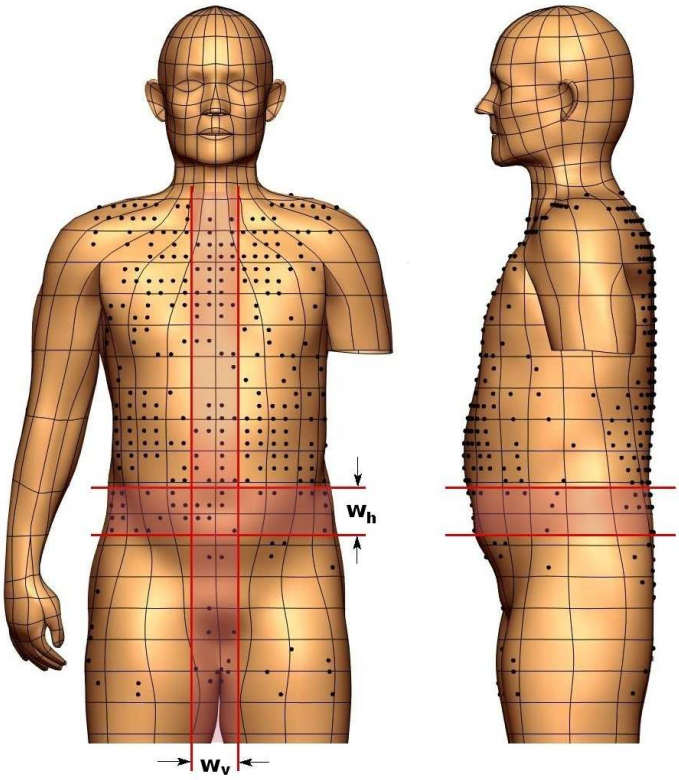

Figure 6.3: Defining a zone of ambiguous drainage either side of Sappey's lines. The vertical width is labelled w_v and the horizontal width is labelled w_h.

Statistical significance testing has been implemented for this purpose. Since there are numerous types of significance tests, a thorough understanding was first required of the LS data format to determine which would be the most suitable. Each patient case in the LS database contains information regarding one melanoma site on the skin, as well as corresponding SN fields. Some patients have only one draining node field, while other patients have multiple draining node fields. Figure 6.4 schematically demonstrates this for three different patient cases. The first case has only one draining node field, the left axilla, while the second and third cases both have lymphatic drainage to multiple node fields.

To test for statistical significance, most methods require that each trial has only one possible outcome. For the LS data this means that each patient case should only have one draining node field. Clearly this rule is not obeyed, since as previously mentioned there are often patients with multiple draining node fields. To avoid this problem, the LS data has been modified so that cases with multiple node fields have been separated into multiple data entries. Figure 6.5 schematically demonstrates this for the same three cases given in Figure 6.4, which have been separated into individual data entries for each draining node field. There are now six data entries instead of the original three.

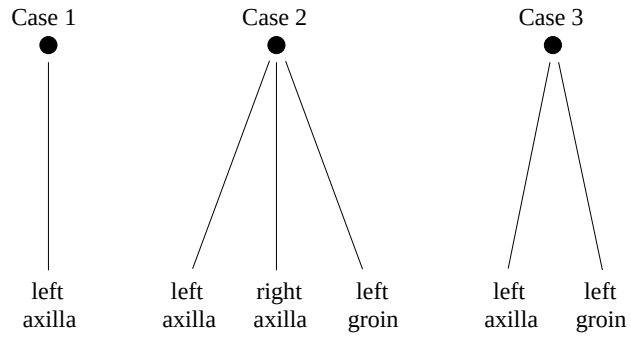

Figure 6.4: LS data format. Case 1 has drainage to one node field, meanwhile case 2 has drainage to three node fields, and case 3 has drainage to two node fields.

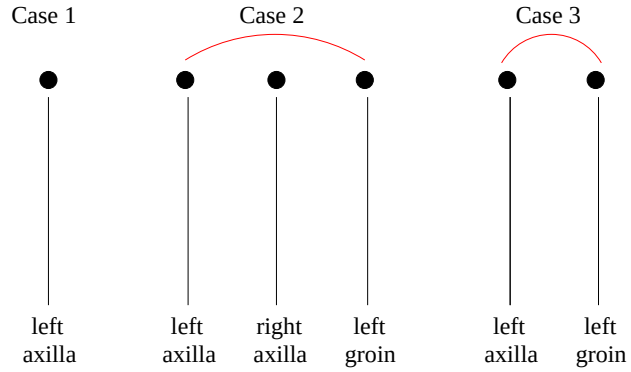

Figure 6.5: Modifying the LS data format to enable mutually exclusive outcomes. Cases with multiple draining node fields have been separated to give multiple data entries.

Unfortunately this modified data is no longer independent, which is an important data characteristic required for most significance tests. Independence means that the occurrence of one event makes it neither more or less likely that another event occurs. For the LS data, separating cases with multiple node fields into individual data entries does make a difference to the drainage probabilities. For example, a patient with two node fields will be separated into two individual data entries. If the first draining node field is the left axilla, then the likelihood that the second node field is also the left axilla will be zero. The first data entry has affected the probability values of the second.

A number of tests as described in the following were investigated to analyse this modified data, using the R statistical package[1]. Initially Chi-squared testing was considered, which can evaluate whether there are statistically significant differences between events occurring for two or more groups (Greenwood & Nikulin 1996). This was applied by analysing regions of skin on the corresponding left and right sides of the body, and testing the likelihood that the drainage properties of the two regions were functionally indistinguishable. Tables of counts (referred to as contingency tables) were generated, recording the node fields to which each region of skin drained. Two rows

[1] www.r-project.org/

were required, one each for the left and right sides of the body, while the columns corresponded to draining node fields.

Although chi-squared testing was theoretically feasible, it was discarded due to very low counts occurring in the tables. Generally, chi-squared testing requires 80% of all counts in the table to be larger than five. Since there are so many possible node fields, the number of columns was often large and contained values that were less than five. To increase these counts, node fields could have been aggregated together. However this approach would have required important spatial characteristics of the draining node fields to be homogenised, and thus this approach was discarded.

An alternate test more appropriate for low count values was then investigated, called Fisher's exact test (Fisher 1938). This test is designed to analyse categorical data, in particular when sample sizes are small, and can be used regardless of sample characteristics. Although the approach was feasible, it was too computationally intensive when there were numerous draining node fields and therefore it has not been used.

Instead, an approach based on generalised linear models (GLMs) has been implemented. GLMs are a generalisation of least squares regression, which models the relationship between a dependent variable (response variable) to one or more independent variables (explanatory variables, also called predictors). Using this approach, response variables are modelled as a function of the explanatory variables, by fitting parameters (constants and coefficients) that give the best fit to the data. Standard errors (SEs) for the coefficients are also calculated as part of the fitting process. These can be used to determine the probability that an explanatory variable has a 'true' coefficient value of zero, and is not needed in the model. Given a coefficient, the smaller its SE, the less likely its true coefficient value is zero and the more likely it is to be included in the model.

For the LS data, the likelihood of lymphatic drainage to a particular node field is largely influenced by the region of skin on which a melanoma site is located. Hence, a GLM can be fitted to the LS data by taking the melanoma skin sites as predictors (defined by the side of the body and skin element each melanoma site is located on), which relates to the probability of drainage to each node field (response variables). Using this model, it can be determined whether side is a significant variable in the model. If side is not significant then the data can be reflected, since the probability that drainage from a region of skin on one side of the body to a particular node field, is the same as the probability of drainage from the opposing region of skin to the corresponding opposite node field.

Fitting a GLM does not account for data dependency however, which is a characteristic of the modified LS data. It is possible to correct for this non-independence by using an extension to the standard GLM, called Generalised Estimator Equations (GEEs) (Hardin & Hilbe 2002). Multiple

measurements on the same case within a dataset tends to result in less variability, as the source of variability between subjects is removed. GEEs correct for this by inflating the SEs, making it more likely that the 'true' coefficient value for an explanatory variable is zero.

Although an implementation of GEEs exists in R, the current `gee` library of functions is unable to handle the quantity of data contained in the LS database. It may be possible to fit a GEE to the LS data with future versions of the `gee` library, but at present a GLM model has been used. Even though the GLM does not adjust for non-independence, it was still considered suitable for this application. Both methods will give the same parameter estimates, however the SEs of these values will differ. The SEs for the GLM model will be smaller than those given by the GEE approach. This is acceptable since it means that the decision about whether to reflect the data will be more conservative, since regions that are asymmetric using the GLM approach may be considered symmetric using GEEs.

Utilising this method requires assumptions to be made about the underlying probability distribution of the data. The LS data has been modelled by a multinomial distribution, using the 'multinom' function in the `nnet` library in R. A summary of the mathematics behind this distribution and the specific approach used is given in the following section.

6.3.1 Multinomial modelling approach

The multinomial distribution is essentially an extension of the binomial distribution where the response of a trial can take more than two values (Zelterman 2006). Within the multinomial model the number of trials is given by n_t, and each trial can be classified into one of k distinct and mutually exclusive categories. The probability that one of these trials is classified as belonging to one of the k categories is given by p_i where $(i = 1, ..., k)$ such that $p_i \geq 0$ and $\sum_{i=1}^{k} p_i = 1$.

Let the random variables Y_i indicate the number of times outcome i is observed over the n_t trials, such that $Y = (Y_1, ..., Y_k)$ which has a multinomial distribution with parameters n_t and p. The probability mass function of the multinomial distribution is given by:

$$P(Y_1 = y_1, ..., Y_k = y_k) = \frac{n_t!}{y_1! \cdots y_k!} p_1^{y_1} \cdots p_k^{y_k} \tag{6.7}$$

where $\mathbf{y} = (y_1, ..., y_k)$ is a vector such that $\sum_{i=1}^{k} y_i = n_t$. Fitting a multinomial model to a set of data as described in Faraway (2006), involves determining a way to link probability values p_i to a set of q predictors $(f_1, ..., f_q)$. For the LS data, as previously described, the melanoma skin sites are considered to be predictors, while the probability values indicate the likelihood that drainage

will occur to each node field. In order to link the probability values p_i to the predictors f_i a 'linear predictor' γ_i is constructed as follows:

$$\gamma_i = \beta_0 + \beta_1 f_1 + ... + \beta_k f_k \tag{6.8}$$

where β_i, $(i = 0, ..., k)$ are the unknown model parameters. A link function is then used to relate the probabilities p_i to the linear predictor, which is given by:

$$\gamma_i = f^T \beta_i = log \frac{p_i}{p_1}, \qquad i = 2, ..., k \tag{6.9}$$

The constraint $\sum_{i=1}^{k} p_i = 1$ must be obeyed, and it is convenient to use this to declare a baseline category (Faraway 2006). Therefore we set $p_1 = 1 - \sum_{i=2}^{k} p_i$ and have:

$$p_i = \frac{e^{\gamma_i}}{1 + \sum_{i=2}^{k} e^{\gamma_i}} \tag{6.10}$$

where $\gamma_1 = 0$. The parameters of this model can then be estimated using the maximum likelihood method. In brief, this method gives parameter values with the largest probability to the observed data, and is detailed in full in Faraway (2006).

Before fitting such a model to the LS data, the data required modification. This has been done by reflecting LS data located within a given skin region on the right side of the body to the corresponding left side of the body. An example of this reflection is shown schematically in Figure 6.6. This skin region shows two cases on the right side and one case on the corresponding left side. The melanoma site location and draining node fields of the two cases on the left side have been reflected to the right side, to give the reflected skin region.

Table 6.2 details the melanoma site location and draining node fields of each case, both original and reflected. The side of the body and skin element each case is located on define the melanoma site location, while each draining node field has been separated into individual data entries for each case. Reflecting case 1 for example, which is located on element 2, has been reflected to element 4 on the right side. Also, since there were two draining node fields, there are two data entries for this case. One node field was the right axilla which has been reflected to the left axilla, while the second node field was the right groin which has been reflected to the left groin. After reflection, by definition each node field located on the left side of the body described ipsilateral drainage. Conversely, each node field on the right side of the body defined contralateral drainage.

Figure 6.7 summarises the approach taken to determine whether the LS data, and hence, lymphatic

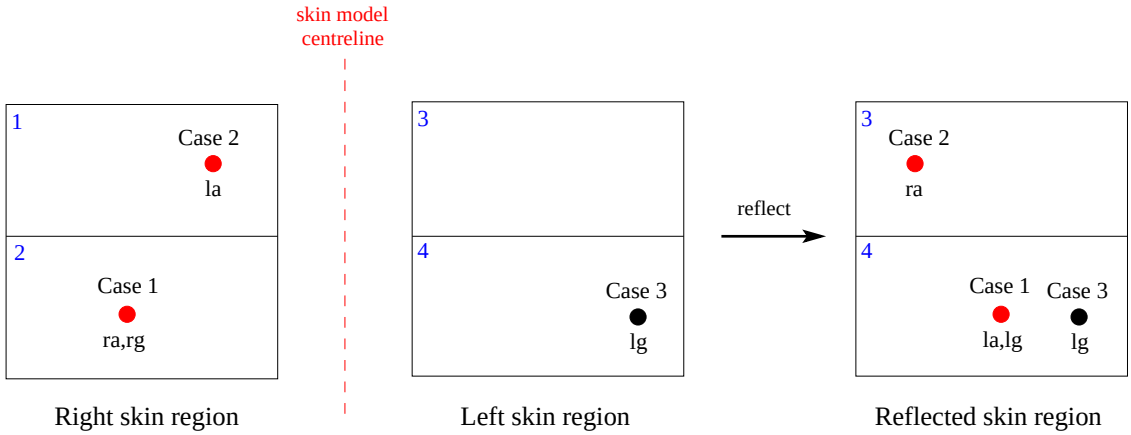

Figure 6.6: Example skin region reflected from the right side onto the left, where two cases are located on the right region and one case is located on the left. Element numbers are given in blue, and draining node fields from each case are labelled according to their codes in Appendix A.

Case	Side	Element		Node Fields	
		Original	Reflected	Original	Reflected
1	R	2	4	Right axilla	Left axilla
1	R	2	4	Right groin	Left groin
2	R	1	3	Left axilla	Right axilla
3	L	4	4	Left groin	Left groin

Table 6.2: Details of each case on the example skin region that has been reflected.

drainage in a given skin region is symmetric. The commands used to carry out this analysis are given in Appendix G. After data reflection, a multinomial model has been fitted to the data contained within a specified skin region. Side, reflected skin element, and the interaction between the side and reflected skin element have been set as predictor variables, while the reflected draining node fields were set as response variables.

After fitting this multinomial model, the Akaike Information Criterion (AIC) has been used via the 'step' function in the `stat` library to determine the most important predictor variables. The AIC criterion balances the goodness of the fit of the multinomial model with its complexity, and is defined by:

$$AIC = n_t \log(\hat{\sigma}^2) + 2K \tag{6.11}$$

where $\hat{\sigma}^2$ is the estimate of the error variance and K is the number of model parameters. The goodness of fit is defined by the error variance estimate, giving a measure of the difference between

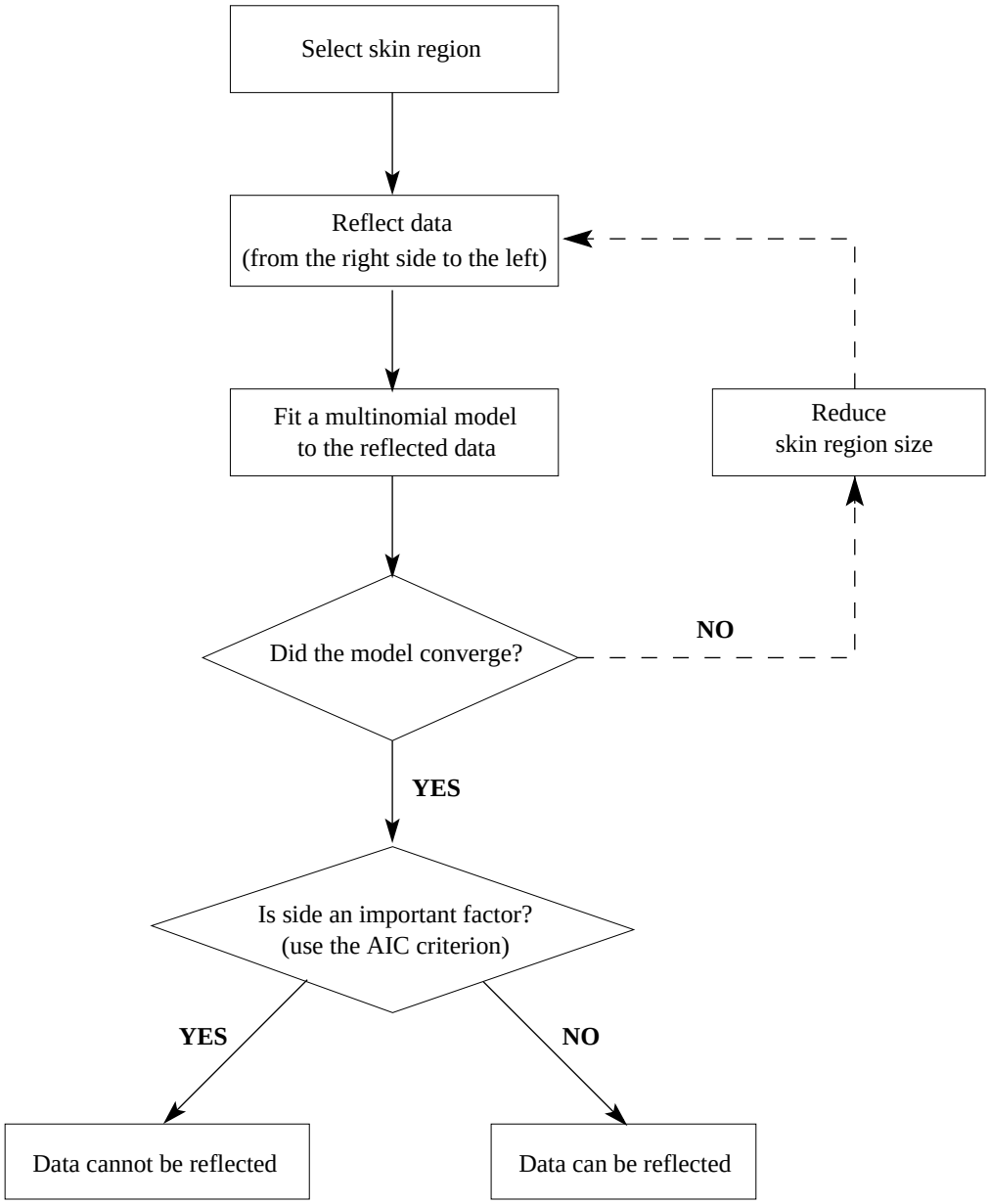

Figure 6.7: Decision flowchart used to determine whether LS data can be reflected.

the fitted model and the data, while the number of parameters gives a measure of the model's complexity. The step function tries to choose explanatory variables to minimise the AIC, where a lower AIC value indicates a better model fit. If side is not a significant factor in the final model chosen by the step function, then it is considered appropriate to reflect the data. For some cases, the multinomial model may not converge since there is too much data, and the skin region size will need to be reduced and the model fitted again.

6.3.2 Reflection method

Investigation was conducted to determine the most appropriate method to reflect symmetrical data. Three different methods for reflection were considered, including: (1) a strict reflection in the x-plane, (2) reflecting according to the SMU's original body map grid unit coordinates, and (3) reflection via corresponding element numbers and local ξ coordinates.

The first method which involved conducting a strict reflection in the x-plane was not possible, since the skin model is not completely symmetric. This is due to the VH dataset that has been used to construct the skin model being asymmetric (detailed in Section 2.2). The upper limbs, legs and feet, head and neck were symmetric since one side of the body was modelled and then reflected to the other side, however skin of the torso and the thigh was modelled in its entirety such that it is asymmetric (see Section 2.5). Carrying out a strict reflection in the x-plane will not, therefore, ensure that each reflected melanoma site is located on the surface of the skin model.

In addition, the second proposed method also contains difficulties with the body map outlines drawn on the 2D body map shown in Figure 1.14. These outlines are not exactly symmetric, particularly for the upper limbs. Hence the initial mapping of melanoma sites (carried out in Chapter 3) has meant their location is not the same on both sides of the body.

The third proposed method was considered the most appropriate, which involved reflection via corresponding element numbers and ξ coordinates. During reflection analysis, each melanoma site on the right side of the body has been reflected to the corresponding element on the left side of the body. By reflecting according to element numbers, consistency is maintained between the reflection analysis methodology and the reflected dataset.

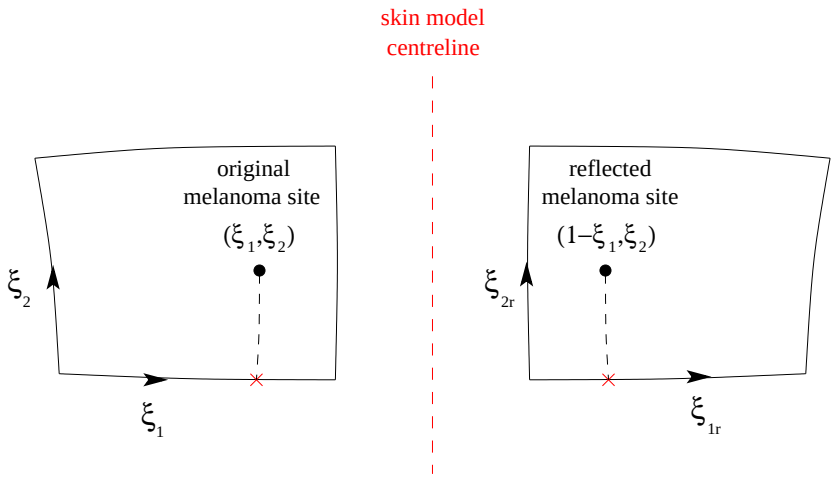

Figure 6.8: Reflecting melanoma sites using corresponding elements and ξ coordinates.

Figure 6.8 schematically demonstrates the reflection of a melanoma site from one side of the body to the other. The original melanoma site is shown located on an element with local coordinates (ξ_1, ξ_2). During reflection, corresponding local coordinates (ξ_{1r}, ξ_{2r}) are determined on the opposing element. Since the skin model has consistent ξ_1-directions circumferentially around the mesh, this coordinate required inverting such that $\xi_{1r} = 1 - \xi_1$, while local ξ_2 coordinates remained the same, so that $\xi_{2r} = \xi_2$.

6.4 Cluster Analysis

Cluster analysis is a numerical method that can be used to group data with similar properties into respective categories. The advantage of this technique is that it does not require any a priori hypotheses, and can be used to discover structures in data without providing an explanation as to why they exist (Everitt et al. 2001). In this thesis, clustering has been used to group regions of skin that have similar drainage behaviour without regard to previous knowledge about skin lymphatic drainage or Sappey's lines. This will allow predictions of lymphatic drainage to move beyond Sappey's lines which are based on anatomy, towards a more data driven approach, providing more accurate and clinically defined regions of drainage.

Classification is fundamental to most branches of science, and is used widely in both biology and medicine. Biologists for example, need to classify animals into various species according to particular characteristics, while in medicine clustering can be used to determine the most appropriate form of treatment depending on the symptoms presented. For example, a study by Wastell & Gray (1987) involved conducting spatial cluster analysis on data from patients with temporomandibular pain dysfunction syndrome. This enabled the development of an objective typology for classifying facial pain in terms of its spatial distribution, which was then proposed as a means for defining more directed treatment plans.

There are several different approaches for cluster analysis, depending on the type of data and the kinds of clusters desired. The approach that has been used here is based on work by O'Sullivan et al. (1998), who implemented a clustering algorithm developed by Vössner & Braunstingl (1996), to provide additional information during software testing of embedded systems. Their cluster analysis enabled optimisation of programme code and helped aid a reliable termination criterion. The following section details the mathematics behind this approach as it has been applied to the LS data.

6.4.1 Theory

Let the number of samples for classification be n_c, and the number of characteristics used to describe these samples be m. For cluster analysis these samples should be organised into the following structure shown in Table 6.3. In this table the rows correspond with each sample, while the columns correspond with the characteristics that define the samples. X_{ij} records the number of objects in sample i that can be classified by the characteristic j.

	Characteristics					
Samples	X_1,	X_2,	...	X_j,	...	X_m
1	X_{11},	X_{12},	...	X_{1j},	...	X_{1m}
2	X_{21},	X_{22},	...	X_{2j},	...	X_{2m}
...			.....			
i	X_{i1},	X_{i2},	...	X_{ij},	...	X_{im}
...			.....			
n_c	X_{n_c1},	X_{n_c2},	...	X_{n_cj},	...	X_{n_cm}

Table 6.3: Data structure for cluster analysis.

By applying this structure to the LS data, regions of skin on the skin model are defined as the samples, while the node fields that drain each region of skin are defined as the characteristics. Most skin regions will contain LS data from a number of melanoma patients, each with corresponding draining node fields from a possible 43 node fields (as listed in Appendix A). For example, say the first sample is a skin region on the left leg containing six melanoma sites each with drainage to the left groin, while two cases also have drainage to the left popliteal node field. If characteristic X_1 indicates drainage to the left groin, X_2 drainage to the left popliteal node field, and the remaining characteristics comprise the remaining node fields, then $X_{11} = 6$, $X_{12} = 2$ and $X_{1j} = 0$ for $j = 3..43$.

To simplify the data for cluster analysis, each X_{ij} value has been normalised to the range $0 \leq X_{ij} \leq 1$ for all i, j. For our example skin region on the leg, each parameter is divided by the total number of melanoma sites within that region of skin. In normalised parameter space this will give $X_{11} = 1$, $X_{12} = \frac{1}{3}$ and $X_{1j} = 0$ for $j = 3..43$. Each X_{ij} value now indicates the probability that skin region i will show lymphatic drainage to the jth node field.

In order to cluster samples that are most closely related together, a method for determining the distance between them is required. Most often this measure is taken as the Euclidean distance, where for any two samples i and k, this is defined by:

$$d_{ik} = \sqrt{(X_{i1} - X_{k1})^2 + (X_{i2} - X_{k2})^2 + ... + (X_{im} - X_{km})^2}$$

This gives a symmetrical distance matrix ($n_c \times n_c$) where $d_{ik} = d_{ki}$ for $i, k = 1, ..., n_c$ as shown in Table 6.4. Clusters can now be determined using this distance matrix. The distances of all samples are compared with a threshold value d_{check} (also called the 'check distance'), and if the distance between the two samples is smaller than d_{check} then they are assigned to the same cluster.

Point	1	2	3	4	...	n_c-1	n_c
1	0	d_{12}	d_{13}	d_{14}	...	d_{1n_c-1}	d_{1n_c}
2		0	d_{23}	d_{24}	...	d_{2n_c-1}	d_{2n_c}
3			0	d_{34}	...	d_{3n_c-1}	d_{3n_c}
4				0	...	d_{4n_c-1}	d_{4n_c}
...					0	$d_{...n_c-1}$	$d_{...n_c}$
n_c-1						0	$d_{n_c-1n_c}$
n_c							0

Table 6.4: Symmetrical distance matrix.

The clustering algorithm can be summarised by the following pseudocode, where a cluster is defined to consist of at least two samples. Given any two samples, i and j, if the distance between them $d_{ij} < d_{check}$ then they should be members of the same cluster. There are three cases:

1. If they do not belong to a cluster yet, they form a new one.
2. If only one of the two samples already belongs to a cluster, the other one joins this cluster.
3. If both samples are members of different clusters, these clusters are combined to form a single cluster.

This algorithm is schematically depicted in Figure 6.9. The distance between individuals 1 and 2, d_{12}, is less than the check distance so they form a cluster together, while the distance between individuals 3 and 4, d_{34}, is shown to be larger than the check distance and therefore they do not form a cluster.

Initially the check distance is set as the hypercube's space diagonal d_0, where exactly one cluster is found. This check distance is then iteratively reduced by discrete factors and the clustering algorithm performed again. The clusters generated are highly dependent on the check distance value. By performing cluster analysis for a number of check distances, a cluster diagram can be drawn, as shown in Figure 6.10.

This diagram shows the results of each cluster analysis for decreasing check distance values (i.e. d/1, d/2, d/3,...). Each circle represents a cluster while the branches indicate how clusters split with decreasing check distance. Initially all objects are within the same cluster, and then as the check distance decreases smaller clusters are formed. It is possible for clusters to drop out if the

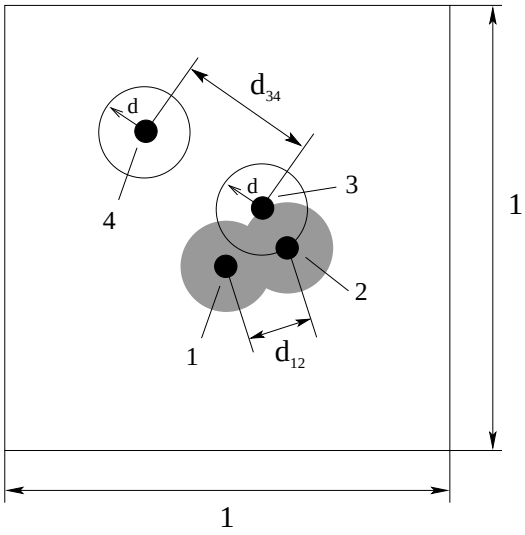

Figure 6.9: Detection of clusters in the unit square. Modified from Vössner et al. (1999).

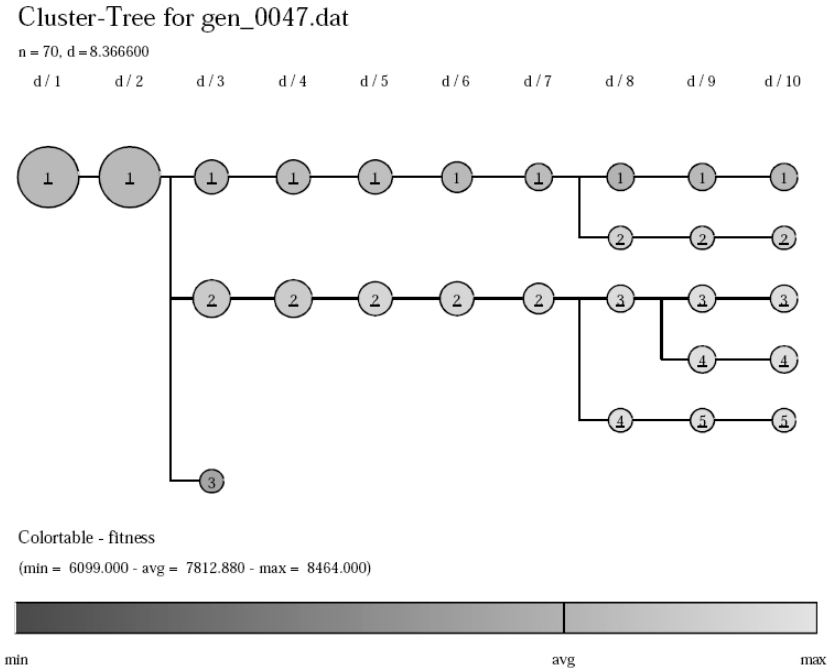

Figure 6.10: Example cluster tree diagram. Reproduced from O'Sullivan et al. (1998).

check distance becomes too small, for example the individuals in cluster 3 at d/3 disappear for following iterations. The number of clusters, their sizes, history of origin and the average fitness of its individuals can be seen on this tree diagram. The cluster number is shown inside the circles, and the size of each circle is proportional to the number of individuals within that cluster. The shade of the circle indicates the average fitness of its individuals. For the LS data, fitness is calculated

by finding the standard deviation of points within each cluster. The smaller the standard deviation, the better the fitness of the individuals within that cluster.

6.5 Confidence intervals

The LS data used in this thesis constitutes the world's largest database of lymphatic drainage patterns in patients with melanoma, however it is still only a sample of the entire human population. It is important therefore that we do not over-interpret observed patterns of skin lymphatic drainage, since any statistics generated will always contain a level of uncertainty. A measure of this uncertainty is required to adequately determine how certain we can be that our sample values are indicative of the population they were sampled from and thereby can be used as an accurate measure for predicting melanoma spread. This will provide quantitative measures for the conclusions reached in this thesis, and will also motivate the need for more LS data to be collected in future.

Various statistical methods exist for determining measures of uncertainty for sample statistics. A number of these methods require knowledge about the underlying probability distribution of the data. For example, whether it takes the form of a poisson distribution, binomial distribution or a normal distribution. For some datasets the underlying probability distribution will not be known, or cannot be assumed, and therefore alternative methods are required. Non-parametric bootstrapping is one such method relevant for these datasets, and has been implemented in this thesis.

The bootstrap method was initially introduced by Efron (1979) as a simulation method for calculating certain kinds of statistical inference values, including confidence intervals. It is only a recently developed and applied technique since it requires intensive computer power that was not previously available. The central idea is that making conclusions about the characteristics of a population strictly from the sample available may be better than making potentially unrealistic assumptions about that population (Mooney & Duval 1993).

Bootstrapping involves resampling a dataset multiple times, with replacement, to generate an empirical estimate of the entire sampling distribution of a statistic. The following describes the non-parametric bootstrapping method as outlined by Efron & Tibshirani (1993) which has been used to calculate confidence intervals in this thesis.

Let $\mathbf{x}$ represent a vector of observations, so that $\mathbf{x} = (x_1, x_2, ..., x_n)$ and n represents the number of observations. A particular statistic of interest calculated from these observations is denoted by $s(\mathbf{x})$, and could represent for example, the sample mean. For our LS data this could represent the percentage likelihood that a region of skin will drain to a particular node field.

From the sample $\mathbf{x}$, a 'bootstrap sample' (denoted by $\mathbf{x}^*$) is obtained by randomly drawing n items, with replacement, from the initial sample. For example, if the initial sample had $n = 5$ entries, a bootstrap sample could take the form $\mathbf{x}^* = (x_3, x_1, x_2, x_3, x_4)$. This process is carried out B times to generate multiple bootstrap samples $\mathbf{x}^{*\mathbf{1}}, \mathbf{x}^{*\mathbf{2}}, ..., \mathbf{x}^{*\mathbf{B}}$ as shown in Figure 6.11. From each bootstrap sample, a corresponding sample statistic $s(\mathbf{x}^*)$ is generated, which in this case is the mean of the bootstrap sample. From these bootstrap sample means, a confidence interval can be determined. If B is equal to 1000, then this is found by ordering the sample means and taking the 25th and 975th values, giving a 95% confidence interval.

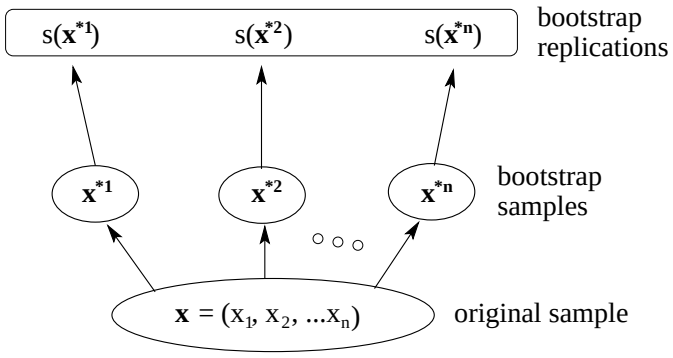

Figure 6.11: Schematic of the bootstrapping process to estimate confidence intervals for the sample mean s(**x**). Modified from Efron & Tibshirani (1993).

Confidence intervals have been determined for our mapped LS data using the above method. Initial samples of size n have been taken as all the melanoma sites located within a predefined region of skin. From this skin region point estimates were calculated to give the probability that lymphatic drainage from that skin region would occur to a specified node field. For example, a skin element which contains data from 21 patient cases may have 15 cases which drained to the left axilla (as demonstrated for a posterior torso element in Figure 5.8). This initial sample gives the point estimate that 71.4% of all patients with a melanoma site within this region of skin will have lymphatic drainage to the left axillary node field.

To determine confidence intervals surrounding this and other point estimates, a bootstrap sample has been randomly selected from the initial sample, with replacement, 1000 times. For each bootstrap sample a corresponding point estimate was calculated giving the likelihood that lymphatic drainage from that area of skin will occur to a specified node field. Hence for our skin element with a sample size of 21 cases, the first bootstrap sample could have 12 cases that drain to the left axilla giving a bootstrap point estimate of 57.1%. Once 1000 bootstrap samples had been generated, they were ordered and the 25th and 975th values chosen to give the 95% confidence interval.

It is important to note that the bootstrap is not appropriate when sample sizes are small. It is generally regarded that the method becomes unreliable for sample sizes that are less than 10 (Chernick 1999). Bootstrap samples may underestimate the true variability when the number of available cases is very small and it is also a concern that any spurious fine structure contained in the original data that is not present in the population may be reproduced in the simulated data.

6.6 Summary

Methods for statistically analysing lymphatic drainage of the skin on the mapped model have been outlined in this chapter. Methodology for testing the accuracy of Sappey's lines has been described, including testing the accuracy of more recent clinical guidelines based on Sappey's work. A statistical significance test was developed to determine whether skin lymphatic drainage is likely to be symmetric. A cluster analysis was outlined as a way to group regions of skin that have similar patterns of lymphatic drainage, allowing for skin regions to be generated regardless of previous knowledge about lymphatic drainage or Sappey's lines. Additionally, the non-parametric bootstrap has been proposed as a method to calculate confidence intervals, allowing for certainty measures to be calculated. Results of this analysis are given in the following chapter.

Chapter 7

Statistical Analysis of Mapped Lymphoscintigraphy Data

This chapter presents results of a detailed statistical analysis that has been conducted on the mapped skin model, employing the methods outlined in the previous chapter. The accuracy of Sappey's lines is investigated, and an optimal position for these lines is determined. The model is then tested for symmetry, to quantify whether lymphatic drainage is likely to be the same on both sides of the body. Regions of skin shown to be statistically symmetric are reflected, thereby increasing the LS dataset. Cluster analysis is used to identify regions of skin on the model that display similar patterns of lymphatic drainage, while appropriate confidence intervals have been calculated to give measures of significance for drainage probabilities from each cluster.

7.1 Analysing Sappey's Lines

As outlined in Chapter 5, there are a significant number of individual LS cases which do not conform to the drainage patterns defined by Sappey's lines. In this context, Sappey's lines have been quantitatively investigated to determine both their accuracy, and whether there is an optimal position that will allow for minimum cross-over drainage (cross-over drainage has been defined in Section 6.2 as a melanoma site 'located on the trunk, which does not drain to its predicted node field but instead 'crosses' over Sappey's lines to drain to other axillary or groin node fields'). The investigative methods used were given previously in Section 6.2, and the positions of Sappey's lines have been defined by planes on the skin model as shown in Figure 6.1.

7.1.1 Results

Initially the position of Sappey's vertical line as shown in Figure 6.1(a) was analysed to determine the number of cases with cross-over lymphatic drainage. Figure 7.1 shows a graph displaying the number of cases crossing Sappey's vertical line for differing positions. The vertical position has been moved in increments of 20 mm to correspond with the melanoma site discretisation defined on the SMU's body maps (shown in Section 1.6.1), where each grid unit defined an area of skin approximately 20 mm^2.

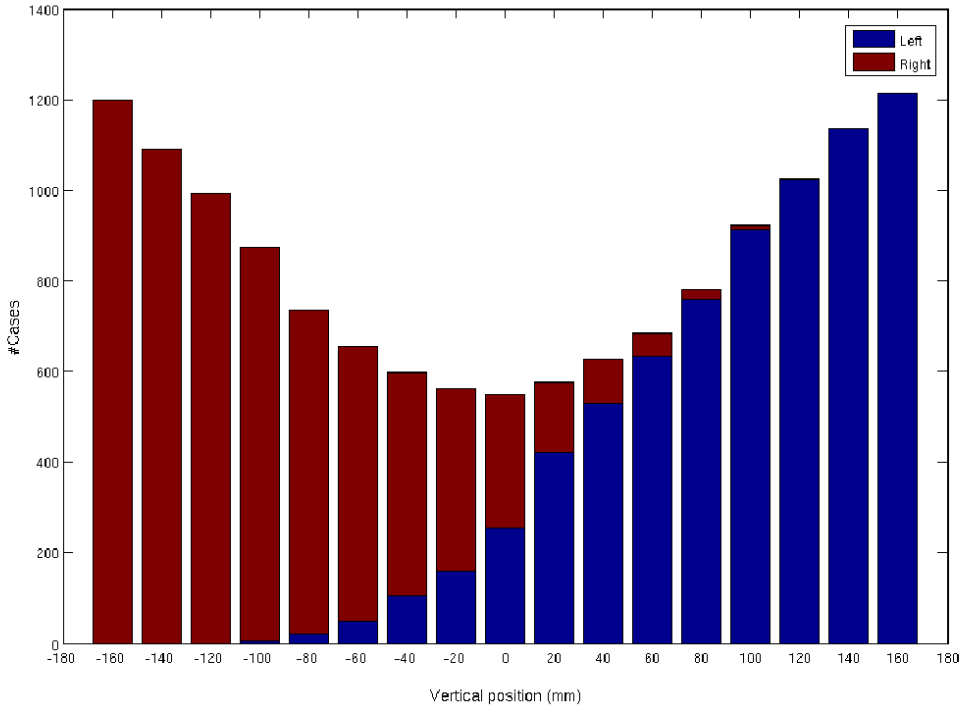

Figure 7.1: The number of cases crossing Sappey's vertical line for different line positions.

This graph shows that as the position of Sappey's vertical line moves away from the anatomical centre of the body, the number of cases draining across it increases. As the line moves further towards the right side of the body (i.e. in the negative direction) the number of cases to the left of this line with drainage to either the right axilla or groin increases. Similarly, as the vertical line position is moved towards the left side of the body (i.e. in the positive direction), the number of cases draining from the right side of this line to either the left axilla or groin increases.

Thus the optimum position for Sappey's vertical line is at the anatomical midline of the body, which corresponds with Sappey's original line. However, although this is the optimal position, there are still 549 cases that cross over it, equating to 10.5% of all melanoma sites in the LS database.

After determining the optimal vertical line position at the anatomical centre of the body, this line has been fixed while the position of Sappey's midline plane (shown in Figure 6.1(b)) has been investigated. Both the height and angle of the midline plane have been varied and the number of cases crossing over either of Sappey's lines calculated, as per Table 6.1.

Figure 7.2 presents graphs demonstrating the number of cases draining across Sappey's lines for height values of the midline plane ranging from -100 mm to 100 mm (as defined relative to the skin model in Figure 6.1(b)), and angle θ ranging from -20° to 20°. Graphs for each of the four skin quadrants, corresponding to those labelled in Figure 6.1(a), are shown.

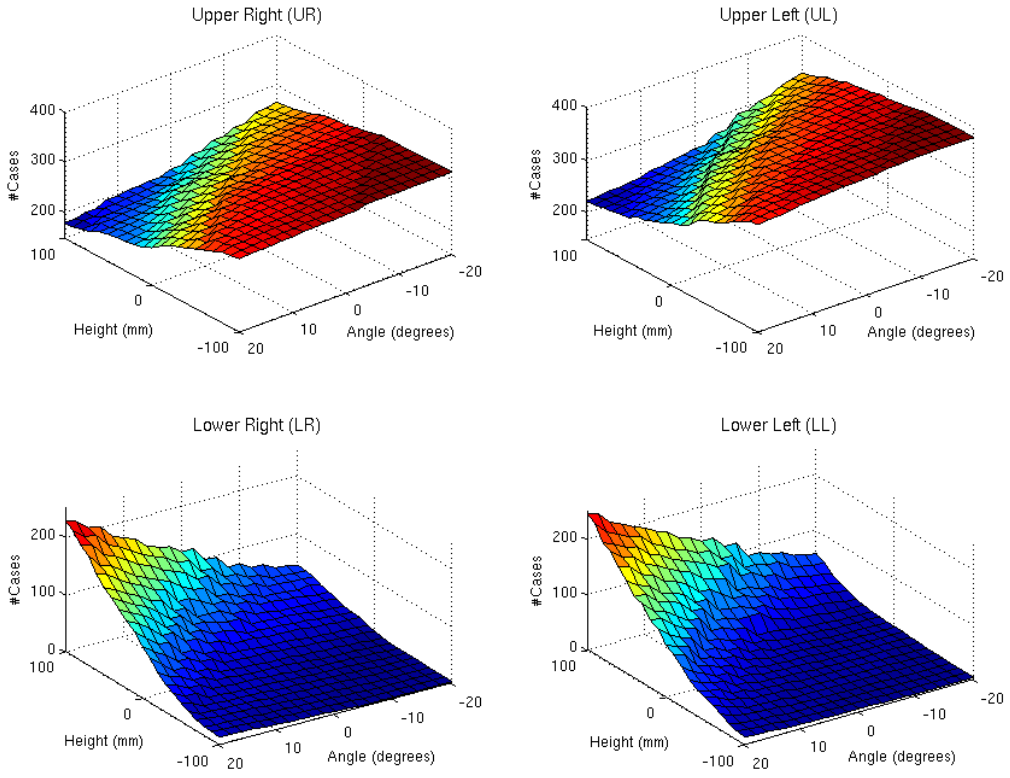

Figure 7.2: The number of cases crossing Sappey's lines for each skin region for various height and angle values of the midline plane.

It can be seen that as the height and angle of Sappey's midline plane decreases the number of cases crossing over from the upper quadrants (UR and UL) increases, while the number of cases crossing from the lower quadrants (LR and LL) decreases. This means that as the midline plane moves upwards towards the axillae there will be more cases in the lower quadrants which drain up towards the axilla and thereby cross Sappey's lines, and less cases in the upper quadrants that cross over to drain downwards to the groin.

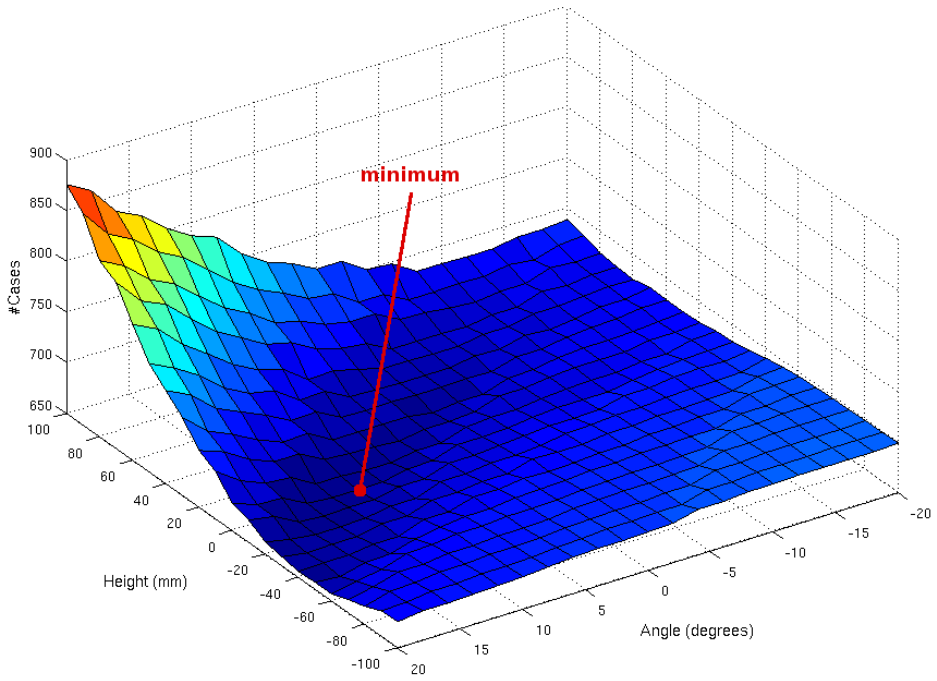

Figure 7.3: The total number of cases crossing Sappey's lines for various height and angle values of Sappey's midline plane.

Combining all cases that cross Sappey's lines from each quadrant gives the resultant graph shown in Figure 7.3. The optimal position of Sappey's midline plane can now be ascertained, as the height and angle combination which gives the minimal number of cases with cross-over drainage. This occurs at height 0 mm and an angle of 10°. At this point, 652 cases cross over Sappey's lines, equivalent to 12.5% of all melanoma sites in the LS database.

Figures 7.4(a) and 7.4(b) show the optimal position calculated for both the vertical and transverse lines defined on the skin model as well as the melanoma sites that drain across them. It can be seen that Sappey's midline plane passes through the umbilicus and is also curved upwards towards the back, which is consistent with Sappey's original lines drawn around the waist.

According to Sappey, the transverse line should be at the level of the second lumbar vertebra (L2) posteriorly. To accurately investigate this line's positioning relative to the vertebrae, an FE model of the vertebral bones created previously has been embedded within the skin model and referenced to VH images as shown in Figures 7.4(c) and 7.4(d). The L2 vertebra is highlighted in red, which is clearly higher than the level of Sappey's midline plane. The posterior position of this line is closer to the level of the third lumbar vertebra (L3) and fourth lumbar vertebra (L4).

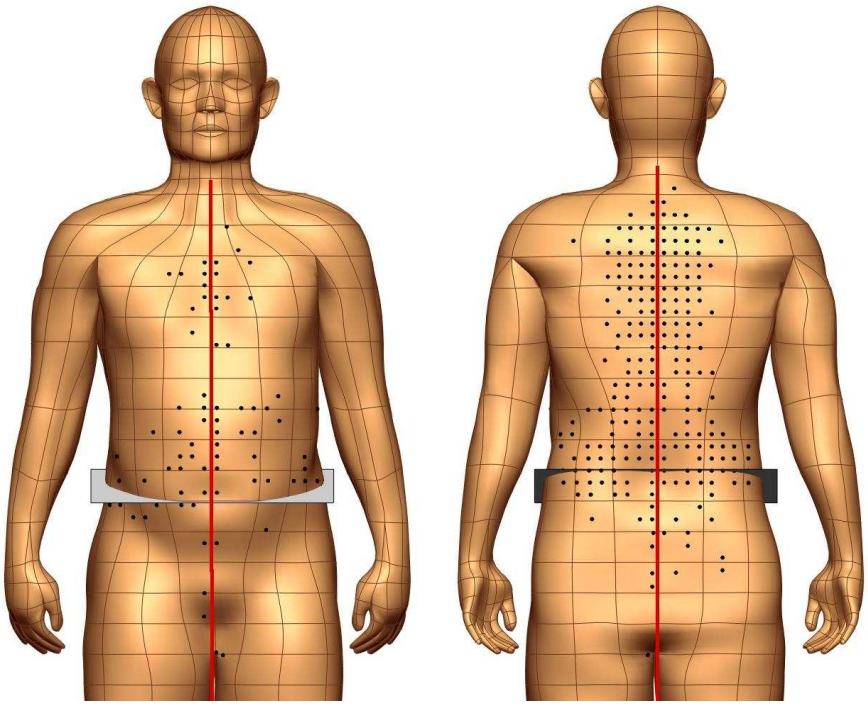

(a) Anterior (b) Posterior

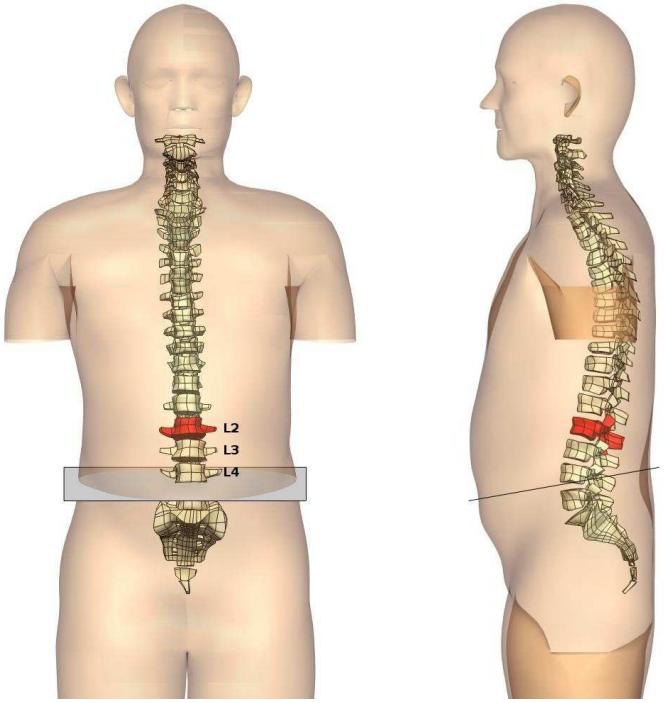

(c) Anterior (d) Lateral

Figure 7.4: The optimal position for Sappey's lines (a,b) shown with cases crossing these lines plotted on the model, and (c,d) shown relative to the vertebral bones.

Further analysis has been carried out to test the number of cases crossing Sappey's lines after including an area of ambiguous drainage either side of the lines, as proposed by Sugarbaker & McBride (1976) and Norman et al. (1991) (reviewed in Section 1.4). The definition of an ambiguous drainage zone is shown schematically on the skin model in Figure 6.3. As previously mentioned, the melanoma sites on the skin model are discrete in nature, covering approximately 20 mm^2 of skin. Therefore the width of ambiguous drainage for Sappey's lines (denoted by w_v and w_h) have been increased by 40 mm increments during investigation.

The graph in Figure 7.5 shows the number of cases crossing Sappey's lines for different widths. Widths w_v and w_h have been kept equal at each increment, and the height of Sappey's midline plane was held at 0 mm. For the purpose of comparison, two angles of the midline plane have been investigated. Initially the plane with an angle of 0° was investigated (shown in blue), and then the optimal angle of 10° was analysed (shown in red). As expected, for both angles, the number of cases crossing Sappey's lines decreases as the width of the ambiguous drainage zone increases. Additionally, it can be seen that the number of cases crossing Sappey's lines is reduced when the optimal angle is introduced, for all width values.

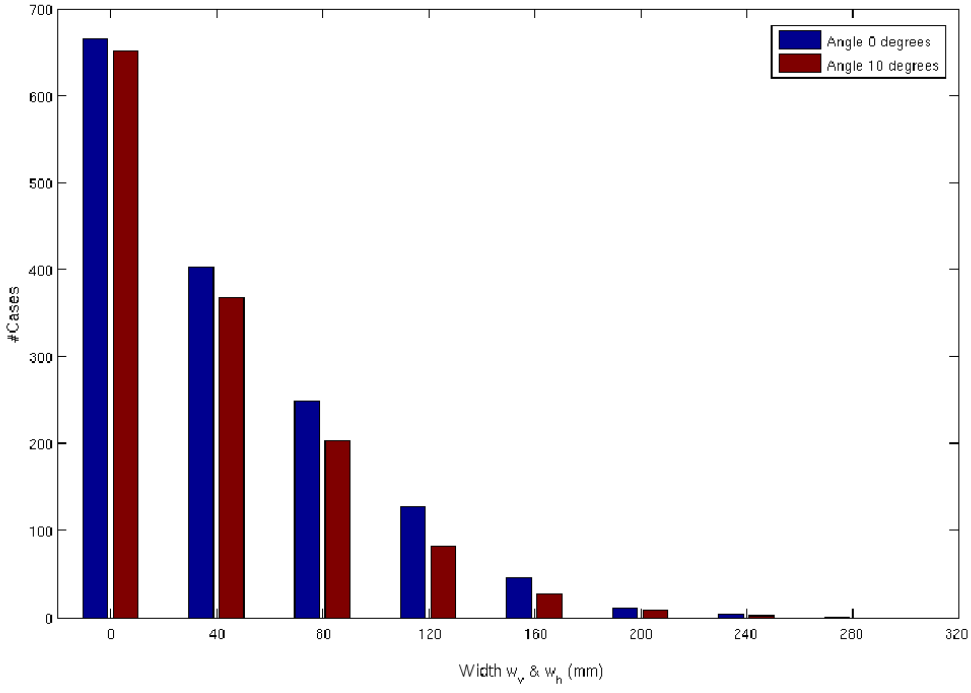

Figure 7.5: The number of cases crossing Sappey's lines including a zone of ambiguous drainage.

However, at the optimum angle, it is not until the width extends to 280 mm that all cases with cross-over lymphatic drainage are located within the ambiguous zone. This corresponds to 140 mm either side of Sappey's lines and is shown schematically on the skin model in Figure 7.6.

Meanwhile, when the angle is kept at 0°, the ambiguous drainage zone extends slightly further to a width of 320 mm.

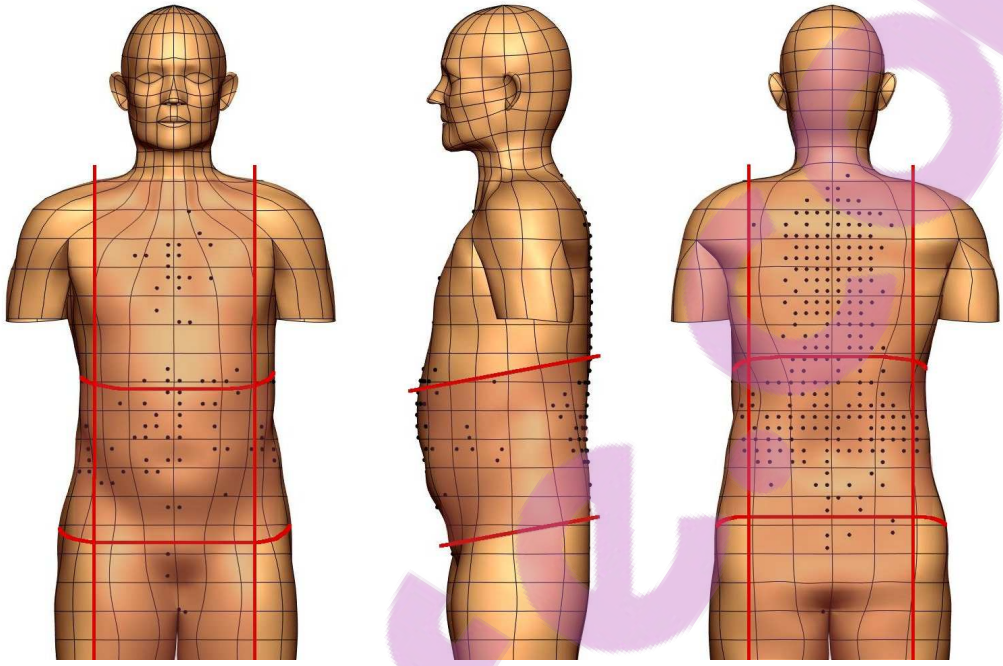

(a) Anterior (b) Left (c) Posterior

Figure 7.6: A zone of ambiguous drainage defined 140 mm either side of Sappey's lines.

The zone of ambiguous drainage in Figure 7.6 almost covers the entire torso region. This area is considerably larger than Sugarbaker and McBride's (1976) zones shown in Figure 1.8 which were 25 mm either side of Sappey's original lines. Additionally, this area is also slightly larger than Norman et al.'s (1991) zone of ambiguous drainage shown in Figure 1.9. This confirms the inaccuracy of Sappey's lines to adequately define lymphatic drainage of the trunk where almost the entire torso region shows possible drainage to unpredicted node fields. This is consistent with the axillary and groin heat maps given in Figure 5.1 and Figure 5.2, as well as Figure 5.6 which shows that significant regions on the torso often drain to multiple node fields.

7.2 Symmetry Testing

Statistical testing has been conducted to determine whether lymphatic drainage of the skin is likely to be the same on both sides of the body, using the methods outlined in Section 6.3. This has allowed the assumption that lymphatic drainage is symmetric to be quantitatively assessed. It also

provides justification for reflecting LS data from one side of the body to the other, with the purpose of increasing the LS dataset. This increased dataset would allow for improved statistical accuracy during subsequent data visualisation and analyses.

To carry out symmetry testing the torso, upper and lower limbs, hands and feet, head and neck have each been separated into regions. Note that LS data from patients who had previous surgery was not included. As mentioned in Section 1.4, patients with previous surgery could have an altered lymphatic drainage pattern that would not be indicative of a normal population. Also, interval nodes have not been included during testing since (as defined in Table 1.5), they do not have a specific anatomical location in the body. The location of melanoma sites that drained to interval nodes which have been removed from the analysis can be seen in Figure B.20.

The multinomial model approach used during symmetry testing (outlined in Section 6.3) required that each case of melanoma was separated into individual data entries for each draining node field. During fitting, the model has been determined with respect to the number of data entries according to the draining node fields, rather than the number of melanoma cases.

Discretisation of the skin into separate skin regions for testing has been carried out by considering: (1) the anatomy of the skin and the lymphatic system, (2) skin regions as defined in previous studies and (3) also ensuring that each skin region contained a sufficient amount of data to be statistically conclusive. Upon investigation of the literature, there was no clearly defined rule to determine the minimum sample size for multinomial model fitting. Therefore the minimum sample size for this analysis was arbitrarily set to 20 melanoma sites. It was important to ensure that enough data was available in each skin region, however there were also advantages for using small sized regions to increase the spatial resolution, allowing for a more refined analysis. The following sections detail the results for each region of skin.

7.2.1 Torso

Skin of the torso contains a large proportion of the LS data, due in particular to a high frequency of melanoma sites located on the upper back. It is also one of the most variable regions for lymphatic drainage as demonstrated in Figure 5.6. Out of the 43 different node fields that can drain the skin (detailed in Appendix A), 32 of them drain the skin of the torso.

In accordance with standard anatomical divisions, the torso has been divided into anterior and posterior skin regions. It was difficult to define clear additional anatomical boundaries on the torso, apart from a horizontal midline through the umbilicus. Hence, initially both the anterior and posterior torso have been divided up into lower and upper regions relative to the umbilicus.

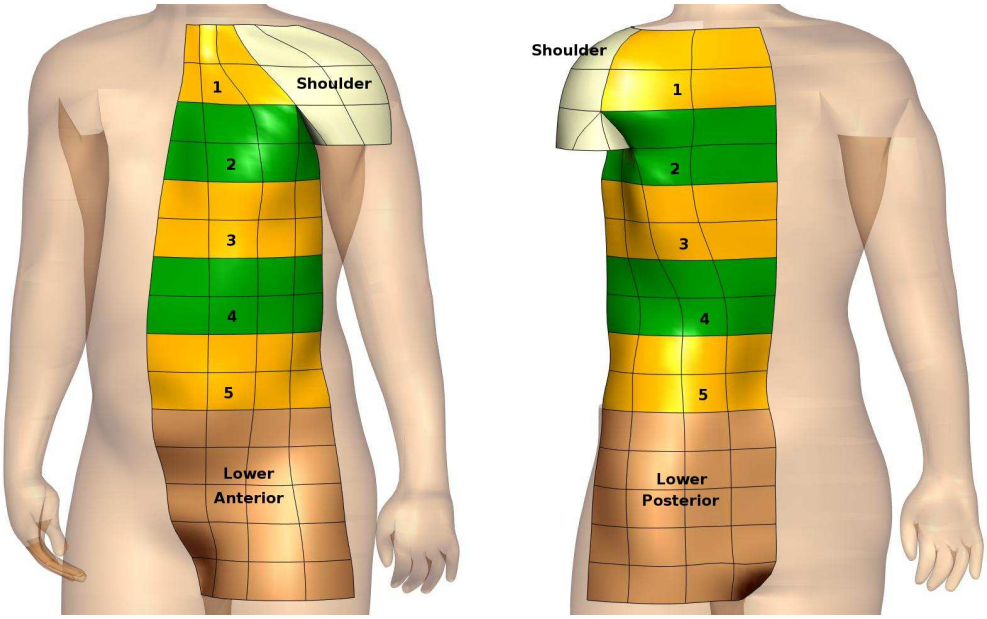

(a) (b)

Figure 7.7: Division of the (a) anterior and (b) posterior torso into separate skin regions.

The large amount of data available on the torso, as well as the large number of possible draining node fields, justified performing a highly spatially refined analysis of this region. Discretisation in the vertical direction as opposed to the horizontal direction was considered appropriate since lymphatic drainage was being tested about the vertical midline of the body. Skin on the upper torso has been discretised into regions two elements high, giving regions 10 cm in height as shown in Figure 7.7. The shoulder has been treated as a separate region. The lower regions of the torso did not contain sufficient amounts of data to warrant further spatial discretisation. The number of melanoma sites contained within each region from each side of the body, and the number of data entries are given in Table 7.1. This table also details the number of cases with sole drainage to interval nodes and individual data entries draining to interval nodes, which have not been used during the analysis.

Each region was then tested for symmetry by fitting a multinomial model to the contained LS data. Table 7.1 gives the results of this analysis, indicating whether the predictor variables (defined as the side of the body and skin element that each melanoma site was located on) were considered significant in the model (according to the AIC criterion defined in Equation 6.11). As the flowchart in Figure 6.7 shows, if side was not a significant factor then it was considered appropriate to reflect the data.

Skin Region	# Cases	# Data entries	Significant factor	Reflect?
Anterior torso				
- *region 1*	60 (1)	93 (2)	-	Yes
- *region 2*	82 (1)	117 (8)	-	Yes
- *region 3*	33 (1)	37 (3)	-	Yes
- *region 4*	78 (2)	106 (14)	-	Yes
- *region 5*	75 (1)	121 (16)	Side	No
- *shoulder*	148	187 (1)	-	Yes
- *lower anterior*	37	50 (1)	Side	No
Posterior torso				
- *region 1*	593 (1)	1056 (92)	Element	Yes
- *region 2*	446 (1)	739 (43)	Element	Yes
- *region 3*	215 (1)	318 (21)	-	Yes
- *region 4*	217 (2)	296 (51)	Side	No
- *region 5*	184 (2)	346 (48)	Element	Yes
- *shoulder*	25	28 (3)	-	Yes
- *lower posterior*	51	70 (7)	-	Yes

Table 7.1: Results of the torso reflection analysis. Number of cases and individual data entries draining to interval nodes are given in brackets.

Analysis indicated that LS data from regions 1 to 4 on the anterior torso could be considered symmetric, while anterior region 5 and the lower anterior region could not. Region 5 was located just above Sappey's horizontal line and had highly complex drainage with 10 different draining node fields. Note that in this analysis, the number of node fields has not been defined according to the left and right sides of the body, but by whether the node field defined ipsilateral or contralateral drainage. For example, melanoma sites on the left side of the body draining to the left axilla, and melanoma sites on the right side of the body draining to the right axilla, defined one node field (i.e. the ipsilateral axilla, rather than the left and right axillary node fields).

From skin of the anterior torso region 5, there were six node fields that did not have drainage to SNs in that field from one side of the body. Also, while the same proportion of melanoma sites drained to the ipsilateral axilla from each side, there were more cases draining from the right side to both the contralateral axilla and the contralateral groin. Of the cases on the right side of the body, 22% drained to the contralateral axilla and 13% to the contralateral groin; while only 7% of cases drained to the contralateral axilla and 2% drained to the contralateral groin from the left side of the body. These large differences in drainage statistics was likely due to the nonuniform and asymmetric distribution of melanoma sites within this skin region (shown in Figure 3.12).

Meanwhile the asymmetry apparent in the lower anterior torso region was also highly influenced by the asymmetric distribution of melanoma sites. This skin region covered a large area, however

since the data was sparse it could not be discretised further to allow a more refined analysis. As shown in Figure 3.12, there were more cases located near Sappey's horizontal line on the right side which evidently caused the drainage characteristics of this region to drain to the ipsilateral axilla more often than the left region (i.e. 32% versus 6%). There were also more cases that drained to the contralateral groin from the right side than the left, again likely due to the asymmetrical location of the primary melanoma sites in this region.

Symmetry in skin lymphatic drainage of the posterior torso has also been tested by dividing the skin into lower and upper regions as shown in Figure 7.7(b). The number of cases in each region on the posterior torso (apart from the shoulder) were greater than the number of cases on corresponding regions on the anterior torso, as indicated in Table 7.1. This is consistent with the higher likelihood of melanoma developing on skin of the back than the anterior torso.

Skin element was output as a significant factor in the multinomial model for regions 1, 2 and 5. This indicated that lymphatic drainage differed across elements in these regions. Since there was sufficient data available, these upper regions have been discretised further and analysed again to allow for a more refined analysis. The lower posterior region however, did not have enough data to warrant further discretisation. Upon testing, this region showed drainage most commonly occurring to the ipsilateral groin, with drainage also to the contralateral groin and both axillae. Statistically the lower posterior region was shown to be symmetric, so it has been reflected.

Further division of the upper posterior torso has been carried out horizontally, resulting in approximately 10 cm square regions (shown in Figure 7.8). The results of symmetry testing for these regions are given in Table 7.2. It was possible that selected skin regions could have been discretised even further since some contained a large amount of data (for example, region 1 has 303 melanoma sites with 651 data entries), meanwhile the smallest sample size was given for region 8 (with 44 melanoma sites and 46 data entries). It was considered important however, to provide consistent skin discretisation, therefore since it was not appropriate to reduce the sample size in region 8 any further, the current discretisation has been maintained. Both regions 1 and 5 output element as a significant factor, indicating that the drainage behaviour differed across element boundaries. Although, even though drainage differed across these regions of skin, side was not considered an important predictor.

In comparison to regions 1 to 5, there were a low number of melanoma sites available in the lateral regions 7 to 10, corresponding with the fact that melanoma more commonly develops in the middle of the back. In addition, the process of mapping sites from 2D into 3D has also contributed to the sparsity of data in these areas (as discussed in Section 3.1.1). Region 8 in particular had a very low number of melanoma sites, with only 44 cases and 46 data entries.

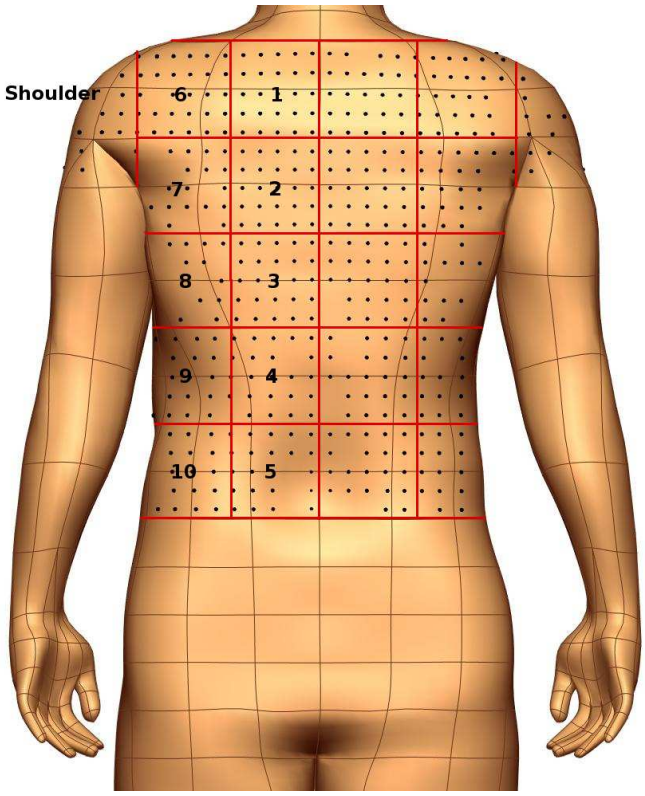

Figure 7.8: Horizontal division of the upper posterior torso into smaller skin regions.

Skin Region	# Cases	# Data entries	Significant factor	Reflect?
1	303	651 (61)	Element	Yes
2	351 (1)	628 (41)	-	Yes
3	171 (1)	272 (21)	-	Yes
4	130	196 (25)	-	Yes
5	98 (1)	200 (24)	Element	Yes
6	280 (1)	393 (30)	-	Yes
7	90	106 (2)	-	Yes
8	44	46	-	Yes
9	87 (2)	100 (26)	Side	No
10	86 (1)	146 (24)	-	Yes
Shoulder	40	45 (4)	-	Yes

Table 7.2: Results of the posterior torso reflection analysis, after further skin region discretisation. Number of cases and individual data entries draining to interval nodes are given in brackets.

Upon testing, nearly all regions showed symmetry and have therefore been reflected. The large number of cases on each side of the upper posterior torso draining to the ipsilateral axilla largely influenced this symmetry. Region 9 however, indicated that it was asymmetric. This skin region drained to seven separate node fields, although four of these fields were not drained to from

melanoma sites located on both sides of the body. Also, drainage occurred from the right side of the body to retroperitoneal and paravertebral nodes, however the left side of the body contained no SNs in these locations. These low counts likely influenced the model, causing side to be a significant factor.

7.2.2 Upper and lower limbs

The upper and lower limbs both contain two lymph node fields. The upper limb has axillary nodes in the armpits and epitrochlear nodes at the elbow, while the lower limb contains nodes in the groin and popliteal nodes behind the knee. Lymphatic drainage of the lower limb was relatively straightforward, with drainage always occurring to the groin (Figure 5.2) and at times to popliteal nodes (Figure B.3). Meanwhile the upper limb had more complex lymphatic drainage, almost always occurring to the ipsilateral axilla (Figure 5.1) and at times to the epitrochlear node field (Figure B.2). At times lymphatic drainage from the upper limb also occurred to triangular intermuscular space, supraclavicular fossa, intercostal and interpectoral node fields.

For symmetry testing, the skin of each limb has been divided into anterior and posterior regions, as well as upper and lower regions according to the location of the elbow and knee. This division was deemed the most suitable since it aligns with the anatomy of the lymphatic system, where the epitrochlear and popliteal nodes are located behind the elbow and knee respectively. Figure 7.9 demonstrates the division of each of the limbs into these skin regions.

Table 7.3 details the results of symmetry testing for each of the limbs. The entire upper limb was statistically likely to have symmetrical lymphatic drainage, owing primarily to its high likelihood of drainage to the ipsilateral axilla. In contrast, although the lower limbs always drain to the ipsilateral groin, they did not show complete symmetry. The posterior leg was not considered symmetric due to a significantly different proportion of melanoma sites that drained to the popliteal node field. Twice as many of the melanoma sites located on the right leg drained to right popliteal SNs (25%) as opposed to melanoma sites on the left leg (12%).

The hands and feet have each been treated as an entire skin region, since there was not enough data to separate them into anterior and posterior segments. Lymphatic drainage from the hand was similar to the upper limb, with drainage nearly always to axillary nodes. The feet always have drainage to the ipsilateral groin, with occasional drainage to ipsilateral popliteal nodes. Testing each of these skin regions showed that both the hands and feet could be considered to have symmetrical lymphatic drainage. Hence, the 47 cases on the hand and 203 cases on the feet, have been reflected.

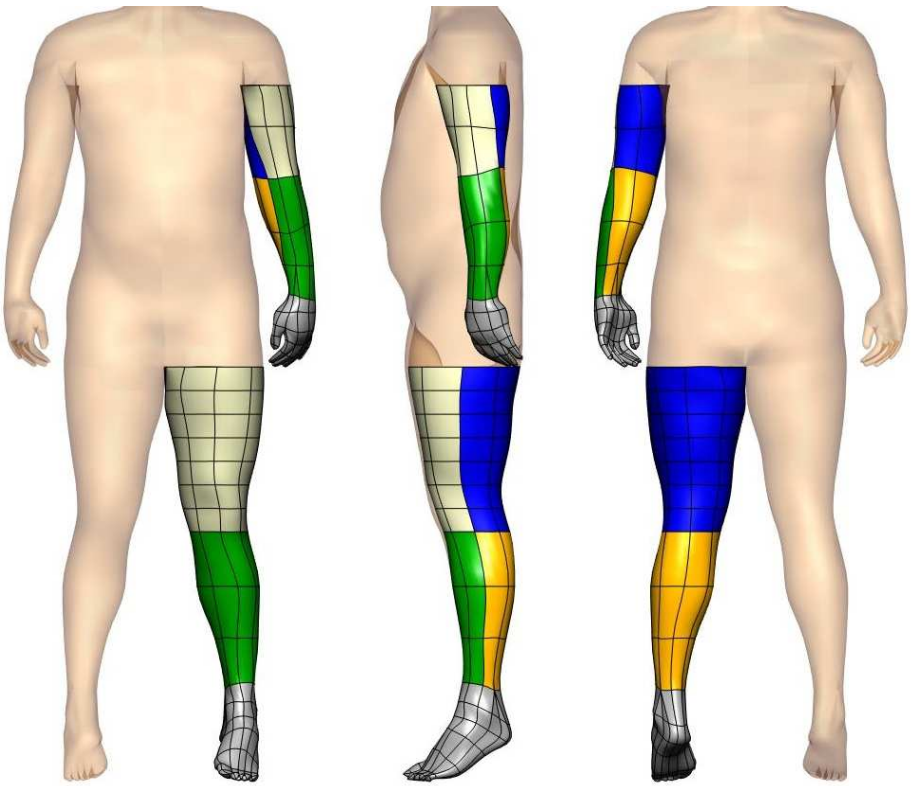

(a) Anterior (b) Lateral (c) Posterior

Figure 7.9: Division of the upper and lower limbs into skin regions.

Skin Region	**# Cases**	**# Data entries**	**Significant factor**	**Reflect?**
Upper limb				
- *anterior arm*	243	257 (19)	-	Yes
- *posterior arm*	161 (1)	165 (13)	-	Yes
- *anterior forearm*	288 (1)	353 (32)	-	Yes
- *posterior forearm*	59	71 (6)	-	Yes
Lower limb				
- *anterior thigh*	317	318 (3)	-	Yes
- *posterior thigh*	102	103 (3)	-	Yes
- *anterior leg*	314	325 (5)	-	Yes
- *posterior leg*	307	344 (6)	Side	No
Hands	47	58 (4)	-	Yes
Feet	203	238 (3)	-	Yes

Table 7.3: Results of the upper and lower limb reflection analysis. Number of cases and individual data entries draining to interval nodes are given in brackets.

7.2.3 Head and neck

The anatomy of the head and neck is highly complex, where the skin can drain to many node fields. It was important therefore, to determine the most appropriate method for dividing the skin into separate regions. To maintain consistency with previous studies, the head and neck has been divided up according to Pathak et al. (2001). This study was conducted at the SMU to investigate whether nodal metastases followed a clinically predicted pattern from melanomas of the head and neck. The skin was divided into 12 regions as shown in Figure 7.10(a). Corresponding division of the skin model is shown in Figure 7.10(b) where the name of each region is given in Table 7.4.

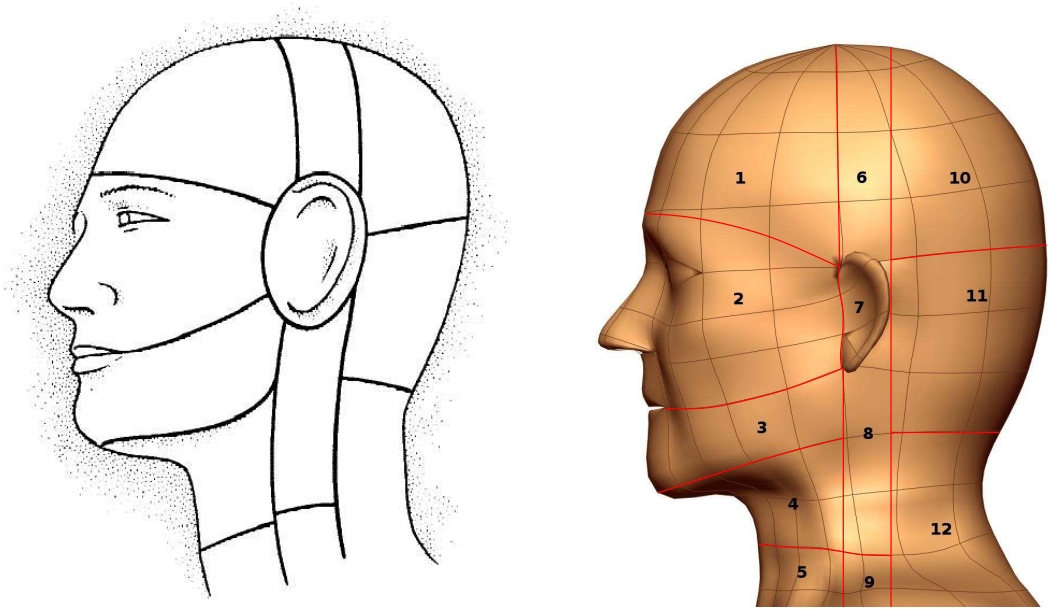

(a) (b)

Figure 7.10: Skin regions on the head and neck, (a) reproduced from Pathak et al. (2001) and (b) similar regions defined on the skin model.

The lower anterior neck and lower coronal neck did not contain sufficient data to be analysed, and have therefore not been assessed. Of the remaining 10 skin regions, all except the lower anterior neck drained to nine or more node fields. This lower anterior neck region showed drainage to only five node field locations, however since there were only four melanoma sites in this region it was highly likely that additional LS data would have shown drainage to more node fields. Nearly all areas of skin drained to all ipsilateral cervical node fields, while all 12 regions showed drainage to the cervical level II node field.

Each of these 10 skin regions on the head and neck with sufficient data have been assessed for

	Skin Region	# Cases	# Data entries	Significant factor	Reflect?
1	Forehead				
	- *upper anterior*	30	61 (5)	-	Yes
	- *lower anterior*	28	70	Side	No
	- *upper lateral*	35	77 (5)	-	Yes
	- *lower lateral*	45	85 (4)	-	Yes
2	Upper face				
	- *upper anterior*	55	122 (8)	-	Yes
	- *lower anterior*	76 (1)	159 (6)	-	Yes
	- *upper lateral*	57	100 (6)	-	Yes
	- *lower lateral*	74 (1)	144 (3)	-	Yes
3	Lower face	61	128	-	Yes
4	Upper anterior neck	49	99	-	Yes
5	Lower anterior neck	4	5 (1)	(not enough data)	No
6	Coronal scalp	29	68 (4)	-	Yes
7	Ear	107	190 (1)	-	Yes
8	Upper coronal neck	49	101	-	Yes
9	Lower coronal neck	0	0	(not enough data)	-
10	Posterior scalp	88	202 (15)	-	Yes
11	Upper posterior neck	71	149 (2)	-	Yes
12	Lower posterior neck	69	136 (6)	Side	No

Table 7.4: Results of the head and neck reflection analysis. Number of cases and individual data entries draining to interval nodes are given in brackets.

symmetry. A summary of the results is given in Table 7.4, which shows that most skin regions on the head and neck were symmetric. The forehead however, when treated as a whole region, indicated that it could not be reflected. Since there was significant data in this region it has been divided further into four smaller regions (shown in Figure 7.11(a)) to determine whether there was localised asymmetry. The division into subregions has been conducted along element boundaries into upper and lower anterior, and upper and lower lateral regions. Symmetry testing showed that three out of four of these forehead regions could be reflected, although analysis of the lower anterior region of the forehead confirmed that side remained a significant factor.

The most common node field from this lower anterior region of the forehead was the ipsilateral preauricular node field, however a large difference in drainage likelihood to this node field from each side of the head probably contributed to this asymmetry. The entire left side of this region had drainage to the left preauricular node field, in contrast to only 57% of the melanoma sites on the right side that drained to the right preauricular node field (compare with Figure 5.3). There was also a difference between the proportion of sites that drained to contralateral preauricular node fields, with 7% of sites on the left side of the head and 36% on the right side. These differences were likely influenced by the uneven distribution of sites within these regions, since melanoma sites

on the right region were closer to the midline than sites on the left, likely causing contralateral drainage to be more likely from the right side. Another contributing factor to the asymmetry is the fact that of 13 possible node fields, seven of them had no drainage from one side of the head.

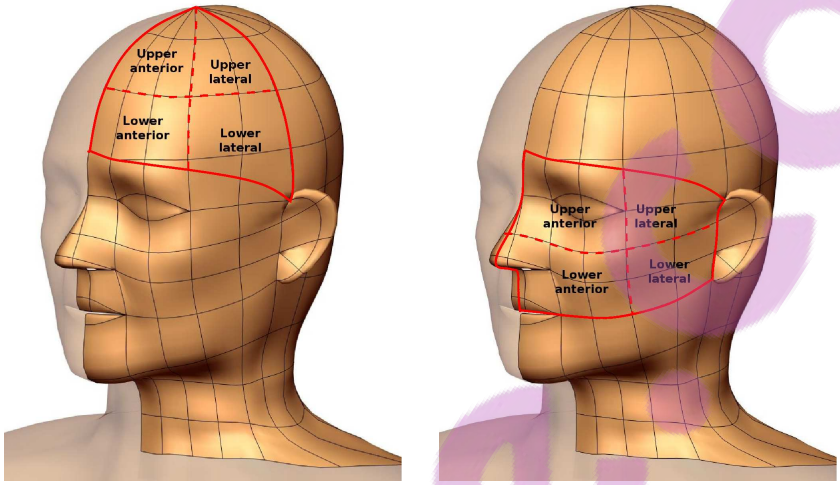

(a) Forehead (b) Upper face

Figure 7.11: Skin of the head that has been divided further into subregions.

The upper face region has also been divided into four separate regions (shown in Figure 7.11(b)) since there was sufficient data to conduct a more spatially refined analysis. Testing each of these regions for symmetry showed that side was not a significant factor and the data could be reflected. The lower anterior region showed the most common node field was ipsilateral cervical level I, while drainage from each region often occurred to ipsilateral cervical level II and preauricular node fields.

The lower posterior neck indicated that it was asymmetric. This region of skin was highly complex, with 16 draining node fields in the head and neck and the torso. There was a significant different in the draining statistics to ipsilateral cervical level II from each side, with 11% of all melanoma sites on the left side in contrast to 40% of melanoma sites on the right side draining here. Also, contralateral cervical level V and ipsilateral cervical level IV showed considerable drainage differences. These differing drainage characteristics were possibly due to the asymmetrical distribution of melanoma sites in this region (which can be seen in Figure 3.12). In addition, since this is such a complex region of skin with numerous node fields more LS data would be required to quantify whether this region is actually asymmetric.

Meanwhile, as previously mentioned, the lower anterior neck and lower coronal neck did not contain enough data to conclude whether lymphatic drainage was symmetric. The sparsity of sites on

the anterior neck was partly due to the mapping process. The neck region of the SMU's anterior body map contained only one grid unit in the Y-direction (shown in Figure 3.9) so the anterior neck region has been stretched considerably to cover a large area on the skin mesh.

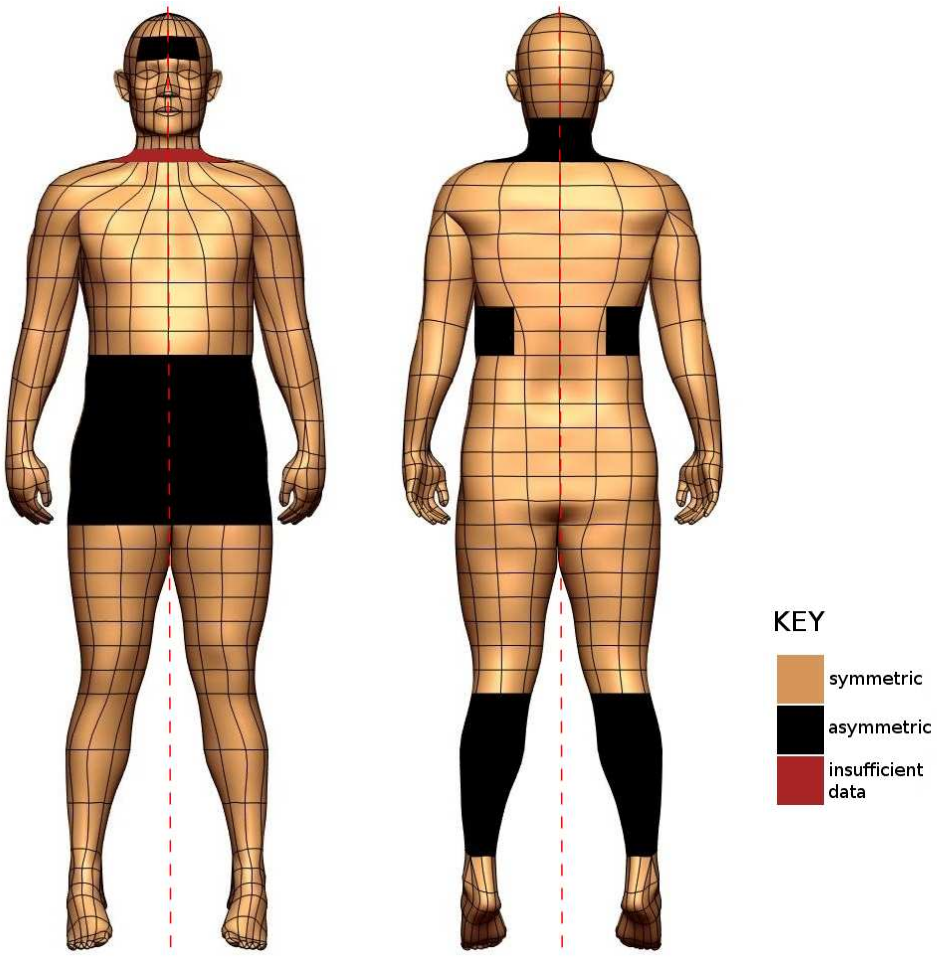

(a) Anterior (b) Posterior

Figure 7.12: Results of the symmetry analysis, displaying regions of skin that were asymmetric in black.

After testing each skin region, melanoma sites within each symmetrical region have been reflected according to the methods described in Section 6.3.2. Figure 7.12 shows the collective results of the symmetry analysis. The total number of cases in each skin region, and the number of cases in each region that have been reflected are outlined in Table 7.5. Out of 5232 cases in the LS database, there were three patients with previous surgery and 17 cases with sole drainage to an interval node, that have been excluded from the analysis. Of the remaining 5212 cases, 4605 cases have been reflected, giving 9817 cases in the reflected LS database.

Skin Region	# Cases	# Reflected
Torso	2244 (13)	2045
Upper limbs	751 (2)	751
Lower limbs	1040	733
Hands	47	47
Feet	203	203
Head and neck	927 (2)	826
TOTAL	5212 (17)	4605

Table 7.5: Number of cases in each skin region that have been reflected. Number of cases with sole drainage to interval nodes are given in brackets.

7.3 Cluster Analysis

Cluster analysis has been carried out to define regions of skin with similar patterns of lymphatic drainage without a priori hypotheses, using methods described in Section 6.4. To carry out this analysis, the reflected LS dataset which contained 9817 cases described above, has been used. This larger dataset allowed for improved robustness in the definition of the boundaries of each resultant cluster. Similar to the reflection analysis, interval nodes have not been included during this analysis. To carry out the clustering algorithm, LS data has been grouped according to skin element, and hence each cluster will contain one or multiple skin elements.

An appropriate check distance value was chosen by assessing the resultant clusters to ensure they made physiological sense and had potential clinical utility. This meant that for each cluster, it was important that the corresponding region of skin showed a clearly defined pattern of lymphatic drainage. Making sure that a sensible number of clusters was reached was also important, since the algorithm will produce too many clusters when the check distance threshold is too high.

7.3.1 Results

The clustering algorithm has been carried out on the reflected dataset for decreasing check distance values starting at $d_0 = 6.48$. This initial check distance was iteratively reduced from d/1 to d/20 in decrements of 1, to give the resultant cluster tree diagram as shown in Figure 7.13. In this diagram, the size of each cluster has been scaled according to the number of skin elements it contained, however since the cluster tree was so large the relative differences in size were small. The colour of each cluster corresponds to the standard deviation of the LS data contained within that cluster, according to the scale bar at the bottom of the diagram. Initially all skin elements were contained within the same cluster, however as the check distance has been iteratively reduced the

skin elements split off into smaller clusters. In some cases if the check distance was too small, clusters or even individual skin elements drop out of the analysis altogether.

As an arbitrary rule, clusters containing more than five elements were considered large, while any clusters with less than five elements were regarded as small. On the cluster tree diagram, large clusters have been joined with a solid yellow line, while small clusters have branched off with a thin black line. A summary of the clustering results is given in Table 7.6, detailing the check distance values and the number of clusters at each check distance. Comments have also been given when the number of large clusters increased, to describe how the clusters have divided. Visualisation of clusters on the skin model has been given for specific check distances in Figures 7.14 through to Figure 7.16.

Check distance	**# Large clusters**	**# Small clusters**	**Total # clusters**	**Comment**
$\leqslant$d/9	1	0	1	-
d/10	1	3	4	-
d/11	1	5	6	-
d/12	2	8	10	Left head cluster splits off
d/13	3	11	14	Right head cluster splits off
d/14	3	9	12	-
d/15	3	8	11	-
d/16	5	8	13	Left axillae cluster splits off & left head cluster divides
d/17	6	12	18	Right head cluster divides
d/18	7	12	19	Right axillae cluster splits off
d/19	9	10	19	Lower limb cluster separates
d/20	7	18	25	-

Table 7.6: Cluster analysis results.

The cluster tree diagram showed that there was only one cluster present until check distance d/10, when three small clusters with two or three elements in each broke off from the main cluster. At the following check distance d/11, additional small clusters separated from the main cluster, then at d/12 a large cluster containing elements on the left side of the head (cluster number 3) split off. Following this, at d/13 another larger cluster split off containing elements on the right side of the head. The three large clusters at d/13 can be seen on the skin model in Figure 7.14. Cluster 1 (shown in red) contained most of the elements on the torso and limbs, while clusters 3 and 6 (shown in silver and white respectively) contained elements on either side of the head. Note that skin elements shaded in black contained no data and therefore have not been included in the clustering algorithm. Meanwhile elements that comprised a small sized cluster or had dropped out of the analysis altogether have not been shaded, and remain skin colour. The elements that dropped out

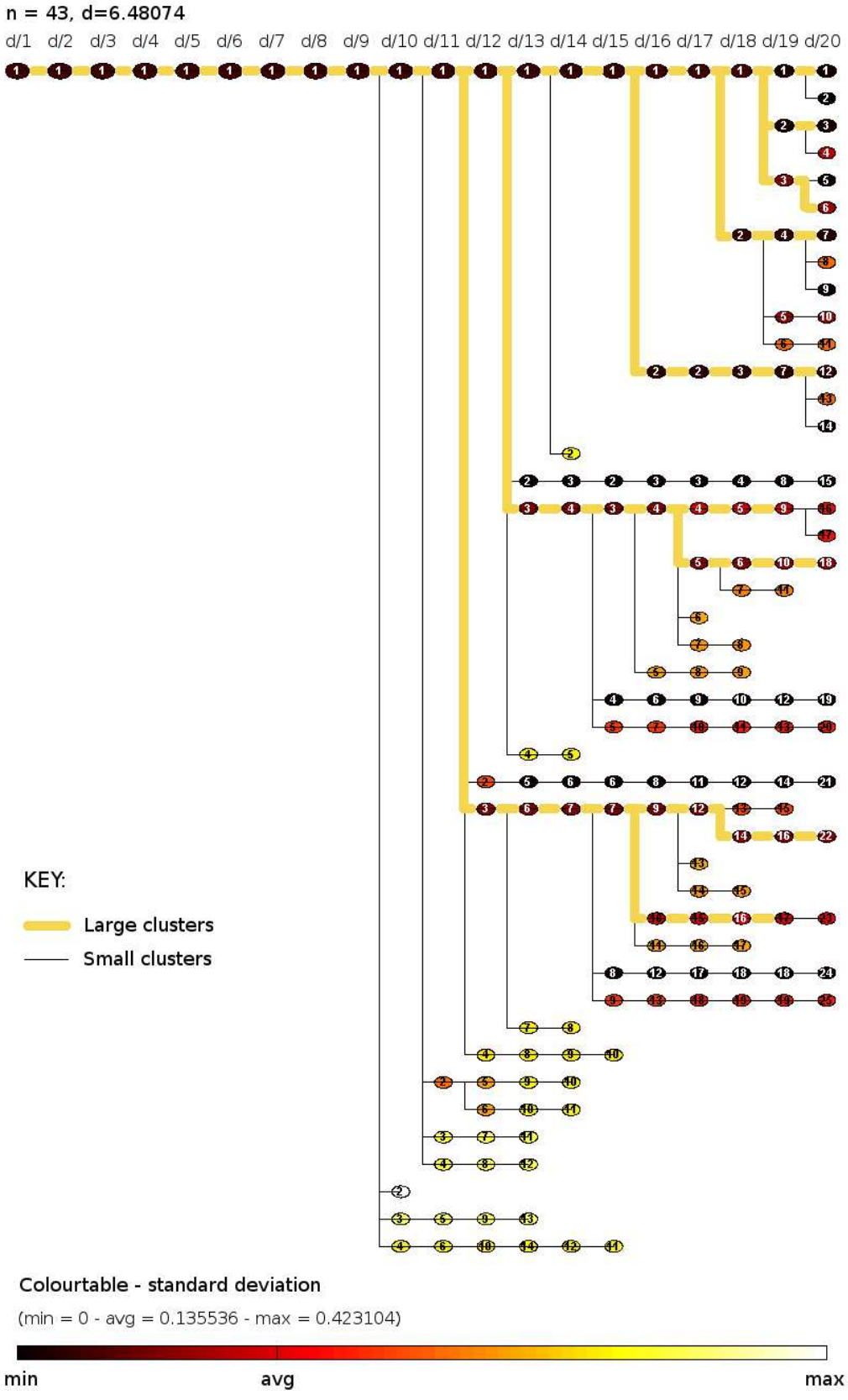

Figure 7.13: Cluster tree diagram for the reflected LS data.

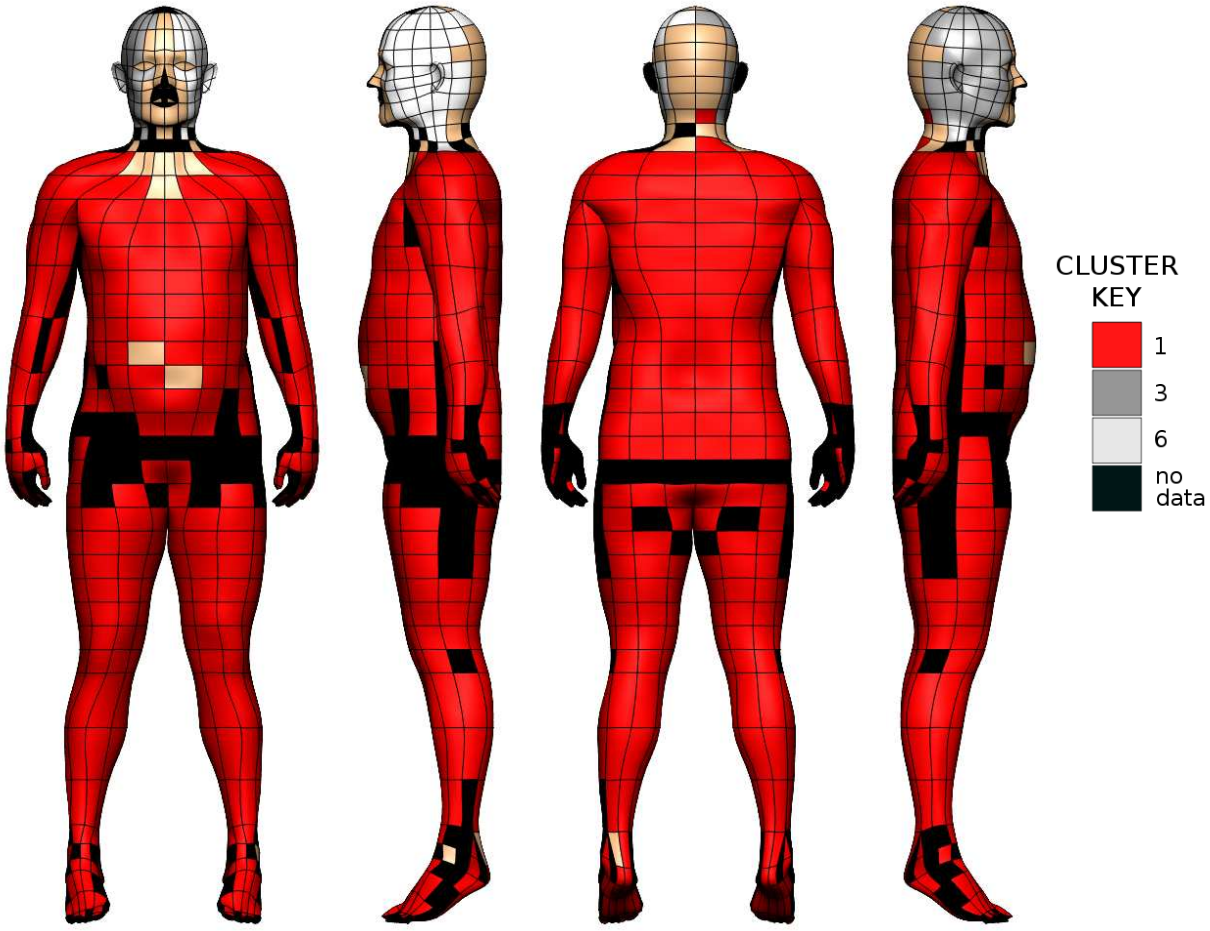

(a) Anterior (b) Left (c) Posterior (d) Right

Figure 7.14: Clusters on the skin mesh at check distance d/13.

of the analysis often contained outlying melanoma sites that displayed unusual lymphatic drainage which did not fit with more common drainage patterns demonstrated by the clusters.

Further decreasing the check distance continued to generate additional clusters, however it was not until d/16 that two more large clusters were formed when one split off from the left torso and upper limb and the left head cluster divided in two. At check distance d/17 another large cluster was formed when the right head cluster divided, and again at d/18 an additional cluster was formed by the right torso and upper limb splitting off together.

Figure 7.15 shows the clusters at check distance d/18. Some elements that were originally in cluster 1 at d/13 (visualised in Figure 7.14) dropped out at this check distance, including two elements on the middle of the posterior torso. These two elements were close to Sappey's lines indicating regions of skin that showed highly variable lymphatic drainage. One of these elements

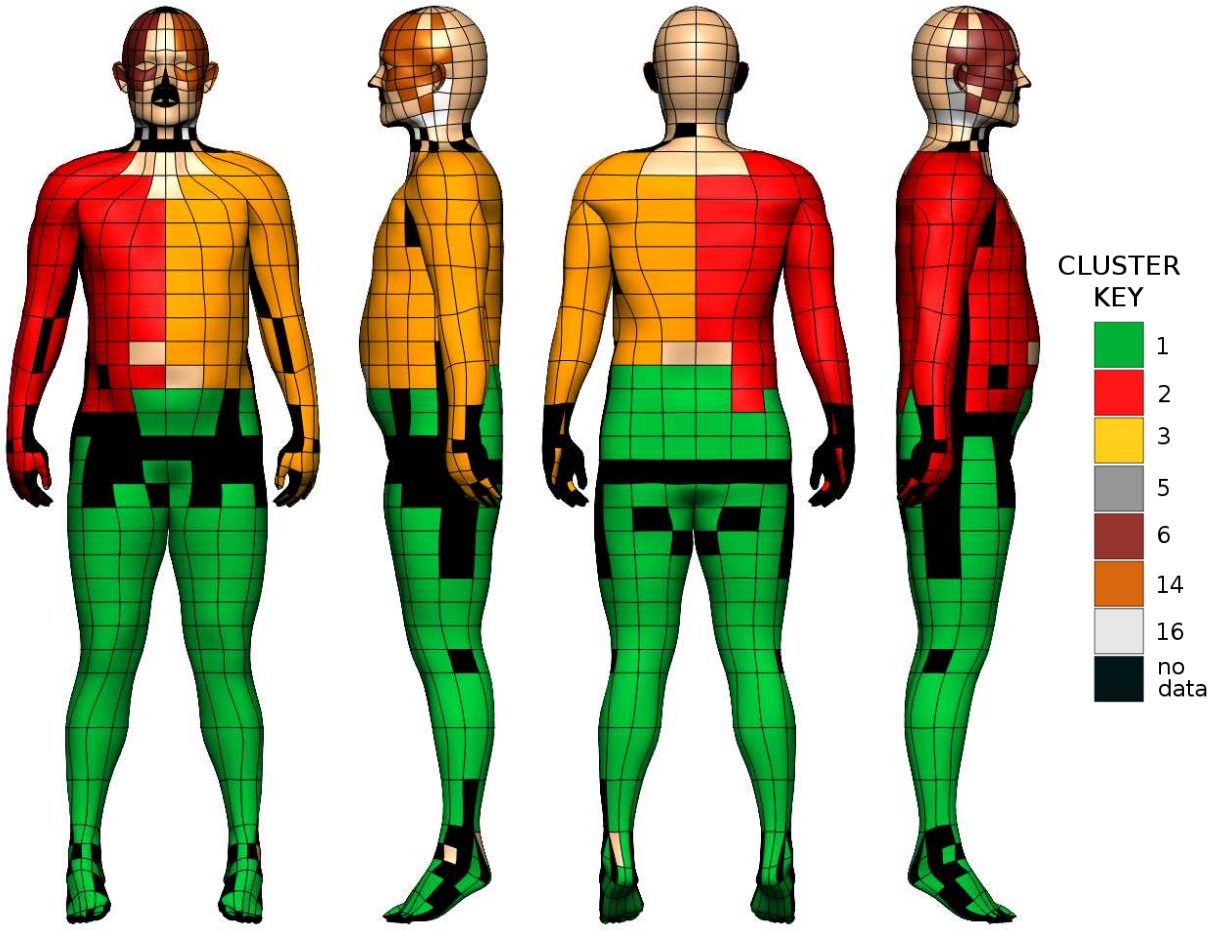

(a) Anterior (b) Left (c) Posterior (d) Right

Figure 7.15: Clusters on the skin mesh at check distance d/18.

was previously demonstrated by the skin selection tool in Figure 5.7, displaying complex drainage to seven different node fields as well as to interval nodes.

Finally at check distance d/19, elements on the lower limbs separated into three individual clusters, as shown in Figure 7.16. One cluster was created for each limb, while an additional cluster was formed from elements on the anterior and posterior lower torso. In total there were 9 large clusters and 10 small clusters at this check distance. The total number of clusters increased considerably past d/19, however the number of large clusters decreased. For example, at d/20, two of the large clusters on the head dropped out of the analysis since the check distance threshold was too high. Meanwhile the number of small clusters increased from 10 to 18. Therefore it was considered appropriate to stop iterating the cluster algorithm at d/19, as this gave a physiologically reasonable result while also ensuring that the check distance threshold was not unnecessarily high.

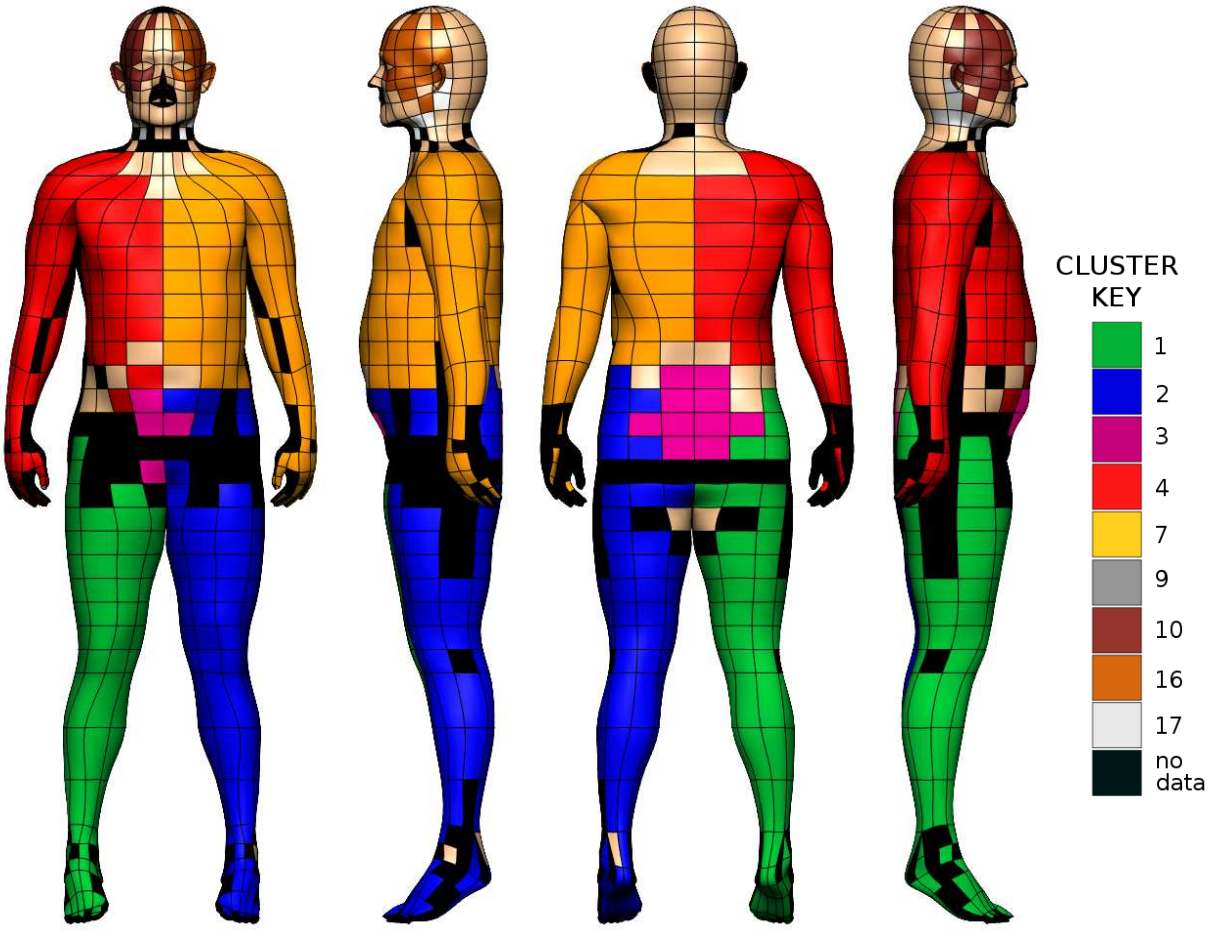

(a) Anterior (b) Left (c) Posterior (d) Right

Figure 7.16: Clusters on the skin mesh at check distance d/19.

Each of the final clusters that were formed at check distance d/19 corresponded with a particular pattern of lymphatic drainage. To further assess the drainage behaviour of each cluster, statistics have been calculated to determine the likelihood of drainage from each cluster to its draining node field. To give measures for these drainage statistics, non-parametric bootstrapping (described in Section 6.5) has been used to determine 95% confidence intervals. Commands implemented in R that were used to calculate these confidence intervals are given in Appendix G.

Table 7.7 details the resultant draining node field statistics from each cluster. Only the dominant draining node fields have been given here. Clusters 1 and 2 on the lower limbs indicated that 100% and 99.74% of all cases within these clusters drained to the right and left groin respectively. A small number of melanoma sites also drained to the popliteal node fields from these clusters. Unexpectedly, there were two elements on the left ankle that dropped out of the analysis altogether.

This was due to each element only containing one melanoma site, which had drainage to both the ipsilateral groin and ipsilateral popliteal node fields. During clustering this would have indicated 100% of sites drained to each field, significantly different to the drainage characteristics of other elements in the cluster which less frequently drained to the popliteal node field.

Cluster	**Location**	**Draining Node Fields**	**Drainage Statistics (%)** Mean	95% CI
1	Right lower limb (n = 1116)	rg	100	(100, 100)
		rpop	6.36	(4.93, 7.89)
2	Left lower limb (n = 1138)	lg	99.74	(99.38, 100)
		lpop	4.92	(3.69, 6.24)
3	Lower mid-torso (n = 111)	rg	70.27	(62.16, 78.38)
		lg	69.37	(60.36, 78.38)
		ra	18.02	(11.71, 25.23)
		la	17.12	(10.81, 24.32)
4	Right torso & upper limb (n = 2613)	ra	95.41	(94.56, 96.13)
		la	16.80	(15.46, 18.29)
7	Left torso & upper limb (n = 2636)	la	95.33	(94.54, 96.09)
		ra	16.81	(15.36, 18.29)
9	Right lateral neck & jawline (n = 100)	rc2	74.00	(65.00, 82.00)
		rc5	30.00	(21.00, 39.00)
		rc3	27.00	(19.00, 36.00)
		rc4	19.00	(12.00, 27.00)
		rsc	15.00	(8.98, 22.00)
10	Right lateral scalp & cheek (n = 367)	rc2	67.57	(62.67, 72.48)
		rprea	60.49	(55.31, 65.12)
		rposta	18.53	(14.44, 22.62)
		rc1	12.81	(9.26, 16.36)
16	Left lateral scalp & cheek (n = 375)	lc2	67.47	(62.93, 72.27)
		lprea	62.13	(57.07, 67.47)
		lposta	17.87	(14.13, 21.60)
		lc1	12.53	(9.33, 16.27)
17	Left lateral neck & jawline (n = 78)	lc2	70.51	(60.26, 79.52)
		lc5	25.64	(16.67, 35.90)
		lc3	25.64	(16.67, 35.90)
		lc4	17.95	(8.97, 25.67)
		lsc	15.38	(7.69, 24.36)

Table 7.7: Drainage statistics of the dominant draining node fields from each cluster at check distance d/19.

Clusters 4 and 7 located on each side of the torso and upper limbs, corresponded to a high likelihood of drainage to the ipsilateral axilla. The drainage statistics indicated that just over 95% of all melanoma sites located within these two clusters drained to the ipsilateral axilla, while nearly 17%

of all sites drained to the contralateral axilla. Owing to the large amount of data in each of these clusters, the confidence intervals were very small.

Cluster 3, which was located in the middle of the lower anterior and posterior torso showed that it was likely to drain to either groin node field (70%), and to either axillary node field (approximately 17%). This region confirmed that there was a relatively large area of skin in the middle of the torso which showed ambiguous lymphatic drainage.

The remaining four clusters were located on either side of the head, and grouped elements together on the lateral scalp and cheek (shaded orange and burgundy), and skin elements on the lateral neck and jawline (shaded white and silver). Elements contained within the lateral scalp and cheek clusters always showed drainage to the preauricular and cervical level II node fields. According to the drainage statistics given in Table 7.7, the ipsilateral cervical level II was the most common draining node field (68%), which was followed very closely by the preauricular node field (approximately 60%). Often drainage was also observed to SNs in the postauricular and other cervical level node fields.

Similar to the lateral scalp and cheek clusters, ipsilateral cervical level II was the most common node field draining the lateral neck and jawline clusters. Over 70% of all melanoma sites from the clusters drained to SNs in this location, and all elements within these clusters also drained to cervical levels II, III and IV node fields. Often drainage also occurred to cervical level V and supraclavicular fossa nodes.

7.4 Discussion

The statistical methods that have been implemented above provide a way to analyse lymphatic drainage of the skin with increasing complexity. Quantifying the accuracy of Sappey's lines and investigating the symmetry of lymphatic drainage had allowed previous anatomically based definitions of drainage patterns to be assessed. The mapped model developed in this thesis has now enabled analysis to move beyond these anatomically based definitions of drainage towards a data driven approach. Cluster analysis allowed LS data to be grouped together according to regions of skin with functionally similar drainage patterns, without reference to previous spatial hypotheses.

Analysis of Sappey's lines showed considerable inaccuracy for predicting lymphatic drainage of the trunk. It is significant to note that during this analysis, melanoma sites located on the trunk with drainage to alternate node fields were removed, since Sappey's conclusions were limited to lymphatic drainage to the axillary and groin node fields. Of the 2196 cases located on the trunk,

only 61% had sole drainage to one axillary or groin node field; 32% of those cases drained to one or more axillary or groin node fields as well as an alternate node field; while the remaining 7% drained to alternate node fields without draining to the axilla or groin at all. This means the predictive inaccuracy of Sappey's lines, even at its calculated optimum position, will be worse than 12.5%. In addition, nearly the entire torso region demonstrated ambiguous drainage (shown in Figure 7.6), which again proved that lymphatic drainage is not accurately predicted by Sappey's lines.

Although Sappey's lines were inaccurate, analysis clearly showed that the optimal position for Sappey's vertical line was located at the anatomical centre of the body. This was significant, since although the body is outwardly symmetric about the body's vertical midline, most of the internal organs are not (Wolpert 2005). The heart for example, is on the left side, as are the stomach and the spleen. Additionally, the right lung has more lobes than the left. It appears that the asymmetrical placement of organs in the torso does not seem to alter the symmetry of the lymphatics draining the overlying skin.

There were a number of factors that were important to take into consideration during interpretation of these results. Firstly, defining Sappey's transverse line using a plane limited the way that the skin model could be divided into quadrants. The amount of curvature resulting in the transverse line around the skin model was restricted by the amount of curvature present in the skin model itself. In reality, this line curves from the umbilicus anteriorly to the level of the second lumbar vertebra posteriorly (as explained in Section 6.2). Although the midline plane may not have enabled all possible divisions of the skin model into quadrants, the advantage was that it could be defined unambiguously and was computationally straightforward to implement.

Also, it is important to be aware that when a patient's melanoma site has been recorded on the posterior torso body map (as shown in Figure 1.14), it was not recorded with respect to the vertebral bones because they had not been drawn on the 2D body maps. However, melanoma sites on the anterior torso body map have been recorded relative to the umbilicus. Therefore, defining Sappey's lines with respect to the umbilicus is acceptable, although determining where they should be relative to the vertebrae may be less accurate. Also, the relative position of the umbilicus to the vertebrae may not be very accurate on the skin model. The individual that was used to create the VH images was lying in a supine position, which is likely to have had internal organs and overlying skin that were not exactly representative of a live individual.

The symmetry in lymphatic drainage patterns suggested by Sappey's optimal vertical line, has been further quantified during symmetry testing. Analysis indicated that most of the skin did in fact show symmetrical lymphatic drainage about the vertical midline of the body. Regions displaying

asymmetry included skin of the lower anterior torso, posterior legs, lower posterior neck and small regions of the anterior forehead and posterior torso. The resulting asymmetry in these regions however, was likely to be due to an asymmetric distribution of melanoma sites within the regions, which would have influenced the draining node fields.

Meanwhile, the lower anterior neck and lower coronal neck could not be analysed because there was insufficient data. It is possible that each of these asymmetrical regions would have shown symmetry if more LS data was available. Also, as discussed in Section 6.3, using GLMs to model the data without correcting for non-independence means that some regions may in fact be symmetric but give an asymmetrical result. Therefore, it is possible that skin lymphatic drainage of the body is entirely symmetric. It was considered important however, during subsequent data reflection, to take a conservative approach to the analysis and only reflect those skin regions that showed conclusive symmetry.

There were a number of aspects of the symmetry testing that could have been carried out differently, which may have varied results. Primarily, the discretisation of the skin into separate regions was not a clearly defined procedure. The torso was divided according to its anatomy, into anterior and posterior regions and above and below the umbilicus. Further discretisation of the upper anterior torso was based on element boundaries which have been arbitrarily chosen during skin mesh construction. Meanwhile, the upper and lower limbs were divided according to the lymphatic anatomy in these regions, even though there was enough data in some areas to support a more spatially refined analysis. Lastly, to maintain consistency the head and neck has been divided according to a previous study. A number of alternate skin divisions for each of these regions could have been used, which may have given different results. However, since the results showed that a significant proportion of regions showed symmetry using different skin discretisation methods, the results were likely to be robust.

Collectively, both Sappey's lines analysis and the symmetry testing demonstrated a distinct functional division of the torso into left and right sides. Subsequent cluster analysis provided additional insight into regions of skin that showed functionally similar patterns of lymphatic drainage, based solely on the LS data. Results showed a clear anatomical division of the skin into nine separate clusters, which primarily grouped regions of skin according to the dominant draining node fields. As detailed in Table 5.1, the most dominant node fields were the axillary, groin, cervical level II and preauricular node fields, being drained to by 62%, 29%, 11% and 7% of patients in the LS database respectively.

Interestingly, the clusters draining primarily to axillary and groin node fields divided the trunk into regions comparable to Sappey's lines. Even though there was variability of lymphatic drainage

on the torso between individuals, Sappey's lines appeared to conform to the most likely drainage behaviour of this data. Cluster 3 (in Figure 7.16), which formed in the centre of the anterior and posterior torso, clearly demonstrated however that there was still a significant region of skin with ambiguous drainage to groin and axillary node fields.

Similar to the previous statistical methods implemented, the cluster analysis also had limitations. Currently the cluster algorithm groups LS data according to skin elements. The advantage of this approach was that it was straightforward to implement, however it also meant that the data was homogenised across elements which were arbitrarily chosen during skin mesh construction. The degree of homogenisation could be reduced in future by dividing the skin further into smaller regions, where there is sufficient data.

Restriction of the boundaries of each cluster to the boundaries of the skin elements was another limitation. In an ideal situation, uniformly sized skin regions would have been used rather than the skin elements which have large variations in size. In addition, there would be adequate LS data to provide probabilities that represent the entire population. A number of elements on the skin mesh did not have any data present, and therefore could not be grouped in a cluster. These elements are shown shaded in black in Figures 7.14 through to Figure 7.16. To enable a more comprehensive clustering analysis, data would be required in these regions.

The clustering algorithm did not have any inherent spatial awareness, which has allowed the formation of clusters which were not all connected. The advantage of this lack of spatial awareness was that it allowed the LS data itself to determine the formation of clusters without any bias towards clusters forming between adjacent elements. This was most markedly seen in Cluster 3 on the lower anterior torso, where elements did not all share adjacent boundaries. Clusters on the head at check distance d/19 also did not always included elements which shared adjacent boundaries.

Although each of these statistical tests has inherent limitations, they have offered additional insights into skin lymphatic drainage. This analysis has allowed Sappey's lines to be assessed to quantify that they are inaccurate to predict lymphatic drainage. However, despite this inaccuracy, they appear to demonstrate common patterns of drainage across the known population. It was shown that skin lymphatic drainage is likely to be entirely symmetric. There were significant areas of skin that nearly always showed drain to the ipsilateral axilla, groin, cervical level II and preauricular node fields. Collectively, this mapped model has provided a novel way to add to current knowledge about the lymphatics, and gives a framework for additional analyses in the future.

7.5 Summary

This chapter presented detailed statistical analysis results of skin lymphatic drainage conducted in 3D, based on methods described in the previous chapter. A detailed analysis of Sappey's lines has been conducted. Investigation has also been carried out to determine whether lymphatic drainage patterns could be considered the same on both sides of the body, using a multinomial modelling approach. Regions that were considered symmetric have been reflected, providing a larger LS dataset to use during subsequent data visualisation and analyses. This reflected LS dataset was used during cluster analysis, to define regions of skin that have similar patterns of lymphatic drainage. Confidence intervals were calculated to determine the statistical significance of drainage statistics from each cluster.

Chapter 8

Conclusions and Future Work

The aim of this research was to develop an anatomically based modelling framework to enable 3D visualisation and analysis of skin lymphatic drainage using melanoma LS data. For this purpose, a highly detailed anatomically based FE model of the skin has been created based on the VH dataset and a Sawbones head and neck model. A discrete model of lymph nodes that directly drain the skin has also been created using the VH dataset. The SMU's entire LS database of over 5000 patients was then mapped from 2D onto this 3D model using host-mesh fitting and various projection techniques.

Visualisation of skin lymphatic drainage was conducted on the mapped model by relating melanoma sites on the skin to draining node fields. Heat maps have been generated by fitting fields across the skin model surface, providing novel displays of the likelihood that any area of skin will drain to a particular node field, or a specified number of node fields. Additionally, a skin selection tool has been developed and provided online, allowing dynamic prediction of draining node fields based on a selected element on the skin model.

Detailed statistical analysis was carried out to further investigate skin lymphatic drainage. The inaccuracy of Sappey's lines was quantified, and an optimal position for these lines has been determined. Tests were conducted to determine whether lymphatic drainage is likely to be symmetric, and cluster analysis was carried out to functionally group regions of skin that showed similar patterns of drainage. Confidence intervals were also calculated to indicate significance measures for the dominant draining node fields from each cluster.

This chapter outlines the limitations of the developed model, as well as possible future work. Finally, a summary of the novel findings and conclusions of this work is given.

8.1 Model limitations

Although the developed model has further improved understanding of skin lymphatic drainage, there are a number of limitations present that should be taken into consideration. The FE model of the skin has been created using two separate datasets, both images from the VH and a Sawbones head and neck model. The head of the VH had an abnormally short neck region which was not considered adequate for mapping melanoma sites onto, or for modelling the detailed lymph node geometry in this region. Using the Sawbones model for the head and neck has allowed for neck melanoma sites and node fields to be modelled accurately, however the combined skin model is not based on one individual. By combining two datasets a generalised anatomical representation of the skin has been created.

The full lymph node model based on the VH dataset has been created with many nodes located in each node field. During mapping however, the full anatomical detail of the model has been considerably underutilised, since this detailed model has been reduced to one representative node in each field. This was the only possible way that the SN node fields could be mapped, in the absence of detailed location information. Although the Sawbones model contained bones and facial muscles, it did not include lymph nodes to allow accurate placing of the head and neck node fields such that the head and neck node fields have been moved relative to the head and neck skin model. These representative head and neck nodes are therefore not exactly anatomically accurate, however they still sufficiently depict the general location of each field.

The skin has been modelled using high order FE interpolation, which accurately captured the anatomical structure of the skin while also using a minimal number of elements. As a result, elements are not uniform in shape and there are large variations in size. This has created limitations in the developed skin selection tool and during the statistical cluster analysis, where LS data has been grouped according to skin elements. Some elements had a large amount of data present so they had high levels of confidence, while other elements with little or no data were statistically inconclusive.

The primary limitation of the model was the sparsity of data in certain regions of skin. In particular, data was sparse on the groin, lateral torso, lateral legs and the hands. This was due to the LS data collection procedures which were implemented at the SMU, the nonuniform distribution of melanoma sites recorded in the database, as well as the mapping process that has been used to convert the 2D LS data into 3D. More LS data would be required in future to improve the predictive accuracy of the model, particularly on elements on the lateral sides of the body and the groin.

8.2 Future work

Although this study has inherent limitations as described above, extensions to the model could address these issues. The model could also provide the basis for the development of additional research projects. Possible future extensions to the model are discussed below.

Recording Additional LS Data

Although the SMU currently has the world's largest LS database at over 5000 patients, ideally more data is required to give an accurate indication of patterns of lymphatic drainage from all over the body. To address this problem, an interactive software tool could be developed to allow clinicians at the SMU to record their LS data directly on the 3D model surface.

Preliminary work has already been initiated towards this goal, using a web-browser extension named ZINC[1], that has been developed at the ABI. This extension embeds the CMGUI visualisation engine within a web page, allowing CMGUI scenes to be rendered directly into it. An example of a potential recording interface which is currently under development can be seen in Figure 8.1. This interface includes three separate scenes which visualise different FE models of the body. User input forms are given on the lower left to allow direct entry of patient information, and buttons are provided to enable different aspects of the model to be seen.

This interface would allow the user to position each patient's primary melanoma site directly onto the 3D skin model surface, improving the anatomical registration of sites. This would be a distinct advantage over the current 2D recording method carried out at the SMU. In particular, melanoma sites on the lateral sides of the torso and lower limbs could be more accurately placed since the model would have the ability to rotate. Also, this interface could provide utility to morph the skin mesh to match the patient's morphology using host-mesh fitting (described in Section 2.4). By changing the shape of the skin model to accurately represent the patient of interest, the primary melanoma site recording could be more precise since clinicians would not be required to subjectively normalise each patient's body morphology.

The location of each patient's SNs could also be more accurately recorded using this tool. The second scene shows selected muscles, bones and vasculature created previously at the ABI using VH data. These models would enable SNs to be placed relative to adjacent anatomical structures. These anatomical landmarks would be invaluable, since lymph nodes are often located alongside blood vessels, and are commonly described relative to muscles and bones.

[1] http://www.cmiss.org/cmgui/zinc

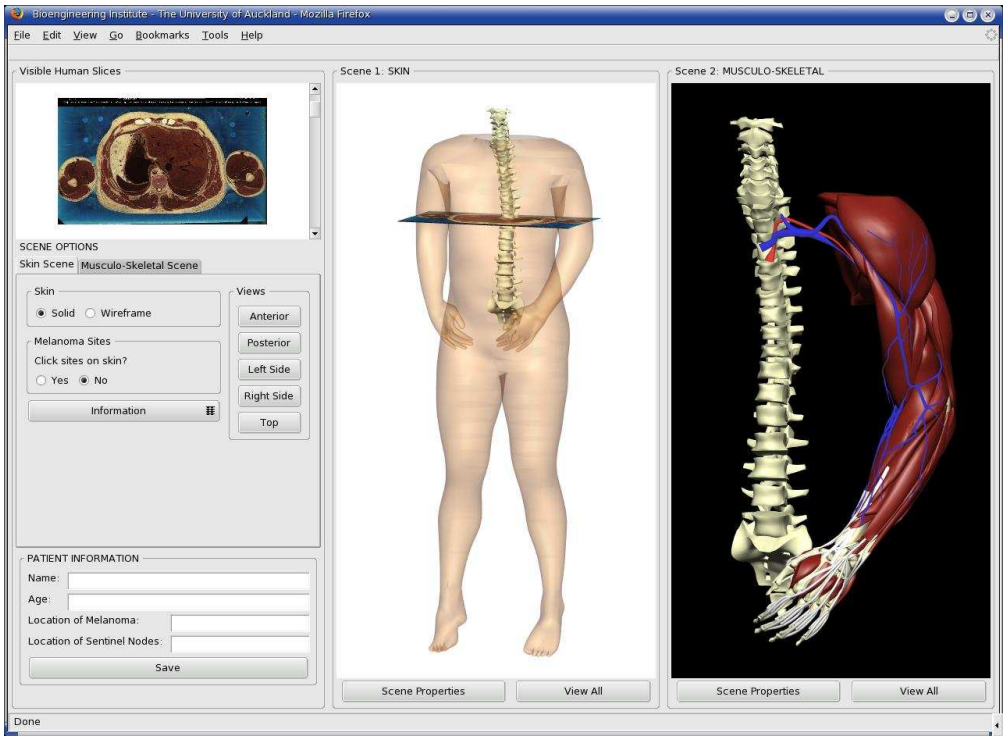

Figure 8.1: Preliminary example of an LS recording interface.

The interface could also provide complex visualisation and dynamic analysis of the data. An example of this kind of utility is shown in Figure 8.2, which displays different heat maps on the model. The model could be combined with the skin selection tool to predict melanoma spread from any element on the skin. To allow for a more statistically sound predictive tool, confidence intervals for drainage predictions from each skin element could also be determined using non-parametric bootstrapping (described in Section 6.5). Initially this tool could be installed at the SMU, however it may be beneficial to provide the tool to melanoma centres globally. This would allow the LS dataset to grow rapidly and provide a means to directly compare skin lymphatic drainage patterns observed around the world.

Improved Localisation of SNs

Further extension of the model could include work to enable more accurate localisation of the SNs. Two possible solutions could be utilised to address this issue. The first option has been previously described, and would involve development of an interface that nuclear medicine physicians or surgeons could use to accurately place the locations of SNs after LS or surgery respectively. A prototype example of such an interface was shown in Figure 8.1.

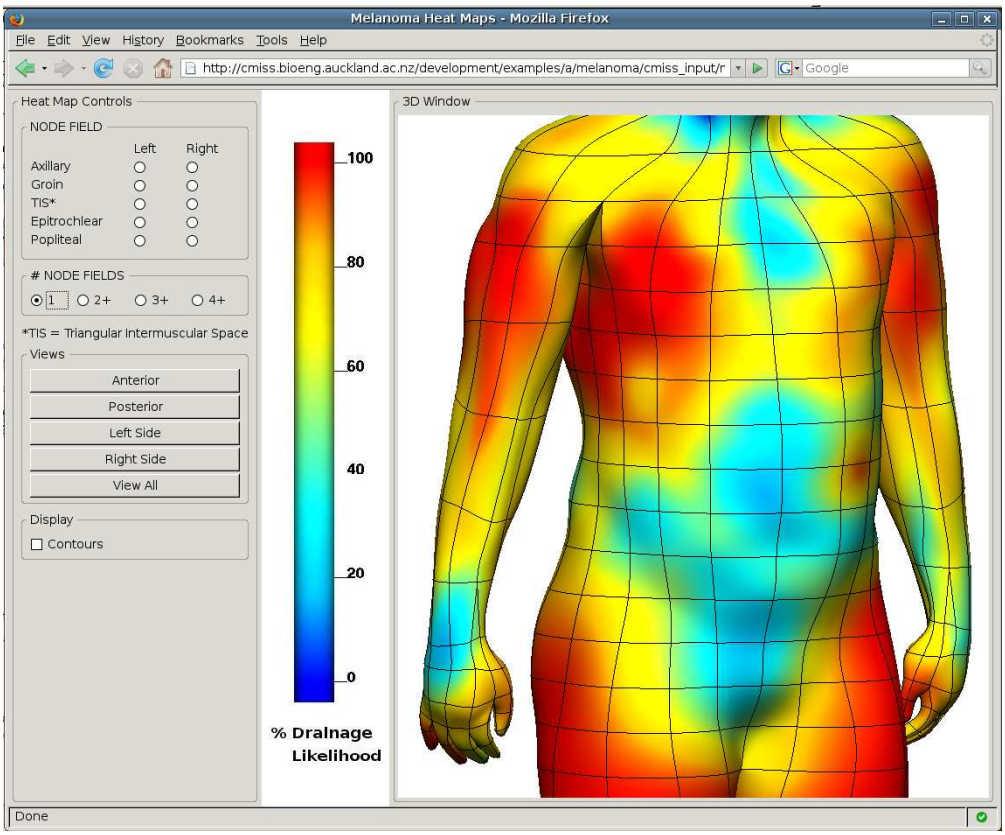

Figure 8.2: Interface enabling dynamic visualisation of the LS dataset.

A second and perhaps more accurate method however, would be to use SPECT/CT images, which accurately localises SN locations relative to each patient's anatomy. A new SPECT/CT machine has recently been purchased by the SMU and will be used during LS imaging in the near future. An example of the images produced by this machine, which combines functional SPECT images with anatomical CT images, is shown in Figure 8.3. Studies have shown that these images provide improved detection and localisation of SNs over LS, at times highlighting SNs that could not be seen on LS images (van der Ploeg et al. 2007). Either of these software solutions would require considerable time to implement, however they would have the potential to greatly improve knowledge about the spatial distribution of lymph nodes in the body.

Enhanced Anatomical Detail

Currently the model contains a detailed skin and lymph node model, however it could be extended to include additional anatomical detail such as the bones and musculature. FE models of the vertebrae used during statistical analysis of Sappey's lines (shown in Figure 7.4), and other bones

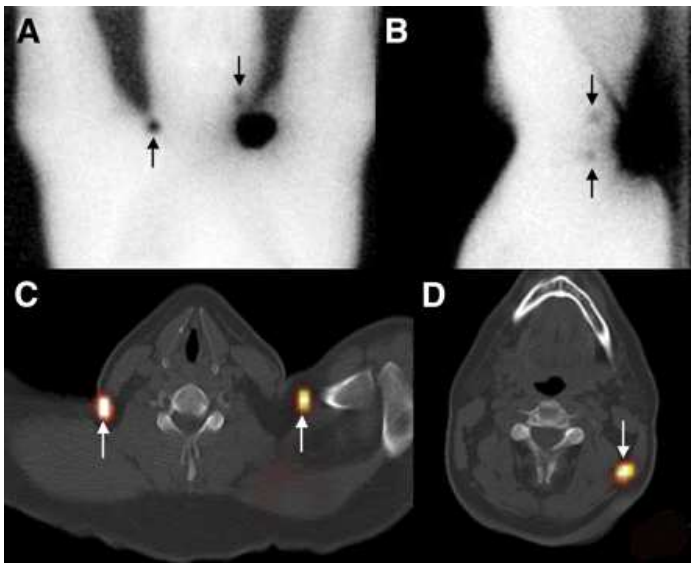

Figure 8.3: Example of (A and B) LS images versus (C and D) SPECT/CT images of a patient with melanoma medial to the scapula and three SNs. One SN was located in each supraclavicular fossa node field and the third SN was located cranial to the tumour site. Reproduced from van der Ploeg et al. (2007)

developed at the ABI could be included. Visualisation of bones and muscles in the interactive skin selection tool (developed in Chapter 4) for example, would provide clinicians with an anatomical reference for the overlaying skin.

It may also be possible to incorporate additional datasets to improve the accuracy of the lymph node model. As mentioned in Section 1.4, Qatarneh et al. (2006) have also developed a detailed lymph node model using VH images. Their model was developed to assist cancer radiation therapy, and was created by two observers who had experience and knowledge in localising lymph nodes. As a result, they have located more lymph nodes than the model created for this thesis. Their model has more nodes located in each of the node fields draining the skin (specified in Table 2.2), as well as additional nodes in other fields that do not drain the skin.

A company in the United States, called Touch of Life Technologies[2], have also investigated the location of lymph nodes on VH images. They have developed software for the purposes of anatomical education, including the VH Dissector Pro. This product is sold as a DVD which allows the user to select different anatomical structures, which it will then visualise in 3D using VH images from various orientations. Lymph nodes can be visualised and appear to have been located using segmentation methods. It is unclear however, how accurately they have been located or how many lymph nodes there are in the model.

[2]http://www.toltech.net/

These two groups offer potential for obtaining lymph node data in VH space that could be incorporated into the lymph node model in this study, providing additional anatomical validation. As mentioned in Section 2.6, it was very difficult to locate lymph nodes on VH images during model creation. Therefore the ability to compare the model with other studies would be highly valuable.

Another potential improvement could be provided by altering the skin model so that it is anatomically symmetric. Currently the skin model is not symmetric in the torso or the thighs, however this could be modified so that the entire skin surface is symmetric and more direct side comparisons and reflections of the LS data could be applied. The skin model could also be modified so that the elements are more equal in size. One method that could be implemented in future to address this problem would be to change the initial linear mesh created in Section 2.5, by moving the nodal positions and then refitting the model to the digitised data points.

Other Clinical Features

It would also be beneficial to increase the amount of data that is recorded during each specific LS study, which in turn would enable additional clinical features to be added to the model. This would allow epidemiological investigation into whether various characteristics of melanoma have any influence over possible lymphatic pathways. Features could include: Breslow thickness, presence or absence of ulceration, or whether metastatic melanoma is present in SNs. Also, it may be useful to include information about second tier nodes observed on LS. While these nodes are not important to locate during SNB, they could give interesting information about the path of lymphatic drainage beyond the first lymph nodes that drain the skin.

To further improve the accuracy of recording LS data for visualisation and analysis, details regarding whether individual patients have had previous surgery should be included. As mentioned in Section 1.4, previous nodal or other major surgery can affect normal lymphatic drainage patterns, and it is therefore important that these patients are not included during data analysis or subsequent drainage predictions. A database that allows clinical features to be recorded fully and systematically on patient examination would increase efficiency of data collection as well as accuracy.

Skin and Lymph Node Model Utility

Other research projects currently underway at the ABI have the capability for using the skin model, which provides the ability to initiate the development of projects with a specific focus on the skin. Currently Jor et al. (2007) are developing a discrete 3D fibre model of human skin, in order to

improve understanding of the relationship between its structure and function. This model has been developed by modelling microstructural properties of skin, which vary across the body. The skin model from this could be used to embed properties of skin in different regions of the body to analyse these differences.

Commercial applications of the skin model are also possible. The ABI has recently purchased a 3D scanning system[3], which is intended to collect data from a number of people with different body morphologies. The FE skin model will then be used as a base model which can then be morphed to fit each individual's specific morphology. From these customised skin models, additional data can be calculated specific to the individual, such as body volume indexes.

Links with the Auckland University of Technology[4] and the fashion industry have recently been established at the ABI, to investigate the utility of a computer model that allows an individual to virtually try on clothing. For this purpose, a skin mesh would be required which could then be morphed to a specific individual's measurements. The model would then visualise selected clothing to assess whether they would fit. The model could also include capability to be articulated, showing how the clothing would move with the individual.

Finally, the lymph node model developed in this work could provide the basis for future projects. Current research being conducted at the ABI into the immune system, in collaboration with the School of Biological Sciences[5] at the University of Auckland, involves modelling the T cell motion in lymph nodes. This could potentially be expanded to investigate and model aspects of the immune response across the whole body. The lymph node model could also be utilised to investigate the most effective means to administer vaccines.

8.3 Thesis summary

This thesis has involved creation of the first 3D anatomical model of skin lymphatic drainage, providing a computational framework to display and analyse patterns of melanoma spread. To create this model, melanoma LS data from over 5000 patients has been mapped from 2D LS images on a 3D FE model of the skin and a discrete lymph nodes model, using various free-form deformation and projection techniques.

Novel spatial heat maps and the interactive software tool developed using this mapped model showed that the most complex lymphatic drainage patterns were located on the torso near Sappey's

[3] http://www.4ddynamics.com/
[4] http://www.aut.ac.nz/
[5] http://www.sbs.auckland.ac.nz/

lines and on the head and neck. The upper limbs and upper regions of the torso were shown to almost always drain to the ipsilateral axilla, while the lower limbs always showed drainage to the ipsilateral groin. Skin of the head and neck frequently had two or more draining node fields, where cervical level II and preauricular node fields were the most common.

Detailed statistical analysis quantified that at least 12.5% of the torso melanoma sites drained across Sappey's lines, proving that they were highly inaccurate for predicting skin lymphatic drainage. Statistical symmetry testing indicated that most regions of skin were symmetric, while skin that indicated asymmetry was likely caused by an asymmetrical distribution of melanoma sites within that region and/or a sparsity of data. LS data from the symmetrical skin regions has then been reflected, providing a larger LS dataset to improve the statistical accuracy of the model.

Subsequent clustering analysis defined nine separate clusters on the skin model, where the torso was divided into regions similar to Sappey's lines. Significantly, a cluster formed in the middle of the torso, quantifying an area of skin that showed highly ambiguous drainage to axillary and groin node fields. Drainage statistics and associated confidence intervals quantified the accuracy of drainage predictions from each of these clusters.

In summary, this study has developed novel 3D visualisation and analysis of lymphatic drainage of the skin. The model and techniques developed provide a platform to record additional melanoma LS data in the future, to both improve knowledge about skin lymphatic drainage and potentially aid the clinical management of melanoma.

Appendix A

Sentinel Node Field Codes

The following table details the 43 separate SN fields as defined by the SMU and corresponding codes used to record them in their LS database described in Chapter 1.

CODE	NODE FIELD NAME	CODE	NODE FIELD NAME
Head and Neck Node Fields			
ro	right occipital	lo	left occipital
rprea	right preauricular	lprea	left preauricular
rposta	right postauricular	lposta	left postauricular
rc1	right cervical level I	lc1	left cervical level I
rc2	right cervical level II	lc2	left cervical level II
rc3	right cervical level III	lc3	left cervical level III
rc4	right cervical level IV	lc4	left cervical level IV
rc5	right cervical level V	lc5	left cervical level V
rsc	right supraclavicular fossa	lsc	left supraclavicular fossa
sm	submental		
Torso and Upper Limb Node Fields			
ra	right axilla	la	left axilla
repit	right epitrochlear	lepit	left epitrochlear
ric	right infraclavicular	lic	left infraclavicular
rtis	right triangular intermuscular space (TIS)	ltis	left TIS
rip	right interpectoral	lip	left interpectoral
rim	right internal mammary	lim	left internal mammary
rcm	right costal margin	lcm	left costal margin
inc	intercostal		
pv	paravertebral		
pa	paraaortic		
rp	retroperitoneal		
um	upper mediastinal		
Lower Limb Node Fields			
rg	right groin	lg	left groin
rpop	right popliteal	lpop	left popliteal
Other Node Fields			
in	interval node		

Table A.1: Sentinel node field codes.

Appendix B

Heat Maps and Frequency Displays

Heat maps visualising the likelihood of lymphatic drainage from the skin to various SN fields are given here, as well as frequency displays for node fields without sufficient LS data to generate heat maps. The methods for generating these displays were given in Chapter 4 and additional heat map results were presented in Chapter 5.

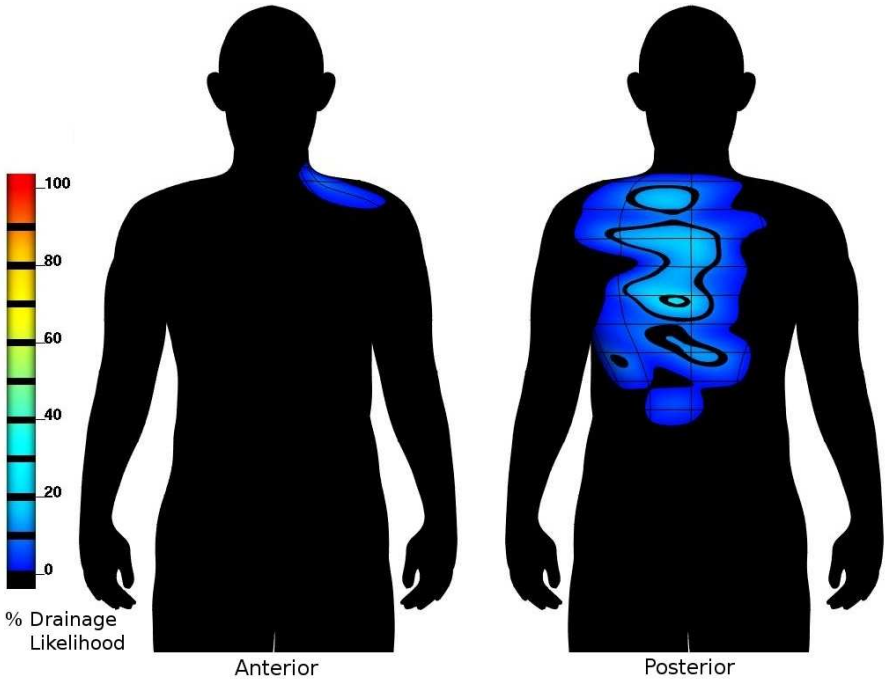

(a)

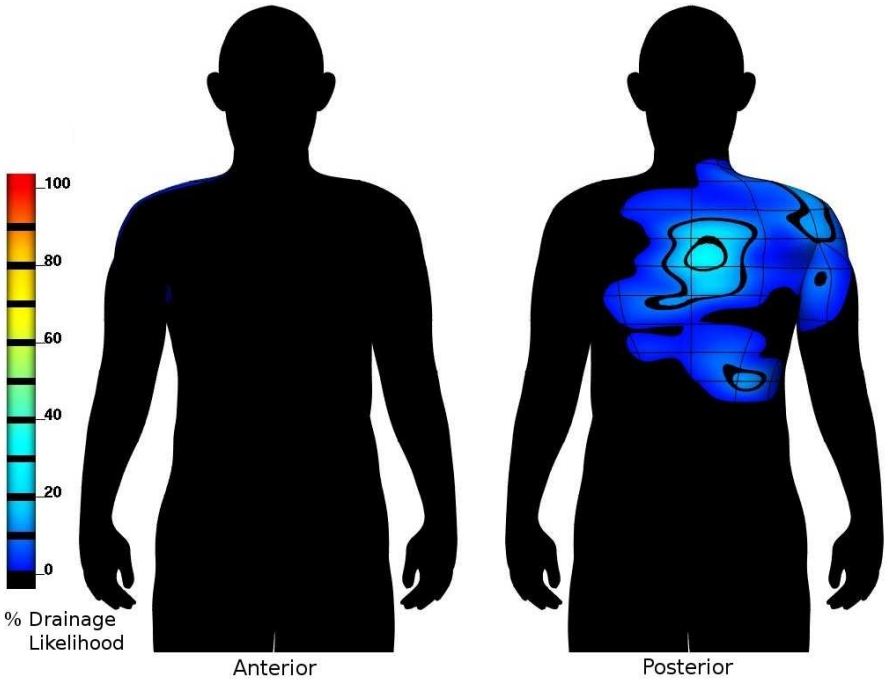

(b)

Figure B.1: Percentage likelihood that lymphatic drainage will occur to the (a) left and (b) right triangular intermuscular space node fields.

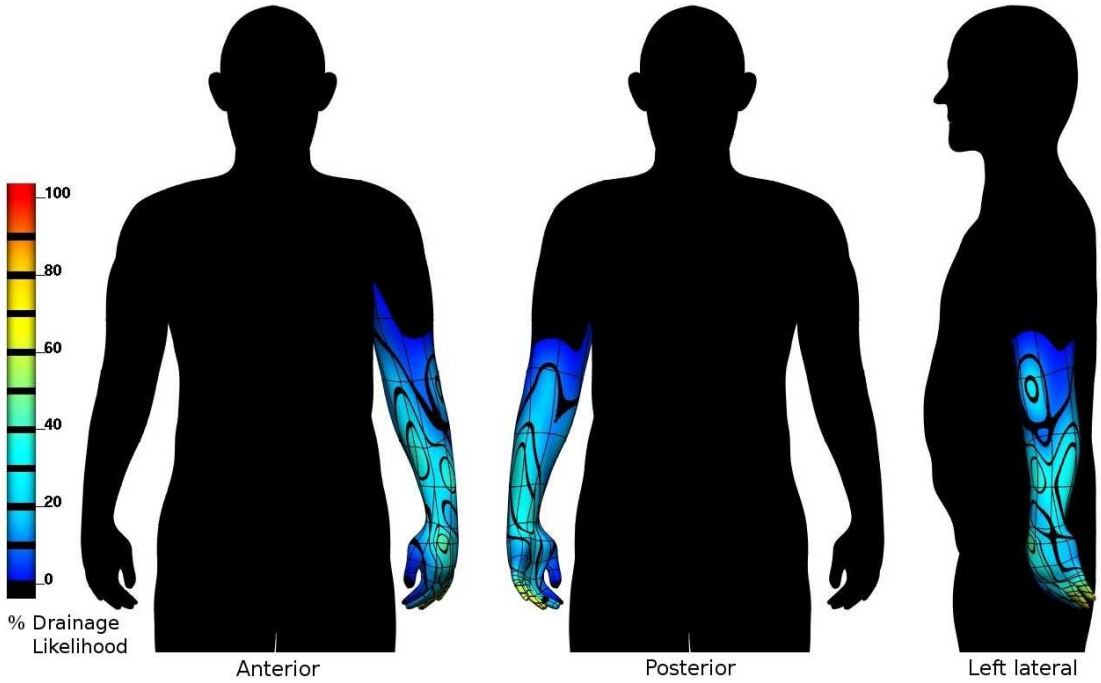

(a)

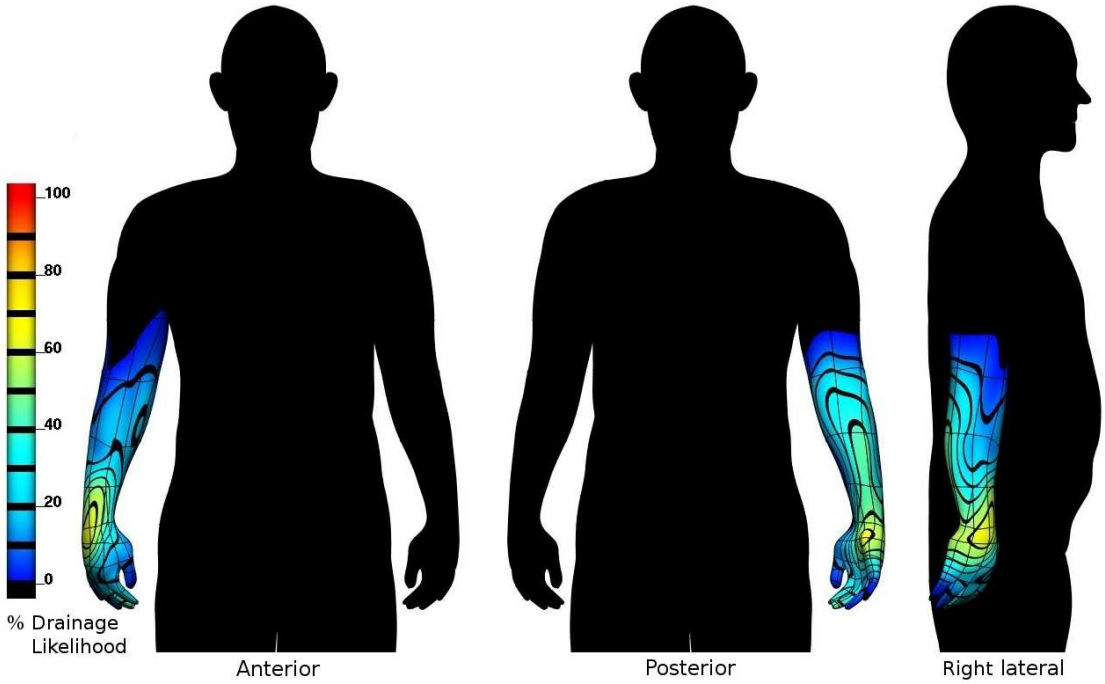

(b)

Figure B.2: Percentage likelihood that lymphatic drainage will occur to the (a) left and (b) right epitrochlear node fields.

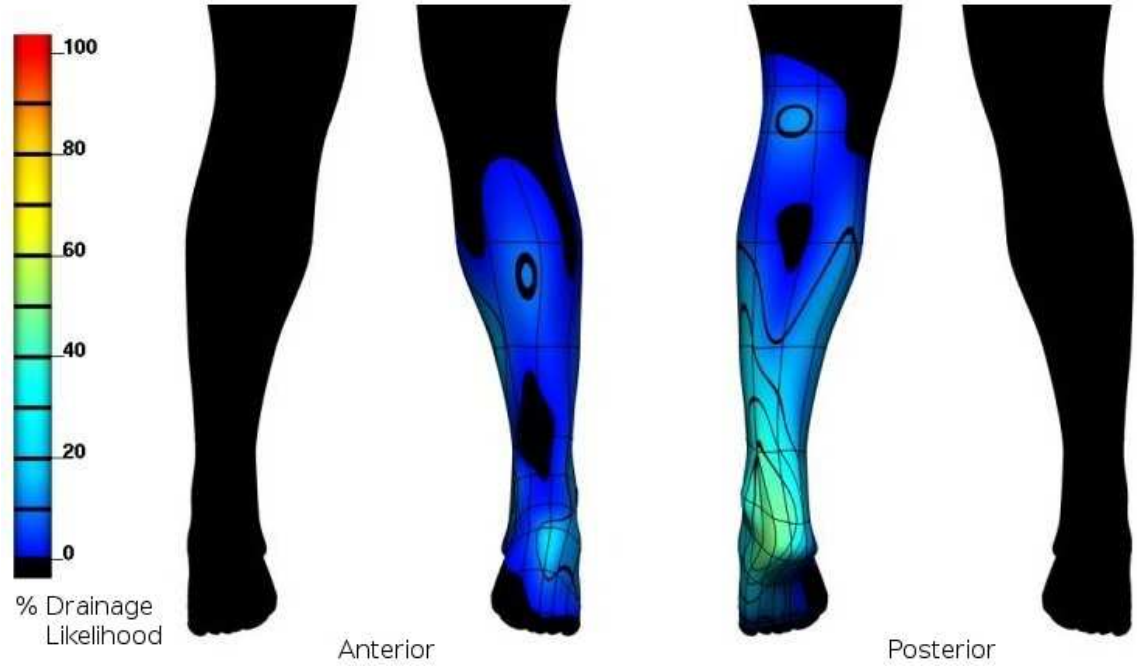

(a)

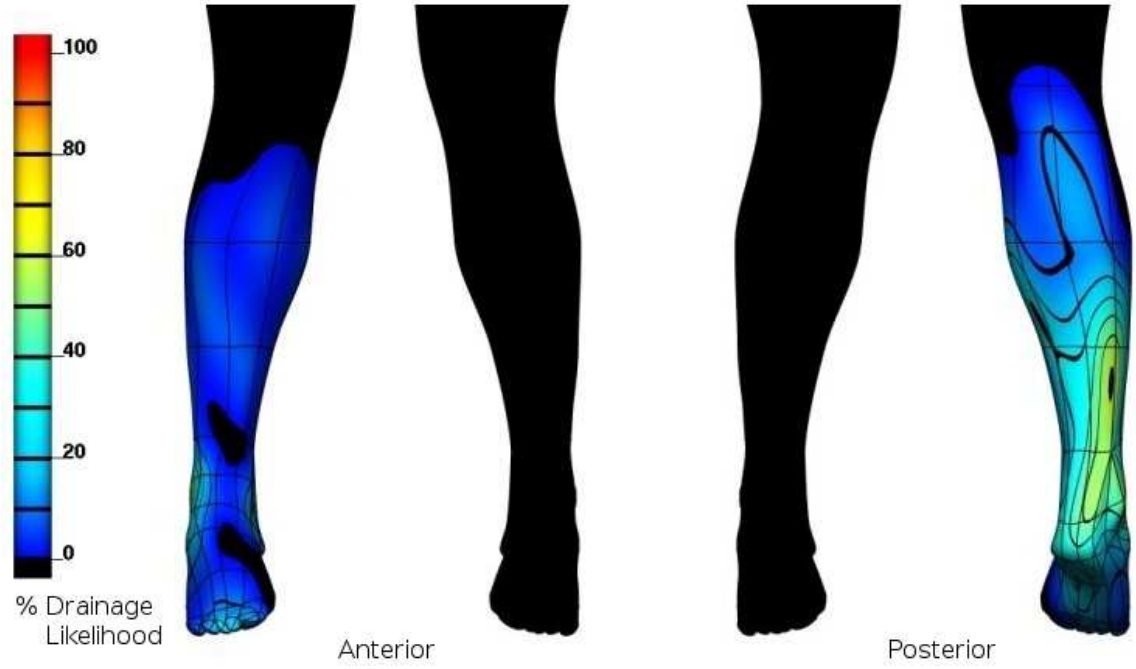

(b)

Figure B.3: Percentage likelihood that lymphatic drainage will occur to the (a) left and (b) right popliteal node fields.

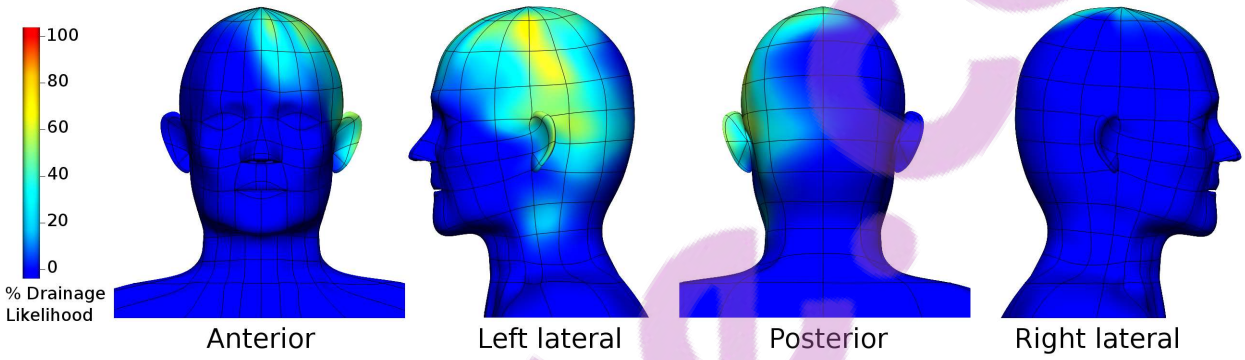

(a)

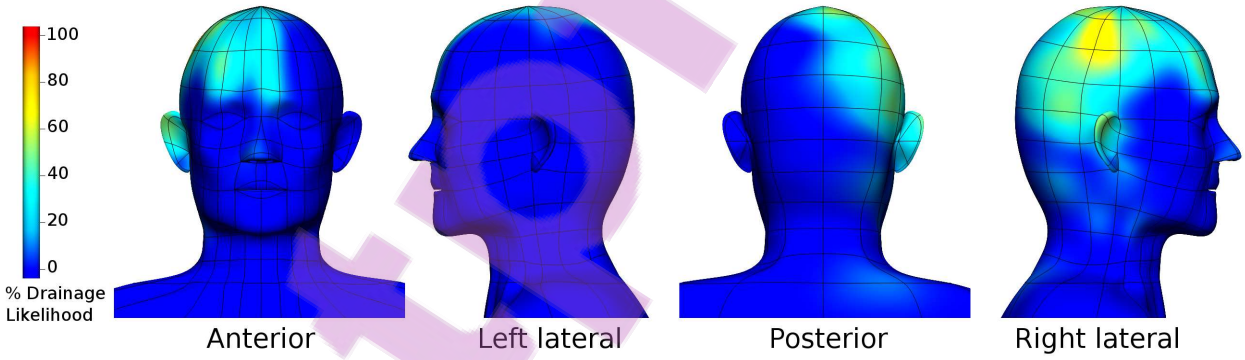

(b)

Figure B.4: Percentage likelihood that lymphatic drainage will occur to the (a) left and (b) right postauricular node fields.

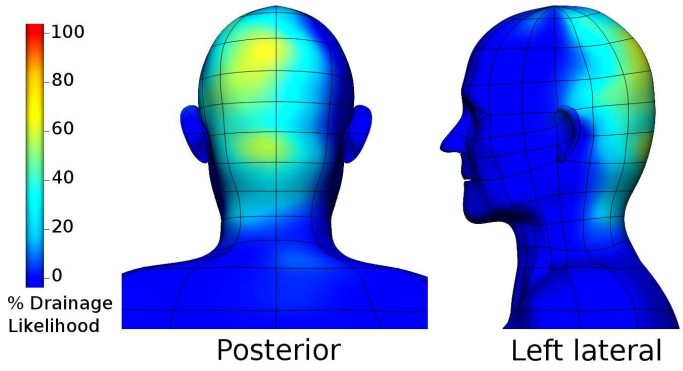

(a)

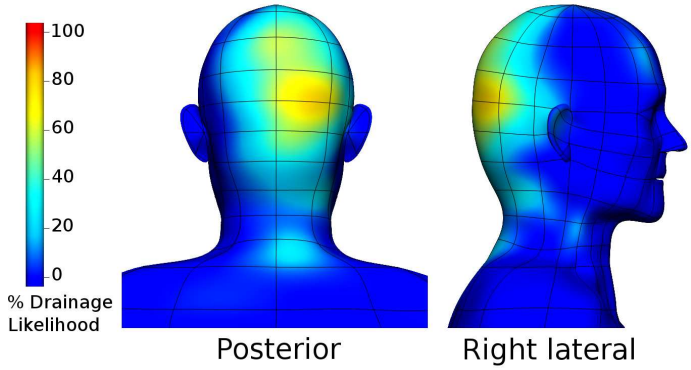

(b)

Figure B.5: Percentage likelihood that lymphatic drainage will occur to the (a) left and (b) right occipital node fields.

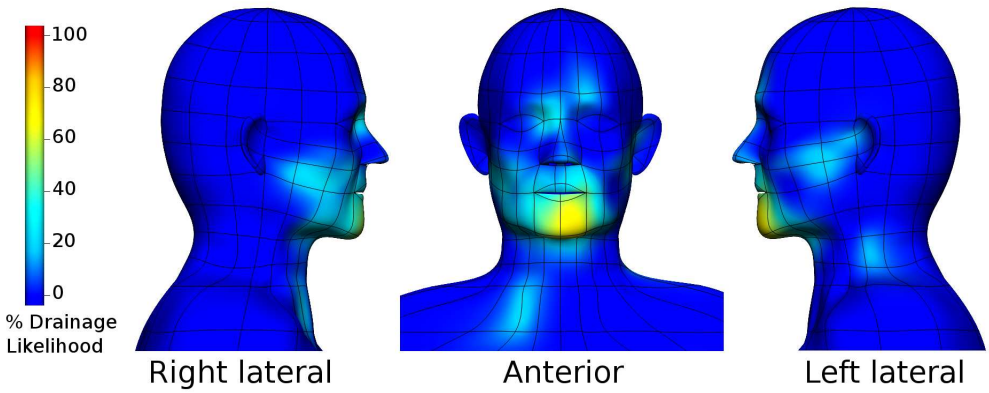

Figure B.6: Percentage likelihood that lymphatic drainage will occur to the submental node field.

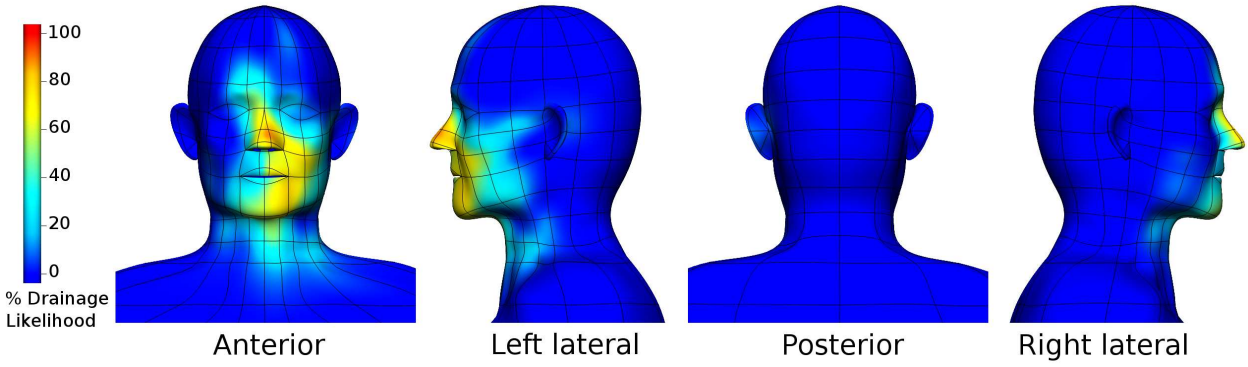

(a)

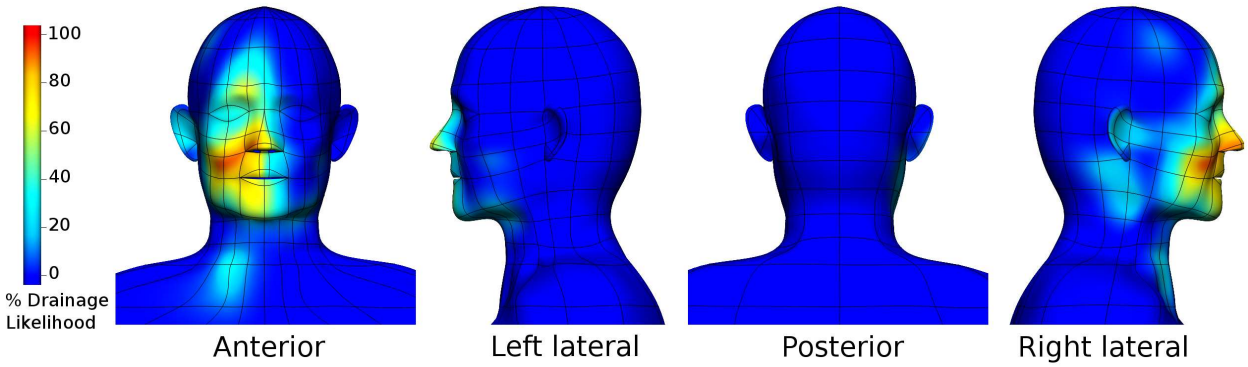

(b)

Figure B.7: Percentage likelihood that lymphatic drainage will occur to the (a) left and (b) right cervical level I node fields. These maps exclude submental nodes.

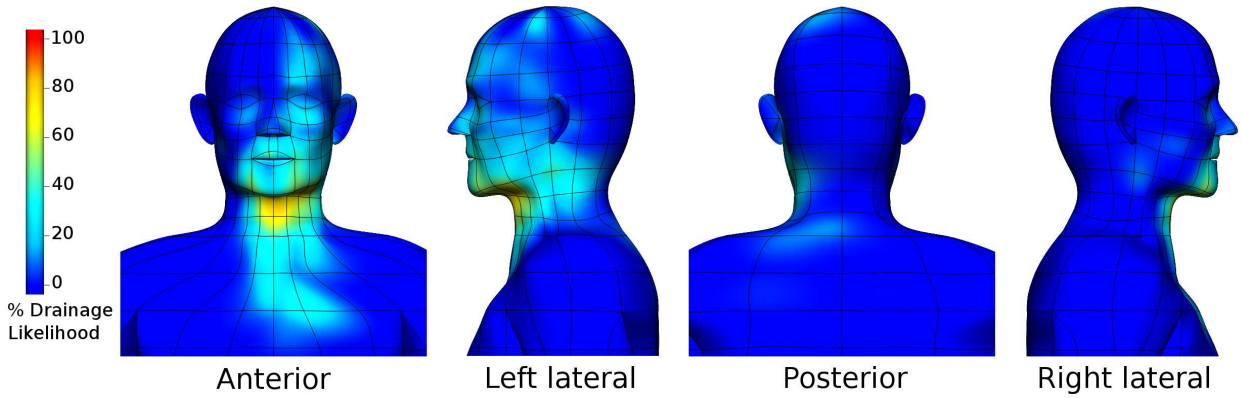

(a)

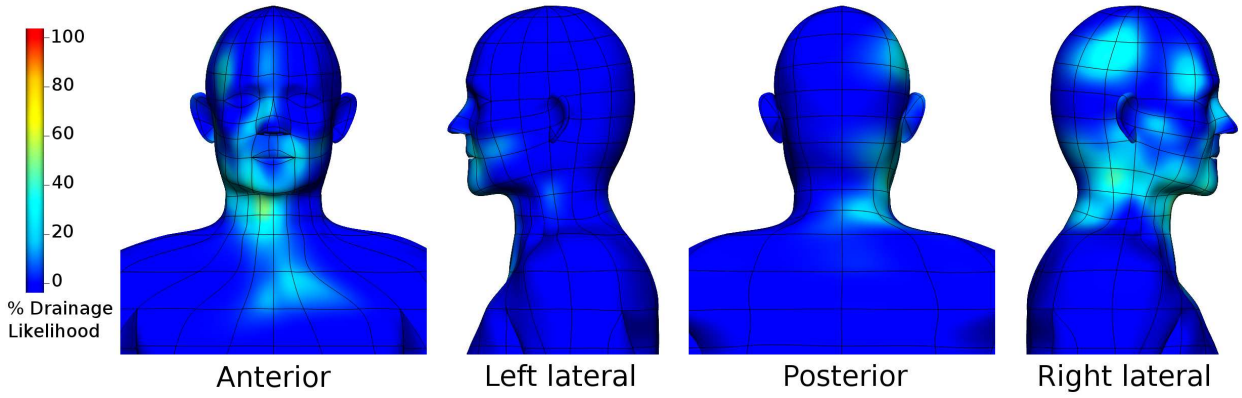

(b)

Figure B.8: Percentage likelihood that lymphatic drainage will occur to the (a) left and (b) right cervical level III node fields.

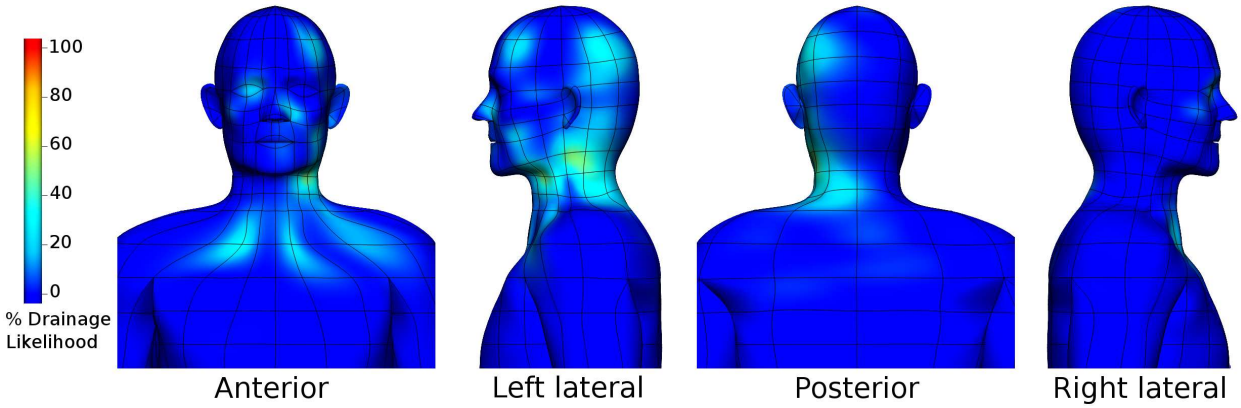

(a)

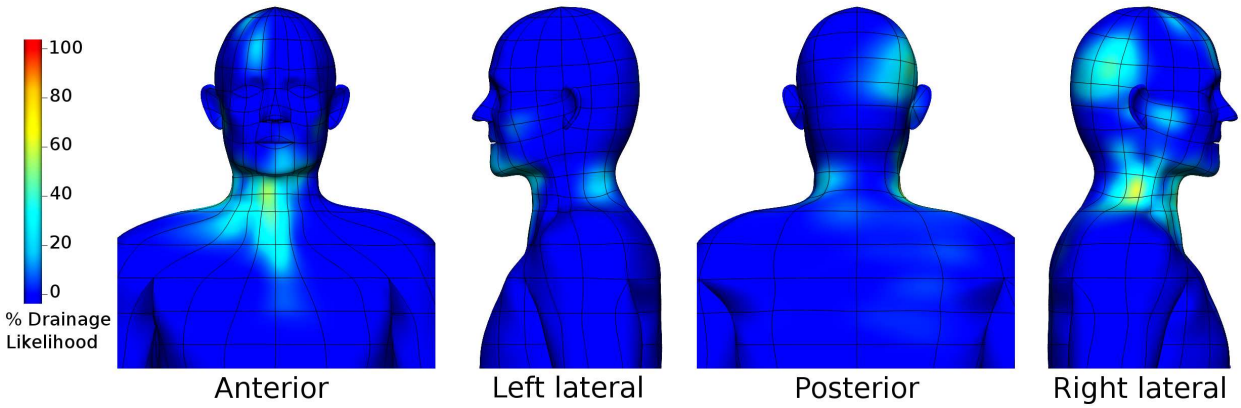

(b)

Figure B.9: Percentage likelihood that lymphatic drainage will occur to the (a) left and (b) right cervical level IV node fields.

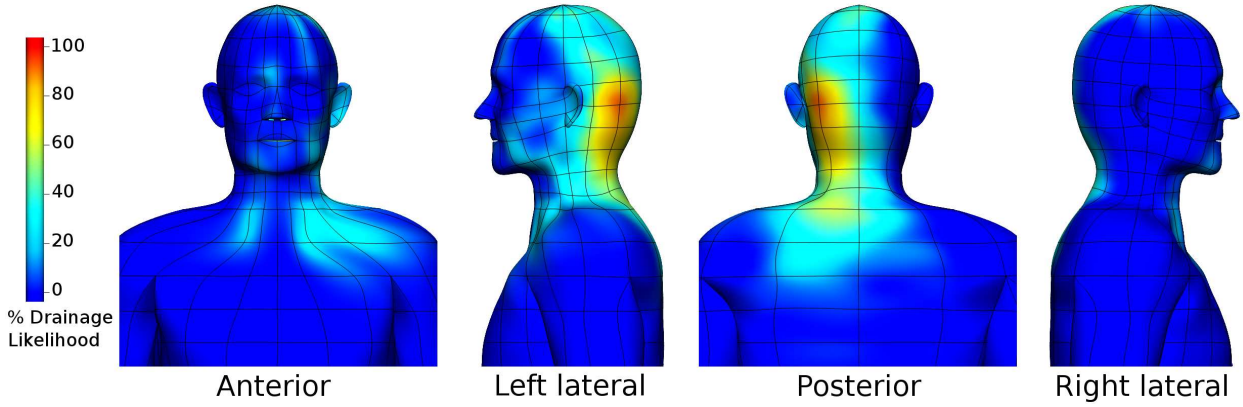

(a)

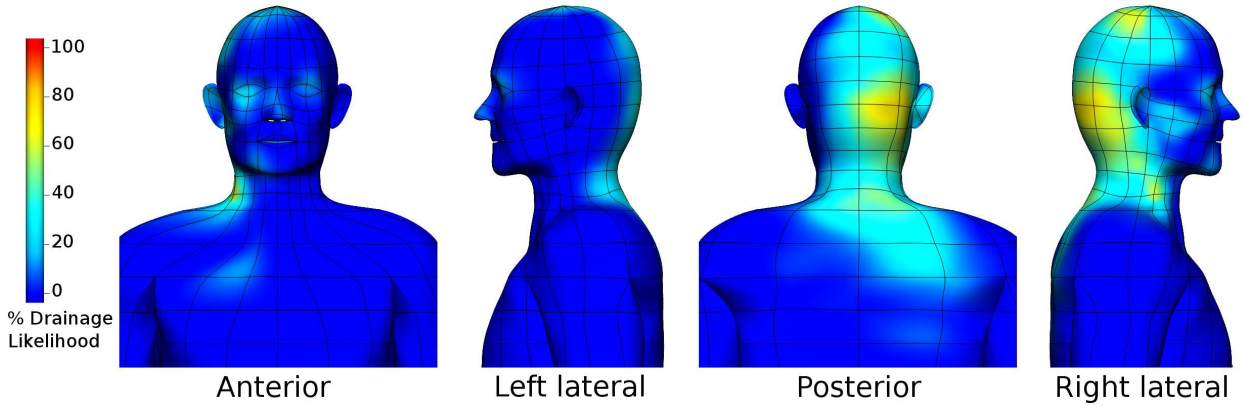

(b)

Figure B.10: Percentage likelihood that lymphatic drainage will occur to the (a) left and (b) right cervical level V node fields. These maps exclude supraclavicular fossa nodes.

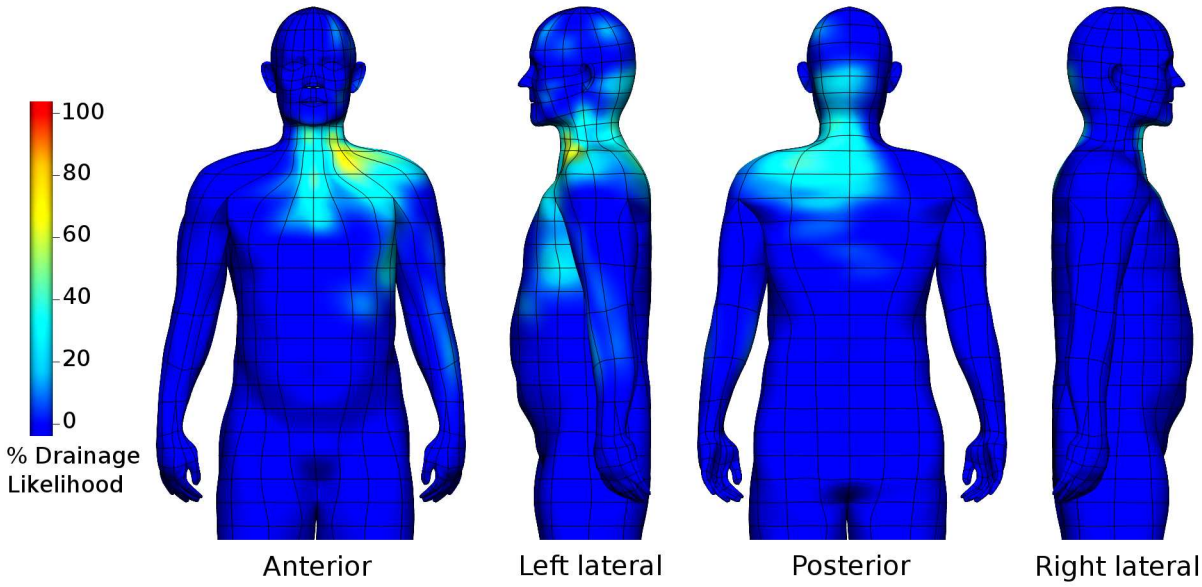

(a)

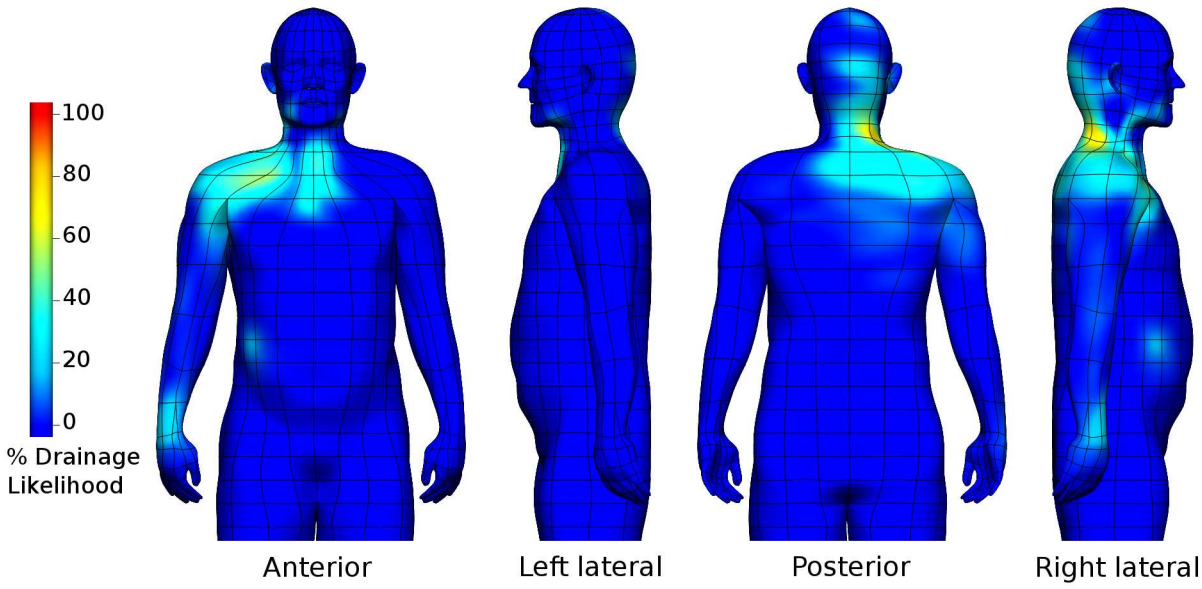

(b)

Figure B.11: Percentage likelihood that lymphatic drainage will occur to the (a) left and (b) right supraclavicular fossa node fields.

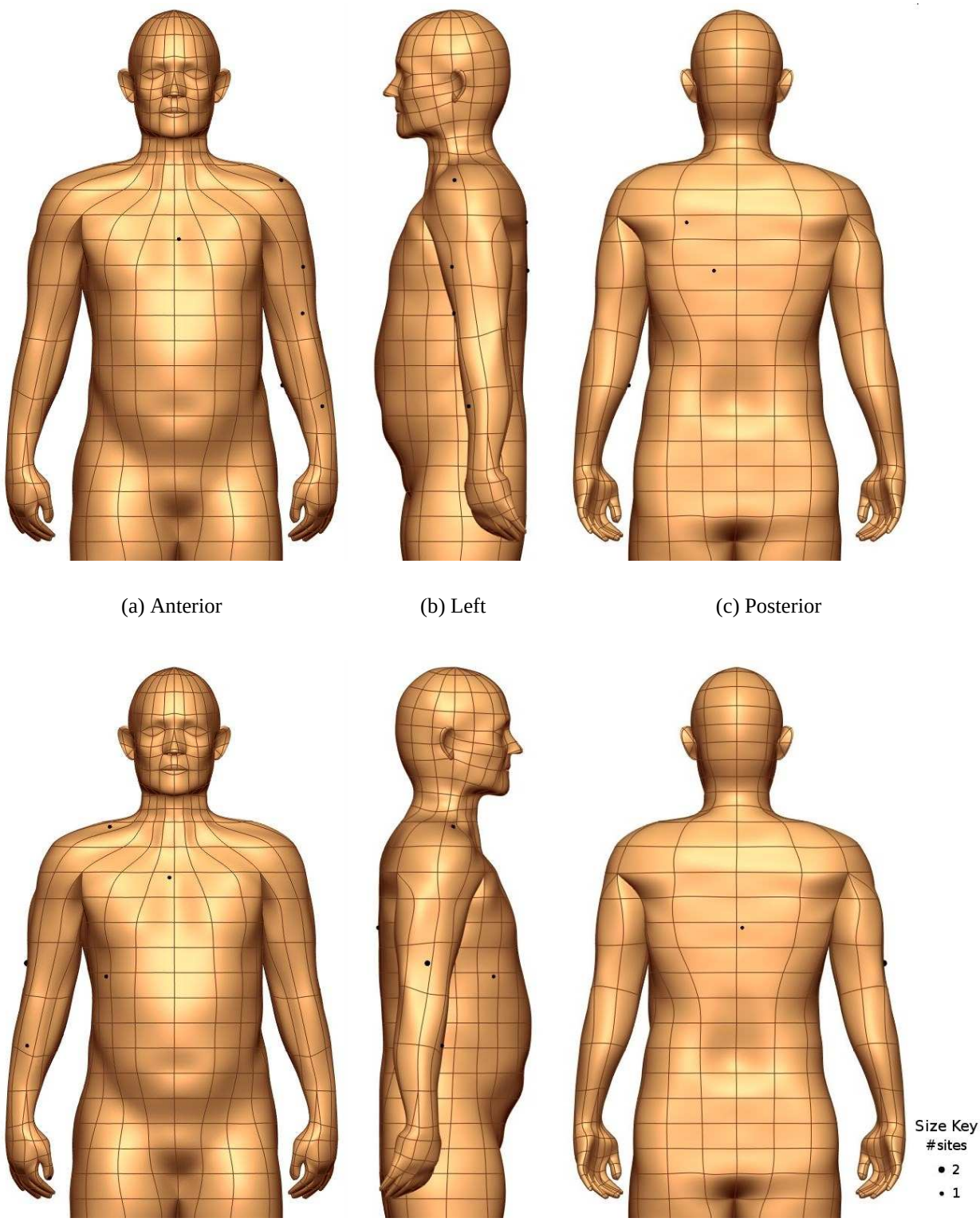

(a) Anterior (b) Left (c) Posterior

(d) Anterior (e) Right (f) Posterior

Figure B.12: Primary melanoma sites that have shown lymphatic drainage to (a-c) left and (d-f) right infraclavicular nodes.

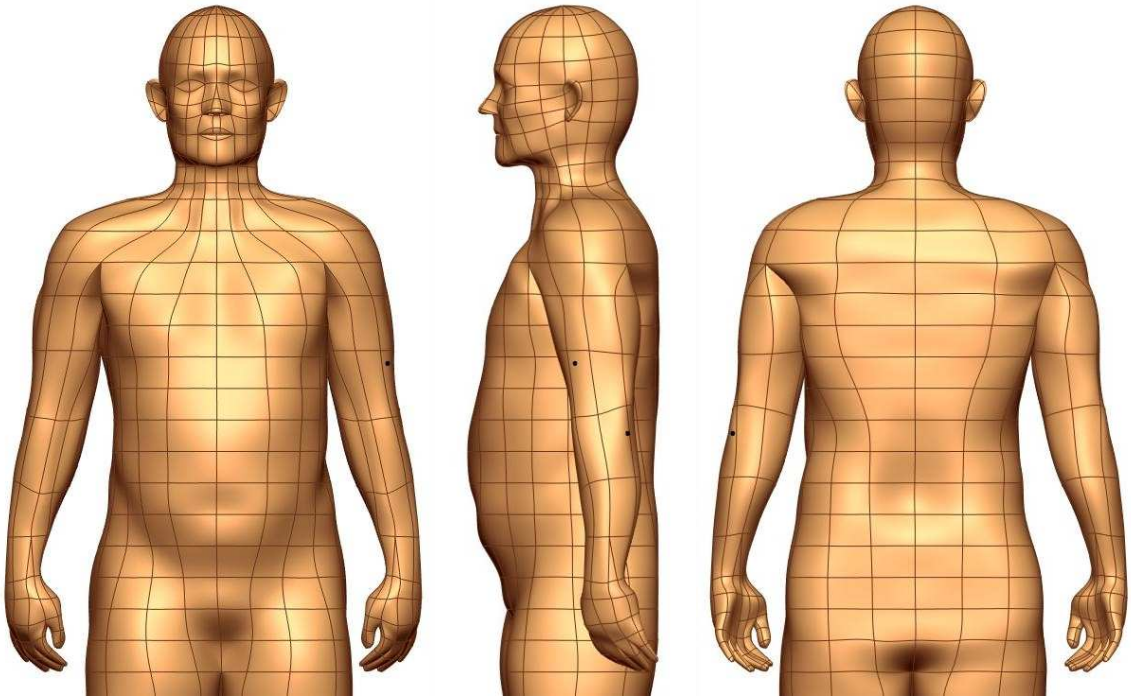

(a) Anterior (b) Left (c) Posterior

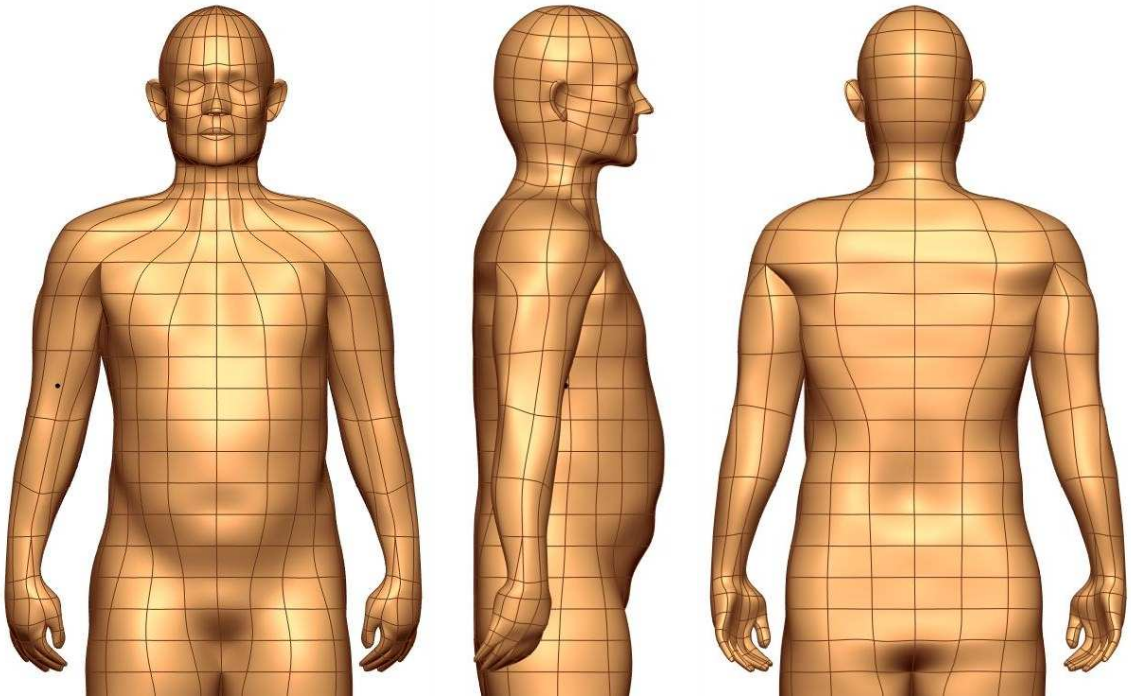

(d) Anterior (e) Right (f) Posterior

Figure B.13: Primary melanoma sites that have shown lymphatic drainage to (a-c) left and (d-f) right interpectoral nodes.

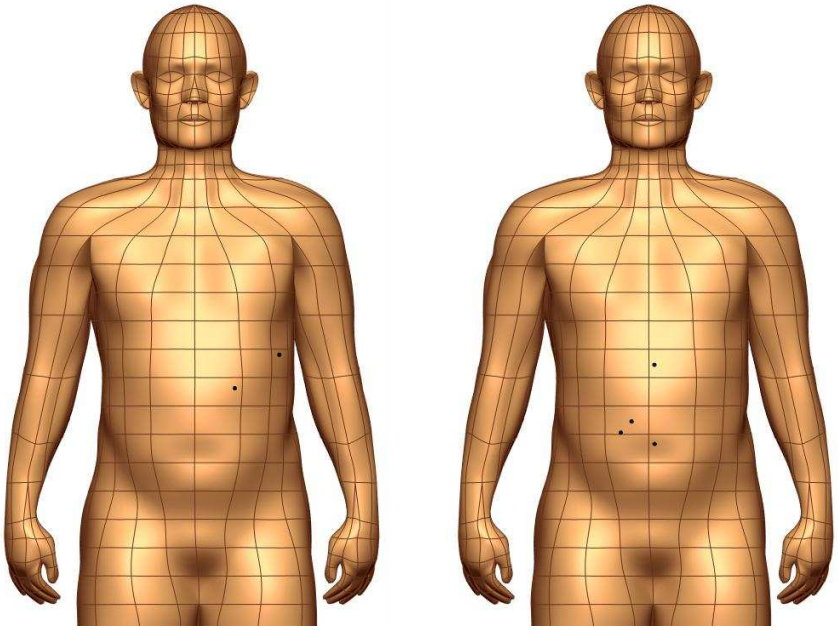

(a) (b)

Figure B.14: Anterior views showing primary melanoma sites that have shown lymphatic drainage to (a) left and (b) right internal mammary nodes.

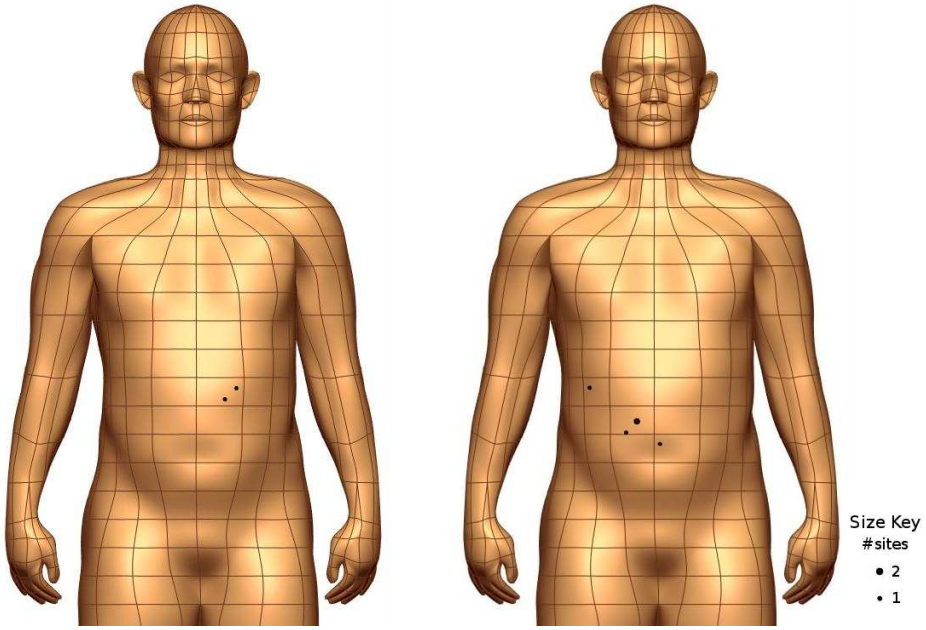

(a) (b)

Figure B.15: Anterior views showing primary melanoma sites that have shown lymphatic drainage to (a) left and (b) right costal margin nodes.

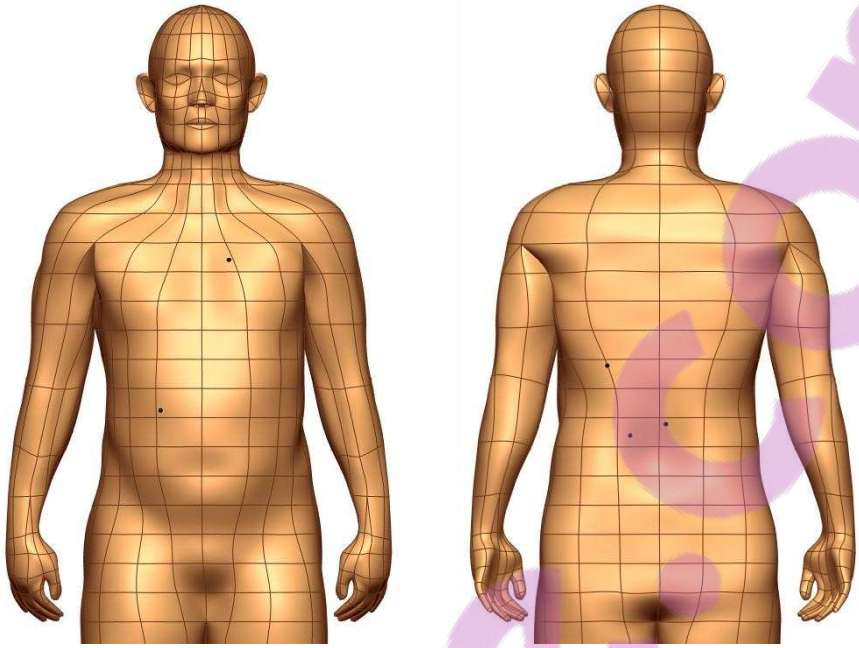

(a) Anterior (b) Posterior

Figure B.16: Primary melanoma sites that have shown lymphatic drainage to intercostal nodes.

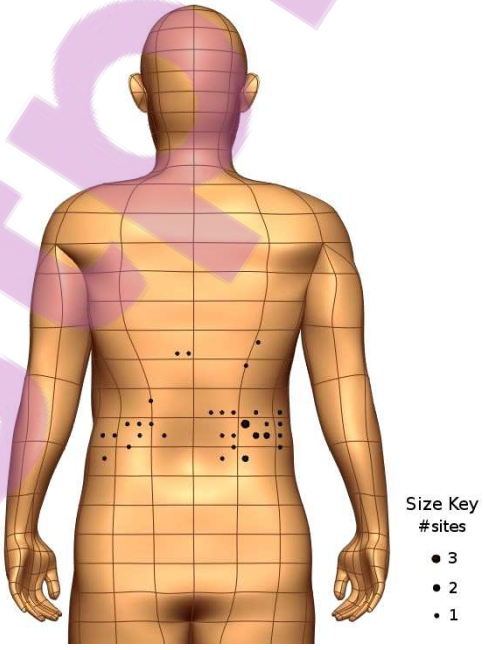

Figure B.17: Posterior view showing primary melanoma sites that have shown lymphatic drainage to paravertebral or paraaortic nodes.

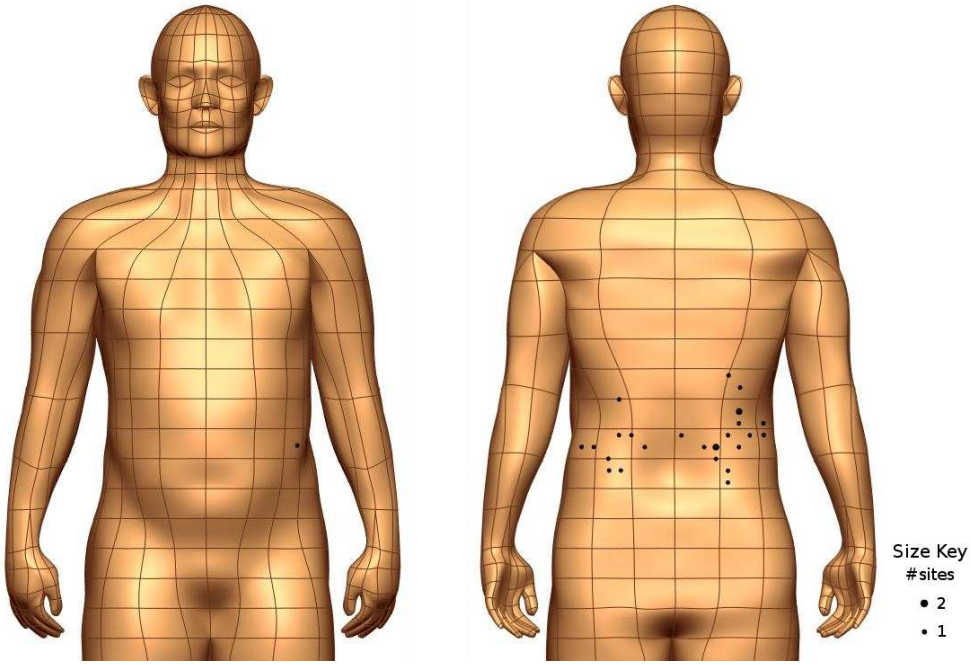

(a) Anterior (b) Posterior

Figure B.18: Primary melanoma sites that have shown lymphatic drainage to retroperitoneal nodes.

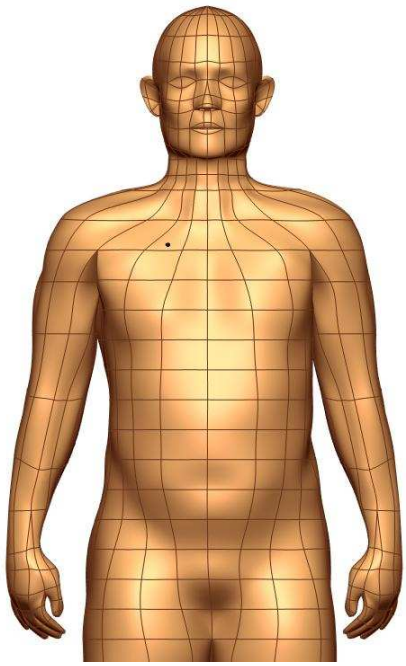

Figure B.19: Anterior view showing primary melanoma sites that have shown lymphatic drainage to upper mediastinal nodes.

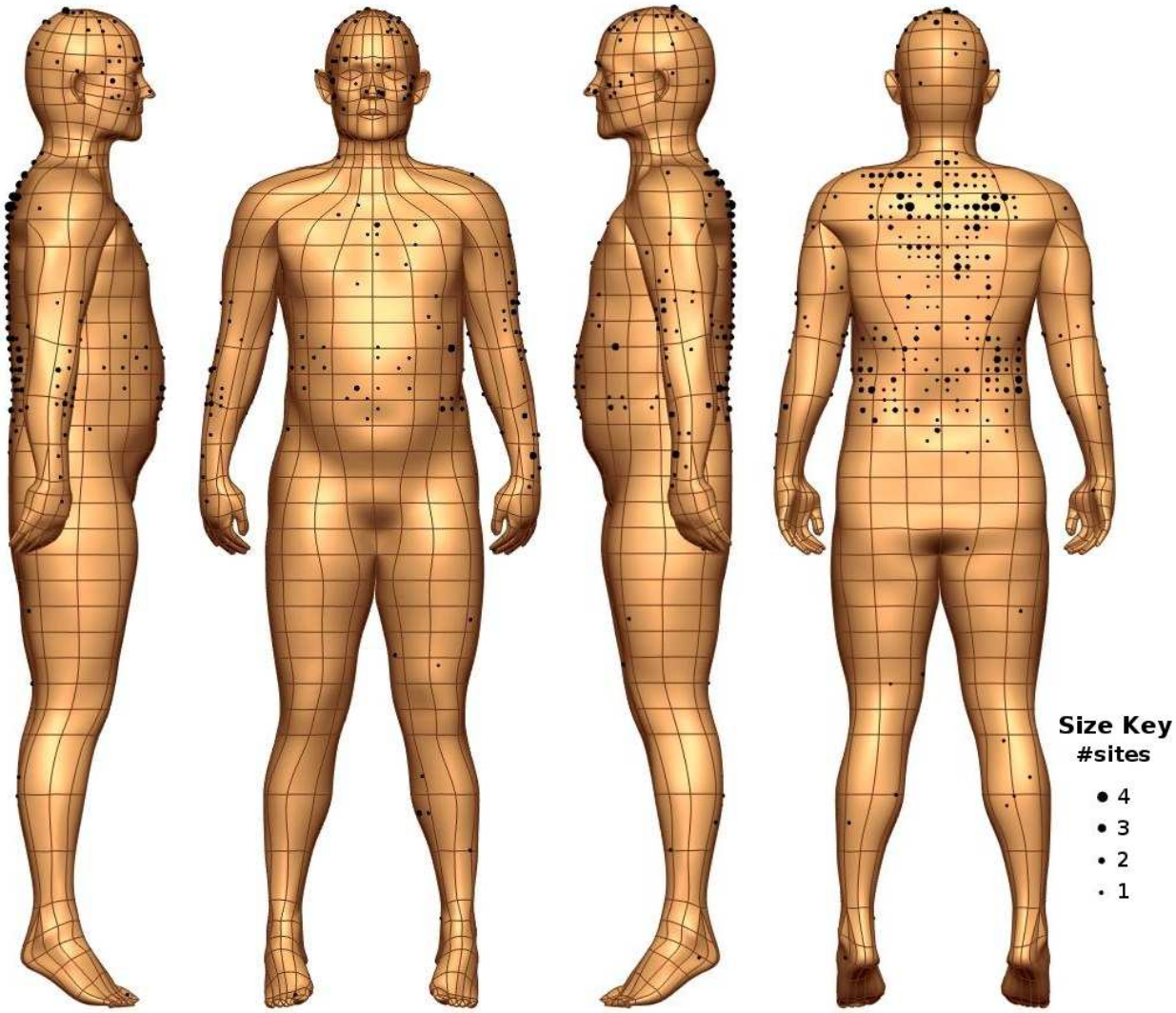

(a) Right (b) Anterior (c) Left (d) Posterior

Figure B.20: Primary melanoma sites that have shown lymphatic drainage to interval nodes.

Appendix C

Anatomical Geometry and Mapping Methods Paper

This paper describes the construction of the anatomical geometry and the methods used to map the SMU's LS data onto this geometry, representing Chapters 2 and 3. This paper was published in *Annals of Biomedical Engineering*.

Annals of Biomedical Engineering, Vol. 35, No. 8, August 2007 *(© 2007)* pp. 1444–1457
DOI: 10.1007/s10439-007-9315-9

Mapping Melanoma Lymphoscintigraphy Data onto a 3D Anatomically Based Model

HAYLEY M. REYNOLDS,[1] P. ROD DUNBAR,[2] ROGER F. UREN,[3,4,5] JOHN F. THOMPSON,[3,6] and NICOLAS P. SMITH[1,7]

[1]The Bioengineering Institute, University of Auckland, Private Bag 92019, Auckland, New Zealand; [2]School of Biological Sciences, University of Auckland, Auckland, New Zealand; [3]The Sydney Melanoma Unit, Royal Prince Alfred Hospital, Camperdown, Sydney, NSW, Australia; [4]The Discipline of Medicine, University of Sydney, Sydney, NSW, Australia; [5]Nuclear Medicine and Diagnostic Ultrasound, RPAH Medical Centre, Sydney, NSW, Australia; [6]The Discipline of Surgery, University of Sydney, Sydney, NSW, Australia; and [7]University Computing Laboratory, University of Oxford, Oxford, UK

(Received 25 August 2006; accepted 9 April 2007; published online 24 April 2007)

Abstract—This study describes three-dimensional (3D) visualization of two-dimensional (2D) melanoma lymphatic mapping data, to provide a framework for analysis of melanoma spread patterns and a platform for recording new lymphoscintigraphy (LS) data more accurately in 3D. Specifically, the Sydney Melanoma Unit's LS database of over 5000 patients' primary cutaneous melanoma sites and sentinel lymph nodes have been mapped from 2D images onto a 3D anatomically based model. Anatomically accurate model geometries were created using the Visible Human dataset, giving a bicubic finite element skin mesh and discrete sentinel lymph node model. The full dataset of 2D melanoma site coordinates, excluding the head and neck, has been transformed onto this 3D skin mesh via free-form deformation and projection techniques. Sentinel lymph nodes were mapped onto the generic lymph node model for each patient. Preliminary spatial analysis indicates that a patient with a primary melanoma on the torso around the waist (on the standardized 3D model this region is 180 mm above and 130 mm below the umbilicus) with lymphatic drainage to the left axilla or left groin, will have a 17.7% probability of dual drainage to both node fields, with 95% confidence limits between 14.5 and 21.0%.

Keywords—Lymphatic mapping, Lymphatic drainage, Skin, Finite element, Mathematical model.

INTRODUCTION

The incidence of cutaneous melanoma is increasing steadily in most Western countries. Furthermore, there is currently no wide effective treatment for disseminated disease and early diagnosis gives the best chance of cure by surgical removal of the primary tumor.[13] Melanoma arises in the epidermis, commonly appearing as a darkly pigmented lesion termed the 'primary' melanoma. Without treatment, melanoma can extend deeper into the skin, enabling cancerous cells to enter the lymphatics or the bloodstream. Usually the earliest sign of metastatic spread beyond the primary melanoma site is located in regional lymph nodes.[14]

Sentinel lymph node biopsy (SLNB) is a technique used to determine whether melanoma has spread to regional lymph nodes.[8] It involves biopsy of the first lymph node(s) that melanoma cells will reach if they have metastasized. These nodes are termed sentinel nodes (SNs), and are best defined as any lymph node receiving direct lymphatic drainage from a primary tumor site.[16] SNs are located with lymphatic mapping via lymphoscintigraphy (LS) imaging, which is conducted by injecting a radioactive tracer into the dermis of the skin around the primary melanoma or excision biopsy site. The radioactive tracer is imaged (as shown in Fig. 1) traveling from the skin site through lymphatic vessels and into the SN(s).[18] Each SN is then surgically removed and examined for tumor.

Physicians at the Sydney Melanoma Unit (SMU), Australia, have been performing LS for more than 15 years and currently have the world's largest LS database containing details of over 5000 treated patients.[14,20] The site of each patient's primary melanoma is recorded at the time of LS as an (X, Y) coordinate on one of six hand-drawn generic body outline maps. The maps describe different regions of the body: anterior and posterior torso including the upper limbs, head and neck (the anterior torso body map is shown in Fig. 2a). The anterior and posterior legs from the hip level downwards, and right and left lateral views of the head and neck. Note that the palms of the hands are facing backwards in the anterior and posterior torso

Address correspondence to Hayley M. Reynolds, The Bioengineering Institute, University of Auckland, Private Bag 92019, Auckland, New Zealand. Electronic mail: h.reynolds@auckland.ac.nz

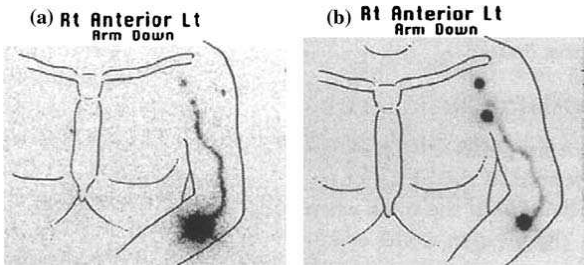

FIGURE 1. LS images of patient with primary melanoma on their forearm: (a) early imaging (10 min post injection) tracks the lymph vessel draining the skin site; (b) late imaging (two and half hours post injection) shows two SNs located in the axilla. Reprinted from Thompson and Uren,[15] Fig. 1, p. 350, Copyright 2004, with permission from Elsevier.

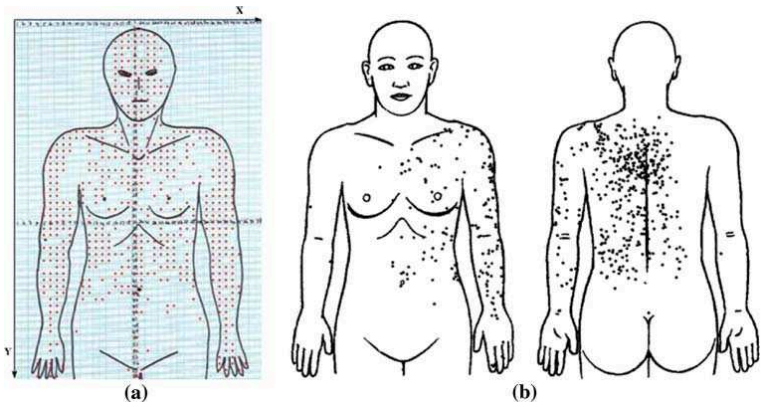

FIGURE 2. The SMU's LS database: (a) the anterior torso body map with melanoma (*X, Y*) coordinates plotted; (b) anterior and posterior 2D displays showing melanoma sites that drain to the left axillary node field. Reprinted from Uren *et al.*,[21] Fig. 4.3, p. 58, Harwood Academic Publishers, Copyright 1999, with permission from Taylor & Francis.

body maps and do not correspond to the standard anatomical position. In this study the term 'arm' describes the region of the upper limb from the level of the armpit to the wrist, while the term 'leg' refers to the lower limb from the level of the hip to the ankle.

Each body map is divided into grid units, where one unit equates to approximately 1.5–2 cm^2 on the skin. Clinicians have recorded the (X, Y) coordinates manually, after visually normalizing each patient's LS images. The node field location of each SN is recorded in the database as an abbreviated code. For example, an SN in the left axillary node field is recorded as 'la'. A list of the 43 node fields are detailed in Table A1.

The SMU data demonstrate that lymphatic drainage of the skin is highly variable between patients, and hence that melanoma does not spread in a clinically predictable manner.[21] Extensive tabulated statistics have been published presenting the relationship between primary melanoma sites and sentinel lymph node locations.[17,20] The SMU has also published two-dimensional (2D) displays[20,21] generated with geographical information systems software (see Fig. 2b), however these displays lack information in the third dimension. Furthermore, these 2D mapping records have had limited capacity for visualization and analysis for both clinical and basic science applications. To date, there has not been an accurate method to visualize melanoma LS data in three-dimensions (3D).

With recent advances in anatomically based computer modeling[4,10] the opportunity is now available to map these data onto a 3D anatomical framework for improved visualization and analysis. This study presents a technique to map the SMU's full LS database onto an anatomically based 3D model of the skin and lymph nodes. This will allow for an improved understanding of the functional role of lymphatic anatomy,

and also create a framework for the spatial statistical analysis of potential patterns of melanoma spread. The ultimate goal of this project is to provide a tool to help aid melanoma diagnosis and treatment and this report outlines the development of the anatomical framework required to achieve this goal.

METHODS

Anatomical Model Geometry

Skin Model Construction

A model of the skin surface has been created using high resolution transverse images of the Visible Human (VH) male dataset.[1] VH image slices are 1 mm in thickness, have a pixel size of 0.32 mm square, and measure 1760×1024 pixels.[11] The following steps have been taken to create the skin mesh:

1. Data digitization: the skin surface was visually located on a series of stacked 2D VH images (Fig. 3a) and manually digitized to create a 3D data cloud. Data points were digitized approximately 20 mm apart on each image slice for the skin of the torso, while data points were placed approximately 10 mm apart for the upper and lower limbs. The torso has been digitized on every 10th VH slice, to create data points 10 mm apart in the vertical direction, while the arms and legs were digitized at 5 mm intervals. A higher resolution of data points was required to accurately describe the anatomy of the hands and toes, therefore the hands were digitized using slices separated at 2 mm and the toes using slices separated at 3 mm. In total, 23,549 data points were digitized to define the VH skin surface.
2. Initial linear mesh: data points were selected from the digitized data cloud at regular intervals. These data points were converted to nodes to construct linear finite elements in rectangular Cartesian coordinates to approximate the skin surface (Fig. 3b). The full skin model has been constructed using 842 nodal points, and the mesh topology has been designed to accurately reflect the skin anatomy with a minimal number of elements. Most elements are standard 4-noded elements, however at complex regions such as the armpits, the groin, and finger and toe bifurcations, collapsed elements[6] were required. At bifurcations in the mesh, such as between the fingers, versions at the nodes were required to enable multiple derivative values to be stored for the ξ directions,[6] where ξ is defined as the local or material coordinate within an element. Figure 4 shows the palmar surface of the left hand which utilizes collapsed elements at the wrist to reduce the number of elements in the arm while maintaining continuity with the elements required to accurately model the fingers. Bifurcations between the fingers can also be seen.
3. Fitting: the initial linear mesh was then fitted to the digitized data points using a non-linear fitting

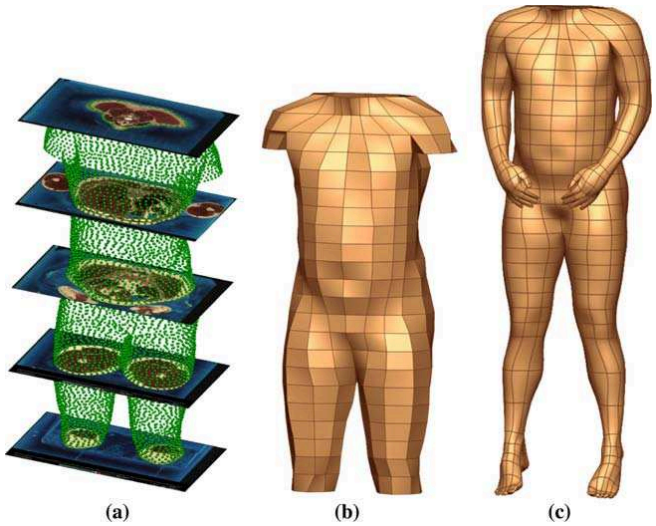

FIGURE 3. Construction of the skin model: (a) digitized data cloud for the torso created from stacked transverse VH images; (b) initial linear mesh of the torso; and (c) the complete fitted skin mesh.

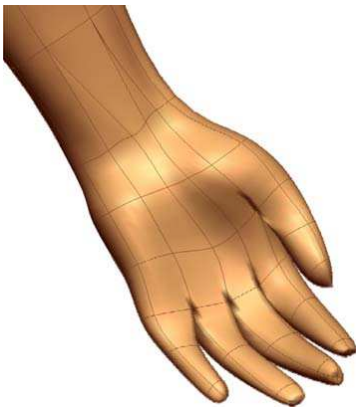

FIGURE 4. The fitted skin of the palmar surface of the left hand. Nodal versions have been used at bifurcations between the fingers. Collapsed elements can be seen at the wrist.

process[2] to minimize the distance between the data points and their orthogonal projections on the mesh surface (see Fig. 5). Bicubic Hermite[4] interpolation has been used for the skin elements to ensure C^1 continuity and provide both an accurate fit to the data and a computationally efficient representation. The objective function, F, to be minimized is given by

$$F(\mathbf{u}_n) = \sum_{d=1}^{N} \|\mathbf{u}(\xi_{1d}, \xi_{2d}) - \mathbf{z}_d\|^2 + F_s(u_n) \qquad (1)$$

where $\mathbf{u}_n$ is a vector of the nodal values being fitted, which are located at vertices in the mesh. $\mathbf{u}$ is the vector of interpolated coordinates which are a function of the fitted nodal values given by $\mathbf{u}_n(\xi_{1d}, \xi_{2d})$ are the local material coordinates for each data point calculated from the orthogonal projections of the data onto the mesh, and $\mathbf{z}_d$ are the global coordinates of the data points. $F_s(\mathbf{u}_n)$ is a Sobelov smoothing penalty function[2] of the mesh derivatives introduced to maintain smoothness of the mesh given a small amount of noise which is introduced via the digitization process.

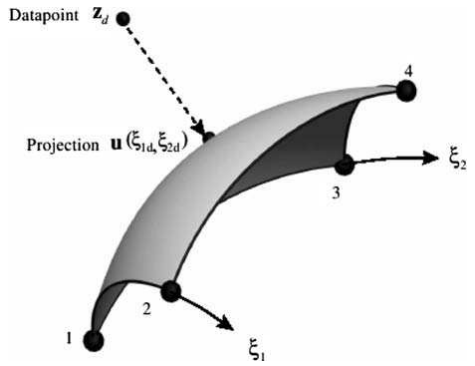

FIGURE 5. Datapoint z_d orthogonally projected onto the face of a 2D element to give the closest point $u(\xi_{1d}, \xi_{2d})$.

Since the skin model construction was a manually labor-intensive process, it has been fitted in sections. The arm and leg from one side of the body were fitted individually and then reflected to produce the opposing limbs. The fitted torso was connected to the arm and leg meshes to create the final skin mesh as shown in Fig. 3c. The final mesh contains a total of 842 nodes and 886 elements, and has an RMS error of 2.29 mm.

Lymph Node Model Construction

Lymph nodes are ovoid or bean shaped structures usually between 5 and 15 mm long, and are commonly located alongside blood vessels. Due to their small size they were often difficult to visually detect on VH image slices, but adjacent blood vessels and anatomical structures were usually easily identifiable. Therefore, the geometric position of each node has been determined via a dual method of digitizing all visible nodes and then positioning the remaining nodes relative to adjacent anatomical structures as described in literature[3,7,9,11,12,19] (more detail is recorded in Table A2). The SMU has identified 43 lymph node fields that drain the skin and are regarded as generic regions for SNs to be located. Each of these node fields have been modeled and are shown in Fig. 6. Note that the legs are not shown in this image, and therefore the popliteal lymph nodes cannot be seen.

Mapping the Primary Melanoma Site

Mapping the 2D melanoma (X, Y) coordinates onto the 3D skin model has been carried out differently for three separate regions of skin: the torso and legs, the arms, and the hands and feet. Since the body map outlines and the skin model were oriented differently, the projection methods required customization for the different skin regions.

Torso and Leg Melanomas

Melanoma sites on the torso and legs were mapped onto the skin model using the following steps:

1. The torso and leg body maps have been morphed to align with the 3D skin model via a 'free-form' deformation (FFD) technique called 'host-mesh' fitting.[6] This process enables a finite element model

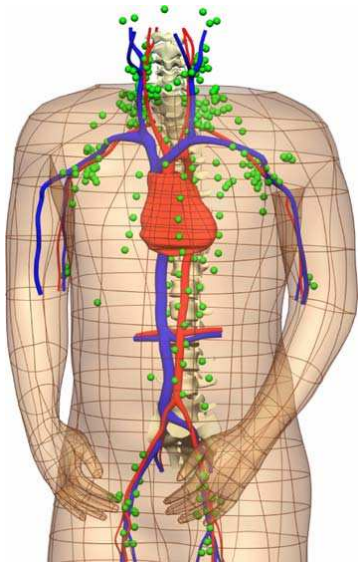

FIGURE 6. Model of the lymph nodes that drain the skin.

to be customized to a specific dataset. The mesh to be transformed is called the 'slave-mesh' and is embedded within a 'host-mesh'. The host-mesh is usually a volume mesh with fewer elements than the slave-mesh.

Deformation of the host-mesh is calculated by minimizing the distance between a set of landmark (initial) and target (final) points. Landmark points are chosen on the slave mesh at important anatomical locations, and target points are the corresponding anatomical locations in the specific dataset. The geometric distance between the landmark and target points is minimized according to Eq. (1). In this case $\mathbf{z}_d$ are the global target points and (ξ_{1d}, ξ_{2d}, ξ_{3d}) are the interpolated landmark points, extended to 3D for a volume host-mesh.

Before host-mesh fitting the midline of each body map was aligned to the midline of the skin model. The umbilicus of the anterior torso body map, and crotch were also aligned with corresponding features on the skin model. Primary melanoma site location is often described relative to the body's midline and umbilicus, therefore it was important to ensure continuity between the 2D coordinates and 3D projections.

Trilinear elements have been used for the host-mesh and bilinear elements for the body map slave-mesh. Although the slave is comprised of 2D elements, each node has three global coordinates and therefore a volume host-mesh was required to completely embed it (Fig. 7a). Landmark points have been digitized on the body map outlines and the target points digitized on the boundary of the skin model (as shown in Fig. 7b). Target points were projected orthogonally in the y-direction onto same 2D plane as the landmark points on the body maps. Thus, host-mesh fitting was reduced to a 2D problem, only requiring fitting in the x- and z-directions. Note that the head, neck, arms and hands have not been included in this process.

The number of elements in the slave and host-mesh was progressively refined from one to a higher number of elements to increase the number of mesh degrees of freedom (DOFs) and therefore increase the accuracy of the fit. Some DOFs at nodes down the midline of the torso, near the umbilicus and also at the crotch have been fixed to ensure continuity of important anatomical locations. Figure 8 shows the resultant host-mesh fitted body outlines for the posterior torso and anterior and posterior leg body maps, while Table 1 details the parameters for each fit. After fitting, the global coordinates of each melanoma site has been updated relative to the deformed slave-mesh.

2. Melanoma sites were projected orthogonally in the y-direction onto the skin mesh (Fig. 7c). To enable direct orthogonal projection the skin model was first reduced from 3D to 2D by setting all skin mesh nodal y-coordinates and their derivatives to zero. Note however, that for each of the four separate projections (listed in Table 1) only the skin mesh elements pertaining to the body map have been reduced to 2D. For example, only skin elements from the anterior torso were reduced for mapping the anterior torso melanoma sites to ensure coordinates did not project incorrectly to the posterior torso due to all skin elements being in the same 2D plane.
3. Local material coordinates of each projected melanoma site on the 2D skin mesh have been used to interpolate global melanoma site coordinates on the 3D bicubic skin mesh (Fig. 7d). A small error is created during this projection at elements of high curvature. Figure 9 schematically demonstrates a body map (X, Y) melanoma coordinate projected onto a 2D skin element and then the interpolated position within the corresponding 3D skin element. Local ξ coordinates are the same for both elements, however the high curvature at Node 2_{3D} and element arc-length causes a change in the global x-coordinates. This change also occurs in the global z-coordinates. Skin elements aligned in the y-direction at the sides of the body and interior legs, largely contribute to this error. Table 2 details the RMS error for each projection, calculated in 2D using the difference in the global x- and z-coordinates between data points on the 2D and 3D skin elements.

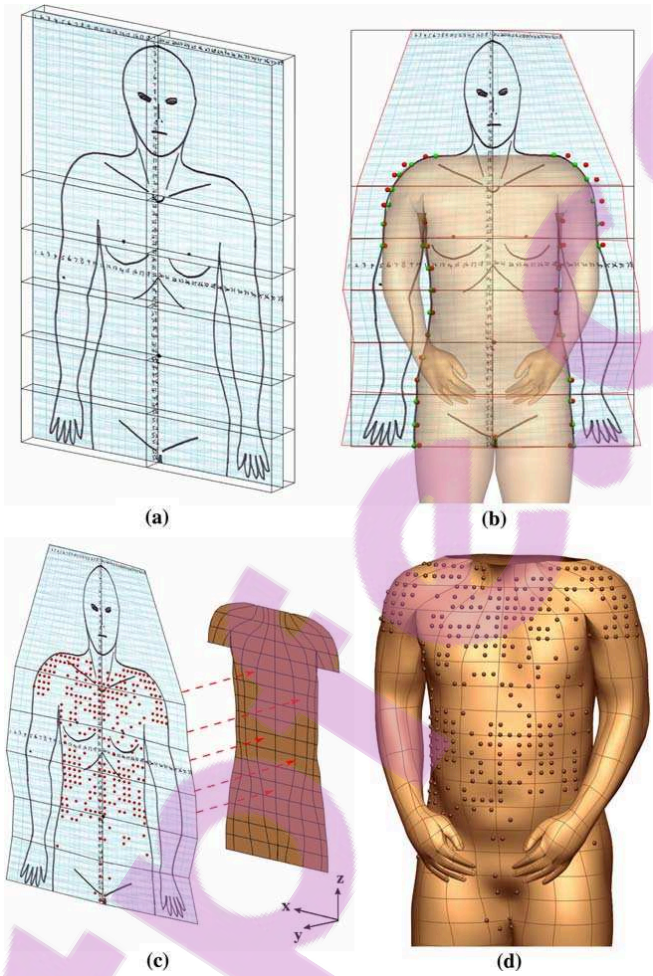

FIGURE 7. Mapping anterior torso melanoma sites from 2D to 3D: (a) trilinear host-mesh embedding the bilinear body map slave-mesh; (b) the body map outline host-mesh fitted to the skin model outline, with visible landmark and target points; (b) projecting melanoma (*X*, *Y*) coordinates orthogonally onto the 2D anterior torso skin mesh; and (c) final melanoma coordinates on the 3D skin mesh.

Arm Melanomas

The VH dataset used to create the skin mesh has the arms oriented anterior to the body, in contrast to the arms' lateral orientation on the body maps. As a result, melanoma sites on the arms could not be linearly projected in the same manner as the torso and leg melanoma sites.

The skin mesh arms have been moved laterally by host-mesh fitting via an extension at the elbow joint. Finite element models of the humerus, ulna and radius bones created previously[6] were used for this transformation. The bones have been treated as rigid bodies which do not undergo deformation during transformation, in contrast to the skin which is a soft tissue that can shear and stretch.

The radius and ulna were translated and rotated manually about the humerus from the initial anterior position to a lateral orientation (Fig. 10a). A total of 31 landmark points have been defined on the surface of the radius and ulna, and 31 corresponding target

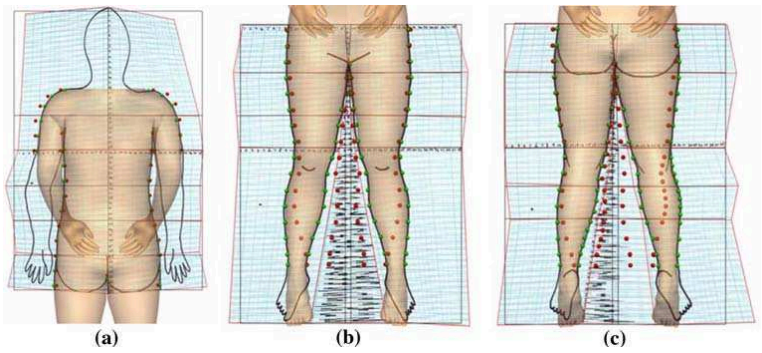

FIGURE 8. The body maps host-mesh fitted to align with the skin model outline: (a) posterior torso body map; (b) anterior legs body map; and (c) posterior legs body map.

TABLE 1. Host-mesh fitting parameters for the torso and leg body maps, giving the number of nodes, DOFs, and elements used in the host-mesh. The slave-mesh utilizes the same number of elements as the host. RMS values give the error between the deformed landmark points and target points after fitting.

Body map	Number of nodes	Number of DOFs	Number of elements	RMS error (mm)
Torso—anterior	42	64	12	3.32
Torso—posterior	42	66	12	3.17
Legs—anterior	38	68	12	3.22
Legs—posterior	46	82	15	3.40

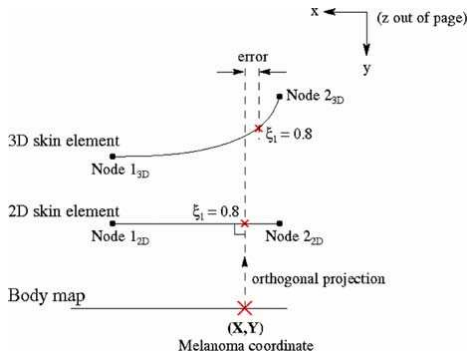

FIGURE 9. Error created during interpolation of projected torso and leg melanoma coordinates from the 2D to 3D skin mesh.

points were calculated by applying this resultant transformation matrix to the landmark point coordinates. Three trilinear elements have been used for the host-mesh, embedding the bicubic skin slave-mesh (Fig. 10b). Nodal coordinates at the upper host-mesh element were fixed to ensure the top nodes of the slave-mesh would remain unchanged and maintain continuity with the remainder of the skin mesh. The middle element surrounds the elbow joint and has undergone the most deformation during fitting. The right and left arms were fitted separately, giving an RMS error of 4.17 and 4.24 mm respectively.

In order to project melanoma (X, Y) coordinates the skin mesh arms have been flattened from 3D to 2D.

TABLE 2. RMS error between melanoma site global coordinates on the 2D and 3D skin mesh.

Body map	Number of melanoma sites	RMS error (mm)
Torso—anterior	527	1.17
Torso—posterior	1774	0.85
Legs—anterior	631	1.59
Legs—posterior	406	1.35

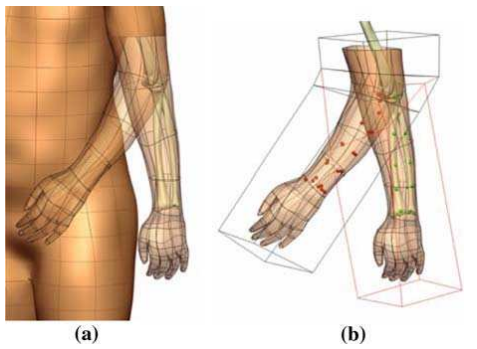

FIGURE 10. The left arm host-mesh fitted about the elbow joint: (a) initial and final left arm mesh with the radius and ulna in the final transformed position and (b) the arm slave-mesh embedded within the trilinear host-mesh before and after deformation, with visible landmark and target points.

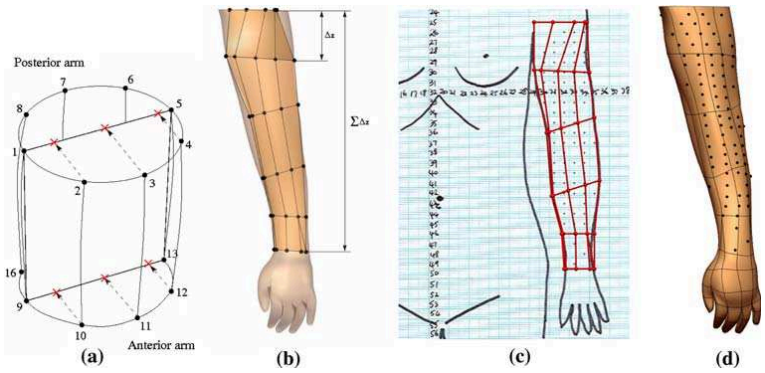

FIGURE 11. Projecting the left anterior arm melanoma sites: (a) arm cross-sections separated into posterior and anterior arm segments. Internal nodes are orthogonally projected onto 2D arm element edges; (b) the refined 2D arm elements; (c) corresponding body map arm element discretization; and (d) final arm melanoma sites on the 3D arm.

Each arm cross-section has been separated into anterior and posterior arm segments. Figure 11a illustrates a cross-section of the arm with the anterior segment reduced to 2D. Segment edge nodes (nodes 1, 5, 9, and 13) are joined to create 2D bilinear elements. Internal nodes (nodes 2–4 and 10–12) have then been orthogonally projected onto the element edges and joined to create refined 2D elements with the same topology as the original 3D skin mesh arms (Fig. 11b).

Correlation between these 2D arm elements and the body maps was established by discretizing the body map arms into elements with the same topology. The vertical distance (ΔZ) between arm edge nodes (Fig. 11b) was used to determine the relative body map arm element sizes. Discretization of the body maps has been rounded to 1/4 of a grid unit and is shown in Fig. 11c.

The local coordinate of each melanoma site on the body map elements was calculated, and corresponded to the 2D arm element local coordinates. Subsequently the final melanoma coordinates on the 3D arm (Fig. 11d) has then been calculated via interpolation of these local coordinates.

It was important to ensure continuity between the projected melanoma sites on the torso and the arms, since they were projected using two different methods. Therefore, the nodal coordinates used for the 2D arms at the junction of the flattened torso and arms have been taken from the 2D torso (the 2D anterior torso can be seen in Fig. 7c). For the anterior arm projections this junction is located at the armpits. For the posterior arm projections the junction is located one element cross-section below the armpits.

Hand and Foot Melanomas

The hand and foot outlines on the body maps could not be oriented with the skin mesh to enable a direct orthogonal projection, so these melanoma sites have been positioned manually. All possible sites have first been defined on the body maps (Figs. 12a and 12c) and then corresponding sites were placed manually on the skin mesh (Figs. 12b and 12c). Entries present in the database have been ascertained from these sites.

Mapping the SNs

The ideal method to map SNs onto the anatomical model would be to directly project SN locations from LS images onto it. However this is not possible due to the low LS image resolution and infrequent registering of the images with respect to anatomical features. Instead, the node field location of SNs has been mapped onto the generic lymph node model.

For each patient, the number of SNs in each node field and the depth below the skin in centimeters has also been recorded. Depth measurements have not been utilized since patients will have different sized anatomical features and cannot be directly compared. Hence, only the SN node field locations have been mapped. Without exact SN locations, the detailed lymph node model has been reduced to one representative node in each node field.

RESULTS

The SMU's full LS database excluding the head and neck has been mapped from 2D onto the 3D skin and lymph node model. The original SMU database contains 5239 individual patient entries, and 4302 of these entries pertaining to skin below the neck have been mapped. This mapped database provides the basis for the development of tools for spatial statistical analysis and visualization. The ultimate goal of this work is to

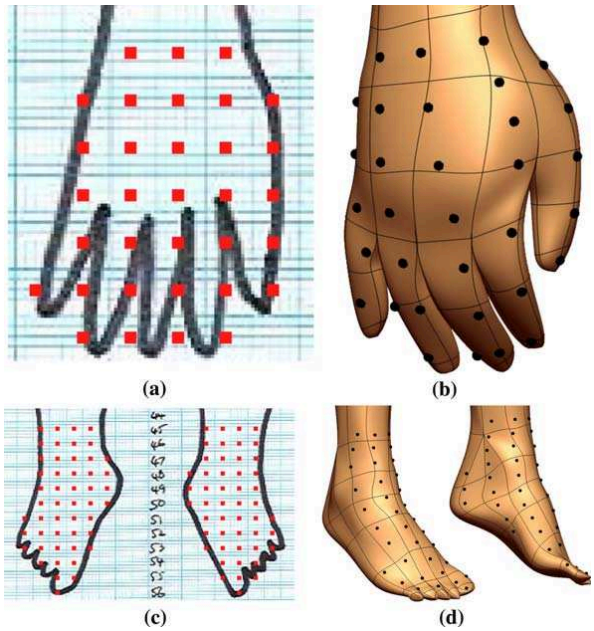

FIGURE 12. All possible melanoma sites on the dorsum of the right hand and the anterior feet: (a) right hand (*X, Y*) coordinates on the anterior torso body map; (b) manually placed sites on the skin mesh right hand; (c) feet (*X, Y*) coordinates on the anterior legs body map; and (d) manually placed sites on the skin mesh feet.

aid clinicians by indicating which lymph node fields are important to check for melanoma spread, given the primary melanoma site location. A full statistical analysis of patterns of melanoma spread will be the subject of a future study, however an example of the ability to visualize and analyze results is now demonstrated.

Using the data, now mapped in our spatially distributed database, even a preliminary statistical analysis reveals potentially important clinical information about the relationship between melanoma sites and sentinel lymph nodes. A qualitative assessment of lymphatic drainage patterns is provided by Fig. 13 which displays melanoma sites on the skin which have shown drainage to the left axillary or left groin node fields. The size of each melanoma site (defined by the size key) is relative to the number of patient cases at that skin location.

Clinically it is important to be aware of skin regions that are highly likely to show multiple lymphatic drainage pathways, to ensure that all potential node fields are checked for melanoma metastasis. Importantly the data points in green highlight 46 skin locations, from 125 individual patient cases, which have shown lymphatic drainage to both node fields. A proportion of these individual cases have shown dual drainage to both the left axilla and left groin, while the remaining cases have shown drainage to one of the two node fields. A similar pattern appears in the data for the right axillary and right groin node fields.

Focusing on this issue of dual drainage we can further quantify the likelihood that a patient presenting with a melanoma situated around the waist will have SNs in both of these node fields. On the standardized skin model this region has been defined on the torso as 180 mm above and 130 mm below the umbilicus, as shown on Fig. 13. Assuming the database is indicative of the population as a whole we can determine within confidence limits the percentage likelihood of dual drainage within this skin region. If P represents the proportion of the population with dual drainage then the probability of finding n cases of dual drainage with a database sample of N is:

$$p(n) = C_N^n P^n (1 - P)^{N-n} \tag{2}$$

Summing $p(0)$ to $p(n-1)$ and implementing a nonlinear root finding algorithm to find the value of P where this sum equals 0.05, we can determine the 95% percentile for the upper proportion of the population which could be expected to have dual drainage.

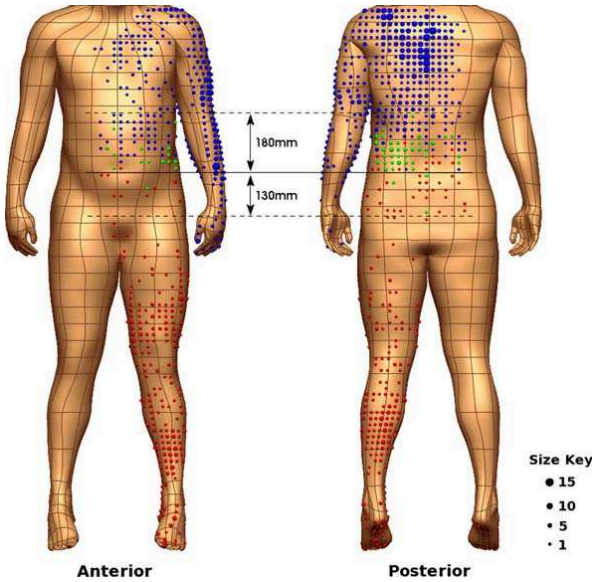

FIGURE 13. Visualization of primary melanoma sites based on sentinel lymph node fields. Skin sites with lymphatic drainage to the left axilla are shown in blue, sites that drain to the left groin node field are shown in red, and skin sites that have shown lymphatic drainage to both node fields are colored green. Data point size corresponds to the number of melanomas in the database at each skin site.

An equivalent calculation can be performed to determine the lower 95% confidence limit. Hence, out of the individual cases in the defined skin region with drainage to the left axilla or left groin, 17.7% of them have shown dual drainage to both node fields. The 95% confidence limits are calculated as being between 14.5% and 21.0%.

DISCUSSION

This study presents a detailed anatomically based method to map 2D LS data onto a 3D anatomical model, enabling the first anatomically based 3D model to analyze and visualize patterns of possible melanoma spread. During analysis of this mapped data, it is important to be aware of the potential sources of error which are present in both the original LS database and created by the mapping process. The following discussion gives a critique of the methods utilized, discussing the limitations in the LS database and in the mapped model.

Limitations imposed by the SMU's database include the low resolution of the primary melanoma site body maps. Since the 2D body maps discretized the skin into 1.5–2 cm^2 grid units, melanoma skin sites cannot be recorded in 2D, or mapped in 3D, with any greater accuracy. Ideally, to avoid the constraint of using a standard grid which will inherently introduce this type of error, each original LS image would need to be morphed via host-mesh fitting to the outline of the skin model. This process would then define a unique map for that patient to the standardized 3D model. While this process is technically feasible there is no generically recorded outline information on the LS images for each patient, and hence it is not possible to implement.

Recording error which is imposed by the grid square resolution on the 2D body maps, is magnified when sites are projected onto the 3D model. This is demonstrated schematically in Fig. 14 for two different skin sites. Note that the error created during interpolation of melanoma coordinates from the 2D to 3D skin mesh (as shown in Fig. 9) has been ignored, since these two sources of error are independent of one another. Melanoma coordinates such as (X_2, Y_2) which are nearly perpendicular to the skin mesh will induce a magnified recording error on the 3D model, while sites that are close to parallel to the screen such as (X_1, Y_1) will have little or no error magnification.

A heat map of the recording error magnification for the 3D skin mesh is shown in Fig. 15, demonstrating

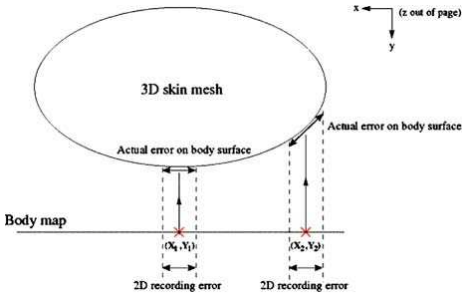

FIGURE 14. Magnification of the melanoma site recording error. The melanoma coordinate (X_2, Y_2) is nearly perpendicular to the skin and will induce a largely magnified recording error, whereas melanoma coordinate (X_1, Y_1) which is close to parallel to the screen will have little or no error magnification.

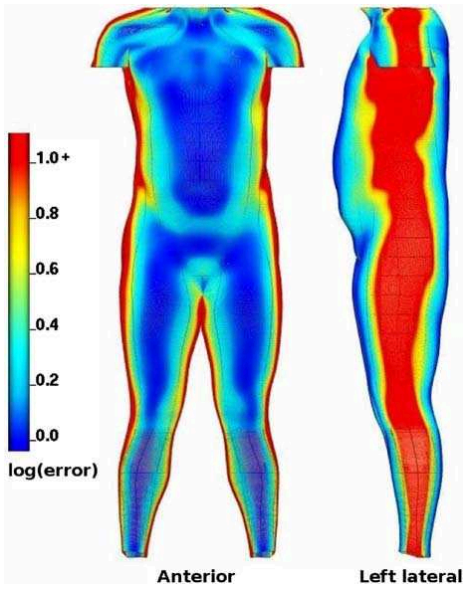

FIGURE 15. Heat map displaying the recording error magnification for the torso and leg melanoma sites projected from 2D onto the 3D skin model.

the relative error induced by the linearly projected torso and leg melanoma sites. As expected, the largest error magnification occurs at the lateral sides of the body and the interior legs, where the skin is nearly perpendicular to the projection direction. At these locations the error magnification approaches infinity. This provides a strong motivation for creating a model to record LS data in 3D as discussed below, since the recording error magnification would be removed.

It is important to be aware that the accuracy of a primary melanoma site's (X, Y) coordinate relies upon the physician recording each LS study consistently between patients. This could potentially give rise to a small amount of human error, the size of which cannot be accurately quantified.

Due to the large size of the LS database, a number of patients have their melanoma (X, Y) coordinates recorded within the same grid square. To enable visualization of the density of sites within each grid unit, the SMU has added a random number between −499 and +0.499 to create (*RandX*, *RandY*) coordinates. This has allowed all melanoma sites in the same grid square to be seen. The 2D displays published by the SMU (as shown in Fig. 2b) have plotted the (*RandX, RandY*) coordinates rather than the original (X, Y) coordinates. The random values are for display purposes only and do not add any extra spatial information, therefore during mapping the primary melanoma site the original (X, Y) coordinates have been used.

Aliasing error due to using grid squares to record melanoma sites instead of a continuous field may cause bias in the results. Melanoma (X, Y) coordinates are located at the center of each grid unit, however if these sites were positioned in one of the four grid unit corners instead, the resultant mapped coordinates could be significantly different. The centralized coordinates however, represent an averaged location for each melanoma site and therefore are the most accurate position to use for projecting onto the skin model.

The skin mesh has been created without genitals or a head and neck. The mesh was required to be a generic representation of the skin for both males and females, since both sexes can develop melanoma. Therefore the skin mesh has been created genderless. Meanwhile the head and neck of the VH dataset was rendered unsuitable for the model because his neck is too short. Skin lymphatic drainage in this region is very complex,[5] and as such will require a highly detailed mesh to visualize it effectively. Future extension of this work will be to create a head and neck skin mesh and map the remaining LS data.

Difficulties arose when creating the lymph node model, as some node fields were very difficult to differentiate from one another when digitizing the VH dataset. For example, the paraaortic and paravertebral node fields are very close together, as are the cervical node fields in the neck. For these difficult node fields, the anatomical model locations have been verified with SMU clinicians.

The RMS error for each torso and leg melanoma projection (listed in Table 2) is kept below 1.6 mm. Since each grid unit equates to between 1.5 and 2 cm square, the error is below 11% of a grid unit. Therefore

these projected melanoma sites on the 3D skin model are highly accurate, and are well within the body map resolution. The smallest RMS error of 0.85 mm is present for projected posterior torso melanoma sites. This is due to a high concentration of melanoma sites at the middle upper back where the elements are largely flat because their adjoining nodes have a low curvature.

Arm segment internal nodes induce a small error when they are projected onto 2D arm element boundaries since the nodes are not all in the same z-plane. An error is also created when discretizing the body map arm outlines into corresponding 2D elements, since they have been rounded to 1/4 of a grid unit. However a melanoma site with a maximum error of 1/4 a grid unit would still remain within the same grid square after projection.

Some hand and foot melanoma coordinates were difficult to place on the skin mesh. For example Fig. 11 shows some hand coordinates are located between the fingers such that the melanoma could be interpreted as being on either adjacent finger. To ensure correct site placement on the skin mesh the coordinates have again been verified with SMU clinicians. Clinicians are also likely to have introduced error in the database due to this coarse grid resolution. For example, it is highly likely that patients with melanomas on different fingers have had their melanoma site recorded in the same grid square, and hence the same finger.

Some skin elements have no melanoma sites projected onto them. This is common at the lateral sides of the body and interior legs, where elements are aligned approximately in the x-plane which is parallel to the projection direction. Also some skin sites do not commonly develop melanoma, such as near the groin and under the armpits, so there are few melanoma sites located here. This has a statistical implication, such that lymphatic drainage patterns at these cannot be ascertained with a high level of confidence. More data would be required at such sites to be able to quantify drainage patterns accurately.

Note that mapping LS data from 2D to 3D does not add any extra clinical information to the database. It is possible that the results presented here could have been shown using the original 2D data rather than using the mapped 3D data. However, the benefit of this mapping is that it provides a platform to record future patient cases in 3D which can be merged with the present mapped data. In particular, skin sites that are difficult to record with accuracy in 2D, can be recorded more accurately directly onto the 3D model. Since the skin model can be rotated to any angle, lateral sides of the body can be oriented parallel to the screen.

Future work will be focused on developing a software tool so that SMU clinicians can record additional LS data themselves directly on the 3D model. This extension will be important as it will increase the dataset and hence improve the statistical confidence when analyzing patterns in lymphatic drainage. It also will eliminate the resolution limitations inherent in the body maps, recording magnification error (as shown in Figs. 14 and 15) and aliasing error, which will provide for a far more accurate model. The developed software tool may be extended to the wider LS community to enable clinicians around the world to add their data as well.

Interpretation of the statistical results must bear in mind the potential sources of error present in the database due to the body maps limited resolution. Since melanoma sites on the skin are limited in their accuracy, when clinicians are determining lymph node fields to check for melanoma spread, they should also look at the behavior of skin surrounding a patient's primary melanoma site on the model.

The developed framework presents a number of advantages for visualizing, analyzing and recording melanoma LS data. The 3D skin and lymph node model provides an accurate and effective way to represent the primary melanoma site and sentinel lymph node locations. Quantitative analysis can be conducted on the mapped database, to visualize patterns of melanoma spread. An example of this has been demonstrated, however a full statistical analysis will be the subject of a future study. The extension and ongoing application of this work is to create a software tool for clinicians to database their LS data more accurately directly in 3D. As a result melanoma diagnosis and treatment may be improved, thereby aiding clinicians in the fight against this aggressive and potentially life-threatening disease.

APPENDIX

TABLE A1. SN node fields.

Head and neck node fields	
Right occipital	Left occipital
Right preauricular	Left preauricular
Right postauricular	Left postauricular
Right cervical level I	Left cervical level I
Right cervical level II	Left cervical level II
Right cervical level III	Left cervical level III
Right cervical level IV	Left cervical level IV
Right cervical level V	Left cervical level V
Right supraclavicular fossa	Left supraclavicular fossa

TABLE A1. continued.

Head and neck node fields	
Submental	
Torso and upper limb node fields	
Right axilla	Left axilla
Right epitrochlear	Left epitrochlear
Right infraclavicular	Left infraclavicular
Right triangular intermuscular space (TIS)	Left TIS
Right interpectoral	Left interpectoral
Right internal mammary	Left internal mammary
Right costal margin	Left costal margin
Intercostal	
Paravertebral	
Paraaortic	
Retroperitoneal	
Upper mediastinal	
Lower limb node fields	
Right groin	Left groin
Right popliteal	Left popliteal
Other node fields	
Interval node	

TABLE A2. Node field location references used to construct the lymph node model.

Node field	Reference
Occipital	Netter [9, p. 68], Gray [7, p. 844]
Preauricular	Clemente [3, p. 455], Gray [7, p. 844], Netter [9, p. 68]
Postauricular	Clemente [3, p. 455], Gray [7, p. 844], Netter [9, p. 68]
Cervical level I–V	Clemente [3, p. 455], Gray [7, pp. 843–845], Netter [9, p. 68, 69], Textbook of Melanoma [12, p. 296]
Supraclavicular fossa	Clemente [3, p. 6], Netter [9, p. 68]
Submental	Clemente [3, p. 455, 460], Netter [9, p. 68, 69]
Axilla	Clemente [3, p. 12, 15], Gray [7, pp. 845–848], Netter [9, p. 177, 466]
Epitrochlear	Gray [7, p. 846], Netter [9, p. 466]
Infraclavicular	Gray [7, p. 846]
Triangular intermuscular space	Uren *et al.* [19], Netter [9, p. 409]
Interpectoral	Gray [7, p. 847], Netter [9, p. 177]
Internal mammary	Clemente [3, p. 6], Netter [9, p. 177]
Costal margin	Clemente [3, p. 93]
Intercostal	Gray [7, p. 841, 856], Netter [9, p. 235, 258]
Paravertebral	Clemente [3, p. 247], Gray [7, p. 850]
Paraaortic	Clemente [3, p. 247], Gray [7, p. 850]
Retroperitoneal	Gray [7, pp. 1336–1342], Netter [9, p. 258]
Upper mediastinal	Clemente [3, p. 119, 144], Netter [9, p. 530]
Groin	Clemente [3, p. 243, 315], Gray [7, p. 849, 854], Netter [9, pp. 258, 306, 329, 386–388, 528]
Popliteal	Gray [7, p. 849], Netter [9, p. 528]
Interval	Uren *et al.* [20]

ACKNOWLEDGMENTS

The authors gratefully acknowledge Shane Blackett for developing the visualization software and Jessica Jor for assisting with the construction of the skin mesh. This work was supported by the Maurice Wilkins Center for Molecular Biodiscovery and the New Zealand Foundation for Research Science and Technology.

REFERENCES

[1]Ackerman, M. J. The visible human project. In: Proc. IEEE., 1998, pp. 504–511.
[2]Bradley, C. P., A. J. Pullan, and P. J. Hunter. Geometric modeling of the human torso using cubic hermite elements. *Ann. Biomed. Eng.* 25:96–111, 1997.
[3]Clemente, C. D. Anatomy: A Regional Atlas of the Human Body. 4th ed. Maryland: Williams & Wilkins, 1997.
[4]Crampin, E. J., M. D. Halstead, P. J. Hunter, P. F. Nielsen, D. Noble, N. P. Smith, and M. H. Tawhai. Computational physiology and the physiome project. *Exp. Physiol.* 89:1–26, 2004.
[5]de Wilt, J. H., J. F. Thompson, R. F. Uren, V. S. Ka, R. A. Scolyer, W. H. McCarthy, C. J. O'Brien, M. J. Quinn, and K. F. Shannon. Correlation between preoperative lymphoscintigraphy and metastatic nodal disease sites in 362 patients with cutaneous melanomas of the head and neck. *Ann. Surg.* 239:544–552, 2004.
[6]Fernandez, J. W., P. Mithraratne, S. F. Thrupp, M. H. Tawhai, and P. J. Hunter. Anatomically based geometric modelling of the musculo-skeletal system and other organs. *Biomech. Model. Mechan.* 2:139–155, 2004.
[7]Gray, H. In: Gray's Anatomy, 37th edn. edited by P. L. Williams, R. Warwick, M. Dyson, and L. H. Bannister. London: Churchill Livingston, 1989.
[8]Morton, D. L., D. R. Wen, J. H. Wong, J. S. Economou, L. A. Cage, F. K. Storm, L. J. Foshag, and A. J. Cochran. Technical details of intraoperative lymphatic mapping for early stage melanoma. *Arch. Surg.* 127:398–399, 1992.
[9]Netter, F. H. Atlas of Human Anatomy. 3rd ed. New Jersey: ICON Learning Systems, 2003.
[10]Smith, N. P., D. Nickerson, E. J. Crampin, and P. J. Hunter. Computational modelling of the heart. *Acta Numerica*. 13:371–431, 2004.
[11]Spitzer, V. M., and D. G. Whitlock. Atlas of the Visible Human Male. Massachusetts: Jones and Bartlett Publishers, 1998.
[12]Thompson, J. F., D. L. Morton, and B. B. R. Kroon. Textbook of Melanoma. London: Martin Dunitz, 2004.

[13]Thompson, J. F., R. A. Scolyer, and R. F. Kefford. Cutaneous melanoma. *Lancet* 365:687–701, 2005.
[14]Thompson, J. F., and R. F. Uren. Lymphatic mapping in management of patients with primary cutaneous melanoma. *Lancet Oncol.* 6:877–885, 2005.
[15]Thompson, J. F., and R. F. Uren. Teaching points on lymphatic mapping from the Sydney Melanoma Unit. *Semin. Oncol.* 31:349–356, 2004.
[16]Thompson, J. F., and R. F. Uren. What is a 'sentinel' lymph node? *Eur. J. Surg. Oncol.* 26:103–104, 2000.
[17]Thompson, J. F., R. F. Uren, H. M. Shaw, W. H. McCarthy, M. J. Quinn, C. J. O'Brien, and R. B. Howman-Giles. Location of sentinel lymph nodes in patients with cutaneous melanoma: new insights into lymphatic anatomy. *J. Am. Coll. Surg.* 189:195–204, 1999.
[18]Uren, R. F., R. Howman-Giles, D. Chung, and J. F. Thompson. Nuclear medicine aspects of melanoma and breast lymphatic mapping. *Semin. Oncol.* 31:338–348, 2004.
[19]Uren, R. F., R. Howman-Giles, J. F. Thompson, M. J. Quinn, C. O'Brien, H. M. Shaw, C. M. J. Bosch, and W. H. McCarthy. Lymphatic drainage to triangular intermuscular space lymph nodes in melanoma on the back. *J. Nucl. Med.* 37:964–966, 1996.
[20]Uren, R. F., R. Howman-Giles, and J. F. Thompson. Patterns of lymphatic drainage from the skin in patients with melanoma. *J. Nucl. Med.* 44:570–582, 2003.
[21]Uren, R. F., J. F. Thompson, and R. Howman-Giles. Lymphatic Drainage of the Skin and Breast: Locating the Sentinel Nodes. Amsterdam: Harwood Academic, 1999.

Appendix D

Data Visualisation Paper

This paper details the visualisation results of the mapped model, showing lymphatic drainage of skin below the neck. This paper represents Chapters 4 and parts of 5, and was published in *The Lancet Oncology*. An online software tool was also developed alongside this paper showing additional results, which can be seen at http://www.bioeng.auckland.ac.nz/melanoma/. Selected screenshots of this website are given in Appendix E.

Articles

Three-dimensional visualisation of lymphatic drainage patterns in patients with cutaneous melanoma

Hayley M Reynolds, P Rod Dunbar, Roger F Uren, Shane A Blackett, John F Thompson, Nicolas P Smith

Lancet Oncol 2007; 8: 806–12

Published Online
July 20, 2007
DOI:10.1016/S1470-2045(07)70176-6

See Reflection and Reaction page 755

Bioengineering Institute (H M Reynolds BE, S A Blackett ME, N P Smith PhD), **and School of Biological Sciences, University of Auckland, Auckland, New Zealand** (P R Dunbar PhD); **Sydney Melanoma Unit, Royal Prince Alfred Hospital, Camperdown, Sydney, NSW, Australia** (Prof R F Uren MD, Prof J F Thompson MD); **Discipline of Medicine, University of Sydney, Sydney, NSW, Australia** (Prof R F Uren); **Nuclear Medicine and Diagnostic Ultrasound, RPAH Medical Centre, Sydney, NSW, Australia** (Prof R F Uren); **Discipline of Surgery, University of Sydney, Sydney, NSW, Australia** (Prof J F Thompson); **and University Computing Laboratory, University of Oxford, Oxford, UK** (N P Smith PhD)

Correspondence to:
Ms Hayley M Reynolds, Bioengineering Institute, University of Auckland, Auckland, New Zealand
h.reynolds@auckland.ac.nz

Summary

Background **Lymphoscintigraphy accurately maps lymphatic drainage from sites of cutaneous melanoma to the draining sentinel lymph nodes. The Sydney Melanoma Unit has accumulated lymphoscintigraphy data from over 5000 patients with cutaneous melanoma over more than 15 years, collectively revealing patterns of skin lymphatic drainage. We aimed to map these data onto a three-dimensional computer model to provide improved visualisation and analysis of lymphatic drainage from sites of cutaneous melanoma.**

Methods **Lymphoscintigraphy data from 5239 patients with cutaneous melanoma were collected between July 27, 1987 and Dec 16, 2005. 4302 of these patients had primary melanoma sites below the neck, and were included in this analysis. From these patients, two-dimensional lymphoscintigraphy data were mapped onto an anatomically based three-dimensional computer model of the skin and lymph nodes. Spatial analysis was done to visualise the relation between primary melanoma sites and the locations of sentinel lymph nodes.**

Findings **We created three-dimensional, colour-coded heat maps that showed the drainage patterns from melanoma sites below the neck to individual lymph-node fields and to many lymph-node fields. These maps highlight the inter-patient variability in skin lymphatic drainage, and show the skin regions in which highly variable drainage can occur. To enable interactive and dynamic analysis of these data, we also developed software to predict lymphatic drainage patterns from melanoma skin sites to sentinel lymph-node fields.**

Interpretation **The heat maps confirmed that the commonly used Sappey's lines are not effective in predicting lymphatic drainage. The heat maps and the interactive software could be a new resource for clinicians to use in preoperative discussions with patients with melanoma and other skin cancers that can metastasise to the lymph nodes, and could be used in the identification of sentinel lymph-node fields during follow-up of such patients.**

Introduction

Cutaneous melanoma is a potentially fatal disease which has increased in incidence over recent decades in most people of European background.[1] Detection of metastatic melanoma in the regional lymph nodes has major implications for treatment and prognosis. Sentinel lymph-node biopsy (SLNB)[2] is used to detect whether melanoma cells have metastasised to the sentinel lymph nodes (SLNs), which are defined as any lymph node receiving direct lymphatic drainage from a primary tumour site. SLNs are located by preoperative lymphoscintigraphy, which involves imaging the lymphatic drainage from a primary melanoma site to the SLNs through a radioactive tracer injected into the skin.[2]

SLNB has substantially improved the accuracy of lymph-node staging in patients with melanoma and has been shown in the large Multicentre Selective Lymphadenectomy Trial (MSLT-I) to improve disease-free survival.[3] In this trial of 1269 patients with primary melanoma of intermediate thickness, the mean 5-year disease-free survival was 78·3% (SE 1·6) in the SLNB group and 73·1% (SE 2·1) in the observation group (hazard ratio [HR] for recurrence, 0·74; 95% CI 0·59–0·93; p=0·009). This trial also showed an improvement in overall survival for patients with metastatic nodal disease who had an immediate complete surgical clearance of the entire lymph-node field[3] (ie, all lymph nodes located within the region where the SLN is located, for example, the axilla or groin). In patients with nodal metastases, the 5-year survival was higher in those who had immediate lymphadenectomy compared with those in whom lymphadenectomy was delayed (72·3% [SE 4·6] *vs* 52·4% [SE 5·9]; HR for death 0·51; 95% CI 0·32–0·81; p=0·004).

However, not all centres have access to lymphoscintigraphy, and clinical follow-up in patients with melanoma then relies on predictions of lymphatic drainage based on historical assumptions that are probably incorrect in 30% of individuals.[4]

Lymphoscintigraphy studies have confirmed that lymphatic drainage of the skin is highly variable between patients, with very few areas of the skin from which lymphatic drainage is clinically predictable.[5] For over 100 years, patterns of lymphatic drainage from the skin were predicted from the work of Sappey,[6] whose 1874 atlas stated that lymphatic drainage never crossed the midline of the body nor a theoretical horizontal line drawn around the waist through the umbilicus. These concepts were challenged in the 1970s, 1980s, and 1990s, largely due to work in patients with melanoma by the use of lymphoscintigraphy, which showed that lymphatic drainage frequently occurs across Sappey's lines, and that, although skin sites usually drain to ipsilateral lymph-node fields, contralateral drainage is not uncommon.[7–12]

The Sydney Melanoma Unit (SMU), Australia, has done preoperative lymphoscintigraphy on more than 5000 patients with cutaneous melanoma.[4] The centre's database includes the precise location of the primary melanoma and the location of every SLN in each patient, located through lymphoscintigraphy. These data have allowed drainage patterns to be tabulated and two-dimensional displays to be generated relating melanoma sites to draining lymph-node fields.[5,13] We aimed to improve the visualisation of these data by developing a three-dimensional model of human skin onto which the data could be mapped. The current study presents the first results of this mapped data; construction of this three-dimensional model and mapping procedures have been reported previously.[14]

Methods

Mapping lymphoscintigraphy data

We constructed a three-dimensional finite element model of human skin with the use of anatomical images from the Visible Human dataset,[15] which was created from a male cadaver. A detailed description of the geometry development and associated metrics was outlined in our previous study.[14] In brief, the shape of the human skin surface was modelled by breaking it up into small regions called "skin elements"; a total of 886 of these curved units, each quadrilateral or triangular in shape, were required to mathematically describe the entire skin surface in three-dimensional space. At present, the model excludes the head and neck because the Visible Human dataset has an abnormally short neck region that does not allow adequate mapping of primary melanoma sites onto it. A head and neck model based on another three-dimensional dataset is being developed because lymphatic drainage of skin on the head and neck is very complex[16] and a highly detailed model is required. The Visible Human dataset also had to be manipulated to allow visualisation of all surfaces of the upper limbs.[14] This manipulation resulted in the palms of the hands being oriented posteriorly in our three-dimensional model, rather than the standard anatomical orientation (in which the palms are facing forwards). 43 distinct lymph-node fields have also been placed within the three-dimensional model.[14] In the work presented here, each node field has been displayed as a single point that represents an approximate anatomical midpoint of the field, with the exception of the interval lymph-node field,[17] which is displayed separately outside the three-dimensional representation of the body. Node fields located in the head and neck region are also located outside the existing three-dimensional skin model; however, their geometric position is based on Visible Human data.

Lymphoscintigraphy data from 5239 patients with cutaneous melanoma, collected between July 27, 1987 and Dec 16, 2005, had already been entered into a database. The location of the primary melanoma site in each patient had been recorded using a two-dimensional grid placed over outlines of an idealised human body viewed from different perspectives.[4,13] After each patient was imaged by use of the appropriate protocol, clinicians from the SMU manually recorded the primary melanoma site on one of these two-dimensional grids by referencing previously recorded clinical drawings of the primary melanoma site, and also visually inspecting the tumour site location. For our studies, these melanoma-site coordinates were mapped onto the skin elements in our three-dimensional model by use of techniques that we have previously reported.[14] Melanoma sites above the neck could not be mapped onto the skin model because the model did not have a head and neck mesh, and consequently, only primary melanoma sites that were located below the neck were used in this current analysis. The density of the melanoma sites recorded in the database was higher than the density of the skin elements in the three-dimensional model, so several melanoma sites have been placed within each three-dimensional skin element (webfigure). For each patient in the database, the location of the SLNs that drained the primary melanoma site located by lymphoscintigraphy were recorded and assigned to one or more of 43 discrete lymph-node fields. As described previously,[5,13] a substantial number of patients had SLNs located in more than one lymph-node field. Patients who showed highly atypical drainage patterns were checked for previous surgery, and if they had undergone previous surgery were excluded from this analysis.

See Online for webfigure

Data fitting and statistical analysis

To create maps of lymphatic drainage patterns, patients were selected from the database based on the drainage pattern of interest—eg, patients showing drainage to an SLN in the right axilla. For each melanoma skin site, the number of patients fulfilling this drainage pattern was divided by the total number of patients at that skin site, to derive a percentage likelihood value for drainage to the specified node field from that skin site. These discrete percentage likelihood values were then fitted as a field over the skin model, to give a smoothed and continuous representation of the discrete field values.[18] This field was then visualised by colour-coded heat maps. Mathematically, the fitting process was established by minimising the difference between each discrete datapoint's field value and its nodally interpolated field value on the skin mesh. During fitting, a smoothing term was introduced to account for noise in the data, and the discrete data values were weighted according to the frequency of points at each skin site.[18] The weights ensured that areas of skin with more data present would have an increased effect on the resulting fitted field, and that outlying values would not skew the results.

The model also enabled the visualisation of SLN positions for each skin site. Melanoma sites on each skin element were grouped together to calculate patterns of lymphatic drainage from that region of skin. The number of melanoma sites located on each skin element and the percentage likelihood that melanomas on each element

Articles

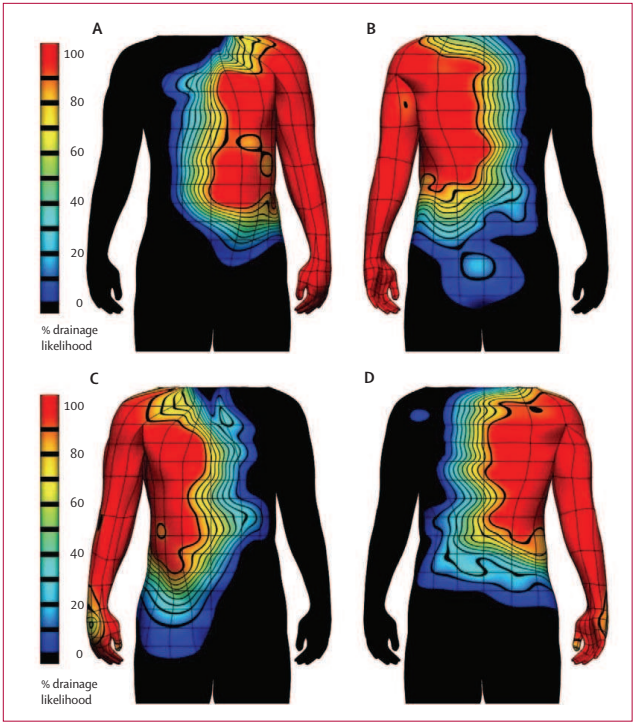

Figure 1: **Heat maps showing percentage likelihood that a primary melanoma site will show lymphatic drainage to axillary lymph-node fields**
Drainage to the left axillary lymph-node field (A, B); and the right axillary lymph-node field (C, D). Regions of skin with no lymphatic drainage to this lymph-node field are coloured black. A and C are anterior views and B and D are posterior views.

would drain to specific lymph-node fields was calculated. The percentage likelihood values often sum to more than 100% because patients can have lymphatic drainage to more than one SLN.

Role of the funding source

The sponsor of the study had no role in the study design, data collection, data analysis, data interpretation, writing of this report, or the decision to publish the report. HMR had full access to all the data (including raw data) and had final responsibility for the decision to publish.

Results

Spatial heat maps visualising lymphatic drainage

Heat maps were analysed from 4302 evaluable patients. Heat maps were generated on the three-dimensional skin model to visualise the percentage likelihood that any skin region will drain to a particular lymph-node field. Although only the heat maps for drainage to the axillae and groins are discussed below, maps of drainage to epitrochlear, popliteal, and triangular intermuscular space node fields have also been generated, and are available to view can be viewed online at http://www.bioeng.auckland.ac.nz/melanoma/.

Figure 1 shows heat maps generated for the left and right axillary lymph-node fields, and shows the percentage likelihood that skin sites will have lymphatic drainage to SLNs within these fields. The heat maps shown here visualise anterior and posterior views only; however, selected lateral views can be viewed online. These heat maps are based on 1639 patients with SLNs in the left axilla and 1597 patients with SLNs in the right axilla; these represent the largest number of patients with lymphatic drainage to any one lymph-node field within this dataset, and highlights that the most common site for melanomas is the skin of the back, an area that usually drains to one or both axillae. Ten patients (five with drainage to the left axilla and five with drainage to the right axilla) could not be plotted on the current model because their cancers were located on the neck.

These heat maps confirm that skin sites on the arm or torso above the umbilicus commonly drain to the ipsilateral axillary lymph-node field. However, the heat maps also quantitatively show that lymphatic drainage often occurs across Sappey's lines, both across the midline and across the umbilical meridian. The heat maps for the two axillae are not exactly the same as each other, but they do have sufficient commonality to show the skin regions in which drainage to the ipsilateral axilla is almost certain, and the range of sites where drainage to the ipsilateral or contralateral axilla should be considered possible or probable. A small number of anomalous patients account for the most dramatic asymmetries, as indicated by contour lines. For example, two patients with primary melanomas on the left anterior torso and one patient with a primary melanoma on the right anterior torso showed direct lymphatic drainage solely to interval nodes, decreasing the percentage of drainage to the ipsilateral axillary lymph-node field below 100% in those regions (figure 1). Two patients with primary melanomas near the right posterior wrist (figure 1) show drainage to a right epitrochlear and an interval SLN, respectively, and a patient with a primary melanoma on the right thumb showed unusual drainage to the right infraclavicular and right cervical level IV lymph-node fields, bypassing the right axilla.

An important note is that previous nodal or other major surgery can alter a patient's skin lymphatic drainage. Two patients who had previously undergone right axillary dissection before lymphatic mapping were excluded from analysis: one of these patients showed drainage from the right anterior torso to a right internal mammary lymph node, and the other patient showed contralateral drainage from the right arm to an SLN in the left axilla, and drainage to SLNs in the right supraclavicular fossa and upper mediastinal lymph-node fields.

We did not check the records of all 4302 patients for previous surgery, so some patients who had previous

surgery have not been removed from the analysis. However, we estimate that the number of such patients would be less than 1% of the patients in this study; this estimate is based on the knowledge of nuclear medicine physicians at the SMU regarding the patients imaged by lymphoscintigraphy in their database.

The data in figure 1 show a difference between the drainage patterns from the left and right sides of the body. To establish whether a true difference between the left and right sides of the body exists, more data will be required.

Heat maps that show drainage to the left and right groin lymph-node fields are shown in figure 2. The groin was the second most common SLN field in the database, with 780 patients showing drainage to the left groin and 758 patients showing drainage to the right groin.

As in the axillary heat maps, drainage across Sappey's lines is noted to occur often, but a very distinct region drains almost always to the ipsilateral groin. All primary melanoma sites on the left lower limb have lymphatic drainage to SLNs in the left groin and all right lower limb melanoma sites have drainage to the right groin lymph-node field (figure 2). Melanoma sites might also show drainage to interval lymph nodes or to the popliteal lymph-node field; however, the data show that for these sites, drainage always occurs to the groin as well.

The heat maps show that lymphatic drainage of the lower limbs is highly predictable. Previous studies have shown that drainage to the contralateral groin can occur if the ipsilateral groin has been disturbed by previous nodal surgery.[19] One patient who had previous excision biopsy of lymph nodes in the right groin had a primary melanoma on the distal right leg, which showed contralateral drainage to the left groin and ipsilateral drainage to the right groin. This patient was excluded from this analysis. However, contralateral drainage without previous nodal surgery can occur. One patient with a melanoma on the right heel (figure 2) had contralateral drainage to the left groin and ipsilateral drainage to the right groin and right popliteal lymph-node fields. This was the only patient in the database without previous surgery who did not show exclusive drainage to the ipsilateral groin lymph-node field.

The upper regions of the groin lymph-node field show some asymmetry. We noted that the density of primary melanoma sites in the skin regions near the groin is especially low (webfigure), and the heat maps over these regions are based necessarily on extrapolations from the nearest skin regions in which data from patients with melanoma are available. The asymmetry noted in the heat maps probably indicates the sparsity of data in these regions.

Heat maps have also been generated for skin sites that have drainage to different numbers of lymph-node fields. Figure 3A shows regions of skin that have drainage to only one lymph-node field, and figure 3B illustrates the probability that drainage from a region will be to more than one lymph-node field. These data show the regions of skin where lymph-node drainage is most predictable.

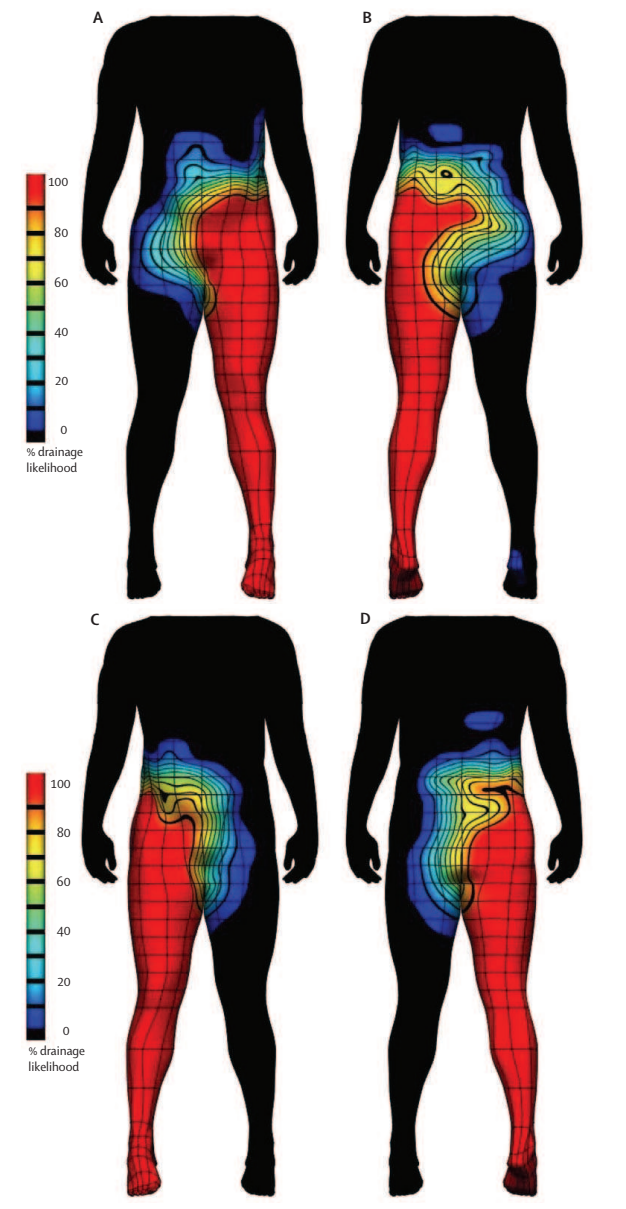

Figure 2: **Heat maps displaying the percentage likelihood that lymphatic drainage will occur to groin lymph-node fields**
Drainage to left groin lymph-node field (A, B); and right groin lymph-node field (C, D). A and C are anterior views and B and D are posterior views.

Articles

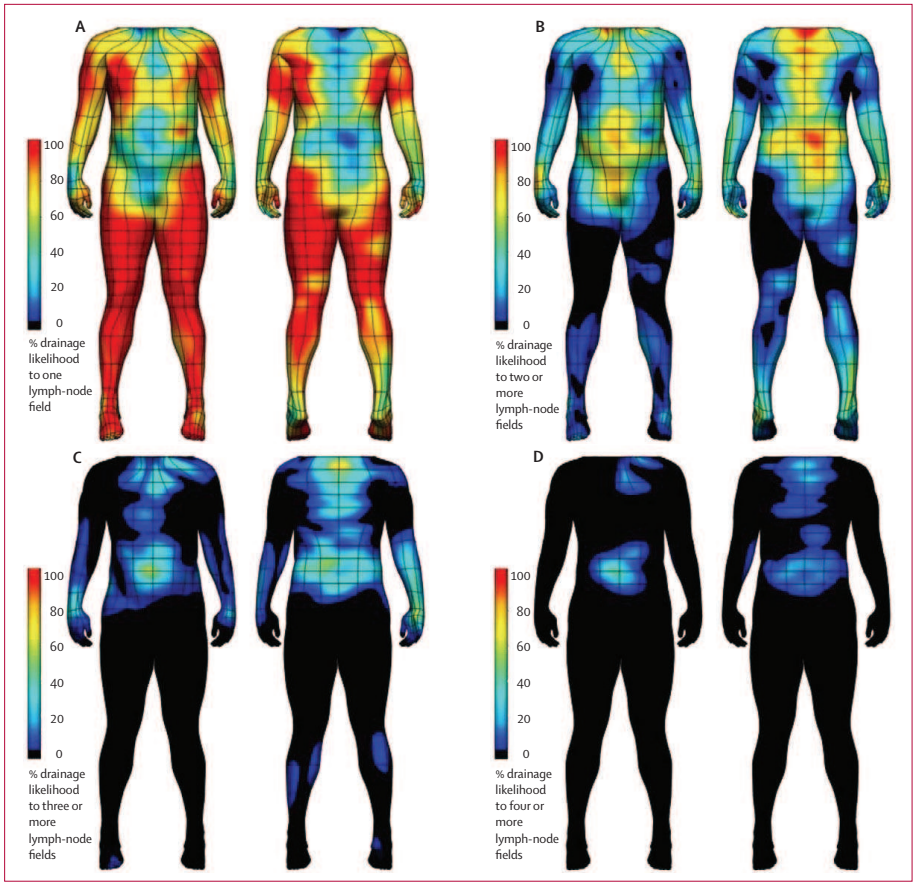

***Figure 3*: Percentage likelihood that a primary melanoma site will show lymphatic drainage to one or more lymph-node fields**
Drainage to one lymph-node field (A); two or more lymph-node fields (B); three or more lymph-node fields (C); and four or more lymph-node fields (D). For each image, left is anterior view and right is posterior view.

For example, figure 3A shows large red regions on the legs indicating that melanoma sites in these areas of skin drained to a single lymph-node field, in this instance, the ipsilateral groin. Whereas figure 3B shows that there are some areas of skin in which drainage is never to a single lymph-node field (the red areas on the upper and lower back) and are therefore highly unpredictable. In figure 3C and 3D, the complexity of drainage patterns from certain areas of skin is shown by the probability that drainage from regions of skin will be to at least three (figure 3C) or at least four (figure 3D) lymph-node fields. For example, more than 20% of patients in some of these areas drained to at least four different lymph-node fields (figure 3D). The regions with the highest likelihood of drainage to many lymph-node fields are close to Sappey's lines (figure 3C and 3D). However, regions outside the torso, most notably on the distal leg and especially the hand and forearm, can also drain to three or more lymph-node fields (figure 3C). Skin sites that commonly drain to many lymph-node fields do not always drain to the same subset of fields (data not shown). Nonetheless, for those areas of skin with complex drainage patterns, the subset of lymph-node fields with noted drainage can still be identified and the relative likelihood of drainage to each field can be calculated.

We also did a preliminary analysis of the effects of sex and age on patterns of skin lymphatic drainage. The results indicated sex-specific differences in the distribution

of primary sites, which affect the frequency of drainage to particular lymph-node fields. However, when the same primary sites were compared, no sex-specific differences in the patterns of drainage were apparent. Preliminary analysis similarly suggests that age does not affect the pattern of lymphatic drainage from each skin site, although age can affect the primary melanoma site locations. For example, the relative frequency of melanoma on the head is increased in older patients compared with younger patients, and is most probably consistent with the increased sun exposure due to less hair coverage. Further analysis of sex, age, and other features of the data are underway in an ongoing study.

Interactive computer software to predict lymphatic drainage

To further predict lymphatic drainage, we developed interactive computer software to enable regions of skin on the three-dimensional model to be selected so that SLN field locations would be displayed. Figure 4 shows the lymphatic drainage from two separate skin regions on the back by the use of our software. Figure 4A shows a region of skin near the midline and waist of the posterior torso, where 21 patients in the dataset had cutaneous melanoma. Eight potential SLN field locations are shown when clicking on this skin region, showing that lymphatic drainage from this site is especially difficult to predict. The likelihood of lymphatic drainage occurring to each of those eight lymph-node fields is displayed on the model (the lymph-node field depicted outside the body represents interval lymph nodes). By contrast, figure 4B shows a region of skin near the left axilla with a much simpler drainage pattern, showing 100% likelihood of having an SLN in the left axilla based on ten patients who had a melanoma at this site. This software can also display the SLN field names or the number of patient cases draining to each particular lymph-node field, instead of the percentage likelihood values.

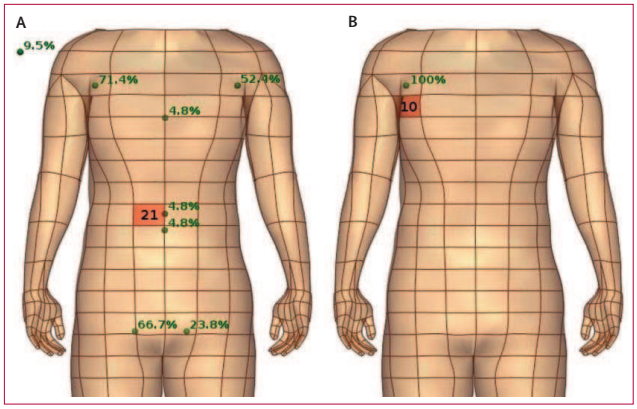

Figure 4: **Interactive SLN software**
A selected posterior torso element left of the midline near the waist shows complex lymphatic drainage to eight potential SLN fields calculated from 21 patients (A). Drainage is 71·4% and 52·4% likely to drain to the left or right axilla respectively, 9·5% likely to drain to an interval lymph node, 4·8% likely to drain to either the intercostal, retroperitoneal, or paravertebral lymph-node fields, and 66·7% and 23·8% likely to drain to the left or right groin lymph-node fields, respectively. Another posterior torso element selected with more straightforward lymphatic drainage (B). All ten patients showed lymphatic drainage solely to the left axillary lymph-node field.

Discussion

We aimed to integrate the SMU's large lymphoscintigraphy dataset from patients with cutaneous melanoma, and present that data in concise and instructive three-dimensional formats. The three-dimensional models that we generated quantitatively show how patterns of lymphatic drainage from skin differ from traditional anatomical descriptions.

From clinical experience gained at the SMU over the past 15 years, for patients with melanomas that are 1·0 mm or more in Breslow thickness, the most accurate staging of the regional lymph nodes is achieved by use of high-resolution lymphoscintigraphy to locate the sentinel lymph nodes and then undertaking selective biopsy of these lymph nodes with blue dye and an intraoperative gamma-detecting probe. We believe that this is desirable in all patients; however, this approach is not possible in some circumstances, including: in geographical areas in which nuclear medicine facilities are unavailable; or situations in which lymphatic mapping is thought to be unreliable due to the unavailability of suitable small particle radiocolloids. Under these circumstances, we believe our model will be clinically useful. The interactive computer software especially should help in planning ultrasonography or clinical follow-up by identifying the appropriate lymph-node fields that need to be monitored and should also be helpful in discussions with patients before surgery when gaining informed consent. The software will show possible variability in lymphatic drainage from the precise point on the skin on which the melanoma exists.

A further clinical application of this model would be if lymphoscintigraphy showed drainage from the melanoma site to an SLN, but did not show drainage to a lymph-node field that the model predicted for 90–100% of patients. In this situation, this other predicted lymph-node field should also be monitored during clinical and ultrasonography follow-up because in some patients with clinically normal lymph nodes, metastatic occlusion of a lymphatic collector can prevent a true SLN receiving radiocolloid on lymphoscintigraphy.[20] Another use of this model and the interactive displays is for teaching medical and nursing undergraduates and postgraduate surgical trainees.

We acknowledge that lymphoscintigraphy is not perfect, but the method is highly reproducible[21] and is probably the cause of a metastatic SLN being missed in under 1% of patients overall. Lymphoscintigraphy remains the best way to identify the location of SLNs for subsequent biopsy. Therefore, the technique is a reliable method of establishing

Articles

skin lymphatic drainage, and inaccuracies in the heat map and web-based software displays should be small.

Although the SMU has the world's largest lymphoscintigraphy database, it is not without limitations: patients with previous surgery were not removed from the analysis. The number of such patients is estimated to be less than 1% based on the knowledge of RFU of patients in the lymphoscintigraphy database (Uren RF, personal communication), but has not been assessed quantitatively.

An absence of patients with melanoma in some skin regions on the three-dimensional model means that lymphatic drainage patterns cannot be calculated accurately for these regions (the total number of patients for each skin element is displayed graphically in the webfigure, with the number of patients with melanoma at each individual skin site ranging from 1 to 16). To make this explicit, the interactive software shows the number of patients that form the basis of the percentage likelihood values displayed, to minimise overinterpretation where there is a paucity of available data. Similarly, heat maps could not be calculated accurately and visualised for all SLN fields due to insufficient data, or where most melanoma sites were located on the head or neck, which cannot currently be mapped onto the skin model. Ultimately, we hope that these limitations will be at least partly addressed as the dataset grows, and after a head and neck skin model is created. We are developing an interface for our three-dimensional model to allow input of both melanoma and SLN sites, which should facilitate case-by-case accrual of new data into the dataset.

In summary, lymphoscintigraphy on a large number of patients with primary cutaneous melanoma has accumulated a large amount of information on the lymphatic drainage of the skin. Disseminating this information effectively to clinicians will be assisted by developing new methods for its display. We have established methods for displaying lymphoscintigraphy data on a three-dimensional computer model that should be useful to clinicians and medical educators. By making the data available to clinicians and others through online software, the information might help in the management of individual patients with melanoma and other skin cancers that have the propensity to spread to lymph nodes.

Contributors

PRD and JFT conceived and initiated the study. RFU and JFT provided access to the SMU lymphoscintigraphy database. RFU collected and recorded the data in the database. NPS conceived the approach and methods for mapping and analysing the data. NPS and PRD obtained funding and gave study supervision. HMR created the anatomical model, mapped the data for three-dimensional visualisation, did the statistical analysis, created the figures, and wrote the initial draft of the report. SAB assisted with data visualisation and the creation of figures. All authors approved the final version of the report.

Conflicts of interest

The authors declared no conflicts of interest.

Acknowledgments

This study was supported by the Maurice Wilkins Centre for Molecular Biodiscovery, the New Zealand Foundation for Research Science and Technology, and the Wellcome Trust.

References

1 Thompson JF, Scolyer RA, Kefford RF. Cutaneous melanoma. *Lancet* 2005; **365:** 687–701.
2 Morton DL, Wen DR, Wong JH, et al. Technical details of intraoperative lymphatic mapping for early stage melanoma. *Arch Surg* 1992; **127:** 392–99.
3 Morton DL, Thompson JF, Cochran AJ, et al. Sentinel-node biopsy or nodal observation in melanoma. *N Engl J Med* 2006; **355:** 1307–17.
4 Thompson JF, Uren RF. Lymphatic mapping in management of patients with primary cutaneous melanoma. *Lancet Oncol* 2005; **6:** 877–85.
5 Uren RF, Thompson JF, Howman-Giles R. Lymphatic drainage of the skin and breast: locating the sentinel nodes. Amsterdam: Harwood Academic, 1999.
6 Sappey MPC. Anatomie, Physiologie, Pathologie des Vaisseaux Lymphatiques considérés chez l'Homme et les Vertébrés. Paris: A Dehahaye et E Lecrosnier, 1874.
7 Fee HJ, Robinson DS, Sample WF, Graham LS, Holmes EC, Morton DL. The determination of lymph shed by colloidal gold scanning in patients with malignant melanoma: a preliminary study. *Surgery* 1978; **84:** 626–32.
8 Meyer CM, Lecklitner ML, Logic JR, Balch CE, Bessey PQ, Tauxe WN. Technetium-99m sulfur-colloid cutaneous lymphoscintigraphy in the management of truncal melanoma. *Radiology* 1979; **131:** 205–09.
9 Sullivan DC, Croker BPJ, Harris CC, Deery P, Seigler HF. Lymphoscintigraphy in malignant melanoma: 99mTc antimony sulfur colloid. *AJR Am J Roentgenol* 1981; **137:** 847–51.
10 Bergqvist L, Strand SE, Hafstrom L, Jonsson PE. Lymphoscintigraphy in patients with malignant melanoma: a quantitative and qualitative evaluation of its usefulness. *Eur J Nucl Med* 1984; **9:** 129–135.
11 Eberbach MA, Wahl RL. Lymphatic anatomy: functional nodal basins. *Ann Plast Surg* 1989; **22:** 25–31.
12 Thompson JF, Uren RF, Shaw HM, et al. Location of sentinel lymph nodes in patients with cutaneous melanoma: new insights into lymphatic anatomy. *J Am Coll Surg* 1999; **189:** 195–204.
13 Uren RF, Howman-Giles R, Thompson JF. Patterns of lymphatic drainage from the skin in patients with melanoma. *J Nucl Med* 2003; **44:** 570–82.
14 Reynolds HM, Dunbar PR, Uren RF, Thompson JF, Smith NP. Mapping melanoma lymphoscintigraphy data onto a 3D anatomically based model *Ann Biomed Eng* 2007; published online May 4, 2007. DOI:10.1007/s10439-007-9315-9.
15 Ackerman MJ. The visible human project. *Proc IEEE* 1998; **86:** 504–11.
16 de Wilt JH, Thompson JF, Uren RF, et al. Correlation between preoperative lymphoscintigraphy and metastatic nodal disease sites in 362 patients with cutaneous melanomas of the head and neck. *Ann Surg* 2004; **239:** 544–52.
17 Uren RF, Howman-Giles R, Thompson JF, et al. Interval nodes: the forgotten sentinel nodes in patients with melanoma. *Arch Surg* 2000; **135:** 1168–72.
18 Fernandez JW, Mithraratne P, Thrupp SF, Tawhai MH, Hunter PJ. Anatomically based geometric modelling of the musculo-skeletal system and other organs. *Biomech Model Mechan* 2004; **2:** 139–55.
19 Thompson JF, Saw RP, Colman MH, Howman-Giles RB, Uren RF. Contralateral groin node metastasis from lower limb melanoma. *Eur J Cancer* 1997; **33:** 976–77.
20 Uren RF, Howman-Giles R, Chung DKV, Thompson JF. Metastatic occlusion of a lymphatic collecting vessel in a patient with cutaneous melanoma and clinically normal lymph nodes. *Clin Nucl Med* 2007; **32:** 312–13.
21 Uren RF, Howman-Giles R, Chung DK, Morton RL, Thompson JF. The reproducibility in routine clinical practice of sentinel lymph node identification by pre-operative lymphoscintigraphy in patients with cutaneous melanoma. *Ann Surg Oncol* 2007; **14:** 899–905.

Appendix E

Web Interface for the Data Visualisation Paper

The following pages present screenshots of the website created alongside the data visualisation paper published in *The Lancet Oncology* (given in Appendix D). This website went online in July 2007 and can be seen at http://www.bioeng.auckland.ac.nz/melanoma/. It includes a version of the skin selection tool presented in Section 5.2 and selected heat maps shown in Section 5.1.1 and in Appendix B.

Google Analytics was used to determine how many visits were made to the website and associated statistics, and screenshots of these results are also given. There have been 782 visits to the website between 1 July 2007 and 28 May 2008, with 511 absolutely unique visitors. Visitors included people from 29 different countries/territories, where New Zealanders and Australians comprised the majority of viewers with 493 and 120 visits respectively. 84 visits have been made from the United States, while directly behind that 24 visits were made from the UK. Other visitors were largely from countries in Europe and Asia.

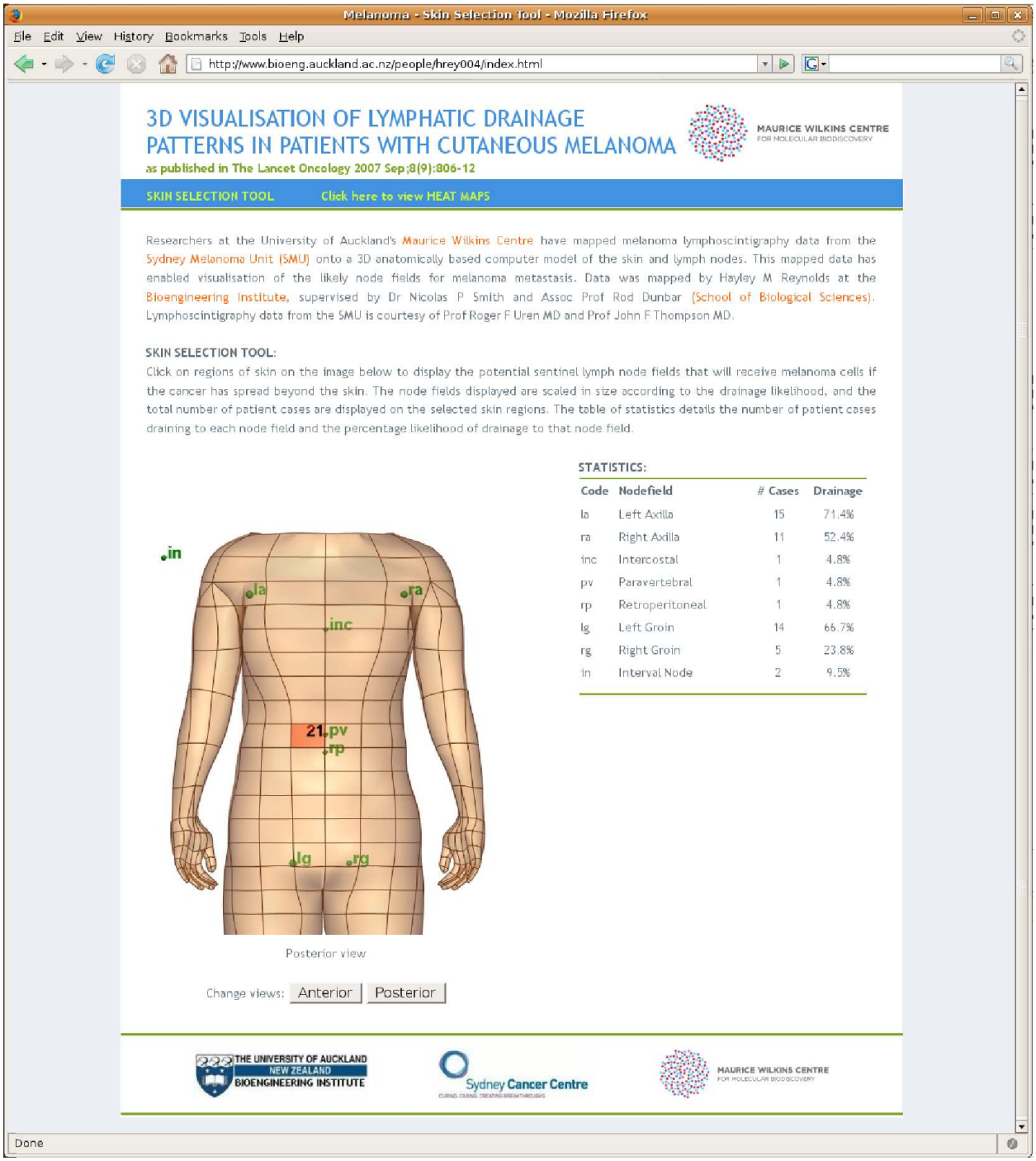

Figure E.1: Screenshot of the skin selection tool given in the data visualisation website.

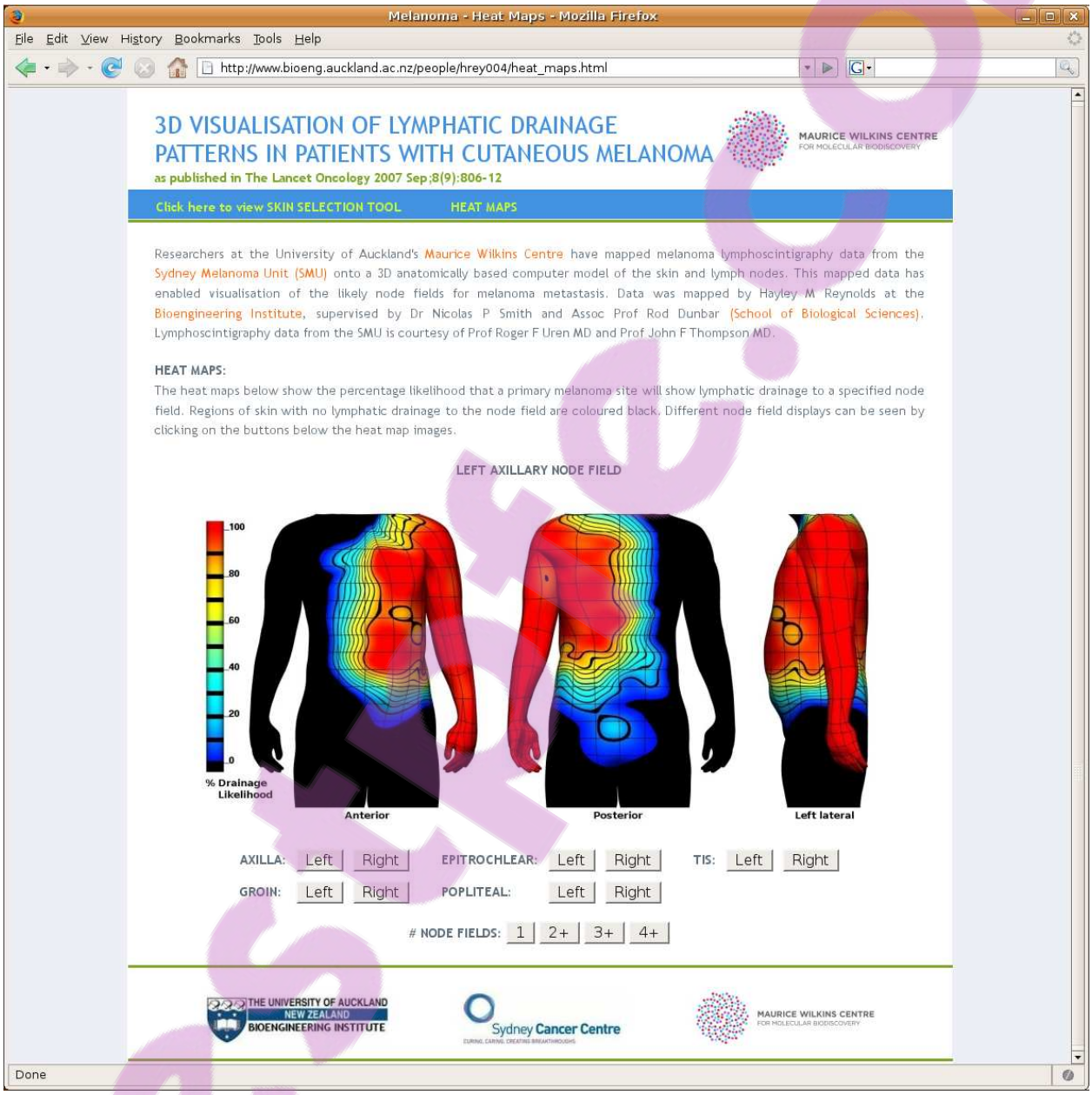

Figure E.2: Screenshot of the heat maps given on the data visualisation website.

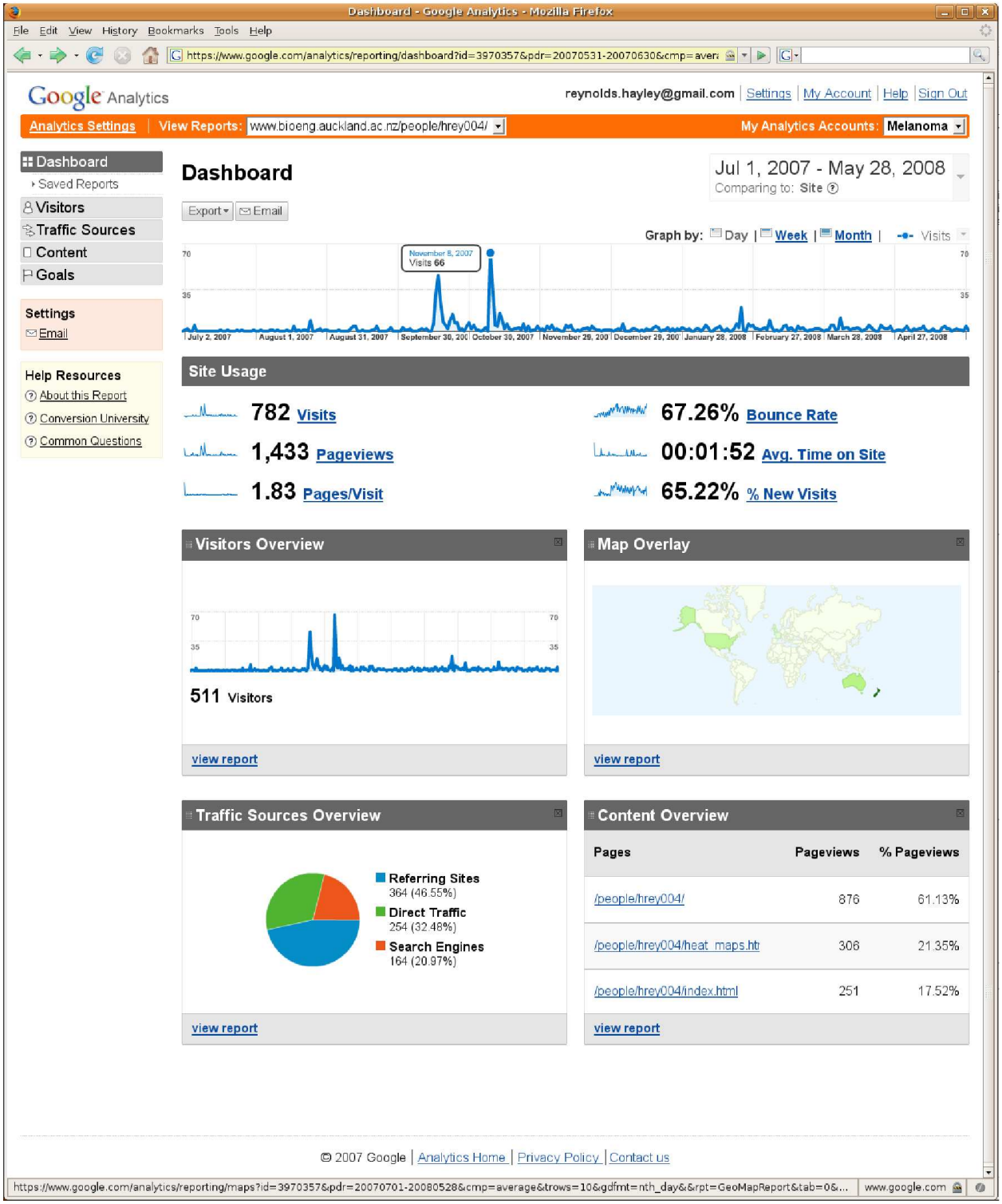

Figure E.3: Google Analytics summary of the visitors accessing the data visualisation website.

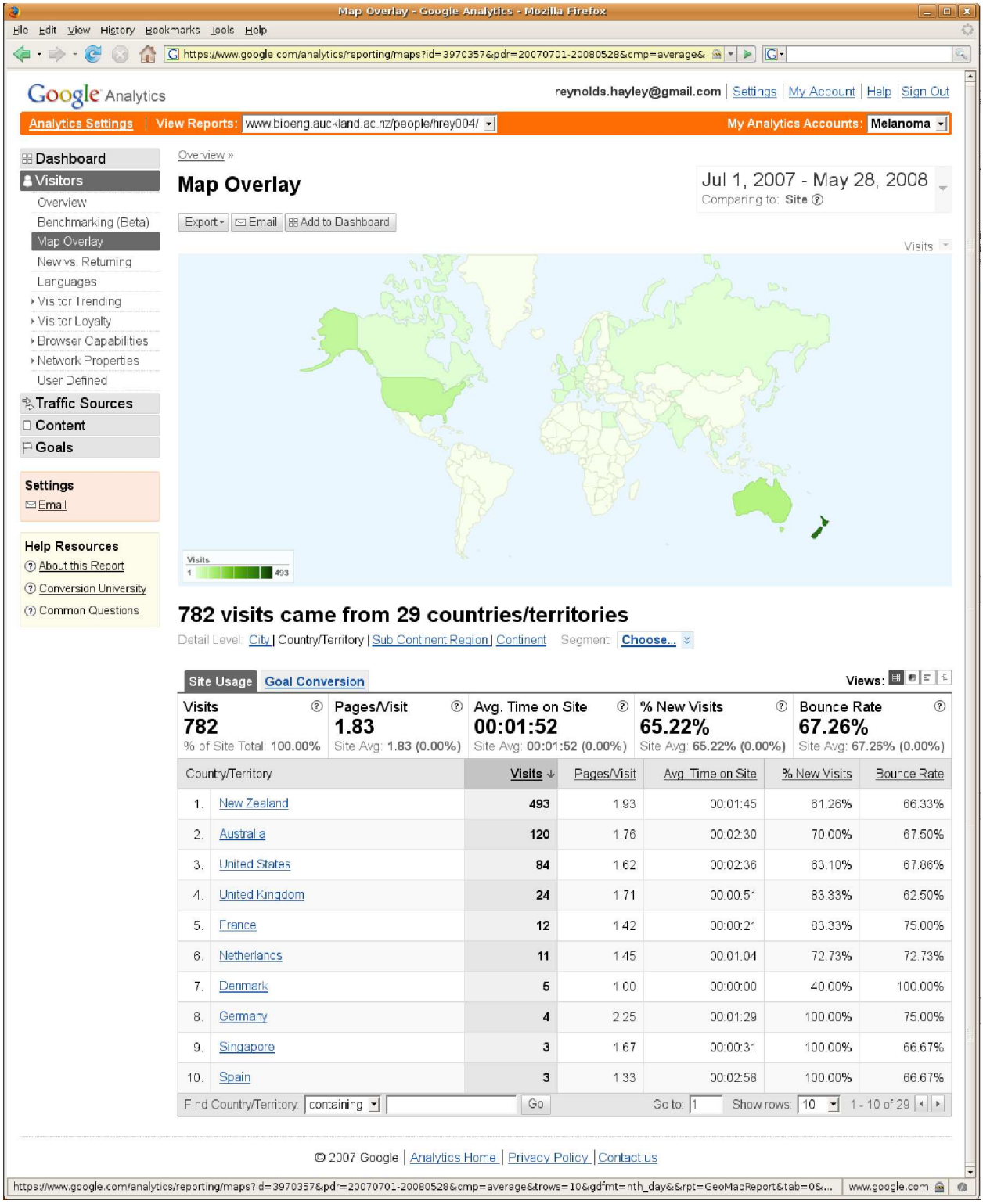

Figure E.4: Google Analytics Map Overlay visualising where website visitors were located.

Appendix F

Editorial Response to the Data Visualisation Paper

This editorial presents a response to the data visualisation paper given in Appendix D, which was published in *The Lancet Oncology*.

by a PET scan as non-responders—to completion or early termination of induction chemotherapy is worth pursuing.

Second, the authors chose a 35% decrease in [^{18}F]FDG avidity after one cycle of chemotherapy to stratify patients into responding and non-responding groups.[2] The rationale for doing so is well-presented in the authors' previous work,[5] but this definition of the optimum decrease in standard uptake value for defining responsiveness needs validation in independent studies, especially as the method proposed suggests dichotomising patients based on a continous variable. In a related issue, the authors have noted a new finding that patients who had a survival benefit associated with chemotherapy were both PET and histological responders.[2] Patients with response by PET, but without histological response, did no better than PET non-responders in terms of overall survival. The underlying mechanism for the observation that a tumour could have decreased [^{18}F]FDG avidity without histological response or survival advantage is not clear, but might be associated with a decrease in an inflammatory component by chemotherapy or the steroids administered without tumoricidal effect. Combined imaging for glycolytic activity and measures of tumour inflammation might be the next step to further minimise over-treatment.

Third, the authors pursued one way of incorporating PET-imaging data into a treatment algorithm: the early termination of treatment held to be ineffective. However, other possible approaches could be considered to treat patients who fail to respond to induction treatment on PET scan. For example, patients who show no PET response to one type of chemotherapy could be shifted successfully to treatment with another regimen during subsequent combined chemoradiation treatment.[7] Alternately, patients who have no evidence of chemosensitivity, and therefore, are at very high risk of recurrent disease, could be considered for definitive radiation treatment to the primary site rather than subjected to the morbidities associated with an oesophagectomy.

Robert J Downey, David H Ilson
Thoracic Service, Department of Surgery (RJD), and Gastrointestinal Oncology Service, Department of Medicine (DHI), Memorial Sloan-Kettering Cancer Center, New York, NY, USA
downeyr@MSKCC.ORG

The authors declared no conflicts of interest.

1 Gebski V, Burmeister Mark Smithers B, Foo K, Zalcberg J, Simes J, for the Australasian Gastro-Intestinal Trials Group. Survival benefits from neoadjuvant chemoradiotherapy or chemotherapy in oesophageal carcinoma: a meta-analysis. *Lancet Oncol* 2007; **8:** 226–34.
2 Lordick F, Ott K, Krause B-J, et al. PET to assess early metabolic response and to guide treatment of adenocarcinoma of the oesophagogastric junction: the MUNICON phase II trial. *Lancet Oncol* 2007; **8:** 797–805.
3 Meyers BF, Downey RJ, Decker PA, et al. American College of Surgeons Oncology Group Z0060. The utility of positron emission tomography in staging of potentially operable carcinoma of the thoracic esophagus: results of the American College of Surgeons Oncology Group Z0060 trial. *J Thorac Cardiovasc Surg* 2007; **133:** 738–45.
4 Rizk N, Downey RJ, Akhurst T, et al. Preoperative ^{18}[F]-fluorodeoxyglucose positron emission tomography standardized uptake values predict survival after esophageal adenocarcinoma resection. *Ann Thorac* 2006; **81:** 1076–81.
5 Weber WA, Ott K, Becker K, et al. Prediction of response to preoperative chemotherapy in adenocarcinomas of the esophagogastric junction by metabolic imaging. *J Clin Oncol* 2001; **19:** 3058–65.
6 Downey RJ, Akhurst T, Ilson D, et al. Whole body 18FDG-PET and the response of esophageal cancer to induction therapy: results of a prospective trial. *J Clin Oncol* 2003; **21:** 428–32.
7 Ku GY, Bains M, Rizk N, et al. Phase II trial of pre-operative cisplatin/irinotecan and radiotherapy for locally advanced esophageal cancer: PET scan after induction therapy may identify early treatment failure. *Proc Am Soc Clin Oncol* 2007; (abstr 9).

Defining the highway of lymphatic patterns for melanoma

See Articles page 806

In 1892, Herbert Snow advocated wide excision and elective lymph-node dissection (ELND) to control lymphatic permeation of melanoma metastases.[1] His studies suggested a connection between primary skin tumours and regional lymph nodes, indicating that treatment of melanoma should routinely include excision of these nodes.[1] Through most of the next century, regional lymph-node dissection was usually based on anatomical landmarks alone. Most of the descriptions of lymphatic drainage patterns were attributed to Sappey, who suggested that the vertical meridian through the torso and horizontal axis through the umbilicus defined four quadrants, each with separate drainage to the axilla or groin lymph-node basins.[2]

While retrospective studies were done to validate Snow's observations as to the importance of ELND, none of the randomised trials studying this procedure have shown a survival advantage of ELND. The apparent absence of therapeutic benefit from ELND, in part, relates to the relatively small number of patients with intermediate thickness melanoma with tumour-positive lymph nodes (about 20%) and perhaps to the inherent

Reflection and Reaction

error of dissecting lymph-node basins based solely on static assessment of lymphatic anatomy rather than dynamic assessment of lymphatic drainage.

In 1992, Morton and colleagues described their initial experience with intraoperative lymphatic mapping and sentinel-lymph-node biopsy (SLNB).[3] This technique, devised as an alternative to ELND, enables the surgeon to map the direct route of lymphatic spread from a primary melanoma to the regional lymph-node basin, and then excise selectively the first (sentinel) draining lymph node or nodes in this basin. Focused pathological examination of the lymphatic mapping and SLNB specimen provides a useful method of ultra-staging the regional lymph nodes. Complete lymph-node dissection (CLND) is reserved for patients who are most likely to achieve a survival benefit from the procedure, ie, those with metastasis to the sentinel lymph node. Patients who do not have regional lymph-node metastases can avoid the cost and morbidity of CLND.

Lymphatic mapping and SLNB is based on observations that afferent lymphatics and draining lymph nodes can be identified by cutaneous lymphoscintigraphy or by the intradermal injection of blue dyes into the primary melanoma site.[4] Lymphoscintigraphy enables precise identification of the lymph nodes at risk of metastases, but also points to occasional aberrant or unpredicted drainage to more than one site.

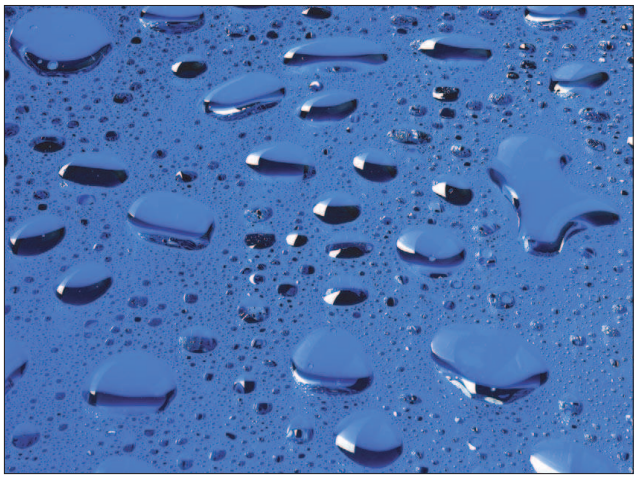

Intradermal injection of blue dye can identify afferent lymphatics and draining lymph nodes

Lymphatic mapping and SLNB has been shown by reseachers to be a reliable indicator of the tumour status of regional lymph nodes, probably upstaging about 15% of cases from ELND. With over 15 years of experience, we and other groups have confirmed the low (about 3%) nodal recurrence rate from the use of lymphatic mapping and SLNB. Based on these studies, lymphatic mapping and SLNB has replaced ELND and has become standard procedure for staging regional lymph nodes. Results of the Multicenter Selective Lymphadenectomy Trial[5] have validated the accuracy of lymphatic mapping and SLNB and have shown the importance of lymphoscintigraphy for mapping regional lymph nodes.

In this issue of *The Lancet Oncology*, Reynolds and co-workers describe their approach to organising lympho-scintigraphy data to provide a sophisticated working road map of the lymphatics of the skin.[6] The group created a mathematical model with three-dimensional computer imaging to replicate the patterns of lymphatic drainage that they had noted from over 5000 lymphoscintigrams in the past 10 years. The researchers compiled all the lymphoscintigraphy images, devised heat maps to predict drainage patterns, and established the relative risk of each skin site to have drainage to a particular lymph-node area, or in some cases, to multiple basins. Their aim was to improve imaging of the lymphatics and give guidance to the variations that they had recorded, as compared with the patterns predicted by Sappey. Reynolds and colleagues studied only non-head and neck primary tumours, and eliminated primary tumours that did not drain to the axillae or groin—making their first attempt at this project relatively straight forward, albeit less broadly applicable. Furthermore, as the authors point out, the model is not valid when lymphatic drainage has been altered by previous surgery. This study was based on the concept that traditional anatomical predictors of lymphatic drainage are inadequate, and the heat maps and interactive software Reynolds and colleagues have created should be valuable for educating clinicians and students. However, while useful for studying the variable anatomy of the cutaneous lymphatics, the heat maps should not be used as an alternative to lymphoscintigraphy, but rather as assurance that all the predicted lymph-node basins are known.

The work by Reynolds and co-workers is timely and provides valuable, interactive information on the anatomy of the skin and the draining lymphatics. Long-term follow-up of their 5000-plus cases might provide

additional information on the relation of the primary skin site to regional and potentially distant patterns of metastases. From their model, it is clear that the highway of lymphatics through the skin is far more complicated than that suggested by Sappey.

Richard Essner
Surgical Oncology and Laboratory of Molecular Therapeutics, John Wayne Cancer Institute, Santa Monica, CA, USA
essnerr@jwci.org

The author declared no conflicts of interest.

1 Snow H. Melanocytic cancerous disease. *Lancet* 1892; **2:** 872–74.
2 Sappey MPC. Anatomie, physiologie, pathologie des vaisseaux lymphatiques considérés chez l'homme et les vertébrés. Paris: A Dehahaye et E Lecrosnier, 1874.
3 Morton DL, Wen DR, Wong JH, et al. Technical details of intraoperative lymphatic mapping for early stage melanoma. *Arch Surg* 1992; **127:** 391–99.
4 Wong JH, Cagle LA, Morton DL. Lymphatic drainage of skin to a sentinel lymph node in a feline model. *Ann Surg* 1991; **214:** 637–41.
5 Morton DL, Thompson JF, Cochran AJ, et al. Sentinel-Node biopsy or nodal observation in melanoma. *N Engl J Med* 2006; **335:** 1307–17.
6 Reynolds HM, Dunbar PR, Uren RF, Blackett SA, Thompson JF, Smith NP. Three-dimensional visualisation of lymphatic drainage patterns in patients with cutaneous melanoma. *Lancet Oncol* 2007; **8:** 806–12.

Causes of thrombotic thrombocytopenic purpura

The mechanism for the development of thrombotic thrombocytopenic purpura (TTP) with gemcitabine and other chemotherapeutic drugs is attributed to endothelial-cell injury. In the excellent review by Zupancic and colleagues[1] in a recent issue of *The Lancet Oncology*, possible explanations for endothelial-cell injury are provided, including circulating immune complexes and cytokines. The downstream effects from the endothelial dysfunction, including release of nitric oxide and von Willebrand factor, and increased levels of tissue plasminogen activator, thrombomodulin, and plasminogen activator inhibitor, are described to promote the development of TTP.

However, the endothelial-cell injury in those treated with chemotherapeutic drugs is more likely to have been caused by the underlying malignancy than by the drugs themselves. This notion is supported by the findings of Snyder and colleagues.[2] In a review of patients who developed TTP with chemotherapy, of the 55 patients who were treated with different therapeutic strategies, 30 died, 17 of who had complications from TTP. 16 of these patients had stable or progressive malignant disease, suggesting the role of malignancy in driving TTP. In those who responded to the treatment for TTP, a decrease in serum concentration of circulating immune complexes was recorded which correlated with a good response of the malignancy to the antineoplastic drugs. This finding suggests that the formation of these complexes was the result of the malignancy rather than the chemotherapy.

Cancer is widely known to be associated with TTP, and thrombotic microangiopathy is seen in a small proportion of patients in almost all types of cancer,[3] which causes dysfunction of the endothelium, especially when metastasis occurs.[4] Endothelial injury results in the released the aforementioned factors, promoting the coagulation process of TTP.

Zupancic and colleagues suggest that more renal and pulmonary manifestations are present in chemotherapy-associated TTP compared with that in cancer-associated TTP. However, lung complications in this setting are nearly always secondary to blood products from fluid overload or possible transfusion-associated lung injury. Renal dysfunction is a common adverse effect of most chemotherapeutic drugs and, therefore, deciding whether or not this is secondary to TTP is difficult.

Furthermore, TTP and haemolytic-uremic syndrome (HUS) should not be used interchangeably. Historically, these two diseases have been considered as the extreme ends of a spectrum, with common features of microangiopathic haemolytic anaemia and thrombocytopenia, but with predominance of neurological symptoms in TTP and renal dysfunction in HUS. The pathogenesis of HUS has been shown to be different to that of TTP, with Shiga-like toxins implicated in typical HUS and genetic abnormalities of complement regulatory proteins in atypical HUS, which commonly occurs in association with antineoplastic drugs.[5] Many of the reports on chemotherapy-associated TTP described in the review by Zupancic and colleagues describe HUS rather than TTP. However, the management strategy for atypical HUS does not differ from TTP and includes interventions like plasma exchange.

The contributory role of chemotherapeutic drugs in the development of TTP is likely to be the impairment

Appendix G

Statistical Analysis Code in R

The following R code details the commands used to carry out selected statistical analysis methods defined in Chapter 6. Commands implemented to run the multinomial model symmetry test (described in Section 6.3) are given, as well as commands to determine 95% confidence intervals using non-parametric bootstrapping (described in Section 6.5) for each cluster.

Symmetry testing

```
## Read in the LS data
infile <- "G:/Significance_testing/reflected_LS_data.txt"
data<-read.table(infile,header=T)
attach(data)
names(data)
detach(data)

## Define the region of skin (using element numbers)
region<-c(467:470,483:486)

## Determine the corresponding LS data located on those elements
nm<-c("case","nodeField","element","numNodes","side","elemMap","nodeFieldMap")
dat<-cbind()
for (i in 1:length(region)) {
  dat<-rbind(dat,data[data$elemMap==region[i],])
}
names(dat)<-nm
attach(dat)

## Calculate number of cases and data entries
## located on each side of the body
num_NFsL<-0
num_NFsR<-0
num_melL<-0
num_melR<-0

ifelse(side[1]=="R",num_NFsR<-num_NFsR + 1,num_NFsL<-num_NFsL + 1)
ifelse(side[1]=="R",num_melR<-num_melR + 1,num_melL<-num_melL + 1)

for (i in 2:length(case)) {
  if (case[i]!=case[i-1]) {
    ifelse(side[i]=="R",num_melR<-num_melR + 1,num_melL<-num_melL + 1)
  }
  if (side[i]=="R"){
    num_NFsR<-num_NFsR + 1
  }
  else{
    num_NFsL<-num_NFsL + 1
  }
}

## Read in the nnet library
library(nnet)

## Define the element vectors as factors
element<-factor(element)
elemMap<-factor(elemMap)

## Fit multinomial model to the LS data
## (with side and elemMap as predictor variables
```

```
## and nodeFieldMap as the response variable)
mmod<-multinom(nodeFieldMap~elemMap+side+elemMap*side)

## Step through the model using the AIC criterion
## to determine the most important predictor variables
nmod_side<-step(mmod)

## Display the fitted model variables
predict(nmod_side,data[1,],type="probs")
summary(nmod_side)
```

Non-parametric bootstrapping

```
## Read in the LS data
infile <- "G:/Significance_testing/clusters/reflected_LS_data_for_CIs.txt"
all_data<-read.table(infile,header=T)
attach(all_data)
names(all_data)

## Define the cluster number
## and the elements within the cluster
cluster=1
element<-c(17,23,25,29,35,37,39,41:45,47:49,51,54:56,59:63,67:76,78,80,82,83,
        85,86,88,91:93,95,96,98:124,325:331,333:363,365:368,370,371,379:383,
        395:397,399,401,415,428,429,431,445,461)

## Determine the corresponding LS data located on those elements
S_nm<-c("S_case","S_nodeField","S_element","S_numNodes")
data<-cbind()
for (i in 1:length(element)) {
  data<-rbind(data,all_data[all_data$element==element[i],])
}
names(data)<-S_nm
attach(data)

## Calculate the number of cases and use this to find the average
## number of cases draining to each node field (point estimate)
numCases<-1
for (i in 2:length(S_case)) {
  if (S_case[i]!=S_case[i-1]) {
    numCases<-numCases + 1
  }
}
pt<-table(S_nodeField)/numCases

nm<-c('cs','nf','elem','nNodes')

## Determine start and end position in array for each patient case
```

```
## (required due to independency)
start<-1
for (i in 2:length(S_case)) {
  if (S_case[i]!=S_case[i-1]) {
    if (start[length(start)]==1) {
      finish<-(i-1)
    } else {
      finish<-rbind(finish,i-1)
    }
    start<-rbind(start,i)
  }
}
finish<-rbind(finish,length(S_case))

sampleProbs<-cbind()

## Draw 1000 bootstrap samples
for (i in 1:1000) {
  detach(data)
  smpl<-sample(1:length(start),length(start),replace=TRUE)
  dat<-cbind()
  for (j in smpl) {
    for (k in start[j]:finish[j]){
      dat<-rbind(dat,data[k,])
    }
  }
  names(dat)<-nm
  attach(dat)
  output<- table(nf)/ numCases
  sampleProbs<-rbind(sampleProbs,output)
  detach(dat)
  attach(data)
}

## Determine the 95% confidence intervals
qt<-cbind()
for (i in 1:length(levels(nodeField))){
  qt<-rbind(qt,cbind(levels(nodeField)[i],t(quantile(sampleProbs[,i],
      probs=c(0.025, 0.975)))))
}

## Write output files with point estimates and confidence intervals
outfilename <- "G:/Significance_testing/clusters/reflected_CI_cluster_"
outfilename <- paste(outfilename,cluster,sep="")
outfilename <- paste(outfilename,".txt",sep="")

write(qt[1,],file=outfilename,ncolumns=3,append = FALSE)
for (i in 2:41){
  write(qt[i,],file=outfilename,ncolumns=3,append = TRUE)
}
write(" ",file=outfilename,ncolumns=1,append = TRUE)
write(pt,file=outfilename,ncolumns=1,append = TRUE)
```

References

AIHW (2008), 'Australian Institute of Health and Welfare - Australian cancer incidence statistics', http://www.aihw.gov.au/cancer/.

AJCC Cancer Staging Manual (2002), 6 edn, Springer, New York.

Alazraki, N. P., Eshima, D., Eshima, L. A., Herda, S. C., Murray, D. R., Vansant, J. P. & Taylor, A. T. (1997), 'Lymphoscintigraphy, the sentinel node concept, and the intraoperative gamma probe in melanoma, breast cancer, and other potential cancers', *Sem. Nucl. Med.* **27**(1), 55–67.

Balch, C. M., Buzaid, A. C., Soong, S., Atkins, M. B., Cascinelli, N., Coit, D. G., Fleming, I. D., Gershenwald, J. E., Houghton Jr, A., Kirkwood, J. M., McMasters, K. M., Mihm, M. F., Morton, D. L., Reintgen, D. S., Ross, M. I., Sober, A., Thompson, J. A. & Thompson, J. F. (2001), 'Final version of the American Joint Committee on Cancer staging system for cutaneous melanoma', *J. Clin. Oncol.* **19**(16), 3635–3648.

Balch, C. M., Soong, S., Gershenwald, J. E., Thompson, J. F., Reintgen, D. S., Cascinelli, N., Urist, M., McMasters, K. M., Ross, M. I., Kirkwood, J. M., Atkins, M. B., Thompson, J. A., Coit, D. G., Byrd, D., Desmond, R., Zhang, Y., Liu, P., Lyman, G. H. & Morabito, A. (2001), 'Prognostic factors analysis of 17,600 melanoma patients: validation of the American Joint Committee on Cancer melanoma staging system', *J. Clin. Oncol.* **19**(16), 3622–3634.

Balch, C. M., Wilkerson, J. A., Murad, T. M., Soong, S., Ingalls, A. L. & Maddox, W. A. (1980), 'The prognostic significance of ulceration of cutaneous melanoma', *Cancer* **45**(12), 3012–3017.

Bergqvist, L., Strand, S. E., Hafström, L. & Jönsson, P. E. (1984), 'Lymphoscintigraphy in patients with malignant melanoma: a quantitative and qualitative evaluation of its usefulness', *Eur. J. Nucl. Med.* **9**(3), 129–135.

Bradley, C. P., Pullan, A. J. & Hunter, P. J. (1997), 'Geometric modeling of the human torso using cubic hermite elements', *Ann. Biomed. Eng.* **25**, 96–111.

Breslow, A. (1970), 'Thickness, cross-sectional areas and depth of invasion in the prognosis of cutaneous melanoma', *Ann. Surg.* **172**(5), 902–908.

Cascinelli, N. (1999), 'WHO declares lymphatic mapping to be the standard of care for melanoma', **13**, 288.

Chernick, M. R. (1999), *Bootstrap Methods: A Practitioner's Guide*, John Wiley and Sons Inc., New York.

Clark Jr, W. H., From, L., Bernardino, E. A. & Mihm, M. C. (1969), 'The histogenesis and biologic behavior of primary human malignant melanomas of the skin', *Cancer Res.* **29**, 705–727.

Clemente, C. D. (1997), *Anatomy: A Regional Atlas of the Human Body*, fourth edn, Williams and Wilkins, Maryland.

Cox, S. L. (2007), Computational ergonomics: An anatomically based finite element model of the lower limbs in the seated posture, Master's thesis, University of Auckland.

Crampin, E. J., Halstead, M., Hunter, P., Nielsen, P., Noble, D., Smith, N. & Tawhai, M. (2004), 'Computational physiology and the physiome project', *Exp. Physiol.* **89**(1), 1–26.

de Wilt, J. H. W., Thompson, J. F., Uren, R. F., Ka, V. S. K., Scolyer, R. A., McCarthy, W. H., O'Brien, C. J., Quinn, M. J. & Shannon, K. F. (2004), 'Correlation between preoperative lymphoscintigraphy and metastatic nodal disease in 362 patients with cutaneous melanomas of the head and neck', *Ann. Surg.* **239**(4), 544–552.

Eberbach, M. A. & Wahl, R. L. (1989), 'Lymphatic anatomy: functional nodal basins', *Ann. Plast. Surg.* **22**(1), 25–31.

Efron, B. (1979), 'Bootstrap methods: Another look at the jackknife', *Ann. Stat.* **7**(1), 1–26.

Efron, B. & Tibshirani, R. J. (1993), *An Introduction to the Bootstrap*, Chapman & Hall, New York.

Everitt, B. S., Landau, S. & Leese, M. (2001), *Cluster analysis*, 4 edn, Oxford University Press, London.

Faraway, J. J. (2006), *Extending the Linear Model with R: generalized linear, mixed effects and nonparametric regression models*, Chapman and Hall/CRC, Florida.

Fee, H. J., Robinson, D. S., Sample, W. F., Graham, L. S., Holmes, E. C. & Morton, D. L. (1978), 'The determination of lymph shed by colloidal gold scanning in patients with malignant melanoma: a preliminary study', *Surg.* **84**(5), 626–632.

Fernandez, J. W. (2004), An Anatomically Based Finite Element Model of Patella Articulation: Towards a Diagnostic Tool, PhD thesis, University of Auckland.

Fernandez, J. W., Mithraratne, P., Thrupp, S. F., Tawhai, M. H. & Hunter, P. J. (2004), 'Anatomically based geometric modelling of the musculo-skeletal system and other organs', *Biomech. Model. Mechan.* **2**(3), 139–155.

Fischer, M., Franzeck, U. K., Herrig, I., Costanzo, U., Wen, S., Schiesser, M., Hoffmann, U. & Bollinger, A. (1996), 'Flow velocity of single lymphatic capillaries in human skin', *Am. J. Physiol.* **270**(1), H358–H363.

Fisher, R. A. (1938), *Statistical methods for research workers*, Oliver and Boyd, London.

Fortner, J. G., Das Gupta, T. & McNeer, G. (1965), 'Primary malignant melanoma on the trunk: an analysis of 194 cases', *Ann. Surg.* **161**(2), 161–169.

Greenwood, P. E. & Nikulin, M. S. (1996), *A Guide to Chi-squared Testing*, John Wiley & Sons, New York.

Hardin, J. W. & Hilbe, J. M. (2002), *Generalized Estimating Equations*, Chapman & Hall/CRC, Florida.

Jor, J. W., Nash, M. P., Nielsen, P. M. & Hunter, P. J. (2007), Modelling the mechanical properties of human skin: towards a 3D discrete fibre model, *in* 'Proceedings of the 29th Annual International Conference of the IEEE EMBS', Lyon, pp. 6641–6644.

Leong, S. P., Achtem, T. A., Habib, F. A., Steinmetz, I., Morita, E., Allen, R. E., Kashani-Sabet, M. & Sagebiel, R. (1999), 'Discordancy between clinical predictions vs lymphoscintigraphic and intraoperative mapping of sentinel lymph node drainage of primary melanoma', *Arch. Dermatol.* **135**(12), 1472–1476.

Martinez-Monge, R., Fernandes, P. S., Gupta, N. & Gahbauer, R. (1999), 'Cross-sectional nodal atlas: a tool for the definition of clinical target volumes in three-dimensional radiation therapy planning', *Radiology* **211**(3), 815–828.

Meyer, C. M., Lecklitner, M. L., Logic, J. R., Balch, C. E., Bessey, P. Q. & Tauxe, W. N. (1979), 'Technetium-99m sulfur-colloid cutaneous lymphoscintigraphy in the management of truncal melanoma', *Radiology* **131**(1), 205–209.

Mooney, C. Z. & Duval, R. D. (1993), *Bootstrapping: A Nonparametric Approach to Statistical Inference*, Sage Publications, California.

Morton, D. L., Hoon, D. S. B., Cochran, A. J., Turner, R. R., Essner, R., Takeuchi, H., Wanek, L. A., Glass, E., Foshag, L. J., Hsueh, E. C., Bilchik, A. J., Elashoff, D. & Elashoff, R. (2003), 'Lymphatic mapping and sentinel lymphadenectomy for early-stage melanoma: Therapeutic utility and implications of nodal microanatomy and molecular staging for improving the accuracy of detection of nodal micrometastases', *Ann. Surg.* **238**(4), 538–550.

Morton, D. L., Thompson, J. F., Cochran, A. J., Mozzillo, N., Elashoff, R., Essner, R., Nieweg, O. E., Roses, D. F., Hoekstra, H. J., Karakousis, C. P., Reintgen, D. S., Coventry, B. J., Glass, E. C. & Wang, H. J. (2006), 'Sentinel-node biopsy or nodal observation in melanoma', *N. Eng. J. Med.* **355**, 1307–1317.

Morton, D. L., Thompson, J. F., Essner, R., Elashoff, R., Stern, S. L., Nieweg, O. E., Roses, D. F., Karakousis, C. P., Mozzillo, N., Reintgen, D., Wang, H. J., Glass, E. C. & Cochran, A. J. (1999), 'Validation of the accuracy of intraoperative lymphatic mapping and sentinel lymphadenectomy for early-stage melanoma: a multicenter trial', *Ann. Surg.* **230**(4), 453–463.

Morton, D. L., Wen, D. R., Wong, J. H., Economou, J. S., Cage, L. A., Storm, F. K., Foshag, L. J. & Cochran, A. J. (1992), 'Technical details of intraoperative lymphatic mapping for early stage melanoma', *Arch. Surg.* **127**, 398–399.

Norman, J., Cruse, C. W., Espinosa, C., Cox, C., Berman, C., Clark, R., Saba, H., Wells, K. & Reintgen, D. (1991), 'Redefinition of cutaneous lymphatic drainage with the use of lymphoscintigraphy for malignant melanoma', *Am. J. Surg.* **162**(5), 432–437.

NZHIS (2007), 'NZ Health Information Service - Cancer: New registrations and deaths 2004', http://www.nzhis.govt.nz/.

O'Brien, C. J., Uren, R. F., Thompson, J. F., Howman-Giles, R. B., Petersen-Schaefer, K., Shaw, H. M., Quinn, M. J. & McCarthy, W. H. (1995), 'Prediction of potential metastatic sites in cutaneous head and neck melanoma using lymphoscintigraphy', *Am. J. Surg.* **170**(5), 461–466.

O'Sullivan, M., Vössner, S. & Wegener, J. (1998), Testing temporal correctness of real-time systems - a new approach using genetic algorithms and cluster analysis, *in* '6th European International Conference on Software Testing, Analysis and Review', EuroSTAR'98, Munich, Germany.

O'Toole, G. A., Hettiaratchy, S., Allan, R. & Powell, B. W. (2000), 'Aberrant sentinel nodes in malignant melanoma', *Brit. J. Plast. Surg.* **53**(5), 415–417.

Park, J. S., Chung, M. S., Hwang, S. B., Shin, B. & Park, H. S. (2006), 'Visible Korean Human: its techniques and applications', *Clin. Anat.* **19**(3), 216–224.

Pathak, I., O'Brien, C. J., Petersen-Schaeffer, K., McNeil, E. B., McMahon, J., Quinn, M. J., Thompson, J. F. & McCarthy, W. H. (2001), 'Do nodal metastases from cutaneous melanoma of the head and neck follow a clinically predictable pattern?', *Head & Neck* **23**(9), 785–790.

Poon, I., Fischbein, N., Lee, N., Akazawa, P., Xia, P., Quivey, J. & Phillips, T. (2004), 'A population-based atlas and clinical target volume for the head-and-neck lymph nodes', *Int. J. Radiat. Oncol. Biol. Phys.* **59**(5), 1301–1311.

Pullan, A., Cheng, L., Yassi, R. & Buist, M. (2004), 'Modelling gastrointestinal bioelectric activity', *Prog. Biophys. Mol. Biol.* **85**(2-3), 523–550.

Qatarneh, S. M., Kiricuta, I., Brahme, A., Tiede, U. & Lind, B. K. (2006), 'Three-dimensional atlas of lymph node topography based on the visible human dataset', *Anat. Rec. B New Anat.* **289**(3), 98–111.

Reintgen, D., Cruse, C. W., Wells, K., Berman, C., Fenske, N., Glass, F., Schroer, K., Heller, R., Ross, M., Lyman, G., Cox, C., Rappaport, D., Seigler, H. F. & Balch, C. (1994), 'The orderly progression of melanoma nodal metastases', *Ann. Surg.* **220**(6), 759–767.

Reynolds, H. M., Smith, N. P. & Hunter, P. J. (2004), Construction of an anatomically accurate geometric model of the forearm and hand musculo-skeletal system, *in* 'Annual Meeting Proceedings, 26th IEEE EMBS Annual International Conference, Sept. 1–5, 2004', San Francisco, pp. 265–269.

Robbins, K. T., Clayman, G., Levine, P. A., Medina, J., Sessions, R., Shaha, A., Som, P., Wolf, G. T., American Head and Neck Society & American Academy of Otolaryngology–Head and Neck Surgery (2002), 'Neck dissection classification update: revisions proposed by the American Head and Neck Society and the American Academy of Otolaryngology-Head and Neck Surgery', *Arch. Otolaryngol. Head Neck Surg.* **128**(7), 747–748.

Sappey, M. P. C. (1874), *Anatomie, Physiologie, Pathologie des vaisseaux Lymphatiques consideres chez L'homme at les Vertebres*, Paris.

Smith, N. P., Pullan, A. J. & Hunter, P. J. (2000), 'Generation of an anatomically based geometric coronary model', **28**(1), 14–25.

SMU (2005), 'The Sydney Melanoma Unit', http://www.smu.org.au/.

Spitzer, V. M., Ackerman, M. J., Scherzinger, A. L. & Whitlock, D. (1996), 'The visible human male: a technical report', *J. Am. Med. Inform. Assoc.* **3**(2), 118–130.

Spitzer, V. M. & Whitlock, D. G. (1998), 'The visible human dataset: The anatomical platform for human simulation', *Anat. Rec.* **253**(2), 49–57.

Statius Muller, M. G., Hennipman, F. A., van Leeuwen, P. A., Pijpers, R., Vuylsteke, R. J. & Meijer, S. (2002), 'Unpredictability of lymphatic drainage patterns in melanoma patients', *Eur. J. Nucl. Med. Mol. Imaging* **29**(2), 255–261.

Suami, H., Taylor, G. I. & Pan, W. R. (2005), 'A new radiographic cadaver injection technique for investigating the lymphatic system', *Plast. Reconstr. Surg.* **115**(7), 2007–2013.

Sugarbaker, E. V. & McBride, C. M. (1976), 'Melanoma of the trunk: the results of surgical excision and anatomic guidelines for predicting nodal metastasis', *Surg.* **80**(1), 22–30.

Sullivan, D. C., Croker, B. P., Harris, C. C., Deery, P. & Seigler, H. F. (1981), 'Lymphoscintigraphy in malignant melanoma: 99mtc antimony sulfur colloid', *Am. J. Roentgenol.* **137**(4), 847–851.

Swartz, M. A. (2001), 'The physiology of the lymphatic system', *Adv. Drug Deliv. Rev.* **50**(1-2), 3–20.

Swartz, M. A. & Skobe, M. (2001), 'Lymphatic function, lymphangiogenesis, and cancer metastasis', *Microsc. Res. Tech.* **55**(2), 92–99.

Tawhai, M. & Burrowes, K. (2003), 'Developing integrative computational models of pulmonary structure', *Anat. Rec.* **275B**, 207–218.

Thompson, J. F., Morton, D. L. & Kroon, B. B. R., eds (2004), *Textbook of Melanoma*, Martin Dunitz, London.

Thompson, J. F., Saw, R. P., Colman, M. H., Howman-Giles, R. B. & Uren, R. F. (1997), 'Contralateral groin node metastasis from lower limb melanoma', *Eur. J. Cancer* **33**(6), 976–977.

Thompson, J. F., Scolyer, R. A. & Kefford, R. F. (2005), 'Cutaneous melanoma', *Lancet* **365**, 687–701.

Thompson, J. F. & Shaw, H. M. (2007), 'Sentinel node mapping for melanoma: results of trials and current applications', **16**(1), 35–54.

Thompson, J. F. & Uren, R. F. (2000), 'What is a 'sentinel' lymph node?', *Eur. J. Surg. Oncol.* **26**, 103–104.

Thompson, J. F. & Uren, R. F. (2004), 'Teaching points on lymphatic mapping for melanoma from the Sydney Melanoma Unit', *Semin. Oncol.* **31**(3), 349–356.

Thompson, J. F. & Uren, R. F. (2005), 'Lymphatic mapping in management of patients with primary cutaneous melanoma', *Lancet Oncol.* **6**(11), 877–885.

Thompson, J. F., Uren, R. F., Saw, R. P. & Stevens, G. N. (2005), 'Internal mammary node metastasis from primary cutaneous melanoma on the anterior chest', *ANZ J. Surg.* **75**, 723–725.

Uren, R. F. (2007), Personal communication.

Uren, R. F., Howman-Giles, R. B., Thompson, J. F., Shaw, H. M. & McCarthy, W. H. (1995), 'Lymphatic drainage from peri-umbilical skin to internal mammary nodes', *Clin. Nucl. Med.* **20**(3), 254–255.

Uren, R. F., Howman-Giles, R., Chung, D. K., Morton, R. L. & Thompson, J. F. (2007), 'The reproducibility in routine clinical practice of sentinel lymph node identification by pre-operative lymphoscintigraphy in patients with cutaneous melanoma', *Ann. Surg. Oncol.* **14**(2), 899–905.

Uren, R. F., Howman-Giles, R., Chung, D. & Thompson, J. F. (2004), 'Nuclear medicine aspects of melanoma and breast lymphatic mapping', *Semin. Oncol.* **31**(3), 338–348.

Uren, R. F., Howman-Giles, R. & Thompson, J. F. (2003), 'Patterns of lymphatic drainage from the skin in patients with melanoma', *J. Nucl. Med.* **44**(4), 570–582.

Uren, R. F., Howman-Giles, R., Thompson, J. F. & McCarthy, W. H. (1998), 'Exclusive lymphatic drainage from a melanoma on the back to intraabdominal lymph nodes', *Clin. Nucl. Med.* **23**(2), 71–73.

Uren, R. F., Howman-Giles, R., Thompson, J. F., McCarthy, W. H., Quinn, M. J., Roberts, J. M. & Shaw, H. M. (2000), 'Interval nodes: the forgotten sentinel nodes in patients with melanoma', *Arch. Surg.* **135**, 1168–1172.

Uren, R. F., Howman-Giles, R., Thompson, J. F., Quinn, M. J., O'Brien, C., Shaw, H. M., Bosch, C. M. & McCarthy, W. H. (1996), 'Lymphatic drainage to triangular intermuscular space lymph nodes in melanoma on the back', *J. Nucl. Med.* **37**(6), 964–966.

Uren, R. F., Howman-Giles, R., Thompson, J. F., Roberts, J. & Bernard, E. (1998), 'Variability of cutaneous lymphatic flow rates in melanoma patients', *Melanoma Res.* **8**(3), 279–282.

Uren, R. F., Thompson, J. F. & Howman-Giles, R. B. (1999), *Lymphatic drainage of the skin and breast: locating the sentinel nodes*, Harwood academic, Amsterdam.

Uren, R. F., Thompson, J. F., Howman-Giles, R. & Chung, D. K. (2006), 'The role of lymphoscintigraphy in the detection of lymph node drainage in melanoma', *Surg. Oncol. Clin. N. Am.* **15**(2), 285–300.

van der Ploeg, I. M., Valdés Olmos, R. A., Nieweg, O. E., Rutgers, E. J., Kroon, B. B. & Hoefnagel, C. A. (2007), 'The additional value of SPECT/CT in lymphatic mapping in breast cancer and melanoma', *J. Nucl. Med.* **48**(11), 1756–1760.

Vössner, S. & Braunstingl, R. (1996), *G.O.A.L (Genetic Optimization Algorithm)*, Genetic Optimisation Lab, Technical University Graz, Austria.

Vössner, S., O'Sullivan, M. & Wegener, J. (1999), Genetic algorithm with cluster analysis for software testing, *in* '12th International Software Quality Week '99 Conference', California.

Wastell, D. G. & Gray, R. (1987), 'The numerical approach to classification: a medical application to develop a typology for facial pain', *Stat. Med.* **6**(2), 137–146.

Wolpert, L. (2005), 'Development of the asymmetric human', *European Review* **13**(S2), 97–103.

Zelterman, D. (2006), *Models for Discrete Data*, Oxford University Press, Oxford.

Zhang, S. X., Heng, P. A., Liu, Z. J., Tan, L. W., Qiu, M. G., Li, Q. Y., Liao, R. X., Li, K., Cui, G. Y., Guo, Y. L., Yang, X. P., Liu, G. J., Shan, J. L., Liu, J. J., Zhang, W. G., Chen, X. H., Chen, J. H., Wang, J., Chen, W., Lu, M., You, J., Pang, X. L., Xiao, H. & Xie, Y. M. (2003), 'Creation of the Chinese visible human data set', *Anat. Rec. B New Anat.* **275**(1), 190–195.